Coupled hydraulic-mechanical-chemical processes in porous and fractured rocks

Zur Erlangung des akademischen Grades einer

DOKTORIN DER NATURWISSENSCHAFTEN

von der KIT-Fakultät für
Bauingenieur-, Geo- und Umweltwissenschaften

des Karlsruher Instituts für Technologie (KIT)

genehmigte

DISSERTATION

von

M.Sc. Sina Katrin Hale

aus Heilbronn

Tag der mündlichen Prüfung:

28. Februar 2022

Referent: Prof. Dr. habil. Philipp Blum

Korreferent: Prof. Dr. habil. Christoph Hilgers

Karlsruhe 2022

Glück und Zuversicht vermag man selbst in Zeiten der Dunkelheit zu finden. Man darf bloß nicht vergessen, ein Licht leuchten zu lassen.

– Albus Dumbledore (Harry Potter und der Gefangene von Askaban, J.K. Rowling)

Dedicated to all my loved ones who have accompanied me on this journey.

ABSTRACT

Coupled hydraulic, mechanical and chemical processes have to be considered for numerous subsurface utilizations and are crucial for analyzing the potential, safety and risks as well as the future development of a geosystem. Some subsurface applications, such as radioactive waste disposal, energy storage and geothermal energy usage, also play a key role in the transition to renewable energy resources as part of the global climate action. This thesis focuses on the development of methodological-analytical approaches and tools that can be used to characterize coupled processes in porous and fractured rocks. By investigating two different lithologies and observation scales in the µm- to m-range, this thesis contributes to a better understanding of coupled processes in reservoir and host rocks.

The first part of the thesis considers hydraulic-mechanical (HM) processes and properties in fractured rocks. Fractures represent important flow paths in the rock but are also highly sensitive to mechanical influences. In the first study, a systematic method comparison for a non-invasive quantification of hydraulic fracture apertures is presented. Three different measuring instruments, a portable air permeameter, a microscope camera and a 3D laser scanner, are applied and evaluated on a natural single fracture in a well-known German reservoir analog (Flechtinger Sandstone). This case study shows that the air permeameter provides the most robust results, has the highest investigation depth, and offers substantial advantages in terms of mobility, time expenditure and data processing. For the optical fracture characterization approaches, the hydraulic aperture is determined indirectly by means of various model assumptions based on the mechanical aperture and the fracture roughness. This results in deviations of up to 27 % (microscope camera) and up to 260 % (3D laser scanner) compared to the results of the air permeameter.

Based on the single fracture analysis, the presented methodology is transferred to the field scale and is optimized for application to a host rock formation for nuclear waste disposal. In the second study, a HM characterization of an excavation damaged zone in the Opalinus Clay of the Mont Terri rock laboratory in Switzerland is performed. The analysis of the discrete fracture network in the investigated EZ-B niche, consisting of tectonic and artificial discontinuities, shows that the uncovered excavation damaged zone is characterized by hydraulic apertures of up to 112 µm. Progressive desaturation of the tunnel walls over a period of about 15 years mostly prevented self-sealing processes. The physico-mechanical rock parameters determined on-site by using needle penetrometer tests also illustrate the sensitivity of the Opalinus Clay to tunnel ventilation and indicate a negative correlation of rock strength or stiffness and water content due to a pronounced hydromechanical coupling behavior.

The second part of the thesis focuses on hydraulic-chemical (HC) processes in the porous medium and addresses reactive transport in a reservoir rock. In particular, porosity and permeability changes induced by dissolution or precipitation reactions can significantly alter reservoir properties. The third study investigates the dissolution of calcite cement in the Flechtinger Sandstone and the transferability of experimental reaction rates from the µm-mm-scale (mineral surface) to the cm-scale (core samples). Flow-through experiments on four sandstone cores are used to determine the range of dissolution rates on the cm-scale for different reaction time periods and varying hydraulic boundary conditions. This is contrasted with temporally and spatially resolved calcite dissolution rates at the µm-mm-scale from surface analyses using vertical scanning interferometry. Based on segmented X-ray micro-computed tomography scans of the core samples, a geometric approach is established to estimate the fluid-accessible surface area of the heterogeneously distributed calcite cement within the low-permeable and complex sandstone. Based on this introduced surface parameter, the rate information on the µm-mm scale is transferred to the core scale, yielding deviations of less than one order of magnitude between the upscaled and measured dissolution rates for all studied samples.

Within the scope of this thesis, different measurement methods and approaches are identified, developed, optimized and validated, which can be used to describe and interpret coupled hydraulic-mechanical-chemical processes and to determine related key parameters in fractured and porous rocks. The investigative approach and the obtained results therefore provide a valuable basis for predicting the behavior of natural systems on higher length and time scales.

KURZFASSUNG

Gekoppelte hydraulische, mechanische und chemische Prozesse sind bei zahlreichen Anwendungen im Untergrund zu berücksichtigen und entscheidend für die Analyse des Potenzials, der Sicherheit und Risiken sowie der zukünftigen Entwicklung eines Geosystems. Einige solcher Untergrundnutzungen wie die Endlagerung radioaktiver Abfälle, die Speicherung von Energieträgern oder die Geothermie haben darüber hinaus einen hohen Stellenwert bei der Energiewende im Rahmen der weltweiten Klimaschutzaktivitäten. Diese Arbeit fokussiert sich auf die Entwicklung von methodisch-analytischen Ansätzen und Werkzeugen, welche zur Charakterisierung von gekoppelten Prozessen in porösen und geklüfteten Gesteinen herangezogen werden können. Durch Betrachtung zweier unterschiedlicher Lithologien sowie Beobachtungsmaßstäben vom µm- bis in den m-Bereich trägt diese Arbeit zu einem besseren Verständnis gekoppelter Prozesse in Reservoir- und Wirtsgesteinen bei.

Der erste Teil der Arbeit befasst sich mit hydraulisch-mechanischen (HM) Prozessen und Eigenschaften in geklüfteten Gesteinen. Klüfte stellen wichtige Fließpfade im Gestein dar, sind jedoch auch hochsensibel gegenüber mechanischen Einflüssen. In der ersten Studie wird ein systematischer Methodenvergleich für eine nicht-invasive Quantifizierung von hydraulischen Öffnungsweiten präsentiert. Drei verschiedene Messinstrumente, ein tragbarer Luftpermeameter, eine Mikroskopkamera und ein 3D-Laserscanner, werden an einer natürlichen Einzelkluft in einem bekannten deutschen Reservoiranalogon (Flechtinger Sandstein) angewandt und bewertet. Dieses Fallbeispiel zeigt, dass der Luftpermeameter die robustesten Ergebnisse liefert, die größte Eindringtiefe besitzt und erhebliche Vorteile in Bezug auf Mobilität, Zeitaufwand und Datenauswertung bietet. Bei den Ansätzen zur optischen Kluftcharakterisierung erfolgt die Bestimmung der hydraulischen Öffnungsweite indirekt mittels verschiedener Modellannahmen auf Basis der mechanischen Öffnungsweite und der Kluftrauigkeit. Dabei ergeben sich Abweichungen von bis zu 27 % (Mikroskop-kamera) und bis zu 260 % (3D-Laserscanner) verglichen mit den Ergebnissen des Luftpermeameters.

Aufbauend auf der Einzelkluftanalyse wird die präsentierte Methodik auf den Feldmaßstab transferiert sowie für die Anwendung an einer Wirtsgesteinsformation für die nukleare Endlagerung optimiert. In der zweiten Studie wird eine HM Charakterisierung einer Auflockerungszone im Opalinuston des Felslabors Mont Terri in der Schweiz vorgenommen. Die Analyse des diskreten Kluftnetzwerks in der untersuchten EZ-B Nische, bestehend aus tektonischen und künstlichen Diskontinuitäten, zeigt, dass die offenliegende Auflockerungszone durch hydraulische Öffnungsweiten von bis zu 112 µm gekennzeichnet ist. Durch fortschreitende Austrocknung der Tunnelwände über einen Zeitraum von etwa 15 Jahren wurden Selbstheilungsprozesse größtenteils unterbunden. Auch die mithilfe von Nadelpenetrometertests vor Ort ermittelten physikalisch-mechanischen Gesteinsparameter verdeutlichen die Sensitivität des Opalinustons gegenüber der Tunnelbelüftung und bilden eine negative Korrelation von Gesteinsfestigkeit bzw. -steifigkeit und Wassergehalt aufgrund eines ausgeprägten hydromechanischen Kopplungsverhaltens ab.

Der zweite Teil der Arbeit konzentriert sich auf hydraulisch-chemische (HC) Prozesse im porösen Medium und adressiert den reaktiven Transport in einem Reservoirgestein. Insbesondere durch Lösungs- oder Fällungsreaktionen hervorgerufene Porositäts- und Permeabilitätsänderungen können die Reservoireigenschaften signifikant verändern. Die dritte Studie untersucht die Auflösung von Calcit-Zement im Flechtinger Sandstein sowie die Übertragbarkeit der experimentellen Calcitlösungsraten von der µm-mm-Skala (Mineraloberfläche) auf die cm-Skala (Kernproben). Anhand von Durchflussexperimenten an vier Sandsteinkernen wird die Bandbreite der Lösungsraten auf der cm-Skala für unterschiedliche Reaktionszeiträume sowie variierende hydraulische Randbedingungen ermittelt. Dem gegenübergestellt werden zeitlich und räumlich aufgelöste Calcitlösungsraten auf der µm-mm-Skala aus Oberflächenanalysen mittels vertikal scannender Interferometrie. Auf Grundlage segmentierter Röntgen-Mikrocomputertomografie Scans der Kernproben wird ein geometrischer Ansatz etabliert, um die fluidzugängliche Oberfläche des heterogen verteilten Calcitzements im niedrigpermeablen und komplexen Sandstein abzuschätzen. Auf Grundlage dieses eingeführten Oberflächenparameters wird die Rateninformation der µm-mm-Skala auf die Kernskala übertragen, wobei die Abweichungen zwischen den aufskalierten und den gemessenen Lösungsraten für alle untersuchten Proben weniger als eine Größenordnung betragen.

Im Rahmen dieser Arbeit werden verschiedene Messmethoden und Herangehensweisen identifiziert, entwickelt, optimiert und validiert, die zur Beschreibung und Interpretation von gekoppelten hydraulisch-mechanisch-chemischen Prozessen und zur Bestimmung damit zusammenhängender Schlüsselparameter in geklüfteten und porösen Gesteinen genutzt werden können. Der Untersuchungsansatz und die erzielten Ergebnisse bilden daher eine wertvolle Grundlage für die Vorhersage des Verhaltens natürlicher Systeme auf höheren Längen- und Zeitskalen.

CONTENTS

LIST OF FIGURES

LIST OF TABLES

INTRODUCTION

1

1.1 General motivation

A rock can generally be considered as a system that consists of a solid phase, represented by one or more minerals, and a void phase, the pore space. As small as this percentage of void phase may be, a rock is a porous medium and never completely impermeable, allowing fluids to migrate through the connected pore space. Such hydraulic (H) processes can trigger chemical (C) processes, and as a result, mineral phases might dissolve or precipitate. In turn, such fluid-rock interactions can have major impacts on the hydraulic properties of the formation. Naturally, rocks also contain discontinuities or fractures that form a network of void structures and, thus, fluid pathways. These can significantly increase the effective hydraulic conductivity of the fractured medium, since the fracture is typically much more permeable than the matrix. However, fractures also represent weakness structures within the rock mass and are prone to mechanical (M) influences, which may also affect fracture hydraulics.

Such coupled hydraulic-mechanical-chemical (HMC) processes, which are often complemented by a thermal (T) component (i.e., THMC processes), are of utmost importance in any use of the geological subsurface (e.g., Birkholzer et al., 2019; Kolditz et al., 2015). Some applications, such as geothermal energy and hydrocarbon production, extract matter or energy from reservoir rocks and crucially rely on such coupled processes to achieve a maximum possible exploitation. Contrastingly, nuclear waste disposal intends to safely store hazardous material in host rocks to prevent migration towards the biosphere. Hence, this application depends on the best possible attenuation of certain coupled processes. In any case, a profound understanding of coupled HMC processes is required for usability analysis, safety assessment and forecasts of future developments in different systems, independent of the actual geoscientific application (e.g., Hudson et al., 2005; Kolditz et al., 2015; Liu, 2018; Stephansson et al., 2004).

In 2015, the United Nations agreed on a total of 17 overarching global “Sustainable Development Goals” as part of the “Agenda 2030” (United Nations, 2015), some of which also relate in particular to the utilization of the geological subsurface (Figure 1.1). Especially in light of climate change, certain subsurface applications are even more important. Tackling the consequences of climate change is a key objective of the “Energiewende” in Germany, i.e., the ongoing transformation from fossil to renewable energy resources (e.g., Kabuth et al., 2017). Specific goals are a nuclear phase-out by 2022, which includes the need to implement geological waste repositories, a coal phase-out no later than 2038 to achieve greenhouse neutrality by 2050, and an increased use of geothermal energy in the heating sector. In context of the transition to renewable energy resources, the geological subsurface also offers great potential as a storage medium for energy to ensure security of supply, for example in the form of power-to-X products (e.g., hydrogen, methane, air) (BMWi, 2021).

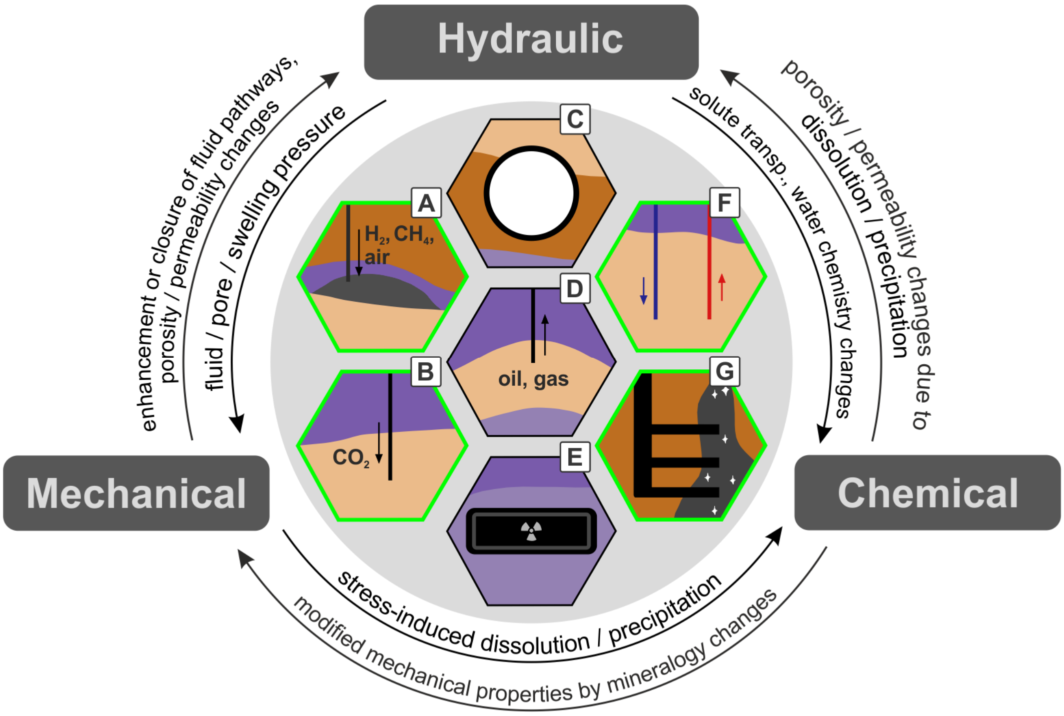

Figure 1.1: Coupled HMC processes in porous and fractured rocks affecting different geoscientific applications (A = energy storage, B = carbon capture and storage, C = tunneling/engineering, D = hydrocarbon production, E = nuclear waste disposal, F = geothermal energy, G = mining). The illustrated subsurface activities support 7 of the 17 UN Sustainable Development Goals (United Nations, 2015), and the four applications outlined in green also significantly contribute to climate action (inspired by the poster "Geoscience for the future", Geological Society of London, 2012).

With regard to the two parts of this thesis, the following introductory chapters focus on coupled HM processes in the fractured medium (Chapter 1.2) and coupled HC processes in the porous medium (Chapter 1.3). These two chapters each highlight specific topics that are relevant with regard to the objective (cf. Chapter 1.4) and the individual studies of this thesis (cf. Chapter 1.5).

1.2 Coupled hydraulic-mechanical processes in the fractured medium

1.2.1 Hydraulic and mechanical fracture parameters

The term fracture generally describes a planar discontinuity feature in rock which can be of tectonic or non-tectonic origin (Nelson, 2001; Reuther, 2012). If loading on a rock mass, caused by gravitational, tectonic, thermal or impact stresses, exceeds the individual rock strength, brittle reaction behavior may occur and fractures are formed (Davis et al., 2011). In addition to their natural formation, fractures can also be created artificially by human action (e.g., Power and Durham, 1997; Vogler et al., 2017). In the three-dimensional space, a fracture consists of two opposing surfaces whose morphology can vary substantially (e.g., Hakami, 1995; Hakami and Larsson, 1996). Depending on the mechanical formation process, a distinction is generally made between tensile fractures (Mode I), which were displaced normal to the fracture plane, and shear fractures (Mode II and Mode III), which were displaced parallel to the fracture plane, although also hybrid forms are observed (Bons et al., 2012; Davis et al., 2011). After their formation, reservoir fractures are commonly filled with secondarily formed minerals (Nelson, 2001). If the fracture is only partially filled or completely open and thus conductive, the shape of the void space between the fracture surfaces determines its hydraulic properties.

Basically, two different fracture aperture parameters are distinguished (Figure 1.2), which were strongly influenced by the pioneering work of Barton (1972) and Tsang and Witherspoon (1981). The mechanical aperture a_m (Barton, 1982) describes the visible and directly measurable distance between two points on the fracture surfaces, in most cases measured perpendicularly to the fracture fitting plane (e.g., Hakami and Larsson, 1996; Olsson and Barton, 2001). The more abstract concept of the hydraulic aperture a_h, introduced by Barton (1982) as conducting or *"theoretical smooth wall aperture"*, expands the purely geometric description with the possibility of characterizing the fracture as a permeable structure for fluid flow. However, natural fracture surfaces always show a varying degree of roughness that modifies the void space, introduces a heterogeneity of the local mechanical aperture, and reduces the hydraulic aperture (e.g., Brown, 1987; Patir and Cheng, 1978; Scesi and Gattinoni, 2007; Tsang and Witherspoon, 1983; Zhao, 2017). For a rough fracture, the hydraulic aperture equals to the aperture of an imaginary parallel-plate fracture that would yield the same volumetric flow rate (Figure 1.2).

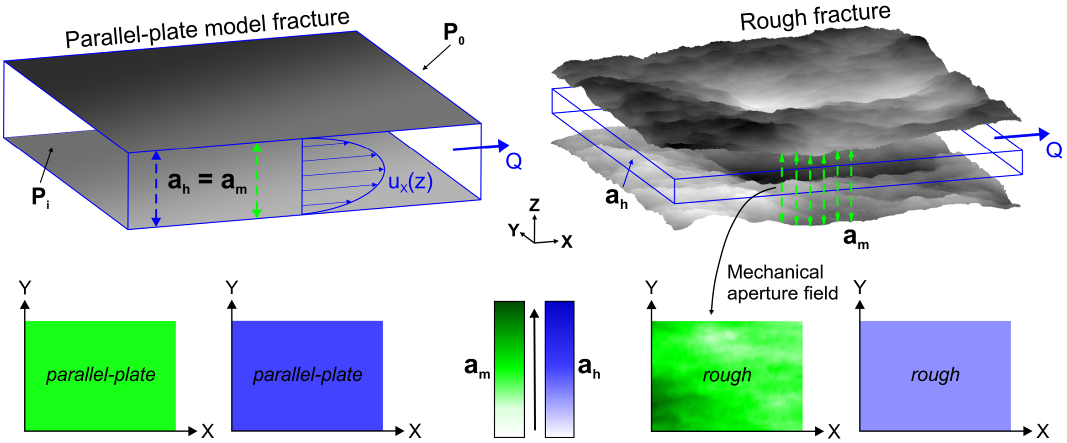

Figure 1.2: Mechanical and hydraulic aperture for the parallel-plate fracture (model case for the derivation of the cubic law, cf. Eq. (1.2)) and for a rough fracture, with volumetric flow rate Q, pressure P and fluid velocity profile $u_x(z)$. For an ideal parallel-plate fracture, a_m and a_h would be identical (Barton, 1982).

Early studies already showed the importance of distinguishing between a_h and a_m, except for certain fracture geometries and boundary conditions, for example high flow rates and smooth open fractures (e.g., Renshaw, 1995; Witherspoon et al., 1980). For natural fractures, one generally applies (e.g., Liu, 2005):

$$a_h < a_m \tag{1.1}$$

When contacts are formed between the fracture surface asperities, the hydraulic aperture is not only reduced, but also flow barriers are created that result in channeling, flow path localization and increased tortuosity (e.g., Hakami, 1995; Liu, 2005; Nemoto et al., 2009). Moreover, this contact area also controls the behavior or stiffness of the fracture under mechanical stress (e.g., Magsipoc et al., 2020), such as normal (e.g., Bandis et al., 1983; Hopkins et al., 1987; Pyrak-Nolte and Morris, 2000) or shear loads (e.g., Asadi et al., 2013; Grasselli, 2011; Zhao, 1997).

The hydraulic efficiency of a fracture can be described by the cubic law (e.g., Witherspoon et al., 1980), or by more advanced approaches such as the local cubic law (LCL) (e.g., Cardona et al., 2021; Marchand et al., 2020) and different modified cubic laws (e.g., Guo et al., 2020; Wang et al., 2018). The classical cubic law represents the steady-state solution to the Navier-Stokes equations assuming laminar viscous flow in a parallel-plate fracture (e.g., Renshaw et al., 2000; Zimmerman and Bodvarsson, 1996, see also Figure 1.2):

$$Q = \frac{-\,|\overline{\nabla P}| \cdot w a^3}{12\mu} \tag{1.2}$$

Here, $|\overline{\nabla P}|$ is the magnitude of the pressure gradient averaged over the fracture plane, w is the fracture width perpendicular to the flow direction, a is the fracture aperture and μ is the fluid viscosity. Taking into account Darcy's law, a relationship between a and the fracture transmissivity or permeability can be formulated (e.g., Zimmerman and Bodvarsson, 1996):

$$T = \frac{wa^3}{12} \;,\; k = \frac{a^2}{12} \qquad (1.3), (1.4)$$

The application of Eqs. (1.2) to (1.4) for rough fractures requires the utilization of a representative aperture, i.e., a_h (e.g., Brown, 1987; Renshaw, 1995; Zimmerman and Bodvarsson, 1996).

The fracture roughness is usually composed of two components, which is large-scale waviness superimposed by small-scale roughness (e.g., Tsang and Witherspoon, 1983). For the characterization of fracture roughness, the dimensionless joint roughness coefficient (JRC) is one of the most prominent parameters and was empirically derived by using the experimental peak shear strength of fracture samples (Barton, 1973; Barton and Choubey, 1977). Alternatively, a variety of statistical roughness parameters has been established (e.g., Lee and Babadagli, 2021; Magsipoc et al., 2020). These have the advantage of being relatively straightforward to determine, in most cases on a profile basis, and are often linked to the original JRC by empirical relationships (e.g., Li and Zhang, 2015; Mo and Li, 2019). For the statistical parameters (e.g., Z_2, R_Z, δ, λ), roughness quantification is performed either by analyzing height differences, profile lengths, slopes, curvatures, or inclination angles in conjunction with statistical quantities such as arithmetic mean or root mean square (RMS) (Lee and Babadagli, 2021; Li and Zhang, 2015; Magsipoc et al., 2020; Wang et al., 2016). However, according to Magsipoc et al. (2020), a disadvantage of all profile-based, two-dimensional roughness parameters is that they can only partially represent the nature of the actual three-dimensional fracture surface.

The analysis of the fractal geometry of fracture surfaces and the derivation of parameters such as the Hurst exponent or the fractal dimension represents a more sophisticated mathematical method of roughness analysis (e.g., Lee and Babadagli, 2021; Magsipoc et al., 2020) and is adopted in many modern studies (e.g., Stigsson and Mas Ivars, 2019; Yu et al., 2020). Although fractal characterization allows the description of the scaling behavior of fractal surfaces and, thus, in principle the upscaling of roughness patterns (e.g., Brown, 1987; Candela et al., 2012), it requires that the investigated surfaces exhibit self-affine properties (e.g., Mandelbrot, 1985; Schmittbuhl et al., 1993), otherwise a correct interpretation and evaluation is hampered (Gutjahr et al., 2021).

1.2.2 Hydraulic-mechanical couplings in reservoir and host rocks

Although the single fracture serves as the base case for the analysis of coupled HM processes, in reality the fractures are embedded in the porous medium (i.e., a rock mass). Several relevant HM couplings exist in both reservoir and host rocks which are briefly outlined below. These processes are often studied numerically, since the conditions under which they occur are not always experimentally reproducible.

Different types of reservoirs exist in different lithologies, e.g. hydrothermal and petrothermal reservoirs, mainly in sandstones, crystalline and carbonate rocks, as well as conventional or unconventional hydrocarbon reservoirs, mainly in carbonates, shales and sandstones (e.g., Moeck, 2014; Zou et al., 2015). Regardless of the reservoir type, hydraulic and mechanical processes are strongly interrelated (H ↔ M) and essential for the sustainable utilization and production capacity of the respective system (e.g., Ganguly and Mohan Kumar, 2012).

- **Before production**: To improve the effective reservoir permeability, hydraulic stimulation is performed, whereby fluids are injected under high flow rate and pressure (hydro-fracturing). This hydraulic manipulation leads to a mechanical response of the rock mass, including stress and strain changes within the rock matrix and along discontinuities, the formation of new fracture networks, and dilatation and shearing of existing natural fractures (e.g., Damjanac and Cundall, 2016; Gaucher et al., 2015; Li et al., 2015; Pandey et al., 2018; Vogler, 2016).
- **Production and exploitation**: During reservoir exploitation, the effective stress state is changed, for example, due to progressive depletion, which initiates a compaction of the fractured rock mass and fracture closure processes. This mechanical response of the reservoir can in turn lead to a permeability decline (e.g., Cao et al., 2018; Schutjens et al., 2004; Smart et al., 2001; Zheng et al., 2019). For geothermal reservoirs, in addition to HM and chemical processes (e.g., redox or precipitation reactions by reinjection of cooled

water or brines, Su et al., 2018; Ungemach, 2003), the heat transfer between the rock matrix and the permeable fractures is the actual key process (e.g., Lee et al., 2018; Pruess, 1990; Shaik et al., 2011; Ye and Wang, 2020).

Also for nuclear waste storage in highly impermeable host rocks, coupled HM processes are of crucial importance, but with a main focus on the integrity of the geological barrier (e.g., IAEA, 2006; Tsang et al., 2012). Argillaceous rocks are considered as suitable host rocks in many countries (Blechschmidt and Vomvoris, 2010), for example, the Opalinus Clay in Switzerland or the Callovo-Oxfordian claystone in France (e.g., Andra, 2005; Nagra, 2002). In the following, predominant HM processes in the near-field of a waste repository in an indurated clay formation are briefly discussed. An essential part of the near-field is the excavation damaged zone (EDZ). The EDZ forms around emplacement tunnels and is characterized by significantly altered hydraulic, mechanical and chemical properties, which furthermore strongly modify the flow and transport properties compared to the intact host rock (e.g., Tsang et al., 2012, 2005).

- **Early stages (pre-closure phase)**: During this phase, mechanical processes influence hydraulic processes and properties of the EDZ (M → H). Pressure relief during tunnel construction and subsequent tunnel convergence result in the formation and reactivation of discontinuities, increasing the effective hydraulic conductivity of the rock mass. In addition, a decrease in pore pressure as well as dehydration is observable (e.g., Amann et al., 2017; Bossart et al., 2004, 2002; Giger et al., 2015; Nussbaum et al., 2011; Tsang et al., 2005; Yong et al., 2017, 2010). These early stage processes in indurated clay formations are often addressed by coupled or decoupled HM models. These include simulations of the spatial distribution and temporal evolution of stress, strain, damage and displacements around the cavity, facture nucleation and growth, emerging fracture patterns, porosity and permeability increases of the rock mass, and the shape and extent of the resulting EDZ (e.g., Lisjak et al., 2015; Popp et al., 2008; Shao et al., 2008; Thoeny, 2014).
- **Later stages (post-closure phase)**: Through gradual resaturation of the EDZ, fracture sealing can principally be reached due to swelling processes within the claystone or the backfilling material (e.g., Bastiaens et al., 2007; Bernier et al., 2007; Bossart et al., 2017; Marschall et al., 2017; Tsang et al., 2005), i.e., hydraulic processes trigger mechanical reactions (H → M). In application, these HM processes in the post-closure phase would be superimposed by a strong thermal perturbation due to radionuclide decay, but also by various chemical processes (e.g., corrosion of metal components, degradation of concrete, Andra, 2005). Numerical simulations particularly address the reduction of fracture aperture and permeability by mechanical self-sealing of the EDZ, initiated by re-compression due to swelling of the backfilling material (e.g., Alcoverro et al., 2014; Lisjak et al., 2016; Walsh et al., 2015). Alcolea et al. (2017) simulated fracture self-sealing by also including clay matrix swelling and estimated the hydraulic conductivity of an EDZ over a time span of 30,000 years.

1.2.3 Quality of characterization methods for fractured rock masses

With regard to Chapter 1.2.2, a solid data basis is needed to draw conclusions on the system behavior of fractured rocks. This involves capturing the as-is state in practical investigations, the creation of conceptual models, and finally the parametrization of fracture models to produce realistic simulation outputs. This applies to the fracture properties (Chapter 1.2.1), where fracture aperture and roughness are *"highly elusive parameters"* (Bigi et al., 2013), but also to the mechanical, physical and hydraulic properties of the surrounding rock matrix.

Hence, adequate measurement methods should, if possible, meet the criteria summarized below. This compilation does not focus on a specific parameter, but offers a more general overview for HM characterization of fractured rocks and makes use of various examples of commonly used measurement techniques.

- **Validity**: A method is valid if it measures exactly what it claims to measure (Kirch, 2008). As an example, Filomena et al. (2014) show that a local measurement with an air permeameter device under transient air flow is generally a valid procedure for the determination of rock permeability, as demonstrated by comparison with the reference procedure using a Hassler cell under steady-state gas flow.
- **Accuracy:** The term accuracy specifies how well a measurement result matches the true or reference value (Trajković, 2008). Current fracture studies increasingly employ optical methods with high accuracy (e.g., Feng et al., 2003; Marsch et al., 2020). However, the measurement accuracy specified by the manufacturer, which is determined under idealized conditions based on defined test protocols (e.g., with standardized objects, Vogler et al., 2017), is difficult to achieve under real conditions due to environmental errors (Mohajan, 2017). The example of terrestrial laser scanning (TLS) shows that various disruptive factors in field application can reduce the actual accuracy (e.g., Buckley et al., 2008; Sturzenegger and Stead, 2009), such as the reflective surface properties of the material (Boehler et al., 2003).
- **Efficiency:** It is also desirable to efficiently generate large data sets (i.e., a high number of measurements in adequate time duration) so that statistical data analysis is enabled; however, without compromising accuracy. An improvement in efficiency can generally be achieved by automated data analysis, but also essentially by avoiding technically demanding and time-consuming procedures. For example, complex hydraulic tests to determine the hydraulic conductivity or transmissivity of fractured aquifers (e.g., Altenbockum et al., 2018; Zeeb et al., 2010) or individual fractures (e.g., Novakowski and Lapcevic, 1994; Weede and Hötzl, 2005), but also elaborate pneumatic and hydraulic cross-hole tests, such as those carried out in the Mont Terri rock laboratory (e.g., Bossart et al., 2004, 2002; Meier et al., 2000), can be mentioned.
- **Reproducibility and objectivity:** The term reproducibility indicates the agreement of different measurements obtained under changed conditions (Trajković, 2008); for example, the measurement result should not depend on the user. As an example, the common JRC determination method by visual comparison with exemplary standard profiles (Barton and Choubey, 1977) is considered less objective. In their survey-based

study, Beer et al. (2002) confirm that the reproducibility of visually estimated JRC values was significantly dependent on the experience level of the participants. A lack of technical standards or standardized workflows also impairs data reproducibility and comparability, as Buckley et al. (2008) illustrate for the application of TLS for generating virtual terrain or outcrop models. Marsch et al. (2020) highlight the influence of the selected surface reconstruction algorithm on the calculated roughness distribution of optically detected fracture surfaces.

- **Versatile applicability**: Ideally, a measurement method should always be as broadly applicable as possible and not be too constrained, for example, by lithology or observation scale. While mechanical characterization methods such as uniaxial compressive strength tests usually work with standardized sample diameter-height ratios (e.g., Wild et al., 2015), Structure from Motion photogrammetry, for example, is very flexible in terms of observation scale. It is suitable for digital roughness mapping on small specimens (e.g., Wernecke and Marsch, 2015; Zambrano et al., 2019) as well as on outcrops or fault surfaces in the field (e.g., Corradetti et al., 2020, 2017).
- **Non-destructive or low-impact approaches**: As an example, the characterization of EDZs in clay formations requires a metrological approach that is appropriate for the highly sensitive setting. Drilling for taking core samples for mechanical laboratory tests on the one hand influences the EDZ itself, e.g., by the formation of borehole damaged zones (Amann et al., 2017), or simply by creating flow connections across the borehole. On the other hand, the properties of the extracted sample can also be altered during transportation or storage. In this case, the needle penetrometer test would be a low-impact alternative for estimating rock strength, since, although a mm-scale indentation zone is created, the rock integrity is essentially preserved (e.g., Ulusay et al., 2014).

1.3 Coupled hydraulic-chemical processes in the porous medium

1.3.1 Reactive transport

The term reactive transport describes the coupling of geochemical reactions with physical mass transport mechanisms such as advection, molecular diffusion or hydrodynamic dispersion (e.g., Steefel and Maher, 2009). When fluid enters a porous medium, the equilibrium state of the system is changed, and as a response, a reaction (i.e., dissolution or precipitation of mineral phases) can be induced (H → C, see also Figure 1.1). Reactive transport processes are of great relevance for a variety of geoscientific topics. These include, for example, chemical weathering (e.g., Maher and Navarre-Sitchler, 2019), contaminant spreading and degradation in groundwater (e.g., Curtis et al., 2006; Mao et al., 2006), carbon capture and storage technologies (e.g., Crawshaw and Boek, 2013; Mohd Amin et al., 2014), acid mine drainage (e.g., Amos et al., 2004; Blowes et al., 2014), or matrix acidizing for stimulating reservoir productivity (e.g., Shafiq et al., 2019; Younesian-Farid and Sadeghnejad, 2020). In principle, an additional coupling of HC processes to superimposed mechanical or thermal influencing factors can also occur, for example, mechanical deformation of the grain skeleton or thermal influence on fluid viscosity (e.g., Kolditz et al., 2015).

To describe a chemical reaction, two basic approaches are generally considered that intend to answer specific questions (e.g., Brantley and Conrad, 2008; Merkel and Planer-Friedrich, 2008):

- **Thermodynamics**: Is a reaction to be expected at all, and if so, in which direction? The thermodynamic approach characterizes a system with respect to its chemical equilibrium state, i.e., the final state which the system is approaching.
- **Reaction kinetics**: How fast is the reaction? The kinetic approach is based on reaction rates which describe the temporal progression of a reaction.

In this thesis, the chemical dissolution process of the mineral calcite ($CaCO_3$) coupled with hydraulic transport processes through the porous rock is examined (cf. Chapter 1.4). For an assumed schematic dissolution reaction of the form $A \rightarrow B + C$, the reaction rate r is principally expressed as (e.g., Brantley and Conrad, 2008)

$$r = -\frac{d[A]}{dt} \tag{1.5}$$

and denotes how many moles of the material A are dissolved per time unit. Taking the dissolution of the mineral calcite as an example, a general rate equation can be formulated as follows (Lasaga, 1998; Morse and Arvidson, 2002)

$$r = k \cdot A \cdot e^{(-E_a/RT)} \cdot \prod_i a_i^{n_i} \cdot f(\Delta G) \ , \tag{1.6}$$

where k is the overall reaction rate constant, A is the participating (or reactive) mineral surface area, and $f(\Delta G)$ is a function of the Gibbs free energy difference which expresses the distance to the chemical equilibrium of the reaction. The third term of Eq. (1.6) accounts for the influence of reaction temperature, with E_a the apparent activation energy, R the ideal gas constant and T the absolute temperature. In addition, the fourth term describes how the rate is affected by extraneous species (with a_i the activity and n_i the exponential factor of the species i), which can act either catalytically or inhibitory on the reaction (Merkel and Planer-Friedrich, 2008; Morse and Arvidson, 2002).

In the rock, dissolution processes alter the composition of both the solid and the fluid phase. Additionally, other properties of the porous medium evolve as well (see also Figure 1.1, Steefel and Maher, 2009), which applies, among others, to

- the **porosity** and **permeability**, through increases in pore volume and connectivity (e.g., Gouze and Luquot, 2011; Lamy-Chappuis et al., 2014; Liu et al., 2018; Luhmann et al., 2014; Miller et al., 2017; Navarre-Sitchler et al., 2009; Tan et al., 2020; Yang et al., 2020), and in the case of carbonate rocks, through the formation of different dissolution patterns (e.g., face, wormhole or uniform dissolution, Fredd and Fogler, 1999; Golfier et al., 2002; Luquot et al., 2014; Luquot and Gouze, 2009; McDuff et al., 2010);
- the **reactive surface area** (cf. Eq. (1.6)) of the considered mineral phase(s), which can both increase and decrease with progressing dissolution reaction (e.g., Colón et al., 2004;

Kieffer et al., 1999; Noiriel et al., 2009; Rötting et al., 2015; Scislewski and Zuddas, 2010; Younesian-Farid and Sadeghnejad, 2020);

- the **flow field** and related parameters such as flow velocity, turbulence, tortuosity, dispersion, diffusivity and residence time (e.g., Gouze and Luquot, 2011; Gray et al., 2018; Menke et al., 2017, 2016, 2015; Navarre-Sitchler et al., 2009; Pereira Nunes et al., 2016).

Due to the chemical and physical heterogeneity of natural rocks, for example, concerning the porosity, permeability or mineral distribution, a real system can be arbitrarily complex (e.g., Li et al., 2007, 2006; Malmström et al., 2004; Meile and Tuncay, 2006). However, the feedback of dissolution or precipitation processes on the transport properties of the porous medium (C → H) is particularly relevant for the transfer of geochemical reaction rates to the reservoir scale (i.e., upscaling), which is discussed in the following Chapter 1.3.2.

1.3.2 Upscaling of hydraulic-chemical processes

According to Rubin (2003), the term upscaling describes the *"process of replacing a heterogeneous domain with a homogeneous one, such that both produce the same response when acted upon by the same boundary conditions"*. On reservoir scale and even on site scale, reactive transport processes can only be observed to a limited extent, either because such processes extend over much too long periods of time, or because only selective insights are possible. Therefore, mainly smaller systems, which are easier to observe and to control, are investigated to draw conclusions about mechanisms or laws in order to aim for a transfer to higher scales. However, providing a link between different scales of observation is still an ongoing scientific challenge (e.g., Luttge and Arvidson, 2008; Noiriel et al., 2020; Steefel et al., 2005; Steefel and Maher, 2009). Hence, the number of published studies on upscaling topics has increased exponentially between 1990 and 2020, as Zhang et al. (2021) illustrate in their review article.

One of the major problems associated with the upscaling of reactive transport processes in porous media is the discrepancy of geochemical reaction rates between different scales, in particular between laboratory and field scales, which can sometimes reach several orders of magnitude (e.g., Daval et al., 2013; Rimstidt et al., 2012; Swoboda-Colberg and Drever, 1993; White and Brantley, 2003; Zhu, 2005). Calcite is a very prominent example of this phenomenon, and significant rate discrepancies were found even for identical chemical conditions (e.g., Arvidson et al., 2003; Liang and Baer, 1997; Morse et al., 2007; Noiriel et al., 2020).

The following listing covers important points that can cause upscaling problems and need to be taken into account when developing upscaling strategies. These aspects are not only limited to the transfer between the laboratory and field scale, but generally refer to distinct system sizes that are being compared:

- **Consistent reaction mechanisms**: It must be possible to assume that the same mechanisms that are observed in the laboratory also operate at higher scales (Kubicki, 2008).
- **Lack of data for higher scales**: Especially for field and reservoir scales, it is extremely difficult to produce adequate and sufficient data sets, i.e., field-scale transport

experiments, for verification or validation purposes of upscaling approaches (Zhang et al., 2021).

- **Oversimplification:** This can apply to both simulations and experiments (Kubicki, 2008). For reactive transport models, a higher spatial resolution or level of detail is always associated with higher computational costs (e.g., Zhang et al., 2021). For experiments, total duration and practical feasibility are important factors (Kubicki, 2008).
- **The scale effect:** This term describes the phenomenon that some parameters have generally proven to show larger values with increasing time or length scale, for example, some transport properties such as hydraulic conductivity or longitudinal and transverse dispersivity (e.g., Zhang et al., 2021).
- **Inequality of *extrinsic* rate-controlling factors**: In addition to the influence of differing physical or chemical conditions on reaction rates, for example, temperature, pressure, solution composition, pH and saturation (e.g., Kubicki, 2008; Meile and Tuncay, 2006; Pedrosa et al., 2021, 2019), the effectiveness or ineffectiveness of the mass transport process (i.e., the flow velocity and residence time of the reactive fluid) determines whether the rate is surface-controlled or transport-controlled. In the surface-controlled case, the molecular reaction at the mineral surface is the slowest step in a dissolution reaction sequence. In the transport-controlled case, the migration or removal of the reaction products represents the limiting step for the resulting rate (e.g., Luttge and Arvidson, 2008; Morse and Arvidson, 2002). Transport control also determines how strong the developing chemical gradients can be in the system under consideration (e.g., Li et al., 2006; Meile and Tuncay, 2006).
- **Inequality of *intrinsic* rate-controlling factors**: In addition to extrinsic influences, there are also various intrinsic rate-controlling factors, such as mineral chemical composition or zonation, defect type and density, and surface morphology (e.g., Bollermann and Fischer, 2020; Noiriel et al., 2020; Pedrosa et al., 2021, 2019). The last points are also closely related to the considered sample type (e.g., cleaved or natural crystals, powders) and to the sample preparation procedure (Noiriel et al., 2020).
- **Spatial heterogeneity of physical and chemical properties:** The heterogeneity of natural rocks is a point that affects many scales of observation, but is also often neglected due to the fixed discretization of reactive transport models (e.g., Li et al., 2006; Zhang et al., 2021). Physical heterogeneity generally leads to the formation of preferential flow paths and patterns. A heterogeneous flow field restricts the contact of the reactive fluid with the minerals in the rock and leads in turn to inhomogeneous or localized dissolution (e.g., Meile and Tuncay, 2006; Menke et al., 2018; Yang et al., 2020). For example, chemical heterogeneity refers to a heterogeneous spatial distribution of reactive mineral phases in the rock (e.g., Li et al., 2007, 2006; Salehikhoo et al., 2013). Furthermore, reactive transport in a heterogeneous medium is also a self-amplifying process: The higher the structural heterogeneity of a system, the more heterogeneity is likely to be formed by reactive transport processes (Noiriel and Soulaine, 2021).
- **Deviations in surface area normalization of experimental reaction rates**: For indirectly determined dissolution rates (i.e., by fluid chemistry), the problem of surface area normalization needs to be mentioned in particular, which has long been seen as a

critical influencing factor in connection with observed rate discrepancies (e.g., Fischer et al., 2012a; Lüttge, 2005), because the reactive surface area (RSA) of a mineral is practically unmeasurable (e.g., Luttge and Arvidson, 2008). However, several alternative and quantifiable surface parameters are generally utilized for normalizing experimental reaction rates, for example, the specific surface area (SSA) obtained by gas adsorption methods (e.g., Hodson, 2006) or the geometric surface area (GSA) obtained by 2D or 3D image analysis (e.g., Beckingham et al., 2016; Landrot et al., 2012; Noiriel et al., 2019). More simple, the pore wall area can also be calculated by assuming regular geometric grain shapes (e.g., Hodson, 2006; Luttge and Arvidson, 2008) or based on the pore size distribution using a tube bundle model (Rötting et al., 2015). In contrast, Waldmann et al. (2014) demonstrate the importance of considering the mineral accessibility, i.e., the so-called effective mineralogy, to avoid significant rate discrepancies.

Due to the mentioned aspects and the complexity of the conditions on field scale, rates can therefore not simply be transferred between different systems and scales, which also represented a starting point for the project ResKin (Chapter 1.3.3).

1.3.3 The ResKin project

The contribution of this thesis to coupled HC processes in the porous rock was carried out within the framework of the project "ResKin - Reaktionskinetik in Reservoirgesteinen: Anwendungsbereite Aufskalierung und Modellierung", funded by the German Federal Ministry of Education and Research (BMBF). The objective of ResKin was to develop enhanced algorithms for the simulation of reactive transport processes from pore to core scales, and to ultimately enable a transfer of these processes to higher length and time scales to contribute to a safe and sustainable use of geological reservoirs. This required to study the complex interrelation between chemical reactions and mechanisms occurring at the mineral surface (nm-µm-scale), and the resulting changes in transport properties (hydrodynamics) of the rock on the µm-cm-scale.

To investigate the reaction kinetics across multiple scales based on a case study, the Flechtinger Sandstone (Permian, Upper Rotliegend, Havel subgroup) was selected as sample material in the project ResKin. These fluvial-aeolian sediments serve as an analog material for the Permian gas reservoirs of the North German Basin (e.g., Fischer et al., 2012b; Kleditzsch and Kurze, 1993; Plein, 1993; Schröder et al., 1995) and have already been used in many studies (e.g., Cheng and Milsch, 2021; Fischer et al., 2007; Hassanzadegan et al., 2014, 2012; Heidsiek et al., 2020; Mayr et al., 2011; Monsees et al., 2021b, 2021a). As an example mineral system, the dissolution of the calcite cement within the Flechtinger Sandstone was examined. Carbonates such as calcite represent a common cement mineral phase in sandstones and can influence reservoir quality both positively (e.g., stabilizing effect, possibility of secondary porosity formation) and negatively (e.g., massive flow barriers, Morad, 1998). Along with dolomite, calcite also accounts for about 20 vol.-% of the Phanerozoic sedimentary rocks (Morse and Mackenzie, 1990). In addition, the interaction between carbonate minerals and reactive fluids is also of environmental relevance due to its involvement in the global carbon cycle (e.g., Zou et al., 2019).

Being the overarching objective of the project ResKin, the development of upscaling algorithms for the numerical simulation of multi-scale reactive transport processes in porous media based on the existing software tool PoreChem (e.g., Greiner et al., 2019; Iliev et al., 2017; Prill et al., 2021) was relying on the input from different experimental and analytical approaches:

- **nm-scale**: Analysis of surface reactivity by kinetic Monte Carlo simulations and atomic forced microscopy (e.g., Kurganskaya and Churakov, 2018; Kurganskaya and Luttge, 2016; Martin et al., 2021; Rohlfs et al., 2018);
- **nm-µm-scale**: Structural analysis of pores and mineral aggregates using X-ray diffraction and different scanning electron microscopy techniques (e.g., Grathoff et al., 2016; Jacob et al., 2021; Saif et al., 2017);
- **µm-mm-scale**: Surface dissolution experiments and rate map analysis by vertical scanning interferometry (e.g., Bibi et al., 2018; Bollermann and Fischer, 2020; Pedrosa et al., 2021, 2019);
- **µm-cm-scale**: 3D rock imaging by classical and synchrotron X-ray computed tomography combined with Digital Rock Physics (DRP) simulations (e.g., Chagneau et al., 2015; Hinz et al., 2019; Jacob et al., 2019; Saxena et al., 2018);
- **cm-scale**: Flow-through experiments on drill core samples (core plugs) and analysis of fluid-rock interactions, i.e., dissolution rates, changes in porosity and permeability (e.g., Huq et al., 2015; Lamy-Chappuis et al., 2014; Luhmann et al., 2014; Luquot and Gouze, 2009; Rötting et al., 2015; Shiraki and Dunn, 2000).

The core scale (cm-scale) represents an important intermediate step towards the field scale, providing the opportunity to investigate relevant aspects such as transport control or local-equilibrium regimes. Many studies work with highly reactive CO_2-charged brines, elevated temperatures and strong undersaturations to allow rapid dissolution of calcite (e.g., Kaufmann and Dreybrodt, 2007; Peng et al., 2015; Pokrovsky et al., 2009; Yang et al., 2020). However, especially for the upscaling of experimental calcite dissolution rates and the prediction of long-term fluid-rock interactions on field scale, it is essential to also perform experiments under more natural conditions and over longer reaction times.

1.4 Objectives and approaches

The objective of this thesis is to improve and deepen the understanding of coupled hydraulic-mechanical-chemical (HMC) processes and properties in the fractured and porous medium. In this context, this thesis especially aims to develop methodical-analytical approaches and tools for the determination of key parameters that are required for characterization, upscaling and prognosis of coupled HMC processes in both reservoir and host rocks.

This thesis aims to

- identify suitable instruments and methods for a quantitative, non-invasive and reliable determination of important fracture parameters such as hydraulic and mechanical aperture and fracture roughness.
  Based on a systematic comparison using the example of a single fracture in the Flechtinger Sandstone, the focus is placed on evaluating three modern methods with regard to applicability, efficiency and existing limitations.
- assess the applicability of methods for characterizing fractured rocks on the larger field scale and in a different geological environment.
  An on-site hydraulic-mechanical characterization is carried out for an excavation damaged zone (EDZ) around a test tunnel in a host rock for nuclear waste disposal (Opalinus Clay, Switzerland), with a special focus on the effect of long-term ventilation and desaturation.
- investigate the upscaling capability of dissolution rates of a reactive mineral phase within a low-permeable reservoir sandstone (Flechtinger Sandstone, Germany).
  Using the example of calcite, which represents a highly abundant cement phase in siliciclastic rocks, experimentally derived dissolution rates on the µm-mm- and cm-scale are compared and linked.

Figure 1.3 provides a graphical overview of the individual studies in this thesis addressing the objectives outlined above, as well as the methods and approaches that are applied to the different investigation scales and settings.

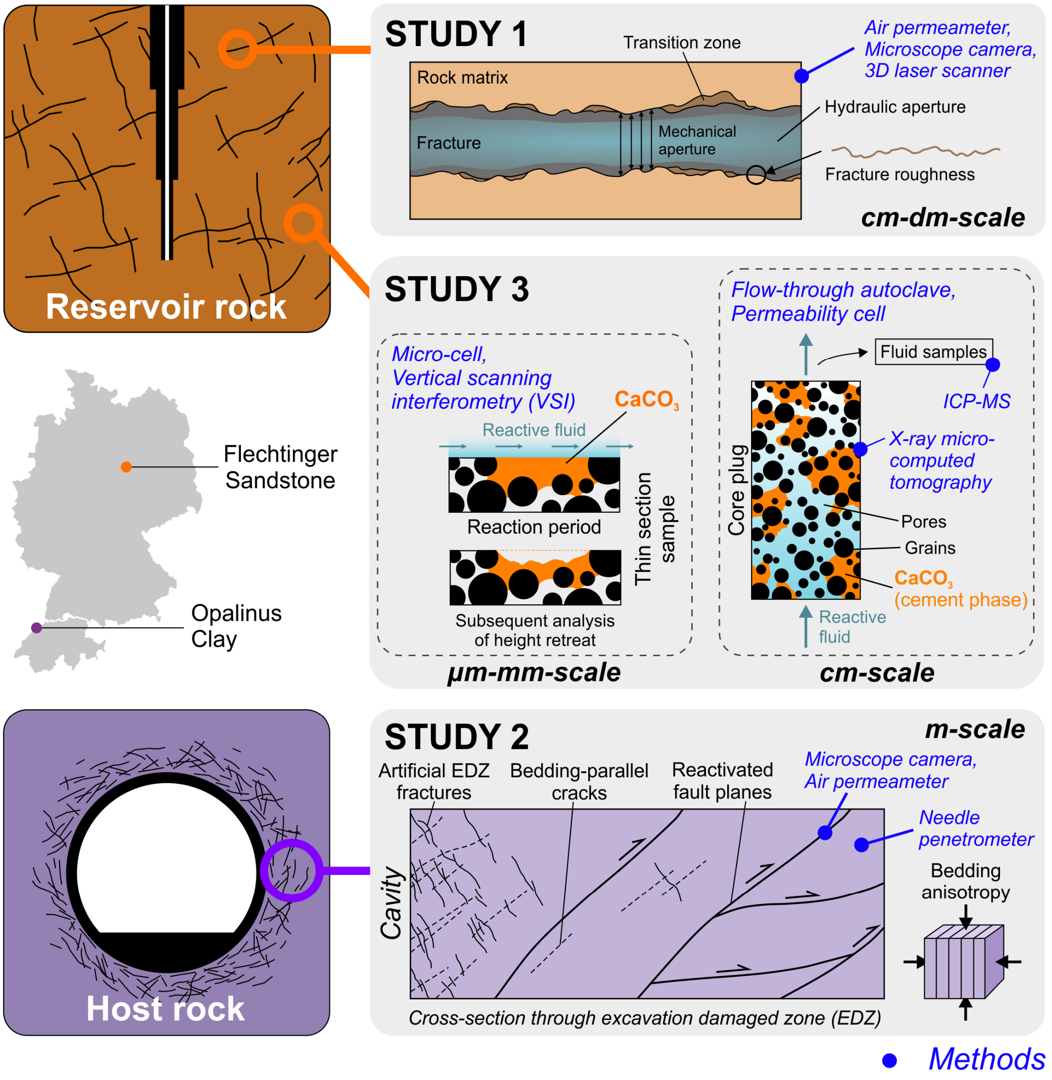

Figure 1.3: Graphical overview of the studies of this thesis on coupled hydraulic-mechanical processes in fractured rock (Study 1 and 2) and on coupled hydraulic-chemical processes in porous rock (Study 3). The investigations focus on two different lithologies, the Flechtinger Sandstone (reservoir analog, Bebertal, Germany) and the Opalinus Clay (host rock formation, Mont Terri rock laboratory, Switzerland).

1.5 Structure of the thesis

This cumulative thesis comprises three individual studies, which are enclosed in Chapters 2, 3 and 4. All studies were submitted to peer-reviewed, international journals. Studies 1 and 2 in Chapters 2 and 3 are already published, Study 3 in Chapter 4 is currently under review.

The thesis is structured as follows:

- **Chapter 2:** *Method comparison to determine hydraulic apertures of natural fractures* (published in *Rock Mechanics and Rock Engineering*)
  In this Technical Note, the hydraulic aperture of a single natural fracture in a reservoir analog (Flechtinger Sandstone) is examined by applying a portable air permeameter, microscope camera imaging and 3D laser scanning. For the indirect optical determination

of hydraulic fracture apertures based on mechanical apertures and roughness parameters, suitable approaches for the evaluation of the raw data are developed. Resulting quantitative differences between the tested methods are discussed and possible influencing factors are identified.

- **Chapter 3**: *Mechanical and hydraulic properties of the excavation damaged zone (EDZ) in the Opalinus Clay of the Mont Terri rock laboratory, Switzerland* (published in *Solid Earth*)
  In this Research Paper, the methodology developed in Chapter 2 is applied to investigate the discrete fracture network of an EDZ in a host rock formation (Opalinus Clay) in the Mont Terri underground rock laboratory in Switzerland. This is complemented by needle penetrometer tests to estimate the physico-mechanical properties of the surrounding rock matrix. By using an automatic algorithm to determine the mechanical aperture and the relative roughness from digital fracture profiles, the microscope camera method is further optimized. The results of the HM characterization of the EDZ are discussed with regard to both self-sealing and desaturation processes in light of nuclear waste storage, and geometrical differences between different fracture types are analyzed. In addition, the suitability of the methodology used is evaluated by comparison with compiled literature data sets from the study site.

- **Chapter 4**: *Upscaling calcite dissolution rates in a tight reservoir sandstone* (submitted to *Environmental Earth Sciences*)
  In this Research Paper, the dissolution behavior of calcite cement in a reservoir analog (Flechtinger Sandstone) is examined on two different scales. On the µm-mm-scale, surface rates are determined from dissolution experiments with a combined analysis of the surface height retreat. On the cm-scale, core dissolution rates are calculated indirectly based on fluid chemical analyses. In order to quantify the fluid-accessible calcite surface area on core scale, its geometry and connectivity to the open pore space is visualized and evaluated by X-ray micro-computed tomography (µXCT). Using the µXCT surface area and considering the saturation state, the surface rates are scaled up to the core scale. Moreover, the effect of highly diverging transport conditions at the mineral surface and within the porous medium is discussed.

- **Chapter 5**: *Related co-authored studies*
  Three related studies of Cheng et al. (2020), Gutjahr et al. (2021) and Jacob et al. (2021) with significant contributions by the author are briefly summarized. The studies in Chapters 5.1 and 5.2 are thematically related to Study 1 in Chapter 2, the study in Chapter 5.3 is thematically related to Study 3 in Chapter 4.

- **Chapter 6**: *Synthesis*
  The results of the presented studies are summarized and evaluated with regard to their importance for the analysis of coupled processes in porous and fractured rocks. Finally, perspectives for future research are addressed in the outlook (e.g., ideas for follow-up studies or proposals).

METHOD COMPARISON TO DETERMINE HYDRAULIC APERTURES OF NATURAL FRACTURES

2

Reproduced from: Hale, S., Naab, C., Butscher, C., Blum, P., 2020. Method comparison to determine hydraulic apertures of natural fractures. Rock Mechanics and Rock Engineering 53, 1467–1476. https://doi.org/10.1007/s00603-019-01966-7

2.1 Introduction

The hydraulic aperture a_h of a fracture is the idealized opening width available for advective flow. It refers to the parallel-plate model, where the fracture is represented by two smooth parallel plates with the orthogonal distance a_h. The parallel-plate model states that the flow rate through the fracture is proportional to the cube of the aperture and the hydraulic gradient ("cubic law", Louis, 1969; Snow, 1965). In contrast, the mechanical fracture aperture a_m represents the real measurable distance between two fracture surfaces perpendicular to a reference plane (Hakami and Larsson, 1996; Olsson and Barton, 2001), which is usually the best-fit plane of a rough fracture surface (e.g., Vogler et al., 2018). Determining hydraulic apertures is crucial, because flow behaviour in fractured aquifers is controlled by the properties of the fractures, with the hydraulic aperture representing a governing hydraulic feature (e.g., Boutt et al., 2006; Renshaw, 1995; Zeeb et al., 2010).

The permeability and flow rate through a fracture is directly related to its hydraulic aperture (Witherspoon et al., 1980; Zimmerman and Bodvarsson, 1996). Thus, it represents a key input parameter for numerical models that aim at predicting fluid flow and solute transport in fractured rock (e.g., Ghasemizadeh et al., 2012; Jørgensen et al., 2002; Xiao and Zhao, 2018; Zhao et al., 2011). Such models are used in a wide range of geoscientific applications such as geothermal energy generation (Chen et al., 2018), hydrocarbon production (Shahraini et al., 2011), nuclear waste disposal (Blum et al., 2005), geological CO_2 sequestration (Deng et al., 2013) and natural hazards (Strauhal et al., 2016).

Typically, a_h is estimated from flow tests with fractured rock samples in the laboratory based on the parallel-plate model as an approximation (Thörn and Fransson, 2015; Weede and Hötzl, 2005), or by hydraulic well tests in the field (Novakowski and Lapcevic, 1994; Sidle et al., 1998). Such approaches are costly and can only characterize fractures in the near vicinity of the tested wells or existing fractures in the specimen or drilling core (Smith et al., 1987). In this study, we therefore present three simple and non-invasive methods for determining hydraulic fracture apertures applicable for laboratory and field work using (1) a syringe air permeameter, (2) a microscope camera and (3) a 3D laser scanner in combination with an articulated arm. We systematically and quantitatively compare these methods with regard to performance, efficiency and limitations by applying them to a natural bedding joint of a Permian sandstone.

2.2 Materials and methods

2.2.1 Aperture determination and experimental setup

The syringe air permeameter TinyPerm 3 (manufactured by New England Research, Inc.) is a portable device for measuring rock matrix permeability and hydraulic fracture aperture between 10^{-15}–10^{-11} m² and 10–2000 µm, respectively (New England Research, Inc., 2015). The applicability of its predecessor TinyPerm 2 for determining matrix permeability has been intensively studied on outcrops (Petrie et al., 2014; Possemiers et al., 2012) and rock samples (Haffen et al., 2013; Lamur et al., 2017). The working principle of the TinyPerm 3 is illustrated in Figure 2.1. For the experiment ten repetitive measurements were conducted for each measuring point.

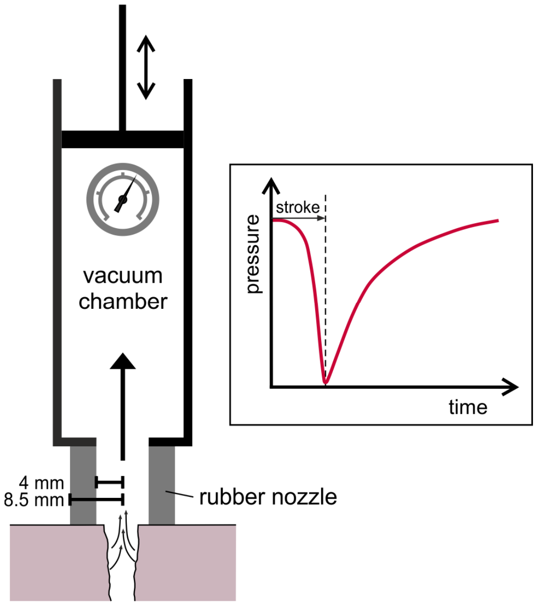

Figure 2.1: Working principle of the air permeameter TinyPerm 3. After pressing the cylindrical rubber nozzle tightly onto the fracture, a transient vacuum pulse is created at the surface by a piston stroke. As air is withdrawn from the fracture, pressure equilibration is monitored by a microcontroller unit. For an isotropic porous medium, the investigation depth is about two to four times the inner radius of the rubber nozzle (Goggin et al., 1988; Possemiers et al., 2012).

A digital microscope camera (DigiMicro Mobile, manufactured by dnt, GmbH) was used to take pictures of the fracture. Additionally, a handheld laser scanner (ModelMaker MMDx100, Nikon Metrology, NV) in combination with an articulated arm (MCA II, Nikon Metrology, NV) and a working range of 2.4 m was used to produce 3D images of the studied rock sample. The line scanner provides a physical resolution of 100 µm with an accuracy of 10 µm (Nikon Metrology, NV, 2010a). The single-point accuracy of the articulated arm is 28 µm, the accuracy of the combined system is not specified (Nikon Metrology, NV, 2010b).

All three methods were tested with the same natural fracture (Figure 2.2). First, the two parts of the sandstone block were separated and the two bedding planes were scanned with the Nikon ModelMaker in order to quantify the surface roughness. Afterwards, the fracture was closed (according to the geometry of the sandstone block) and fixed with bar clamps to ensure a constant stress level during aperture determination using all tested devices within a total measurement time of about three hours. According to Kling et al. (2018), a pre-loading of at least 0.25 MPa would be useful for the application of the proposed contact model. However, in this experimental setup a clamping stress of about 0.03–0.04 MPa, estimated based on fracture area and the achievable clamping force, was applied manually.

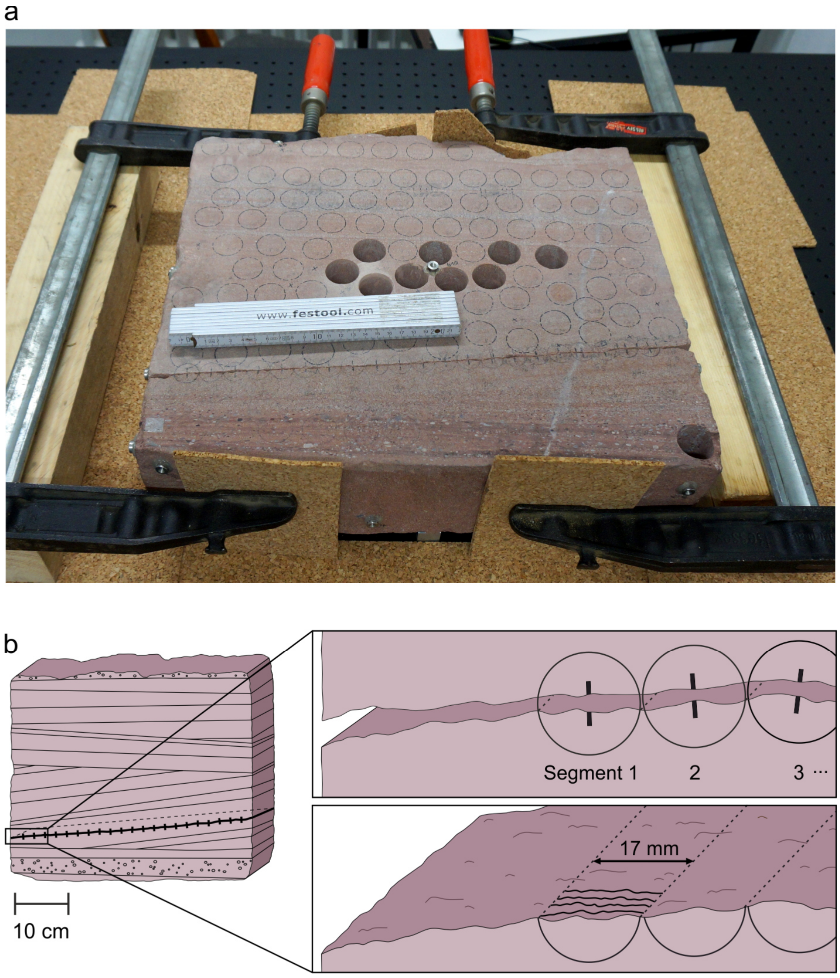

Figure 2.2: Sample with bedding joint in a Permian sandstone block (Fischer et al., 2012b) (a). Aperture determination and roughness profile extraction along the bedding joint was conducted by analyzing 21 adjacent segments (b). The segment width of 17 mm corresponds to the outer diameter of the rubber nozzle of the TinyPerm 3.

2.2.2 Data evaluation

To determine the mechanical fracture aperture with the microscope camera pictures, manual distance measurements at evenly spaced spots along the imaged fracture segment were conducted using the included software PortableCapture (Figure 2.3a). With the arithmetic mean of the measured distances from the pictures representing the mechanical fracture aperture a_m and its standard deviation σ_{a_m}, the hydraulic aperture a_h was estimated for each of the 21 segments along the bedding joint using the equations based on relative roughness σ_{a_m}/a_m given in Table 2.1.

Table 2.1: Equations for estimating the hydraulic aperture (a_h) as a function of relative roughness (σ_{a_m}/a_m) taken from Kling et al. (2017). This subset of equations is in compliance with the studied natural bedding joint, which exhibits a log-normal aperture distribution.

No.	Equation	Fracture type	Reference
2.1	$a_h \approx \frac{a_m}{\sqrt[3]{1 + 20.5\left(\frac{\sigma_{a_m}}{2a_m}\right)^{1.5}}}$	Natural granite fractures	Barton and De Quadros (1997)
2.2	$a_h \approx \frac{a_m}{\sqrt{\left(1 + \frac{\sigma_{a_m}}{a_m}\right)^3}}$	Numerical model of fracture sealing by hydrothermally grown quartz	Kling et al. (2017)
2.3	$a_h \approx a_m \cdot \sqrt[3]{1 - \frac{1.13}{1 + 0.191\left(\frac{2a_m}{\sigma_{a_m}}\right)^{1.93}}}$	Tensile granite fracture	Matsuki et al. (1999)
2.4	$a_h \approx \frac{a_m}{\sqrt[3]{\left(1 + \frac{\sigma_{a_m}{}^2}{a_m{}^2}\right)^{1.5}}}$	Theoretical equation based on stochastics for log-normal aperture distribution	Renshaw (1995)
2.5	$a_h \approx a_m \cdot \sqrt[3]{1 - \frac{\sigma_{a_m}}{a_m}}$	Replicas of a split sandstone and natural granite fracture	Xiong et al. (2011)

For evaluation of the 3D laser scanning data, the point cloud covering the entire closed bedding joint was first segmented corresponding to the TinyPerm 3 and microscope camera (Figure 2.2b). Within each point cloud segment, the distance between the two fracture edges was determined at several evenly spaced locations using the software SpatialAnalyzer (New River Kinematics, Inc.). In Figure 2.3b, the applied distance measurement procedure is illustrated in detail. As in case of the microscope camera pictures, the arithmetic mean (a_m) and standard deviation (σ_{a_m}) of the measured distances were calculated for each segment.

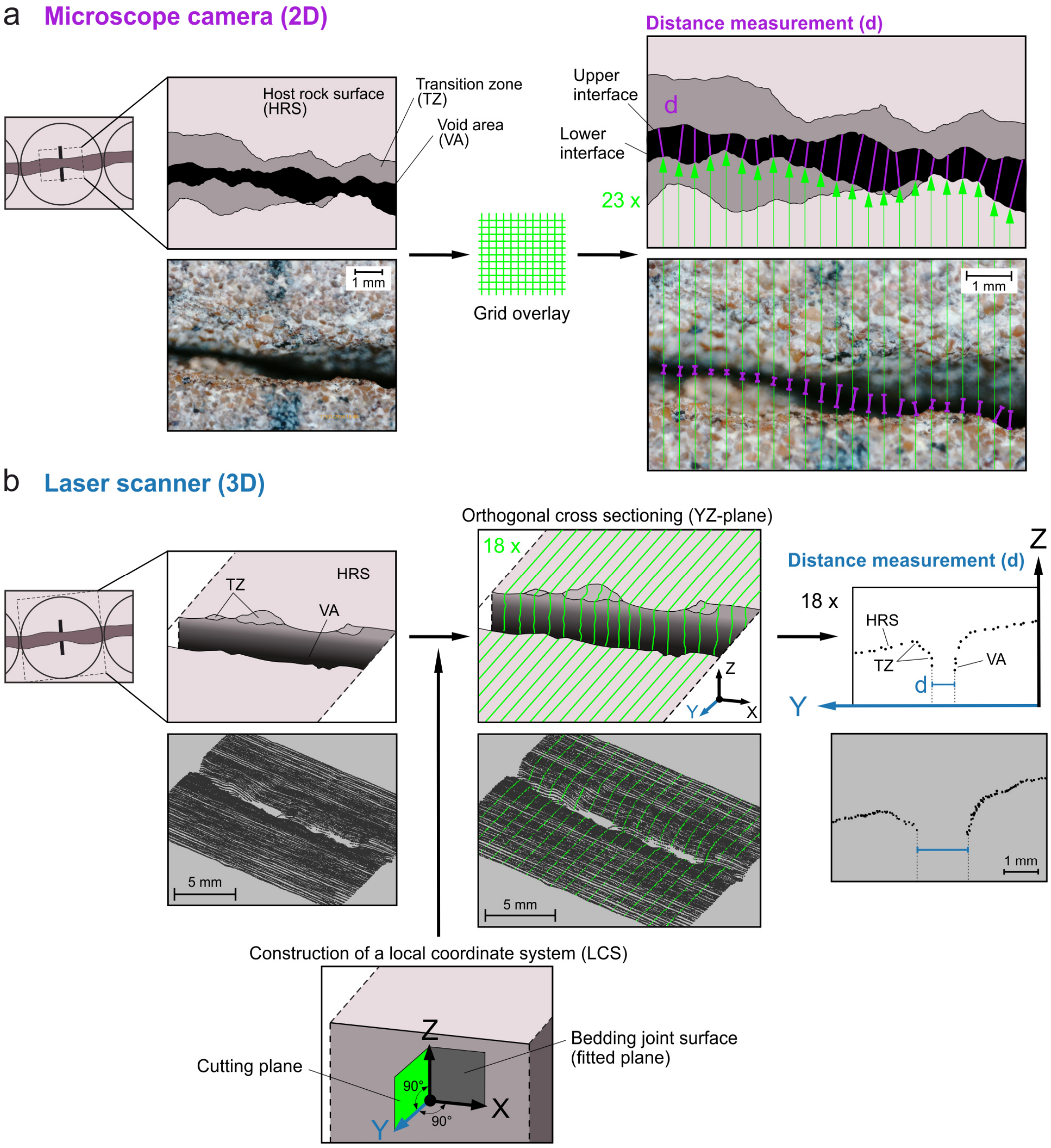

Figure 2.3: Distance measurement approach for 2D microscope camera pictures (a) and 3D point clouds (b). Both clearly show a transition zone (TZ) between the host rock surface (HRS) and the deeper void area (VA) of the bedding joint caused by breakouts at the fracture edges. (a) For evaluating the 2D image data, twenty-three evenly distributed measurement points at the lower interface between the HRS or TZ and the VA were defined by overlaying the picture with a grid. Afterwards, the orthogonal distance to the upper interface was determined using the software PortableCapture. The interfaces could be clearly identified due to a difference in brightness. By entering the magnification factor of the camera, the calculated distances are displayed. (b) For the 3D point cloud segment, distance measurement was carried using a local coordinate system (LCS), which was initially created based on fitted planes (least squares). In a second step, eighteen evenly distributed cutting planes parallel to the YZ-plane were constructed, allowing to create cross sections through the point cloud segment. Finally, the distance in Y-direction was determined at the deepest possible point for each cross section.

For each segment of the bedding joint, four roughness profiles parallel to the fracture edge and within the presumed TinyPerm 3 investigation depth (Figure 2.1) were extracted from the laser scanner point cloud of the initially captured rough bedding plane (Figure 2.2b). From each roughness profile, the roughness parameters Z_2, R_Z, λ and δ were determined (Li and Zhang, 2015) and used to estimate the joint roughness coefficient (JRC) of the respective segment with the equations listed in Table 2.2. Finally, the hydraulic aperture a_h was estimated from the measured mechanical aperture a_m and the corresponding JRC mean value using the empirical relation by Barton (1982):

$$a_h = \frac{{a_m}^2}{JRC^{2.5}} \tag{2.6}$$

Due to the fact that for field work (i.e., outcrop studies) it is not possible to scan the rough fracture surfaces and to determine the JRC, the laser scanning data was additionally evaluated with the approach used for the microscope camera pictures based on relative roughness (Table 2.1), which also represents an appropriate "field option" for the laser scanning method.

Table 2.2: Empirical equations for estimation of the joint roughness coefficient (JRC) using the roughness parameters Z_2, R_Z, λ and δ (Li and Zhang, 2015). The selected equations exhibit high correlation coefficients with JRC of at least 0.9 and were derived from 72–120 mm long natural roughness profiles.

No.	Equation	Reference
2.7	$JRC = 98.718 \cdot {Z_2}^{1.6833}$	Li and Zhang (2015)
2.8	$JRC = 4.4192 \cdot {R_Z}^{0.6482}$	Li and Zhang (2015)
2.9	$JRC = 89.9971 \cdot \lambda^{0.6601}$	Li and Zhang (2015)
2.10	$JRC = 199.6443 \cdot \delta^{0.8665}$	Li and Zhang (2015)
2.11	$JRC = 411 \cdot \delta$	Maerz et al. (1990)
2.12	$JRC = 32.69 + 32.98 \cdot \log(Z_2)$	Yang et al. (2001)
2.13	$JRC = 92.07 \cdot \sqrt{\delta} - 3.28$	Yu and Vayssade (1991)
2.14	$JRC = 61.79 \cdot Z_2 - 3.47$	Yu and Vayssade (1991)

2.3 Results and discussion

Only the syringe air permeameter TinyPerm 3 is capable of directly measuring hydraulic fracture apertures. The other two optical methods provide mechanical apertures and therefore require additional data for conversion into hydraulic apertures. With respect to a_m, the laser scanner delivers significantly higher mean mechanical apertures, inter-quartiles and total ranges compared to the results of the microscope camera (Figure 2.4).

The higher mechanical aperture values obtained from the laser scanning data can be attributed to the fact that mainly the transition zone (Figure 2.3b), caused by breakouts at the fracture edges, was captured by the line scanner, although the distance between the fracture surfaces (i.e., a_m) was measured as deep as possible. During measurement, the laser scanner was moved with a constant orientation over the closed fracture to achieve a sufficiently high measurement accuracy. However, the more representative area deeper in the fracture (void area) could rarely be reached by the scan line. Thus, the point cloud density in the region of interest is generally very low, resulting in overestimation of a_m by the laser scanning method. In contrast, the optical imaging method with the microscope camera was able to capture the more representative void area. Like the laser scanner, the microscope camera is not sensitive to ambient light because it has an active light source (LED ring around camera lens). In case of inclined fracture surfaces (relative to the exposed host rock surface), shadowing must also be considered for aperture measurement. However, as the average inclination angle of the studied bedding joint is only 11°, this effect can be neglected.

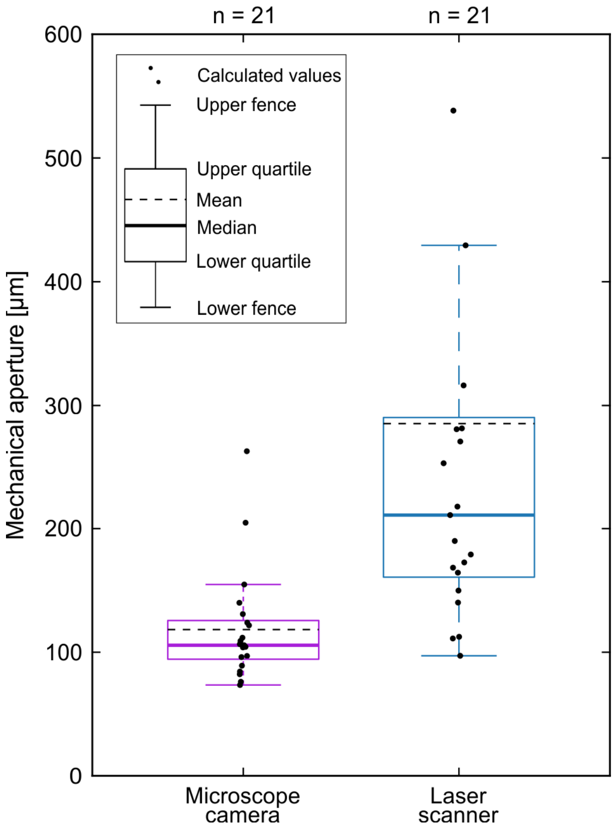

Figure 2.4: Mechanical bedding joint aperture a_m derived from microscope camera pictures and 3D laser scanning. For the laser scanning data, two aperture values > 600 µm are not shown.

To determine a_h with the two optical methods, fracture roughness needs to be used (Chapter 2.2.2). The relative roughness σ_{a_m}/a_m calculated from both microscope camera pictures and laser scanning data as well as the JRC derived from the 2D roughness profiles extracted from the initial bedding joint surface scans are plotted in Figure 2.5. With one exception (Equation (2.9)), the JRC values yielded by the equations in Table 2.2 are in the range of JRC values additionally estimated by visual comparison with the standard profiles of Barton and Choubey (1977) using a Barton comb (Figure 2.5b).

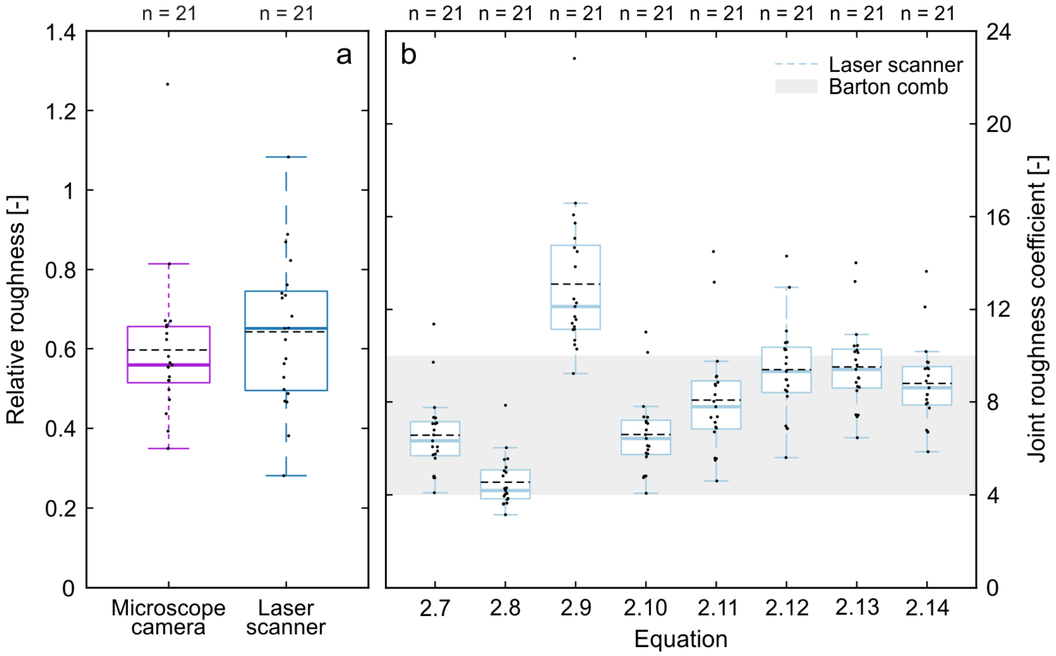

Figure 2.5: Bedding joint roughness derived from 2D microscope camera pictures and 3D laser scanning, given as relative roughness (a) and joint roughness coefficient (b). Visual comparison of Barton comb profiles with the standard profiles (Barton and Choubey, 1977) indicates that the JRC of the bedding joint ranges between 4 and 10.

An overall comparison of a_h determined by the TinyPerm 3, microscope camera and laser scanner reveals significant differences (Figure 2.6). The mean hydraulic aperture of the bedding joint derived from the microscope camera pictures differs by only 7–22 µm from the mean hydraulic aperture of 82 µm measured by the air permeameter. With the camera, almost similar results were obtained using Equation (2.5), a relation by Xiong et al. (2011) established for natural sandstone fractures (Table 2.1).

In contrast, the higher mechanical apertures derived from laser scanning (Figure 2.4) directly led to much higher hydraulic apertures in comparison to the TinyPerm 3 and the microscope camera, independently of the estimation approach that is used for evaluating the laser scanning data (Figure 2.6). The only exception is the derivation from Equation (2.9), where a_h is calculated based on JRC using λ (Table 2.2). However, Equation (2.9) overestimates the roughness of the bedding joint in comparison to the Barton and Choubey (1977) method (Figure 2.5) and therefore underestimates a_h with respect to a_m.

The additional approach of evaluating the laser scanning data using relative roughness allows for direct comparability with the microscope camera data. When comparing the results originating from identical equations in Table 2.1, the difference of mean a_h between these two data sets amounts to 79–143 µm (Figure 2.6) and is clearly affected by the larger a_m values derived from the laser scanning data (Figure 2.4).

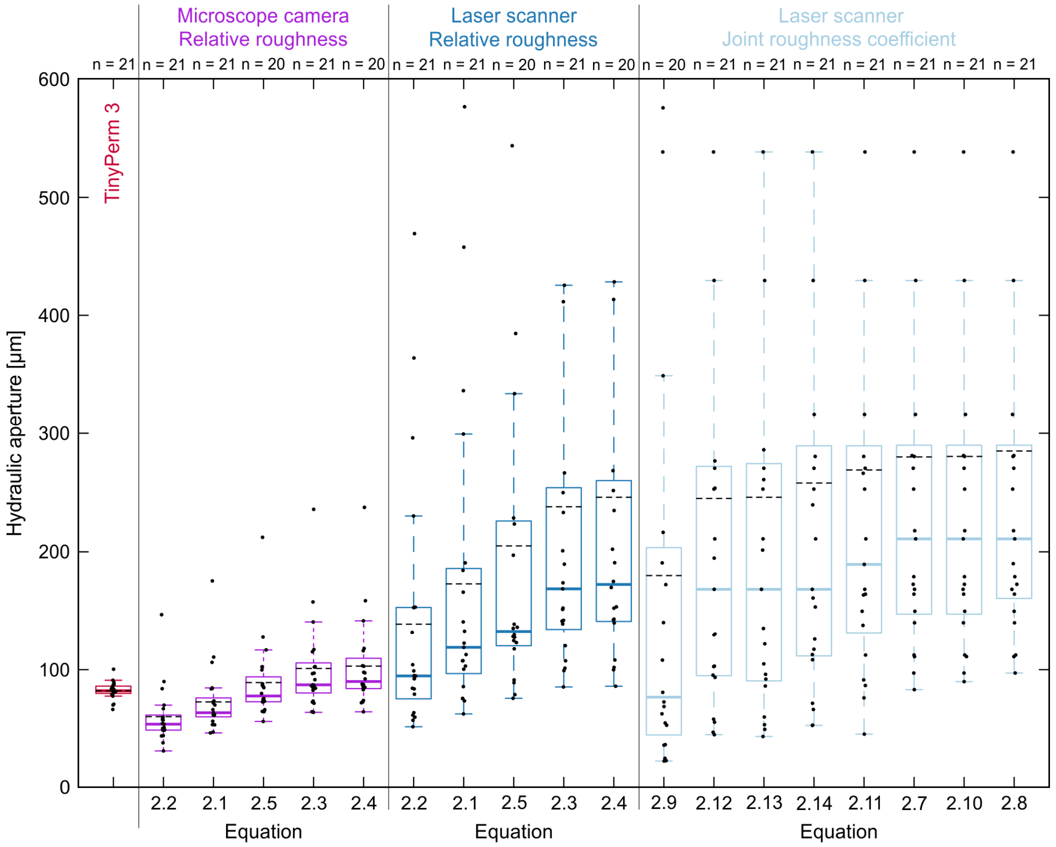

Figure 2.6: Comparison of hydraulic bedding joint aperture a_h determined by TinyPerm 3, microscope camera and 3D laser scanner and estimated based on relative roughness and joint roughness coefficient (sorted by mean values). In five cases, one value had to be discarded due to the validity range of the respective equation (n = 20). For the laser scanning data, 20 aperture values > 600 µm are not shown.

The distribution of estimated a_h values along the bedding joint (Figure 2.7) clearly shows that in case of 3D laser scanning the resulting hydraulic bedding joint aperture (arithmetic mean of all 21 segments, Figure 2.6) is strongly influenced by a few individual segments with a distinct transition zone, such as segment 21, where the deeper void area could not be sufficiently captured. As a consequence, high a_m and a_h values were determined for segment 21. By moving and tilting the handheld scanner more strongly during measurement, the representative void area might be better detected. In contrast, for several other segments the estimated a_h values do not diverge much. For segment 7, which only shows a weakly developed transition zone, the maximum difference in estimated a_h between the different measurement devices and estimation approaches (relative roughness and JRC) is only 75 µm. In this case, the representative void area is closer to the host rock surface, resulting in similar a_m values obtained by the microscope camera (104 µm) and the laser scanner (97 µm).

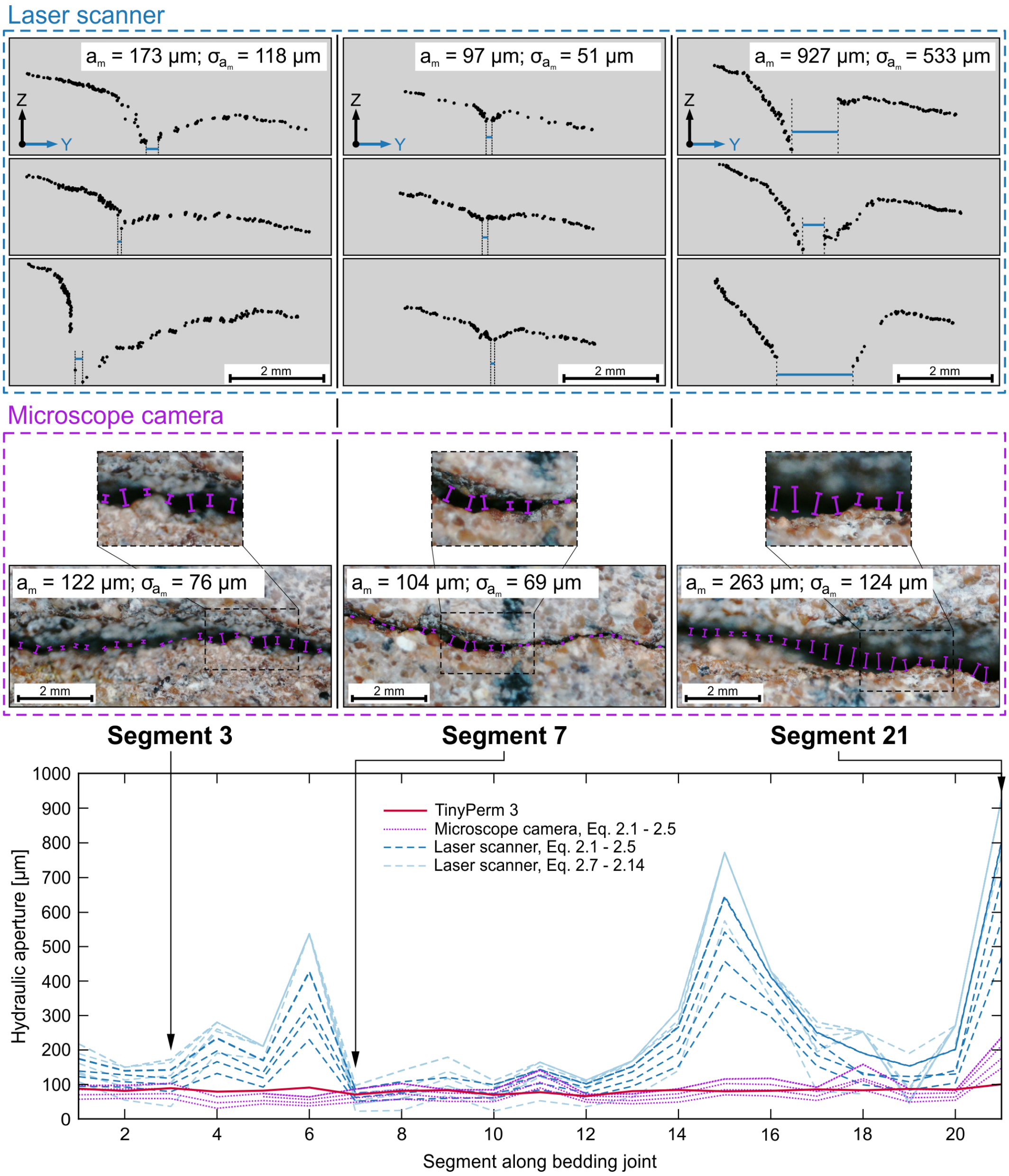

Figure 2.7: Distribution of hydraulic aperture a_h determined by TinyPerm 3, microscope camera and laser scanner along the bedding joint. For exemplary segments of the bedding joint, three (out of 18) representative cross sections through the point cloud (3D laser scanning), microscope camera images as well as the respectively derived mechanical aperture a_m and standard deviation σ_{a_m} are compiled. For determination of the indicated distances (2D and 3D data), the distance measurement approach in Figure 2.3 was used.

The comparison of estimated hydraulic apertures shows that main difference between the three tested methods certainly is their investigation depth: The TinyPerm 3 has the highest investigation depth because the zone of influence of the vacuum pulse reaches deeper into the fracture than the optical methods, although it cannot exactly be specified. Goggin et al. (1988) and Possemiers et al. (2012) suggest the investigation depth being about two to four times the inner radius of the rubber nozzle for an isotropic porous medium. The investigation depth of the laser scanner is the lowest and averages to 1.04 mm with a standard deviation of 0.53 mm, showing significant differences between individual fracture segments. The investigation depth of the microscope camera cannot be quantified because the penetration depth of the emitted light rays is influenced by numerous factors (e.g., fracture geometry, fracture width at the surface). However, the pictures clearly demonstrate that in contrast to laser scanning also the deeper (representative) part of the fracture is captured by the camera method (Figure 2.7).

Despite the high initial cost, the air permeameter TinyPerm 3 is a convenient method for determining hydraulic fracture apertures due to its fast and easy application for laboratory and field investigations (Table 2.3). In contrast to the optical methods, no additional data processing is required and large amounts of data can be produced efficiently.

For larger fractures exceeding the measurement range of the TinyPerm 3 ($a_m > 2$ mm), we recommend using the microscope camera to determine a_m and a rock specific equation to estimate a_h. The measured hydraulic aperture values by the TinyPerm 3 and by microscope camera data are comparable. By applying an automated digital image analysis of the microscope camera pictures instead of the distance measurement approach used here, data evaluation time could be even reduced. In the future the performance of these two devices should be compared to flow tests (e.g., Thörn and Fransson, 2015).

The most expensive device, the laser scanner, yielded considerably higher mean apertures and requires careful handling and extensive data evaluation (Table 2.3). However, one important advantage of 3D laser scanning is the possibility to measure fractures up to several meters and to obtain aperture fields, providing that the relative position of the fracture surfaces is known. This can be achieved by reference points (e.g., Thörn and Fransson, 2015).

Table 2.3: Comparative assessment of the tested aperture measurement methods with regard to cost, time, mobility, dimensions and weight, handling of the device and data evaluation effort. Time (in hours) includes both measurement time and data processing, the latter is not necessary for the syringe air permeameter TinyPerm 3.

	Net cost	**Time**	**Mobility**	**Dimensions and weight**	**Handling**	**Data processing**
TinyPerm 3	< 10.000 US$	10^0 h	good	38 × 13 × 5 cm^3 1.2 kg	moderate	-
Microscope camera	100–200 US$	10^0–10^1 h	good	13 × 10 × 4 cm^3 0.2 kg	simple	moderate
Laser scanner	> 50.000 US$	10^1 h	poor	120 × 40 × 20 cm^3 8.7 kg	complex	complex

2.4 Conclusions

The method comparison for determining hydraulic fracture apertures (syringe air permeameter TinyPerm 3, microscope camera, 3D laser scanner) and their application to a natural sandstone bedding joint reveal different results. Only the air permeameter allows direct measurement of hydraulic apertures, while the other two methods provide only mechanical apertures. Thus, additional data on fracture roughness and model assumptions are necessary.

While the bedding joint roughness derived from 3D laser scanning is comparable with the results of the Barton and Choubey (1977) method, the mechanical aperture a_m is generally larger than the a_m estimated by the microscope camera, despite the use of comparable distance measurement approaches. Since in this study the laser scanner shows a lower investigation depth compared to the microscope camera, in some fracture segments mainly the rounded transition zone between the host rock surface and the deeper void area was captured. Thus, the laser scanning derived mean hydraulic aperture of 139–295 μm is significantly higher than the hydraulic aperture obtained by the microscope camera (60–103 μm) and the TinyPerm 3 (82 μm). In case of the laser scanner, the resulting hydraulic bedding joint aperture is strongly increased by individual fracture segments with a pronounced transition zone and a large mechanical aperture. For segments without a distinct transition zone, comparable hydraulic aperture values result from the different measurement methods.

3D laser scanning is less favorable when the high data evaluation effort and cost are considered. In terms of efficiency and investigation depth, the studied air permeameter is clearly recommended for laboratory and field investigations. The microscope camera is a good alternative in cases where the applicability of the TinyPerm 3 is limited. Manual distance measurement using microscope camera pictures and conversion of the mechanical aperture with a sandstone specific relation yields a mean hydraulic aperture of 89 μm. This only differs by 7 μm from the mean value measured by the TinyPerm 3. Since the reliability of the obtained fracture apertures cannot be fully assessed here, future work should focus on the validation of the studied methods with direct hydraulic tests and valuation of their performance under field conditions and for different rock types.

Acknowledgments

Financial support by the Federal Ministry of Education and Research (03G0871D) as part of the project ResKin (reaction kinetics in reservoir rocks) is gratefully acknowledged. The authors thank Maria Hennes and Thomas Mutschler for supporting the experimental work. The constructive comments of the two reviewers are also gratefully acknowledged.

MECHANICAL AND HYDRAULIC PROPERTIES OF THE EXCAVATION DAMAGED ZONE (EDZ) IN THE OPALINUS CLAY OF THE MONT TERRI ROCK LABORATORY, SWITZERLAND

3

Reproduced from: Hale, S., Ries, X., Jaeggi, D., Blum, P., 2021. Mechanical and hydraulic properties of the excavation damaged zone (EDZ) in the Opalinus Clay of the Mont Terri rock laboratory, Switzerland. Solid Earth 12, 1581–1600. https://doi.org/10.5194/se-12-1581-2021

Abstract

Construction of cavities in the subsurface is always accompanied by excavation damage. Especially in the context of deep geological nuclear waste disposal, the evolving excavation damaged zone (EDZ) in the near field of emplacement tunnels is of utmost importance concerning safety aspects. As the EDZ differs from the intact host rock due to enhanced hydraulic transmissivity and altered geomechanical behavior, reasonable and location-dependent input data on hydraulic and mechanical properties are crucial. Thus, in this study, a hydromechanical characterization of an EDZ in the Mont Terri underground rock laboratory, Switzerland, was performed using three different handheld devices: (1) air permeameter, (2) microscopic camera and (3) needle penetrometer. The discrete fracture network (DFN), consisting of artificially induced unloading joints and reactivated natural discontinuities, was investigated by a portable air permeameter and combined microscopic imaging with automatic evaluation. Geomechanical and geophysical characterization of the claystone was conducted based on needle penetrometer testing at the exposed rock surface. Within the EDZ, permeable fractures with a mean hydraulic aperture of 84 ± 23 μm are present. Under open conditions, self-sealing of fractures is suppressed, and cyclic long-term fracture aperture oscillations in combination with closure resulting from convergence processes is observed. Based on measured needle penetration indices, a uniaxial compressive strength of 30 ± 13 MPa (normal to bedding) and 18 ± 8 MPa (parallel to bedding) was determined. Enhanced strength and stiffness are directly related to near-surface desaturation of the claystone and a sharp decrease in water content from 6.6 wt.-% to 3.7 wt.-%. The presented methodological approach is particularly suitable for time-dependent monitoring of EDZs since measurements are non-destructive and do not change the actual state of the rock mass. This allows for a spatially resolved investigation of hydraulic and mechanical fracture apertures, fracture surface roughness, and physico-mechanical rock parameters and their intra-facies variability.

3.1 Introduction

For all types of man-made underground structures, the formation of a so-called excavation damaged zone (EDZ) or excavation disturbed zone (EdZ) is inevitable (Pusch and Stanfors, 1992; Shen and Barton, 1997). As geologic formations are affected by regional or local stress fields, stress redistribution during excavation leads to displacement and convergence, accompanied by the formation of unloading fractures in the rock mass around the cavity (Bossart et al., 2002). The EDZ is characterized by severe hydraulic, mechanical and geochemical modifications as well as newly formed connected porosity (Dao et al., 2015; Kupferschmied et al., 2015; Labiouse and Vietor, 2014; Sato et al., 2000; Yong et al., 2017). Thus, significant changes in flow and transport properties can be observed in the EDZ due to an enhanced permeability of the connected fracture network creating preferential flow paths. In the EdZ, flow and transport properties are only scarcely affected (Bossart et al., 2004, 2002; Tsang et al., 2005).

The EDZ and its impact on hydraulic and mechanical rock properties are of particular importance for the underground storage of radioactive material (Blümling et al., 2007; Fairhurst, 2004). According to the current state of knowledge, multi-barrier systems for geological disposal are the preferred option for effectively isolating high-level nuclear waste and spent fuels (Birkholzer et al., 2012; Chapman and Hooper, 2012). A service life of up to 1 million years will essentially be guaranteed by the sealing function of a natural barrier (Apted and Ahn, 2010; Wilson and Berryman, 2010). In Switzerland, the Opalinus Clay, an overconsolidated Jurassic claystone, was selected as a host rock for deep geological storage of high-level radioactive waste (Bossart et al., 2017; Nagra, 2002). In the context of host rock characterization and site assessment, the Mont Terri generic underground rock laboratory (URL) provides a valuable site for research, testing and development of in-depth technical know-how. Since 1996, numerous studies and experiments have been conducted in order to evaluate essential properties of the undisturbed and altered rock, as well as to examine the behavior of the Opalinus Clay when exposed to short- or long-term THMC (thermal, hydrological, mechanical and chemical) impacts (Bossart et al., 2017; Pearson et al., 2003). Besides the Mont Terri URL in Switzerland, a number of underground laboratories in other countries and their potential or selected host rock formations are in operation, mainly in crystalline rocks (e.g., Äspö Hard Rock Laboratory in Sweden) and plastic or indurated clays (e.g., HADES URL in Belgium, Meuse/Haute-Marne URL and Tournemire URL in France) (Blechschmidt and Vomvoris, 2010; Delay et al., 2014). Similar to the Opalinus Clay in Switzerland, the EDZ and its impact on the hydromechanical characteristics of the rock mass in the near field of underground structures are of particular interest for the Callovo–Oxfordian claystone in France (e.g., Armand et al., 2014; Baechler et al., 2011; Menaceur et al., 2016) and for the Boom Clay in Belgium (e.g., Bastiaens et al., 2007; Dao et al., 2015).

In the Opalinus Clay of the Mont Terri URL, the EDZ is characterized by a significantly enhanced hydraulic conductivity of 1×10^{-14} to 1×10^{-5} m s^{-1} (Bossart et al., 2004; Jaeggi and Bossart, 2014; Marschall et al., 2017), whereas for undisturbed conditions it ranges between 2×10^{-14} and 5×10^{-12} m s^{-1} (Jaeggi and Bossart, 2014; Lavanchy and Mettier, 2012). Within the EDZ, advective transport is facilitated due to fracture permeability, which is several orders of magnitude higher than the matrix permeability of the claystone (Marschall et al., 2017). Hydraulic fracture parameters such as permeability, transmissivity and flow rate are in turn directly related to the hydraulic fracture aperture a_h (Zimmerman and Bodvarsson, 1996), which therefore represents a key parameter for assessing the hydraulic characteristics of a fractured rock mass or an EDZ. The hydraulic aperture is usually derived from the cubic law (Louis, 1969; Snow, 1965) and relates to the mean opening width of a fracture accessible to advective transport. Due to the confirmed self-sealing capacity of the Opalinus Clay caused by swelling of mixed-layer illite–smectite clay minerals (e.g., Bernier et al., 2007), the hydraulic conductivity of the EDZ is expected to decline within a period of several tens to hundreds of years by progressive fracture closure (Jaeggi and Bossart, 2014). In addition, fractured rock masses are also characterized by a pronounced hydromechanical coupling; i.e., changes in the mechanical stress state result in changes in permeability and therefore hydraulic fracture aperture (Cammarata et al., 2007; Min et al., 2004; Rutqvist and Stephansson, 2003). Generally, a_h is nonlinearly linked to the mechanical fracture aperture a_m as a function of fracture surface roughness (Blum et al., 2009; Renshaw, 1995), for example via the Barton–Bandis model using the joint roughness coefficient (JRC) (Barton, 1982; Barton et al., 1985). The mechanical fracture aperture represents the average geometrical distance between the fracture surfaces (e.g., Hakami and Larsson, 1996) and is needed to examine the response of fracture networks due to normal or shear stresses (e.g., Blümling et al., 2007; Cuss et al., 2011; Zhang, 2016) and mechanical self-sealing of artificial fractures (e.g., Marschall et al., 2017; Nagra, 2002).

Similar to the hydraulic properties, mechanical properties of the Opalinus Clay diverge significantly depending on direction, facies and stress regime (Bock, 2009; Giger et al., 2015). Furthermore, due to a clay-specific hydromechanical coupling (Amann et al., 2017; Marschall et al., 2017), geomechanical parameters such as uniaxial compressive strength, tensile strength, shear strength and the Young´s modulus of the Opalinus Clay generally increase with decreasing water content (Blümling et al., 2007; Wild et al., 2015). Furthermore, geomechanical properties of the Opalinus Clay in the EDZ are also modified in comparison to the undisturbed rock mass. In the short term, a reduction in effective stress caused by pore pressure excess in the vicinity of the advancing excavation front leads to early damage of the rock around the cavity. Right after excavation, pore water drainage and increased suction of the rock mass can be observed close to the cavity (Amann et al., 2017; Giger et al., 2015). In the long term, a general decrease in water content caused by dehydration of the rock leads to locally enhanced rock strength and stiffness (Wild et al., 2015).

An accurate and comprehensive hydraulic and mechanical characterization of the EDZ is therefore essential for confirming the integrity of the host rock in terms of risk and performance assessment (e.g., Blum et al., 2005; Popp et al., 2008; Tsang et al., 2015; Xue et al., 2018). This key information serves as an appropriate starting point for numerical modeling studies investigating the development of the EDZ in the post-closure phase of the repository, and it is also useful for the selection and adaptation of engineering designs or adequate constructional measures (e.g., Hudson et al., 2005; Marschall et al., 2017; Nagra, 2019; Tsang et al., 2012). This not only applies to the issue of nuclear waste disposal, but also generally to other underground structures in different geological materials and settings (e.g., Li et al., 2012; Sheng et al., 2002; Wu et al., 2009).

Hydraulic fracture apertures are usually determined in the laboratory by permeameter tests, with either gases or liquids being used to flow through fractured rock samples (Kling et al., 2016; Li et al., 2018; Shu et al., 2019; Zhang, 2018). In the field, hydraulic properties can be derived from hydraulic or pneumatic borehole tests (Aoyagi and Ishii, 2019; de La Vaissière et al., 2015; Jakubick and Franz, 1993; Shao et al., 2008). Mechanical fracture apertures can generally be obtained by different fracture imaging methods, whereby visibility can be improved by injecting dyed or fluorescent resin into the fractured rock (Armand et al., 2014; Bossart et al., 2002).

Seismic velocity measurements can be carried out in the laboratory by using ultrasonic pulse devices (Popp et al., 2008; Wild et al., 2015) and in the field, for example, by applying mini-seismic methods (Schuster et al., 2017). Geomechanical strength and deformation parameters are usually determined by laboratory experiments. For this purpose, many different test setups are utilized such as compressive strength tests, tensile strength tests, shear tests and triaxial tests under drained or undrained conditions. For the Opalinus Clay, numerous geomechanical tests were carried out on drill cores, primarily examining bedding anisotropy in addition to the hydromechanical coupling by adapting the water content of the samples (Amann et al., 2017, 2012, 2011; Wild et al., 2015). In the field, handheld probes such as a Schmidt hammer or needle penetrometer are used to estimate the uniaxial compressive strength and other mechanical parameters of rock material (Aydin, 2009; Buyuksagis and Goktan, 2007; Erguler and Ulusay, 2009; Hucka, 1965; Okada et al., 1985; Ulusay and Erguler, 2012).

For most investigations drilling is required, either directly for performing borehole tests or for taking standard-compliant samples. However, drilling is not always feasible and boreholes also affect the EDZ by creating additional fluid pathways. Core samples do not necessarily reflect the initial state as they can suffer from disturbance or damage during extraction and transport, leading, for example, to a change in water content. Hence, the objective of this study was to investigate the hydromechanical properties of the EDZ in the Opalinus Clay of the Mont Terri URL from in situ measurements on the exposed rock surface. We carried out a non-destructive and holistic determination of hydraulic and mechanical parameters of the fractured rock mass around a small tunnel niche by combining transient-flow air permeametry, photomicroscopy and needle penetration tests. We characterized bulk rock properties of the claystone and quantified mechanical and hydraulic apertures of different fracture types of the EDZ, since these discontinuities can significantly control the overall material and flow behavior. We have also explored the alteration of the non-lined niche that was directly exposed to air for several years. By using the water content of the claystone, we compared the determined physico-mechanical parameters with data from other studies to assess the effect of desaturation directly on-site at the tunnel wall.

3.2 Material and methods

3.2.1 Study site

Fieldwork was performed in the EZ-B niche of the Mont Terri underground rock laboratory (URL) in St. Ursanne, Switzerland (Figure 3.1a). The axis of the niche is oriented almost normal to Gallery 04 and to the minimum principal stress direction of the in situ stress field (Yong et al., 2010). The niche is located in the upper shaly facies of the Opalinus Clay, which consists of dark gray, mostly mica and pyrite containing calcareous silty-sandy claystones (Hostettler et al., 2017). Bedding dips 45° towards 150°, and thus the niche axis is oriented perpendicular to the strike of the bedding. As the URL is located in the southern limb of the Mont Terri overthrust anticline, the Opalinus Clay has experienced tectonic deformation (Nussbaum et al., 2011). As a consequence, pre-existing natural discontinuities, i.e., bedding-parallel tectonic faults, steeper splays and bedding planes, are present (Nussbaum et al., 2005). The EZ-B niche provides direct access to the overconsolidated claystone of the shaly facies of the Opalinus Clay and to the excavation-induced fracture network of Gallery 04. It was excavated from December 2004 to March 2005 mainly by a road header and pneumatic hammering (Nussbaum et al., 2005). Numerous experiments were carried out in the niche, focusing, for example, on determining the extent and degree of damage of the EDZ (Schuster et al., 2017), fracture network analysis and small-scale mapping (Nussbaum et al., 2011; Yong, 2007), or long-term hydromechanical coupling processes (Möri et al., 2010; Ziefle et al., 2017).

Excavation-induced unloading joints (EDZ fractures) that are related to the construction of Gallery 04 are present within the first 1.3 m of depth into the EZ-B niche (Nussbaum et al., 2005). Strike direction is mostly parallel to Gallery 04 and therefore perpendicular to the axis of the niche. At greater distances, artificial EDZ fractures that originate from the excavation process of the EZ-B niche itself are mainly oriented parallel to the side walls. In addition to the artificially induced unloading fractures, the EDZ also includes tectonic faults and splays, referred to as tectonic fractures. These tectonic fractures were reactivated by stress redistribution and convergence processes after the niche excavation and therefore show measurable fracture apertures (Nussbaum et al., 2011, 2005). In contrast, tectonic discontinuities outside the EDZ are completely closed. In the entrance area of the EZ-B niche, the rock is partly covered by shotcrete, making a section of the EDZ inaccessible (Figure 3.1b). The on-site measurements in the Mont Terri URL were carried out on 16–17 April 2019. At that time, the average air temperature in the EZ-B niche was 16.5 °C, while relative humidity was in the range of 67–72 %.

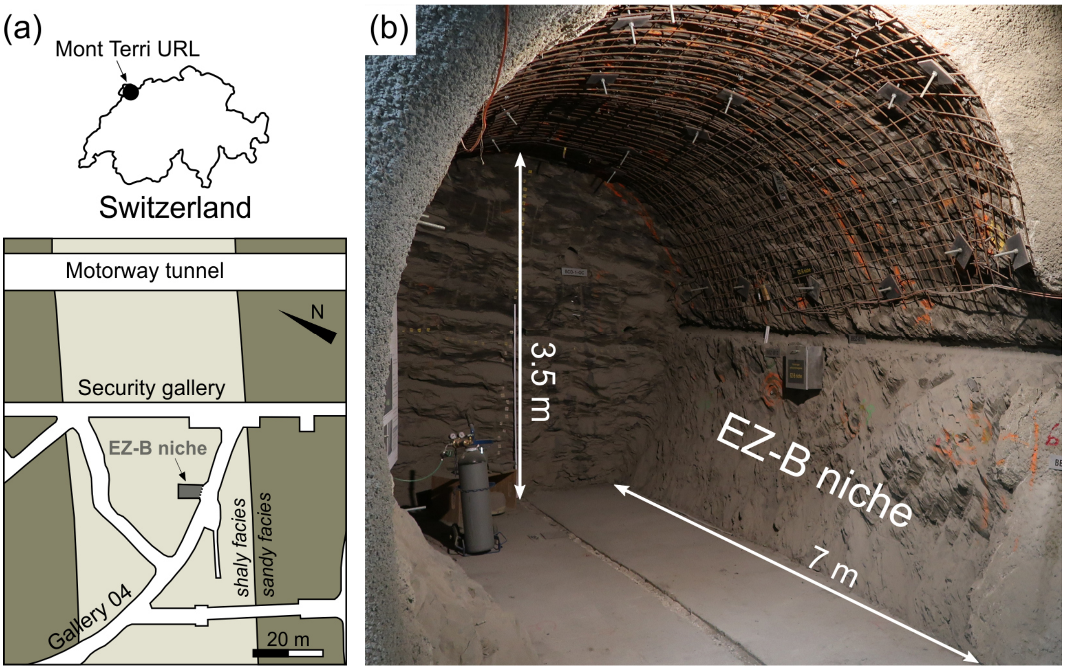

Figure 3.1: (a) Location of the Mont Terri underground rock laboratory (URL) alongside the security gallery of the Mont Terri motorway tunnel and the EZ-B niche situated in the shaly facies of the Opalinus Clay. (b) Photo and dimensions of the EZ-B niche where data acquisition was conducted. In the entrance area, shotcrete partly covers the rock surface on the left and right side wall.

3.2.2 Air permeameter

A handheld transient-flow air permeameter (model TinyPerm 3, New England Research, Inc.) was used to measure the hydraulic aperture (a_h) of accessible fractures in the EZ-B niche. The working principle of the device was outlined by Brown and Smith (2013) and illustrated in Figure 1 of Hale et al. (2020a). Further specifications are provided by New England Research, Inc. (2015). For each fracture, measurement was repeated at least three times. In the case that the mean absolute deviation of measured values was above 10 μm, the measurement was continued. Clear outliers were rejected in order to eliminate erroneous data, e.g., caused by fracture fillings (dust or loose material) or by leaks at the rubber nozzle tip of the air permeameter. Hydraulic fracture apertures are determined directly based on the time-dependent pressure equilibration and the internal calibration of the device (Brown and Smith, 2013; New England Research, Inc., 2015). Thus, no post-processing of data is required for the air permeameter.

For most rocks, the hydraulic aperture derived from air permeameter measurements agrees with the hydraulic aperture available for advective flow. For sandstone, this was demonstrated by Cheng et al. (2020), wherein the air permeameter was validated by steady-state flow tests and different types of artificial fractures with apertures ranging between 7 and 62 μm. For all tested samples, hydraulic apertures were in excellent agreement, with deviations below 5 μm (Cheng et al., 2020). Since clay minerals represent the main constituents of the Opalinus Clay (Bossart and Thury, 2008), diffusive double layers (DDLs) are formed on exposed clay mineral surfaces in water-saturated fractures (Soler, 2001), which could potentially reduce the hydraulic aperture of fractures in argillaceous rocks. For the Opalinus Clay, the maximum thickness of the DDL is only 22 nm, which can be approximated by the Debye length (Wigger and Van Loon, 2018) using representative pore water ionic strength values (e.g., Pearson et al., 2003; Van Loon et al., 2003). Thus, in this case the DDL effect on a_h is negligible.

3.2.3 Microscope camera

For the same set of fractures (Chapter 3.2.2), high-resolution images of fracture traces were taken with a microscope camera (DigiMicro Mobile, dnt GmbH) in order to estimate mechanical fracture apertures (a_m) in the EZ-B niche. The digital camera, with an image resolution of up to 12 million pixels, is comprised of a microscope with an adjustable magnification factor of up to 240. By adjusting the focus dial, the rock surface can be brought into sharp focus. Subsequently, the set magnification factor has to be recorded to evaluate the images. While taking the photo, the field of view should be aligned parallel to the fracture axis and the camera should look vertically into the fracture.

Microscope camera images can be evaluated both manually and automatically. The arithmetic mean of distances measured evenly along the fracture trace corresponds to the mechanical fracture aperture a_m, whereas the associated standard deviation (σ_{a_m}) provides a reasonable measure for fracture surface roughness (e.g., Brown, 1987; Kling et al., 2017). The manual evaluation method uses image analysis software to determine the distance between the two fracture edges regularly along the imaged segment. For a detailed description of the manual image analysis approach, we refer to Hale et al. (2020a). A minimum of 20 distance measurements was needed to gain representative mechanical apertures. Additionally, an automatic approach for determining a_m and σ_{a_m} was applied in this study. The code for running the workflow in Figure 3.2 is written in MATLAB (cf. Appendix A). As input data, microscopic grayscale images with specified magnification factors are used. For an applied image resolution of 9 million pixels, the resulting image size is 3456 pixels in the x direction. As the images should be cropped adequately before analysis according to the extent of the fracture void area, the image size in y direction is variable (Figure 3.2).

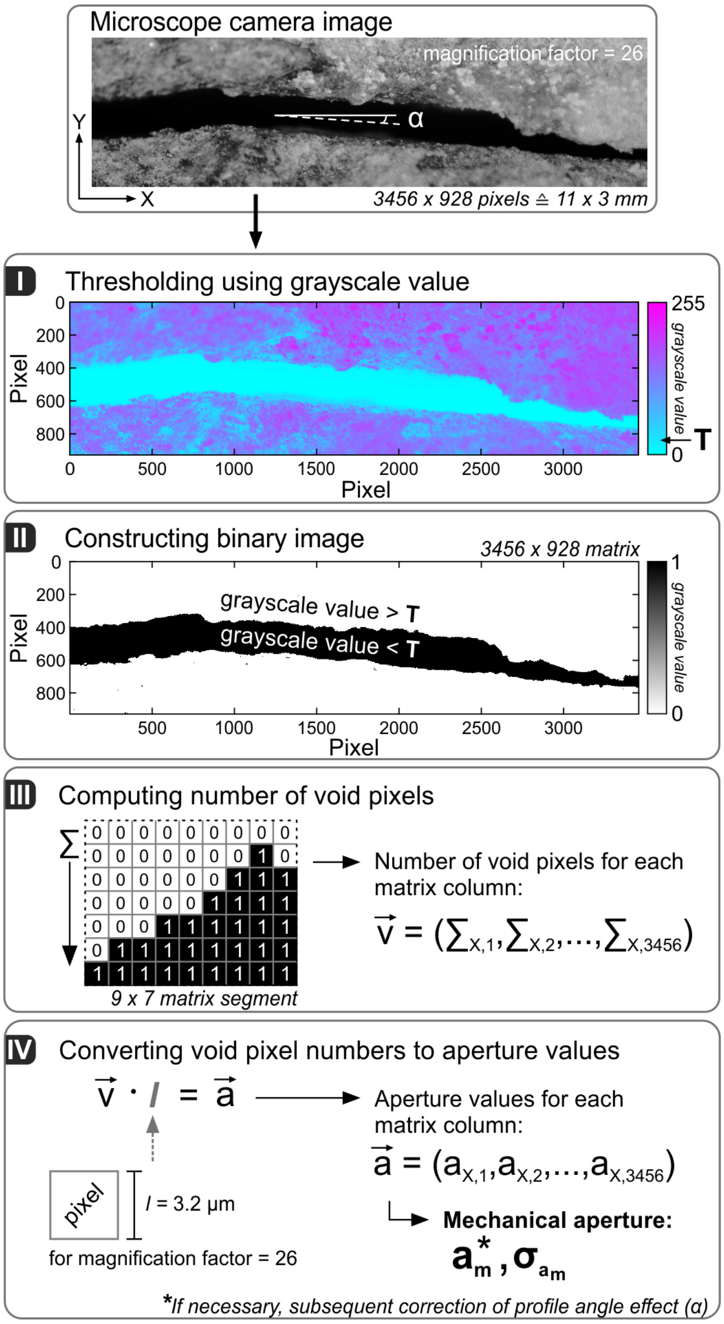

0	0	0	0	0	0	0	0	0
0	0	0	0	0	0	0	1	0
0	0	0	0	0	0	1	1	1
0	0	0	0	0	1	1	1	1
0	0	0	1	1	1	1	1	1
0	1	1	1	1	1	1	1	1
1	1	1	1	1	1	1	1	1

Figure 3.2: Workflow of the automatic approach for determining the mechanical fracture aperture based on microscope camera images of fracture trace segments.

The automated workflow is delineated in Figure 3.2 and involves four steps. Based on the grayscale values of the image (0–255), a suitable threshold value T is first defined in order to segment the void area (region of interest) as precisely as possible. As a second step, the image is binarized; i.e., a value of 1 is assigned to the pixels of the void area and a value of 0 is assigned to all remaining pixels. Based on the resulting binary pixel matrix, the total number of void pixels ($\vec{v}$) is determined column-wise. In order to convert the number of void pixels into aperture values $\vec{a}$ (in µm), the real length of one image pixel is required as a conversion factor. The pixel length directly depends on the magnification of the microscope camera that was set when taking the photo. It can be determined by using the software PortableCapture (Hale et al., 2020a). Finally, the mechanical aperture of the analyzed fracture segment corresponds to the arithmetic mean of the computed aperture values in $\vec{a}$. If the fracture trace deviates from the x direction of the image (denoted by angle α), a_m is corrected accordingly. Using a_m and σ_{a_m}, hydraulic fracture apertures a_h can be subsequently estimated by applying different empirical equations (Table 3.1).

Table 3.1: Equations for estimating the hydraulic fracture aperture based on the mean mechanical fracture aperture and the standard deviation of measured distance values along a fracture trace.

Reference	**Equation**	**No.**
Kling et al. (2017)	$a_h \approx a_m \left(1 + \frac{\sigma_{a_m}}{a_m}\right)^{-1.5}$	3.1
Rasouli and Hosseinian (2011)	$a_h \approx a_m \sqrt[3]{abs\left(1 - 2.25\frac{\sigma_{a_m}}{a_m}\right)}$	3.2
Barton and de Quadros (1997)	$a_h \approx a_m \frac{1}{\sqrt[3]{1 + 20.5\left(\frac{\sigma_{a_m}}{2a_m}\right)^{1.5}}}$	3.3
Xiong et al. (2011)	$a_h \approx a_m \sqrt[3]{abs\left(1 - \frac{\sigma_{a_m}}{a_m}\right)}$	3.4
Renshaw (1995)	$a_h \approx (\overline{a_m})_{Geom}$	3.5
Matsuki et al. (1999)	$a_h \approx \sqrt[3]{1 - \frac{1.13}{1+0.191\left(\frac{2a_m}{\sigma_{a_m}}\right)^{1.93}}}$	3.6
Renshaw (1995)	$a_h \approx a_m \frac{1}{\sqrt[3]{\left(1 + \frac{{\sigma_{a_m}}^2}{{a_m}^2}\right)^{1.5}}}$	3.7
Amadei and Illangasekare (1994)	$a_h \approx a_m \frac{1}{\sqrt[3]{1 + 0.6\left(\frac{a_m}{\sigma_{a_m}}\right)^{-1.2}}}$	3.8

3.2.4 Needle penetration test

A needle penetrometer device (model SH-70, Maruto Corporation Limited, Japan) was used to determine the needle penetration index (NPI) of the Opalinus Clay normal and parallel to bedding, which is directly dependent on the strength of the rock (e.g., Ulusay and Erguler, 2012). For testing, the needle is pushed into the rock by manually applying a maximum load of 100 N. The quotient of the applied load and the attained needle penetration depth (in N mm^{-1}) corresponds to the NPI (Aydan et al., 2014; Ulusay et al., 2014). Needle penetrometer tests were carried out at different measurement points on the rock surfaces in the EZ-B niche. If microcrack formation around the needle hole or tensile splitting along bedding planes was observed, the measured value was excluded from the dataset. For a detailed description of the working principle and testing procedure we refer to the ISRM-suggested method for needle penetration testing by Ulusay et al. (2014).

Several physico-mechanical parameters are directly related to the NPI. For example, a strong correlation between the NPI and the uniaxial compressive strength of intact rock was proven (e.g., Aydan, 2012; Uchida et al., 2004). Established empirical equations were used in this study to estimate uniaxial compressive strength (UCS), Brazilian tensile strength (BTS), Young´s modulus (E), elastic P-wave (v_p) and S-wave velocity (v_s), cohesion (c), and friction angle (φ) (Table 3.2). In order to enable a direct comparison of the estimated parameters with existing literature data, the water content of the Opalinus Clay was additionally determined by oven drying according to DIN EN ISO 17892-1 (2015-03) using two representative rock specimens from the walls of the EZ-B niche, which were sampled at the time of the on-site measurements.

Table 3.2: Equations for the estimation of physico-mechanical rock parameters using the needle penetration index (NPI), taken from Ulusay and Erguler (2012), Ulusay et al. (2014), and Aydan et al. (2014). The relations are based on compiled experimental data obtained from various lithologies.

Parameter	**Equation**	**Reference**
Uniaxial compressive strength [MPa]	$UCS \approx 0.418 \cdot NPI - 0.004$	Uchida et al. (2004) [a]
	$UCS \approx 0.2 \cdot NPI$	Aydan (2012) [b]
	$UCS \approx 0.402 \cdot NPI^{0.929}$	Ulusay and Erguler (2012) [c]
Brazilian tensile strength [MPa]	$BTS \approx 0.02 \cdot NPI$	Aydan et al. (2014) [b]
Young’s modulus [GPa]	$E \approx 0.05 \cdot NPI$	Aydan et al. (2014) [b]
Cohesion [MPa]	$c \approx 0.04 \cdot NPI$	Aydan et al. (2014) [b]
Friction angle [°]	$\varphi \approx 13.375 \cdot NPI^{0.25}$	Aydan et al. (2014) [b]
P-wave velocity [km s^{-1}]	$v_p \approx 0.33 + 0.3 \cdot NPI^{0.5}$	Aydan et al. (2014) [b]
S-wave velocity [km s^{-1}]	$v_s \approx 0.1 + 0.18 \cdot NPI^{0.5}$	Aydan et al. (2014) [b]

[a] Clay. [b] Mudstone, sandstone, siltstone, marl, lignite, tuff, soapstone, pumice, soft limestone, sheared shale.
[c] Marl, siltstone, mudstone, tuff.

In Ulusay and Erguler (2012), the term needle penetration resistance (NPR) is used instead of NPI.

3.3 Results and discussion

3.3.1 Hydraulic and mechanical fracture properties

3.3.1.1 Measured hydraulic fracture aperture

The hydraulic aperture a_h of artificially induced unloading joints, reactivated fault planes, and bedding-parallel desiccation or unloading cracks of the EDZ in the EZ-B niche of the Mont Terri URL was determined at 43 measuring points on both side walls using the handheld transient-flow air permeameter (Figure 3.3a). The mean hydraulic fracture aperture in the EZ-B niche was 84 ± 23 µm, with values in the range of around 100 µm occurring most frequently (Figure 3.3b). On average, artificially induced unloading fractures (hereinafter referred to as EDZ fractures), mainly oriented sub-parallel to the axis of Gallery 04, showed the smallest hydraulic apertures of 61 ± 30 µm (n = 9) compared to reactivated fault and bedding planes. They were also characterized by the largest range of measured aperture values from 20 to 100 µm, which is also evident from the high standard deviation.

Reactivated tectonic discontinuities, namely fault planes and splays of the SSE-dipping thrust system (hereinafter referred to as tectonic fractures), showed an average hydraulic aperture of 89 ± 18 µm (n = 31). The hydraulic fracture aperture of bedding-parallel cracks was highest (94 ± 8 µm), although the obtained average value cannot be considered representative due to a small number of measurements (n = 3). On the right side wall of the EZ-B niche, most of the sampling points were arranged near borehole BEZ-B1 (Figure 3.3b) due to good accessibility and beneficial surface conditions. Based on the measured aperture values, no indication of a "borehole damaged zone" (Amann et al., 2017) is observable, which is related to the fact that borehole BEZ-B1 is oriented perpendicular to the strike of the bedding.

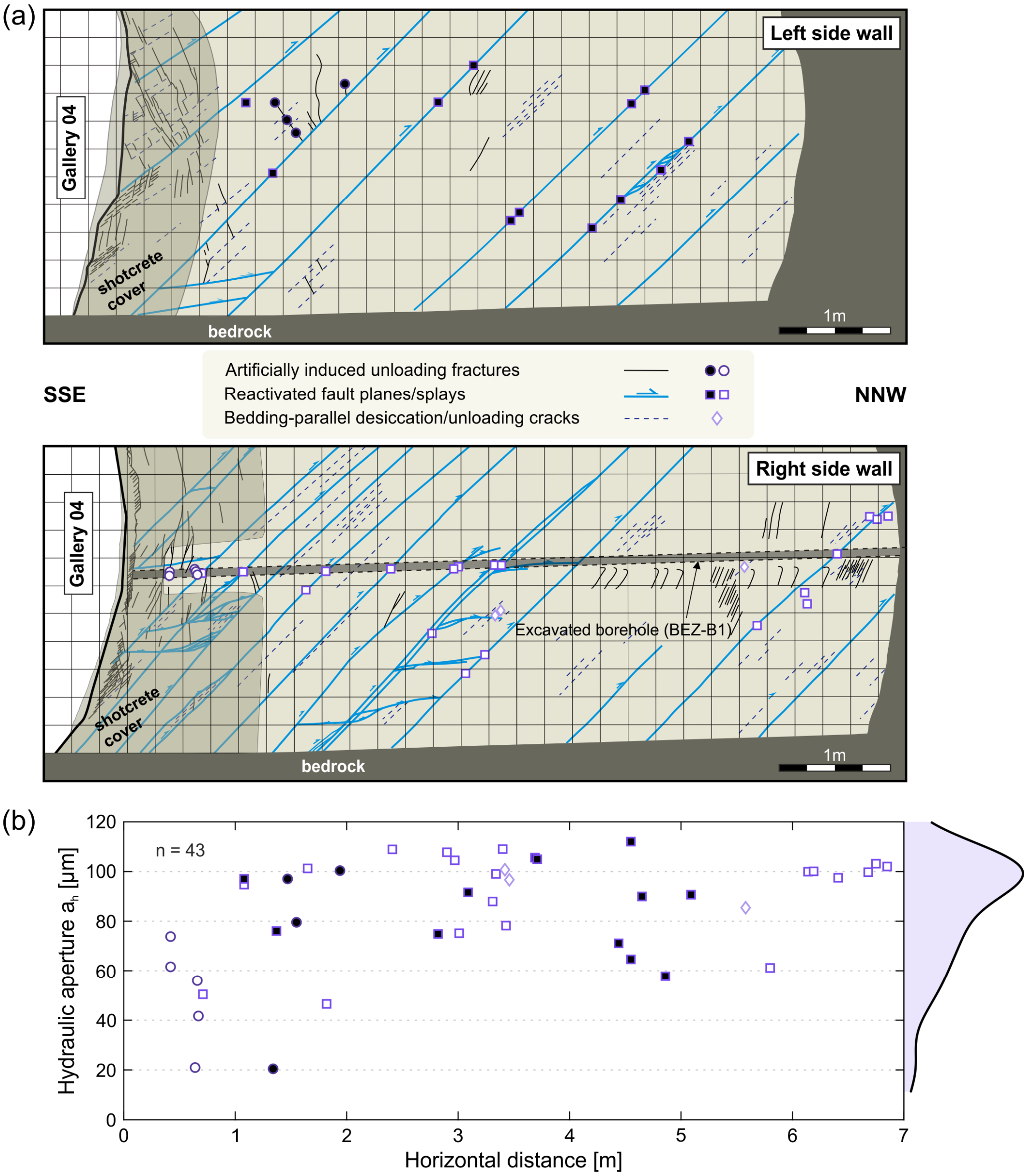

Figure 3.3: (a) Structural maps of the EZ-B niche with measurement points for hydraulic and mechanical aperture determination on the left (closed symbols) and right side wall (open symbols), modified after Nussbaum et al. (2005). (b) Hydraulic fracture apertures measured by the air permeameter plotted against the distance to Gallery 04. On the right side, the distribution of a_h is visualized by a probability density function obtained by kernel density estimation (KDE).

The on-site aperture measurements in the EDZ clearly show that about 15 years after excavation, hydraulically open fractures and therefore accessible fluid pathways are still present in the EZ-B niche. In the Opalinus Clay, fractures are successively closed by self-sealing processes, which lead to a significant permeability reduction in the EDZ, finally approaching the hydraulic conditions of undeformed rock again (Bernier et al., 2007; Jaeggi and Bossart, 2014; Nagra, 2002). However, this only applies for saturated conditions after backfilling and sealing, when progressive resaturation of the host rock around the underground facility is initiated (Bossart et al., 2017; Marschall et al., 2017). Under open conditions the EDZ is an unsaturated zone, as shown, for example, by Ziefle et al. (2017). Since 2006, the temporal evolution of the EDZ in the EZ-B niche was assessed by jointmeter time series obtained from a single tectonic fracture. Based on this dataset, a cyclic long-term closure of the monitored fracture was demonstrated (Ziefle et al., 2017), but this is probably primarily due to niche convergence.

For shales or argillaceous rocks, changes in the saturation state are directly linked to structural modifications (Valès et al., 2004; Yurikov et al., 2019). In the highly saturated state, a large portion of the pore water is adsorbed onto the clay mineral surfaces, while for high external suction, i.e., desaturation, it is extracted from the rock through the pore network (Zhang et al., 2007). Dehydration of claystone leads to a decrease in total porosity (Yurikov et al., 2019) and induces a reduction of pore and swelling pressure, which in turn impedes self-sealing processes (Tsang et al., 2005; Zhang et al., 2007). In addition, secondary shrinking-induced tension fractures can develop parallel to bedding with progressive dehydration (Delage, 2014). In contrast, hydration of claystones leads to a significantly enhanced creep and swelling capacity (Yurikov et al., 2019; Zhang et al., 2007). In the case of the non-lined EZ-B niche in Mont Terri, self-sealing is inhibited due to a sharp decrease in water content of the rock mass close to the niche caused by sustained ventilation since tunnel excavation. This observation is of particular importance for the second phase in repository development, the open drift stage, where ventilation-induced damage and dehydration in the tunnel systems are also expected (Tsang et al., 2005). The presented results therefore serve as a valuable analog and provide information on the state of the EDZ in a non-lined niche in indurated clay after prolonged exposure.

With increasing distance to Gallery 04, a general decrease in hydraulic fracture aperture a_h was expected. When leaving the EDZ, the degree of damage or disturbance generally decreases as deconfinement, displacement and deviatoric stresses within the rock mass are highest directly next to the cavity (Lisjak et al., 2016; Yong et al., 2010). Based on the results of the air permeameter measurements, however, a weak positive correlation between a_h and the horizontal distance could be observed (correlation coefficient r = 0.43). A decrease in hydraulic aperture with greater distance to Gallery 04 could not be observed, since the fractures in the EZ-B niche originate from two different excavations. Due to the applied excavation technique and favorable orientation of the niche (Chapter 3.2.1), the EDZ of the EZ-B niche is less pronounced compared to the EDZ around Gallery 04. However, two EDZs, i.e., two fracture systems, are superposed. Hydraulic apertures in the immediate vicinity of Gallery 04 are comparatively small (Figure 3.3b). Presumably, this is caused by shotcrete application to the exposed claystone surface associated with increased water availability, leading to partial resaturation of the rock. This water supply most likely promoted swelling of clay minerals and fracture closure to a certain degree, resulting in a general reduction of hydraulic apertures in the entrance area of the EZ-B niche.

Due to the limited measuring range of the air permeameter, hydraulic apertures of widely opened fractures (a_h > 2 mm) could not be quantified. Thus, the mean a_h of open fractures in the EZ-B niche was rather underestimated with this method. It is also noticeable that for 49 % of the measurement points, the first measured value was smallest. This can be explained by dust or loose material inside the fracture which was removed by the first stroke with the air permeameter. As outlined above and supported by continuously recorded jointmeter data from the EZ-B niche, the saturation state of the Opalinus Clay has a major influence on measured fracture apertures. From 2015 to 2019, the investigated single fracture was subject to annual aperture fluctuations of up to 500 μm due to seasonal fluctuations of relative humidity (RH) (Ziefle et al., 2017). However, over the long period since the niche was completed in 2005, the observed trend of cyclic aperture closure has decreased substantially, and seasonal fluctuations of fracture aperture are by now far less pronounced. In the EZ-B niche, relative humidity is highest between July and October ($RH = 100$ %), while the lowest values are usually recorded in February ($RH \approx 60$ %). Since the measurement campaign for the present study was carried out in April, it can be assumed that the obtained hydraulic and mechanical aperture values roughly represent an annual average state of the continuously changing fracture system.

For the Opalinus Clay in the Mont Terri URL, no direct information on hydraulic fracture apertures is available, which further illustrates the difficulty of conducting practicable and accurate a_h measurements in the field. In order to compare the measured values with literature values in terms of plausibility, fracture transmissivities (T_f) obtained from extensive hydraulic testing in the Mont Terri URL were utilized (Table 3.3). Based on the cubic law, an equivalent hydraulic fracture aperture ($a_{h,eq}$) can be calculated from T_f using the relation (Brown, 1987)

$$a_{h,eq} = \sqrt[3]{T_f \cdot \frac{12 \cdot \mu_W}{\rho_W \cdot g}} \qquad (3.9)$$

where μ_W is the kinematic viscosity of water, ρ_W is the density of water and g is the gravitational acceleration. It should be noted that hydraulic tests are generally used to characterize certain borehole intervals. Transmissivity values that are derived from these tests therefore relate to a certain rock volume, while the number of hydraulically active fractures intersecting the test interval is usually unknown (Gustafson and Fransson, 2006). In this case, fracture densities must be considered for calculating equivalent hydraulic apertures. However, some studies also provide single-fracture transmissivities which could therefore directly be converted to $a_{h,eq}$ using Eq. (3.9) for direct comparison with a_h measured by the air permeameter (Table 3.3).

Table 3.3: Comparison of measured hydraulic fracture aperture (this study) and equivalent hydraulic aperture values derived from reported single-fracture transmissivities from the Opalinus Clay in the Mont Terri URL.

Reference	**Description**	**Fracture transmissivity**	**Equivalent hydraulic aperture**
Martin et al. (2004)	Transmissivity from high-resolution probe testing in four boreholes (EDZ + undisturbed rock)	$T_f = 1.0 \times 10^{-14}$ – 1.0×10^{-9} m^2 s^{-1}	< 1–11 μm [a]
Meier et al. (2000)	Single-fracture transmissivity from long-term hydraulic testing (EDZ)	$T_f = 2.0 \times 10^{-8}$ m^2 s^{-1}	29 μm
Bossart et al. (2004)	Single-fracture transmissivity from hydraulic cross-hole testing (EDZ)	$T_f = 1.9 \times 10^{-8}$ – 4.0×10^{-8} m^2 s^{-1}	29–37 μm
Blümling et al. (2007)	Reported maximum local fracture transmissivity (EDZ)	$T_f = 5.0 \times 10^{-7}$ m^2 s^{-1}	85 μm
This study	Air permeameter (EDZ)	–	20–112 μm

[a] Assumption of a single hydraulically dominant fracture (short test intervals, typically 5 cm).

Although slightly larger, the hydraulic fracture apertures measured by the air permeameter are of the same order of magnitude compared to equivalent hydraulic apertures that were derived from single-fracture transmissivity testing (Table 3.3). Due to the previously outlined processes related to the successive dehydration of the claystone, hydraulic apertures in the EZ-B niche were expected to differ slightly from the literature values due to the elongated exposure time. Nevertheless, the measured values are plausible and clearly show that the air permeameter is suitable for the measurement of hydraulic fracture apertures within the EDZ of the Opalinus Clay.

3.3.1.2 Measured mechanical fracture aperture

For the same set of fractures, the mechanical fracture aperture a_m was determined based on microscope camera images. For seven measurement points the mechanical aperture could not be evaluated due to poor quality of the microscopic images. The measured mechanical fracture apertures in the EZ-B niche showed a widespread range between 19 μm and 833 μm, while most values were clustered around 115 μm (Figure 3.4). Artificial EDZ fractures showed the lowest values among the studied fracture types (127 ± 92 μm), whereas the mean mechanical aperture in the EZ-B niche was 233 ± 205 μm. Again, no distinct trend with increasing distance to Gallery 04 could be observed. For the vast majority of sampled fractures, a_m was greater than or equal to a_h as expected (Figure 3.4). As is the case for hydraulic apertures, almost no information on mechanical fracture apertures within the EDZ of the Opalinus Clay was available for comparison. Bossart et al. (2004) mention unloading fractures with mechanical apertures of up to 1 cm. However, as the specified measurement range of the air permeameter is limited to hydraulic apertures of 2 mm, such widely opened fractures were not investigated in this study.

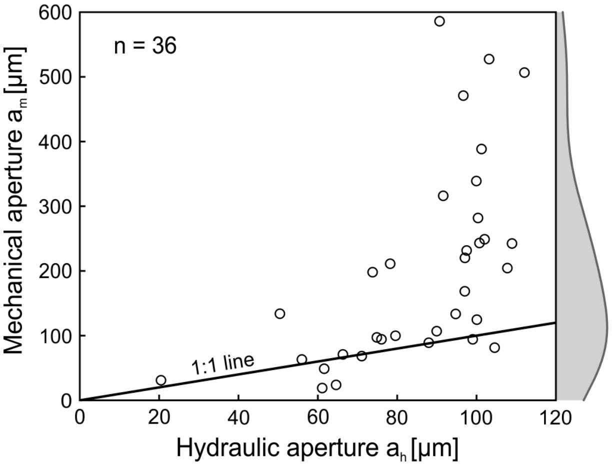

Figure 3.4: Comparison of measured mechanical and hydraulic fracture apertures in the EZ-B niche with probability density function for a_m. Two outliers with mechanical apertures of 789 µm and 833 µm are not shown for better visibility.

The newly implemented analysis algorithm for microscopic images (Figure 3.2) provided similar results compared to the manual approach used in Hale et al. (2020a) (correlation coefficient $r = 0.93$). Thus, automatic image analysis is highly recommended. In addition to significant time savings, more representative results for a_m and σ_{a_m} of the imaged fracture trace segment can be obtained due to the large number of distance measurements. For images that could not be evaluated automatically, manual analysis was employed. This particularly applied to images that were not sufficiently focused and fissures with very small mechanical apertures. In these cases, the void area could not be properly distinguished from the rock, thus hampering the selection of an appropriate threshold value for automatic analysis.

3.3.1.3 Estimated hydraulic fracture aperture

Based on the mean mechanical aperture (a_m) and the corresponding standard deviation (σ_{a_m}), which provides a statistical measure for fracture surface roughness, hydraulic apertures were estimated using established empirical relations (Eq. (3.1) to (3.8), Table 3.1). For eight different equations, the results are shown in Figure 3.5. With regard to the mean hydraulic fracture aperture, the full dataset of the discrete fracture network (DFN) in the EZ-B niche was best reproduced by Eq. (3.1) (Kling et al., 2017), which is therefore recommended for future studies. The median of this dataset was also in excellent agreement with the measured data (Figure 3.5). However, there were generally large deviations between the measured and estimated mean a_h. With regard to the frequency distribution of data points, Eq. (3.6) to (3.8) performed better because a_m is reduced to a lesser extent. Similar to the dataset of the TinyPerm 3 (air permeameter), most values were clustered around 100 µm. However, few very high values led to a significant overestimation of the arithmetic mean (216–221 µm). In order to provide a representative measure of the central tendency of the estimated hydraulic aperture for a given fracture set or DFN, the use of the median is highly recommended. For EDZ fractures in particular, a_h was best estimated by Eq. (3.2) (Rasouli and Hosseinian, 2011).

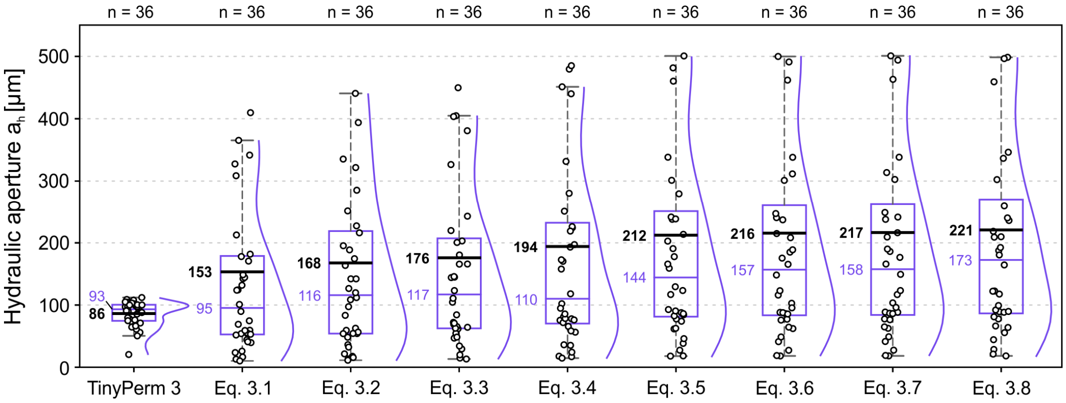

Figure 3.5: Comparison of hydraulic fracture apertures measured by the air permeameter (TinyPerm 3) and estimated based on mean mechanical fracture apertures and standard deviations from microscopic fracture trace analysis. For each dataset, the arithmetic mean (bold black line), the median (thin purple line) and the probability density function (obtained by kernel density estimation) are shown. Values above 550 µm are excluded from the graph.

Higher deviations between estimated and measured hydraulic apertures were observed for fractures with either very low or very high mechanical apertures in relation to the measured value range. This was confirmed by a strong correlation between a_m and the resulting deviation between estimated and measured a_h values; for example, for Eq. (3.1) the correlation coefficient was 0.96. It was noticeable that for EDZ fractures far higher agreement of estimated and measured hydraulic apertures could be observed in comparison to tectonic fractures, independently of the relation that was used for conversion. This is most likely related to smaller mechanical apertures. While EDZ fractures seem to better correspond to the general model concept of an “ideal plane-parallel fracture”, tectonic fractures are most probably characterized by a different a_m–a_h relation. While implied by the presented measurement data, this issue should still be examined based on larger datasets.

Despite the good performance of the microscope camera method for EDZ fracture analysis, direct measurement of $a_h$with the air permeameter is always preferable. Nevertheless, the data derived from microscopic imaging can provide explicit information on fracture geometry and formation mechanism. Presumably due to their formation mechanism, EDZ fractures (artificial unloading joints) showed comparatively little variation in aperture along the fracture traces, resulting in a rather low mean standard deviation σ_{a_m} of 58 µm. For EDZ fractures, a_m was on average 1.7 times larger than a_h. In contrast, for tectonic fractures (reactivated fault planes), an average σ_{a_m} of 90 µm and an a_m/a_h ratio of 2.4 were determined in the EZ-B niche. However, the higher mean standard deviation for the measured aperture values along the fracture segment obtained for tectonic fractures is not necessarily caused by a higher roughness of the fault surfaces themselves. Namely, observations in the Mont Terri URL showed that fault surfaces are generally polished with slickensides, while EDZ fracture surfaces often show plumose structures (Nussbaum et al., 2011, 2005; Yong, 2007). On the other hand, since EDZ fractures originate from tensile stresses, these fracture surfaces also show a high degree of matching. This directly leads to a comparatively small standard deviation of measured aperture values along an imaged EDZ fracture segment. Fault planes in the EZ-B niche were reactivated by stress redistribution during excavation and subsequent convergence, which is why the investigated tectonic fractures even show measurable apertures. Due to shear loading, relative displacement led to a higher mismatch of the two fracture surfaces. For the tectonic fractures, the higher mean standard deviation σ_{a_m} that was observed by microscopic image analysis therefore primarily reflects the increased variance of measured distances due to mismatched fracture walls rather than the actual fracture surface roughness.

3.3.2 Geomechanical and geophysical properties

Needle penetration testing (NPT) was performed at 47 sampling points on both side walls of the EZ-B niche, including 18 tests normal to bedding and 29 tests parallel to bedding. The measured needle penetration index (NPI) clearly confirmed the significant strength anisotropy of the Opalinus Clay (Jaeggi and Bossart, 2014). Normal to bedding, strength was significantly higher than parallel to bedding, indicated by an NPI of 98 ± 29 N mm^{-1} and 59 ± 19 N mm^{-1}, respectively. For all measurements a constant load of 100 N was selected. Thus, the NPI only depended on the observed needle penetration depth. Measurements normal to bedding resulted in several invalid tests due to formation of microcracks around the needle hole. In this case, the measured value was discarded (Chapter 3.2.4). The results of the parameter estimation based on the measured NPI are listed in Table 3.4.

Figure 3.6 provides a graphical overview and enables comparison with available literature data to assess the quality of the applied in situ parameter estimation. As discussed in Chapter 3.1, geomechanical and geophysical parameters in the EZ-B niche are significantly affected by the desaturation of the rock. Compared to the natural water content of the shaly facies of about 6.6 wt.-% (Bossart and Thury, 2008), the water content of the Opalinus Clay in the EZ-B niche has decreased drastically to 3.7 wt.-% due to direct air contact and long-time ventilation of the URL (Jaeggi and Bossart, 2014; Ziefle et al., 2017). Since samples for water content determination were taken directly from the rock surface at the walls of the EZ-B niche, this value represents the state of the Opalinus Clay after 15 years of direct atmospheric exposure. The NPI, and therefore estimated geomechanical and geophysical parameters, are not influenced by the distance to Gallery 04.

Table 3.4: Estimated geomechanical and geophysical parameters for the Opalinus Clay in the EZ-B niche normal and parallel to bedding based on the needle penetration index.

Parameter	**Normal to bedding**	**Parallel to bedding**	**Reference**
NPI	98 ± 29 N mm^{-1} (n = 18)	59 ± 19 N mm^{-1} (n = 29)	
Water content	3.7 wt.-%		
UCS	29.7 ± 12.5 MPa	18.2 ± 8.0 MPa	all UCS equations (average)
	41.0 ± 12.2 MPa	24.8 ± 8.1 MPa	Uchida et al. (2004)
	19.6 ± 5.8 MPa	11.9 ± 3.9 MPa	Aydan (2012)
	28.3 ± 7.7 MPa	17.7 ± 5.4 MPa	Ulusay and Erguler (2012)
BTS	2.0 ± 0.6 MPa	1.2 ± 0.4 MPa	Aydan et al. (2014)
E	4.9 ± 1.5 GPa	3.0 ± 1.0 GPa	Aydan et al. (2014)
c	3.9 ± 1.2 MPa	2.4 ± 0.8 MPa	Aydan et al. (2014)
φ	41.8 ± 2.7°	36.8 ± 2.8°	Aydan et al. (2014)
v_p	3.3 ± 0.4 km s^{-1}	2.6 ± 0.4 km s^{-1}	Aydan et al. (2014)
v_s	1.9 ± 0.2 km s^{-1}	1.5 ± 0.2 km s^{-1}	Aydan et al. (2014)

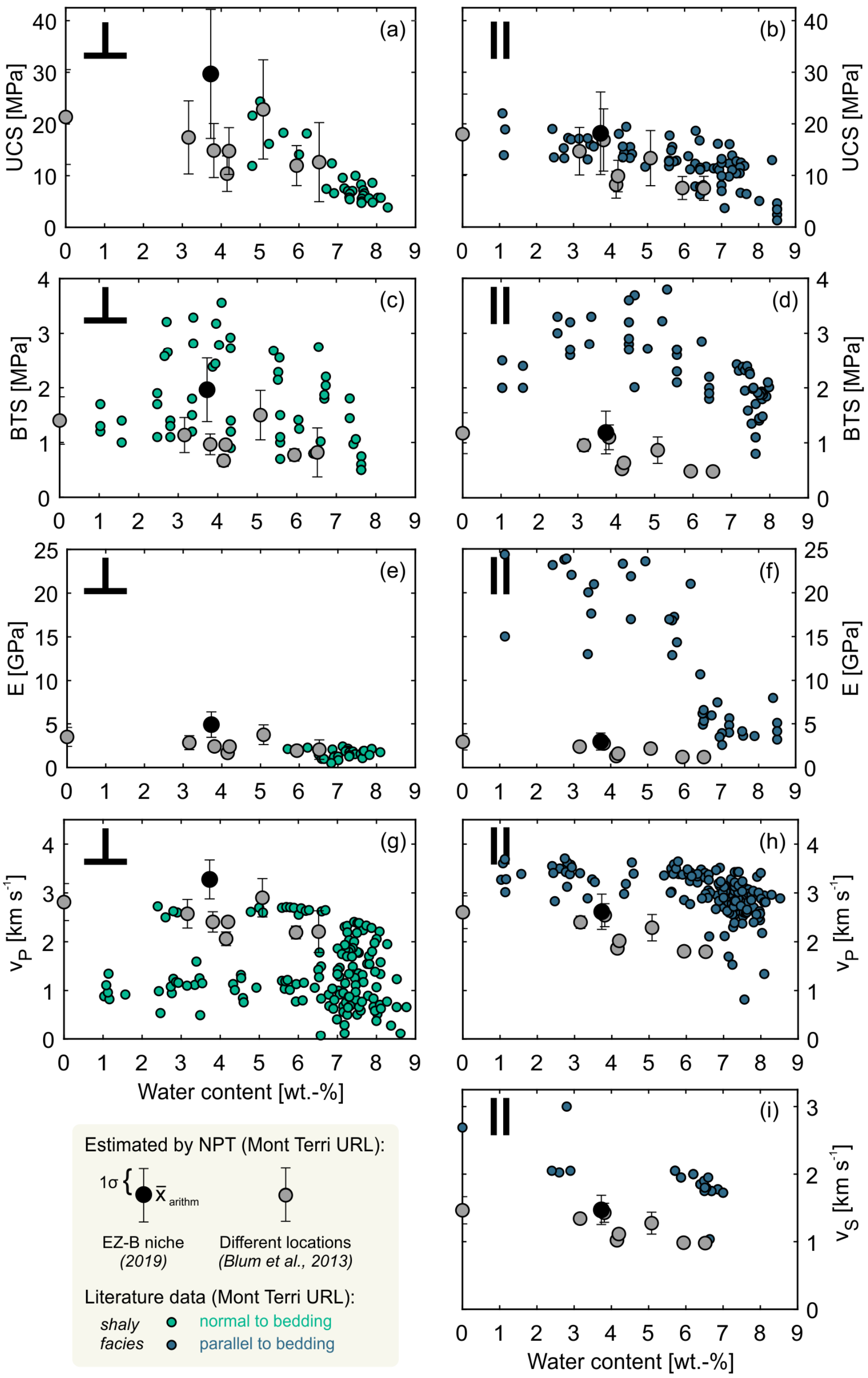

Figure 3.6: Comparison of estimated geomechanical and geophysical parameters of the Opalinus Clay in the EZ-B niche of the Mont Terri URL (black symbols, this study) with literature data for the shaly facies normal (a–g) and parallel (b–i) to bedding. In addition, a second NPT dataset of Blum et al. (2013) from various locations in the URL (shaly facies) is shown (gray symbols). Literature data (green and blue symbols) originate from other niches in the Mont Terri URL and are mainly adapted after Jaeggi and Bossart (2014) and references herein (the full list of source documents is provided in Appendix A).

Based on the needle penetrometer data obtained in the EZ-B niche, the estimated uniaxial compressive strength (UCS) was 29.7 MPa for a water content of 3.7 wt.-% normal to bedding (Figure 3.6a). For water contents below 4.5 wt.-%, no literature data on UCS are available for the shaly facies of the Opalinus Clay. Due to the fact that UCS is increasing linearly with decreasing water content (Wild et al., 2015), the estimated mean value can be considered reasonable and complements the literature dataset in Figure 3.6a. The additional NPT dataset of Blum et al. (2013) also confirms the negative linear correlation of UCS and water content. Parallel to bedding, the estimated UCS of 18.2 MPa is consistent with literature data on the shaly facies for a similar water content (Figure 3.6b). The two NPT datasets, acquired from the EZ-B niche and different locations in the Mont Terri URL (Blum et al., 2013), exactly reproduce the trend that is evident from the available literature data. The estimated UCS values in Figure 3.6a and b were obtained by using different empirical equations, leading to a comparatively high standard deviation. The individual results for each empirical equation are listed in Table 3.4. As needle penetration testing is widely used for estimating the UCS of rocks (Ulusay et al., 2014), several functions are available which have been deduced from various rock types (Table 3.2). For the Opalinus Clay, the applied combination of different established equations has proven to be suitable.

The Brazilian tensile strength (BTS) of the Opalinus Clay normal to bedding could also be estimated by the needle penetration tests. The mean value of 2 MPa that was obtained from the on-site measurements in the EZ-B niche is located approximately in the center of the literature value range for a comparable water content (Figure 3.6c). Apparently, the literature data for the shaly facies are divided into two subgroups. Lower BTS values normal to bedding are most likely related to pre-damaged sample material, i.e., desiccation cracks, which preferentially form parallel to the bedding features in the drill core and therefore reduce the tensile strength of the tested sample perpendicular to bedding. Parallel to bedding, the estimated BTS deviates by about 2 MPa from the available literature data and is therefore underestimated (Figure 3.6d).

Similar to UCS, the Young´s modulus E is increasing monotonically with declining water content as evident from both literature data and the NPT dataset of Blum et al. (2013). For water contents below 5.7 wt.-%, no literature data are available for the shaly facies normal to bedding. As the derived Young´s modulus of 4.9 GPa normal to bedding for a water content of 3.7 wt.-% was significantly higher than the available literature values for natural water contents (maximum of 2.4 GPa), the estimation was assumed to be applicable for the Opalinus Clay (Figure 3.6e). With a mean value of 3 GPa, E was largely underestimated parallel to bedding compared to the available literature data ranging between 13 and 31 GPa for similar water contents (Figure 3.6f). This is most probably due to the fact that rather well-preserved drill core specimens are compared to the long-exposed and highly damaged rock surface of a niche.

The elastic P-wave velocity (v_p) is slightly overestimated normal to bedding (Figure 3.6g). Similar to Figure 3.6c, two sub-datasets can be identified within the literature data. Here, pre-damage of the core sample material or an insufficient coupling of the ultrasonic source was most likely responsible for these reduced P-wave velocities, which are therefore not representative for the intact rock body (Jaeggi and Bossart, 2014). According to Jaeggi and Bossart (2014), the core samples belonging to the lower sub-dataset of literature values in Figure 3.6g were partially penetrated by microcracks. The estimated v_p data seem to represent the upper subset of the literature data. Since the needle penetrometer only samples a small area on the rock surface, the NPT is able to reflect the actual in situ conditions. Parallel to bedding, v_p is slightly underestimated but fairly represents the data range of the shaly facies (Figure 3.6h). The observed trend of a slight P-wave velocity increase with decreasing water content of the Opalinus Clay normal and parallel to bedding is also well represented by the datasets obtained from needle penetration testing.

For the elastic S-wave velocity v_s of the Opalinus Clay, a mean value of 1.9 km s^{-1} was estimated normal to bedding. Due to strong absorption and attenuation of wave energy and insufficient signal retrieval during ultrasonic velocity measurement (Gräsle and Plischke, 2010; Schnier and Stührenberg, 2007), few literature data are available. For the shaly facies of the Opalinus Clay, Bock (2009) reports v_s values of 1.51 km s^{-1} for a natural water content of 6.4 wt.-%. Wileveau (2005) provides S-wave velocities of 1.45–1.58 km s^{-1} for water contents varying between 2.4 and 2.9 wt.-%. Hence, normal to bedding v_s is most likely overestimated by the NPT. Parallel to bedding, a value of 1.5 km s^{-1} was determined. In comparison to existing literature data, v_s is underestimated in this direction (Figure 3.6i). As ultrasonic velocity is explicitly dependent on the internal structure of the rock, such as cementation, anisotropy and porosity structure (Jaeggi and Bossart, 2014; Schuster et al., 2017), it can be assumed that the relationship of ultrasonic velocity and NPI is probably rather weak.

For the cohesion c and the friction angle φ, reliability of the estimated values (Table 3.4) could not be assessed due to limited literature data, especially for samples with low water contents. In Bock (2009), mean values for the cohesion (3.7 MPa and 5.4 MPa) and friction angle (22° and 23°) of the Opalinus Clay for an average water content of 6.7 wt.-% are given normal and parallel to bedding, respectively. In contrast, Lisjak et al. (2015) used a cohesion of 24.8 MPa (normal) and 2.4 MPa (parallel) as an input parameter for their calibrated finite–discrete-element model. The implemented friction angle of 22° complies with Bock (2009), but no information on the assumed water content is included. Cohesion values of 3.9 MPa (normal) and 2.4 MPa (parallel) derived from needle penetrometer measurements in the EZ-B niche were of the same order of magnitude as the data given by Bock (2009). However, the estimated friction angles of 42° and 37° normal and parallel to bedding, respectively, were significantly higher in comparison to the literature data.

Generally, the applied empirical functions performed better normal to bedding. The poor estimation of parameters parallel to bedding (apart from UCS) may be linked to unperceived (possibly micro-scale) shrinking or desiccation cracks, which preferentially form parallel to the bedding features (e.g., Amann et al., 2017; Schnier and Stührenberg, 2007). Microcracks would facilitate needle penetration, thus reducing the measured NPI and the estimated parameter values. It should also be noted that the existing empirical relations for estimating physico-mechanical parameters do not specifically apply to claystones or shales, but were derived based on compiled experimental data obtained for various types of soft rocks (Aydan et al., 2014). In addition to the factors mentioned above, sedimentary heterogeneity might also be responsible for geomechanical variability as well as the observed deviations between the NPI-based values and the considered literature data. However, heterogeneity of the shaly facies of the Opalinus Clay in Mont Terri is comparatively low (Jaeggi and Bossart, 2014). More likely, the observed deviations are due to variant surface constitution caused by the hugely varying exposure time of the rock walls in the non-lined EZ-B niche in contrast to sampled specimens from drill cores. Although the measurements were conducted at the upper end of the specified application range of the needle penetrometer, physico-mechanical parameter estimation based on needle penetration testing can be recommended for indurated clays, especially for determining the anisotropic uniaxial compressive strength.

3.4 Conclusions

An excavation damaged zone (EDZ) in the Opalinus Clay of the Mont Terri rock laboratory, Switzerland, was characterized with regard to hydraulic and mechanical properties using three different methodological on-site approaches: (1) air permeameter, (2) microscope camera and (3) needle penetration test. About 15 years after excavation, artificially induced unloading joints (EDZ fractures), reactivated fault planes (tectonic fractures) and bedding-parallel desiccation cracks with a mean mechanical aperture of 233 µm and a mean hydraulic aperture of 84 µm were observed in the EZ-B niche, serving as potential flow paths for advective transport in the indurated clay formation. This is not only limited to the area of the strongly pronounced EDZ around Gallery 04, where a dense network of interconnected fractures is encountered, but also applies to potentially reactivated tectonic discontinuities at greater distances, e.g., due to large-scale stress redistribution or injection of fluids. After an initial continuous aperture closure observed by long-term jointmeter data records in the non-lined niche, which can be attributed to seasonally controlled shrinkage and swelling cycles in combination with niche convergence, this process seems to be decelerating significantly after 15 years of monitoring. Locally, fractures are influenced by shotcrete application, leading to reduced hydraulic and mechanical apertures due to enhanced water availability and swelling of clay minerals in the immediate vicinity. Among the studied discontinuity types, the EDZ fractures showed the smallest hydraulic apertures. However, as 60 % of all measured values were within the range of 80–120 µm, a clear distinction was not possible.

From direct measurement with the portable transient-flow air permeameter, plausible hydraulic aperture data could be acquired on-site, even if the entire range of fractures in the EZ-B niche could not be reproduced due to a limited measuring range. This means that the permeameter measurements tend to overrepresent smaller fractures. Here, indirect determination of hydraulic fracture apertures based on the automatic evaluation of high-resolution microscope camera images of fracture traces offers a practical alternative. Due to the smaller mean mechanical aperture of the artificially induced unloading fractures compared to the investigated tectonic fractures, conversion was most appropriate for the EDZ fractures. Tectonic fractures on average exhibit a higher variance of measured distances along imaged fracture traces, which can be explained by a higher degree of mismatch between the fracture surfaces due to the reactivation of fault planes during excavation. However, the statistical significance of the observed differences between the different fracture types would have to be tested based on a larger data set. For specifying the mechanical aperture of a fracture network based on fracture trace micro-imaging, the median of measured values is most representative.

The needle penetration test proved to be a valuable tool, especially for accurate estimation of the anisotropic uniaxial compressive strength, as the needle penetration index satisfactorily reflects the in situ conditions of the intact rock mass. For the shaly facies of the Opalinus Clay in the EZ-B niche, a mean uniaxial compressive strength of 30 MPa (normal to bedding) and 18 MPa (parallel to bedding) was determined. While parameter estimation based on needle penetration indices normal to bedding showed high agreement with available literature data, physico-mechanical parameter values were mostly underestimated in the bedding-parallel direction. Due to damage of the exposed rock surface associated with the formation of microcracks parallel to stratification, needle penetration was facilitated in this case. Due to direct air contact and ventilation of the rock laboratory, the desaturation of the claystone in the near field of the niche led to a sharp decrease in water content to 3.7 wt.-%, which is directly linked to an increased uniaxial compressive strength, Young´s modulus and elastic P-wave velocity normal to bedding.

The applied on-site measurement methodology and evaluation approach are suitable for the hydraulic and mechanical characterization of excavation damaged or disturbed zones in different geological environments, especially since drilling is not always feasible and the validity of estimated parameters is limited to the investigated location. With comparatively little effort, non-destructive analysis of time- and location-dependent variability of important parameters is permitted. Besides confirming the suitability of the methodological approach for flexibly determining hydraulic and mechanical properties, the study assesses the state of an EDZ in a non-lined niche after long-term exposure and therefore serves as an important guideline for diverse tunneling projects and future performance assessments of nuclear waste disposal sites in argillaceous rocks.

Acknowledgments

We thank swisstopo, the Federal Office of Topography in Switzerland, for enabling and supporting our field work at the Mont Terri Rock Laboratory and for providing valuable documentation. This work was financially supported by the German Federal Ministry of Education and Research (BMBF) “Geological Research for Sustainability (GEO:N)” program [grant no. 03G0871D] within the framework “Research for Sustainable Development (FONA3)”.

UPSCALING CALCITE DISSOLUTION RATES IN A TIGHT RESERVOIR SANDSTONE

4

Reproduced from: Hale, S., Pedrosa, E.T., Jacob, A., Reinhardt, M., Enzmann, F., Kersten, M., Butscher, C., Blum, P. Upscaling calcite dissolution rates in a tight reservoir sandstone. Environmental Earth Sciences *(under review)*

Abstract

Calcite is a highly abundant mineral in the Earth's crust and occurs as a cement phase in numerous siliciclastic sediments, where it often represents the most reactive component when a fluid percolates through the rock. Hence, the objective of this study is to derive calcite dissolution rates on different scales in a reservoir sandstone using surface experiments combined with vertical scanning interferometry (VSI) and two types of core plug experiments. The 3D geometry of the calcite cement phase inside the rock cores was characterized by X-ray micro-computed tomography (μXCT) and was used to attempt dissolution rate upscaling from the surface to the core scale. Initially (without upscaling), our comparison of the far-from-equilibrium dissolution rates at the mineral surface (μm-mm-scale, low fluid residence time) and the surface normalized dissolution rates obtained from the core experiments (cm-scale, high fluid residence time) revealed differences of 0.5 to 2 orders of magnitude. The μXCT geometric surface area connected to the open pore space ($GSA_{Cc,open}$) considers the fluid accessibility of the heterogeneously distributed calcite cement that can largely vary between individual samples, but greatly affects the effective dissolution rates. Using this parameter to upscale the surface rates, the deviation of the upscaled total dissolution rates from the measured total dissolution rates was less than one order of magnitude for all investigated rock cores. Thus, $GSA_{Cc,open}$ showed to be reasonably suitable for upscaling the surface rates to the core scale.

4.1 Introduction

Beside mono-mineral rocks, calcite occurs frequently as a cement phase in sandstones (Bjørlykke et al., 1989). Many reservoir rocks consist of carbonate cemented siliciclastic sediments including, for example, the Triassic Edvard Grieg sandstone in the Norwegian Sea (Markussen et al., 2019), and the Devonian Old Red Sandstone in the United Kingdom (Hillier et al., 2006). Knowing the rate of calcite cement dissolution under different environmental conditions is extremely important for predicting the temporal evolution of the mineral composition and the reservoir quality, and for estimating the reservoir exploitation capacity, since acid injection (matrix acidizing) is commonly used to stimulate production wells (McLeod, 1984; Shafiq et al., 2019; Younesian-Farid and Sadeghnejad, 2020). After their active service life, depleted carbonate cemented reservoirs have the potential to serve as storage for energy and environmentally-important substances, such as hydrogen (e.g., Henkel et al., 2014) and carbon dioxide (e.g., Bachu and Adams, 2003), which also requires to account for potential fluid-rock interactions.

Due to their heterogeneous mineral composition and texture, carbonate cemented sandstones are complex systems. It is unclear whether it is possible to transfer the existing knowledge acquired by mono-mineral studies on carbonates (e.g., Gray et al., 2018; Kahl et al., 2020; Luquot and Gouze, 2009; Molins et al., 2014; Rötting et al., 2015) to the understanding of multi-mineral systems with complex fluid-flow pathways, where calcite occurs within an assemblage of higher and lower stability minerals (e.g., silicates, feldspars, clays). With this question in mind, we investigated the dissolution kinetics of calcite at different time and length scales using a well-studied reservoir-type sandstone of the Upper Rotliegend from northern Germany (e.g., Fischer et al., 2012b, 2007; Heidsiek et al., 2020; Henkel et al., 2014; Jacob et al., 2021; Monsees et al., 2021a; Pedrosa et al., 2021, 2019).

Although calcite reaction kinetics has received great attention in science for several decades (e.g., Chou et al., 1989; Morse and Arvidson, 2002; Plummer et al., 1978; Sjöberg and Rickard, 1984), the upscaling of experimental rates remains challenging (e.g., Meile and Tuncay, 2006; Noiriel et al., 2020; Noiriel and Soulaine, 2021). Modern methods for quantifying dissolution rates (e.g., atomic force microscopy, vertical scanning interferometry) can directly provide reliable reaction rates with a high spatial and temporal resolution (e.g., Bollermann and Fischer, 2020; Kahl et al., 2020; Vinson and Luttge, 2005). When transferring these micro-scale rates to larger scales, however, discrepancies or scale effects are likely to occur (e.g., Bouissonnié et al., 2018; Li et al., 2006). In core samples, the shape and connectivity of the pore space (and its heterogeneity) determines the flow and transport properties, which additionally influence or limit both local and bulk averaged dissolution rates (e.g., Al-Khulaifi et al., 2017; Flukiger and Bernard, 2009; Molins et al., 2014). A heterogeneous distribution of the reacting mineral phase (i.e., chemical heterogeneity) introduces an additional uncertainty factor into the system. For example, pore scale network models from Li et al. (2007) indicated that a varying size and orientation of the reactive mineral clusters lead to differences in dissolution rates at the mm-scale. By performing column experiments on magnesite-quartz mixtures, Salehikhoo et al. (2013) found rate deviations of up to 14 % due to a different spatial distributions of the reacting mineral phase.

For the tight sandstone under investigation, most of the calcite cement dissolution is expected to occur in the proportion of the mineral surface that is in direct contact with the major fluid-flow paths. Predicting this proportion is a practical problem, since the accessibility of a mineral phase in a rock is not directly quantifiable solely based on its volume fraction (Beckingham et al., 2016; Landrot et al., 2012; Peters, 2009; Waldmann et al., 2014). The problem of fluid-accessible surface area is directly related to the difficulty in quantifying the reactive surface area (RSA) of a mineral or rock, which represents a key parameter in reactive transport modeling and is required to normalize chemical reaction rates (Fischer et al., 2014). Given the impossibility of a direct measurement method of the RSA (Luttge and Arvidson, 2008), parameters such as the specific surface area (SSA) or the geometric surface area (GSA) are used to calculate "surface normalized" reaction rates (e.g., Hodson, 2006). Measuring the SSA by gas adsorption (BET) is the preferred analytical tool, but it does not allow to determine the surface area of separate mineral phases in consolidated rock. Thus, only an optical determination of a geometric calcite cement surface is appropriate for the studied sandstone. As a non-destructive method, X-ray micro-computed tomography (μXCT) is primarily used for characterizing the structure of mineral or rock samples and the geometry of the solid-pore interface in recent studies (Hinz et al., 2019; Lai et al., 2015; Noiriel et al., 2020, 2019, 2009; Svensson et al., 2019). If a sufficiently high spatial resolution or mineral surface retreat is reached, the evolution of fluid-solid interfaces can be observed and local reaction rates can be resolved (Noiriel and Soulaine, 2021).

The objective of this study was to analyze, to compare and to link the reaction rates of the calcite cement within a low-permeable (i.e., tight) reservoir sandstone under acidic conditions (pH 4.0) on surface and core scales: (1) surface flow-through experiments were made using polished unreacted sandstone samples from the same sample block. Vertical scanning interferometry (VSI) provided quantitative surface dissolution rates and microstructural information at the grain scale (μm to mm); (2) flow-through dissolution experiments on core samples (cm-scale) were conducted to investigate the long-term dissolution behavior. Inductively coupled plasma mass spectrometry (ICP-MS) was used to measure the calcium content of the effluent fluid and μXCT was used to parametrize the geometric surface area of the calcite cement for calculating core dissolution rates.

Based on this experimental study, we quantify the difference of calcite dissolution rates between the surface and the core scale with highly divergent transport conditions. In contrast to the far-from-equilibrium conditions at the surface scale, more natural transport conditions were simulated at the core scale by using low flow velocities, high chemical gradients, and near-equilibrium fluid conditions. Using μXCT imaging, we also aim to investigate the variability in geometry and fluid accessibility of the cement phase in the sandstone, which controls the reaction-available surface area and the effective dissolution rates. Finally, the μXCT derived geometric calcite cement surface area connected to the open pore space is used to link the measured surface rates to the measured core rates.

4.2 Materials and methods

4.2.1 Sample material

Samples of a natural reservoir-type sandstone from the Bebertal outcrop (Sachsen-Anhalt, Germany) were used in all experiments. The outcrop belongs to the Parchim formation (Havel sub-group, Upper Rotliegend) of the South Permian Basin (Kleditzsch and Kurze, 1993; Plein, 1993), with the facies investigated having similar deposition conditions and age as the reservoir rocks of the North German Basin (Fischer et al., 2012b). The sample material for the experiments was drilled from a sandstone block originating from the "Schwentesius" quarry, which was also used in earlier studies (Heidsiek et al., 2020; Jacob et al., 2021; Pedrosa et al., 2021, 2019).

The mineralogical composition of the sandstone sample block (Figure 4.1a) was investigated by X-ray diffraction analysis and Rietveld analysis in Jacob et al. (2021). Calcite is mainly present as poikilitic eodiagenetic and mesodiagenetic cement (Figure 4.1b) (Heidsiek et al., 2020). Under the experimental conditions used (Chapter 4.2.2), calcite is thermodynamically least stable and therefore considered the most reactive mineral phase in the sandstone. Four samples were drilled from the sandstone block for the core scale percolation experiments (Figure 4.1a, C14, E6, F11, and G12), and one for the surface dissolution experiments on the µm- to mm-scale (Figure 4.1a, E7). The cylindrical samples had a diameter of 2.54 cm (1 inch), and were shortened to the required length of 5 cm or 1.5 cm for core experiments, and 5 mm for surface experiments.

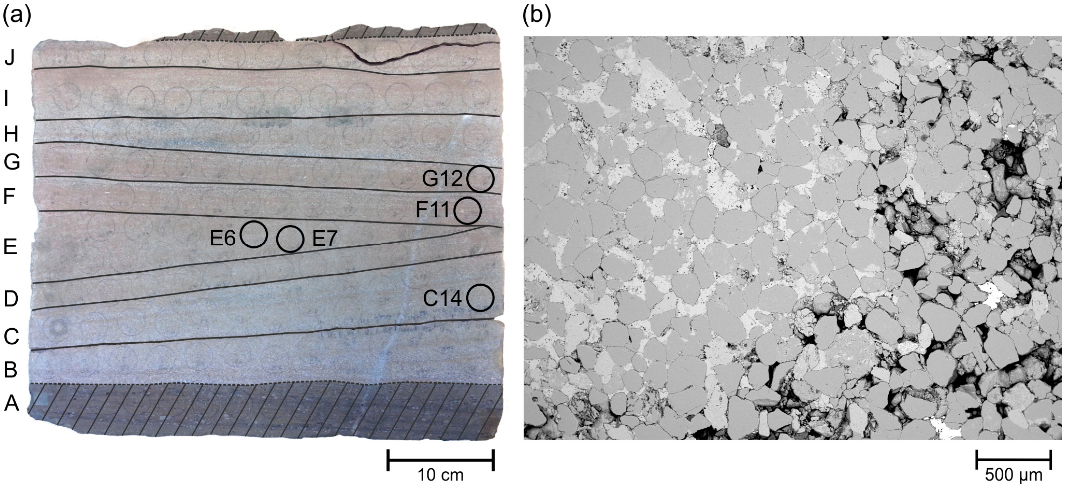

Figure 4.1: (a) Sampled sandstone block from the Upper Rotliegend formation (Bebertal, Germany). All samples for the dissolution experiments were drilled in the laminated and cross-bedded aeolian facies (unmasked area). (b) SEM image of the Rotliegend sandstone with porous calcite cement (light gray).

4.2.2 Dissolution experiments

To determine dissolution rates of the calcite cement in the sandstone, dissolution experiments were performed using three types of flow-through setups: (1) an in-house built cell for surface dissolution experiments (“micro-cell”); (2) an in-house built triaxial permeability cell; (3) an ICARE4 flow-through autoclave (Figure 4.2). All experiments were carried out at room temperature using an infiltration solution containing 1×10^{-4} mol L^{-1} HCl and 1×10^{-3} mol L^{-1} NaCl prepared with ultra-pure water (resistivity > 18.2 MΩcm). Table 4.1 includes the main similarities and differences between the three experimental apparatus.

Table 4.1: Experimental details of the dissolution experiments on the calcite cemented sandstone.

Reactor	**Fluid-solid interface**	**Length scale**	**T [°C]**	**P_{out} [bar]**	**Q [mL min^{-1}]**	**pH_{in}**	**pH_{out}**	**Reaction time**	**Rate calculation method**
Micro-cell	Surface	µm-mm	21	1	1.2	4.0	n.m.	120 min	Direct (solid)
Triaxial permeability cell	Core	cm	22	1	0.0008 – 0.004	4.0	7.6 – 8.8	90 – 153 days	Indirect (fluid)
Flow-through autoclave	Core	cm	24	55	0.4 – 1	4.0	6.8 – 7.3	22 days	Indirect (fluid)

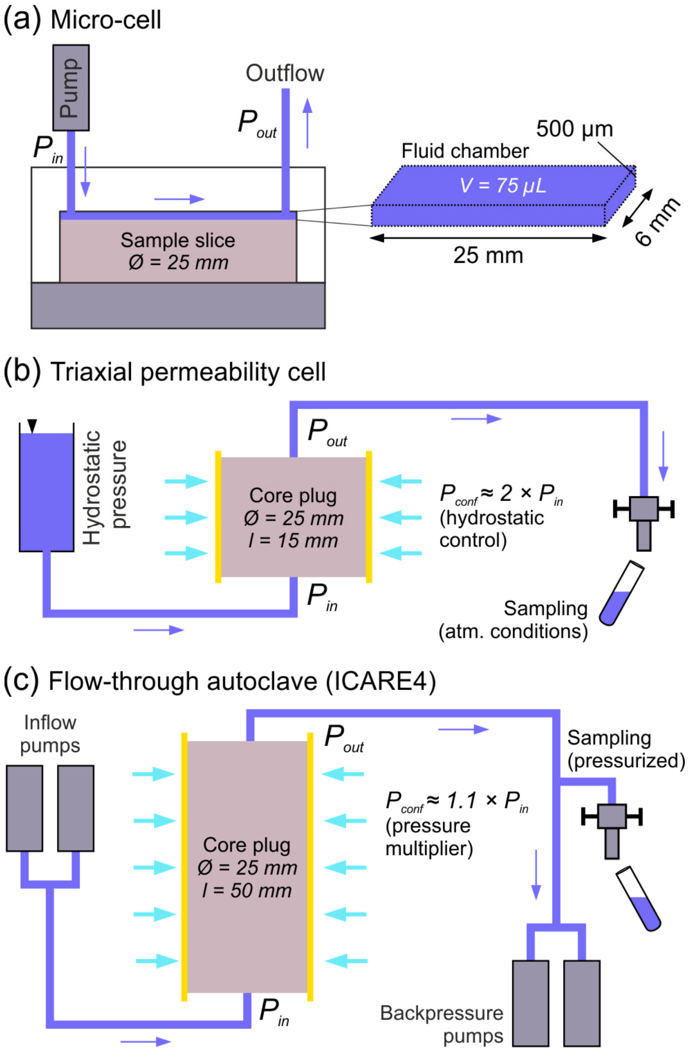

Figure 4.2: Overview of the three experimental setups (schematically simplified): (a) micro-cell on the surface scale, (b) triaxial permeability cells and (c) flow-through autoclave on the core scale.

4.2.2.1 Micro-cell

Surface dissolution experiments were performed using an in-house designed flow-through cell (Figure 4.2a, University of Bremen) (e.g., Li et al., 2021; Pedrosa et al., 2021, 2019). The fluid chamber of the cell has an elongated shape with only 500 µm height, allowing for a relatively wide coverage of the sandstone sample while providing a small hydraulic residence time (HRT) (photo in Appendix B, Figure B1). The flow rate was set to 1.2 mL min^{-1}, which results in a HRT of 3.8 s. Hence, the bulk fluid inside the cell was at all times fully undersaturated with respect to any mineral phase in the sandstone. The sample was reacted for a total of 120 min using the infiltration solution specified in Chapter 4.2.2. Thus, reaction time was much lower compared to the core experiments. Every 30 min the sample was taken out of the fluid cell and its topography was measured using VSI.

4.2.2.2 Triaxial permeability cell

Flow-through experiments with a triaxial permeability cell were performed to investigate calcite cement dissolution in the core plugs under low differential pressures of < 0.5 bar (details in Appendix B, Figure B11). Initial sample saturation of the sandstone sample was achieved by using a vacuum pump and an equilibrium solution (infiltration solution without acid). The pressure at the inlet of the cell (P_{in}) was controlled by the hydrostatic pressure of the infiltration solution and was regulated using compressed air. To inhibit sample bypass, a radial confining pressure ($\sim 2 \times P_{in}$) was applied by pressurized ultrapure water in the chamber of the cell (Figure 4.2b). Initially, the differential pressure was set to 0.2–0.3 bar and was afterwards continuously monitored by digital manometers.

The outgoing fluid was sampled under atmospheric pressure using microtubes. After a minimum sample volume of 2.5 mL had been reached, the microtube was exchanged. The volumetric fluid flow rate Q was quantified by measuring the sampled fluid volume V_{fluid} and sampling time Δt:

$$Q = \frac{V_{fluid}}{\Delta t} \tag{4.1}$$

The pH of the solution at the sample outlet was measured with a WTW SenTix Mic pH electrode immediately after retrieving each fluid sample. The ionic concentration of calcium in the outlet fluid was measured using ICP-MS in an X-Series 2, Thermo Fisher Scientific.

4.2.2.3 Flow-through autoclave

A flow-through autoclave ICARE4 (designed at the Geosciences Department, University of Montpellier, France) was used for reacting the core plugs under elevated differential pressures of up to 20 bar (Figure 4.2c). The ICARE4 (details in Appendix B, Figure B12) and similar devices have been previously used for reactive percolation experiments, such as for studying CO_2-brine-rock interactions in context with carbon capture and storage (e.g., Myrttinen et al., 2012).

Radial sample confinement is controlled by an integrated pressure multiplier with a free-moving piston in order to prevent fluid bypass. The confining pressure was fixed to ~ 1.1 × P_{in}. The experimental setup also comprises two motorized piston pumps to produce the flowrate and two back-pressure pumps to maintain a constant pressure at the outlet of the percolation cell (Table 4.1). The volumetric fluid flow rate was adjusted according to the observed differential pressure ranging between 12 and 20 bar. Before starting the percolation, a complete saturation of the rock sample was achieved by an integrated vacuum pump. Sampling ports before and after the percolation cell enable fluid sample extraction with a fixed volume of 2.5 mL without a significant decrease in system pressure. For the subsequent chemical fluid analysis, the methodology described in Chapter 4.2.2.2 was applied.

4.2.3 Analytical methods

4.2.3.1 Direct calcite dissolution rates on the surface scale

For the calculation of the surface dissolution rates, a ZeMapper white light interferometer (Zemetrics, Tucson, AZ, USA) was used to collect topography data using Mirau objectives with 20× and 50× magnification. This provides a measure for the surface height retreat by subtracting the sample's height between each reaction interval (see Appendix B, Figure B2 for a 3D visualization example of the topography maps). Surface normalized calcite dissolution rates can be determined directly by

$$r_{Cc} = \frac{\Delta h}{\Delta \mathrm{t} \cdot V_m}, \tag{4.2}$$

where Δh is the height difference of the surface between two consecutive topography measurements, Δt the reaction time interval (30 min), and V_m the molar volume of calcite (3.693×10^{-5} m^3 mol^{-1}). Six locations (calcite cement patches) and twelve areas of interest were selected from the reacted areas for a statistical rate analysis as described in Pedrosa et al. (2019).

4.2.3.2 Indirect calcite dissolution rates on core scale

Total calcite dissolution rates for the core plugs (in units mol s^{-1}) were calculated for different reaction times using the ionic calcium concentration obtained from ICP-MS analysis (C_{Ca}) and the volumetric flow rate Q:

$$r_{Cc,total} = C_{Ca} \cdot Q \tag{4.3}$$

Surface normalized calcite dissolution rates (in units mol m^{-2}s^{-1}) were needed for the comparison with the surface rates and were calculated using

$$r_{Cc} = \frac{r_{Cc,total}}{A} = \frac{r_{Cc,total}}{GSA_{Cc,open}} \tag{4.4}$$

In this study, a geometric surface area ($GSA_{Cc,open}$) obtained by µXCT imaging (see Chapter 4.2.3.3) was used for core rate normalization.

Alternatively, the reactive surface area RSA of the mineral involved in the reaction can be estimated from the saturation state of the outlet solution according to Rötting et al. (2015)

$$RSA = \frac{r_{Cc,bulk}}{k_c \cdot (1-10^{SI})}, \tag{4.5}$$

with $r_{Cc,total}$ (in units mol L^{-1}) acquired from the experiments, k_c the overall rate constant of the reaction (in units mol m^{-2}s^{-1}), and SI the saturation index of the fluid. Equation (4.5) is derived from a general rate law for mineral dissolution (Lasaga, 1998) based on the transition state theory (TST)

$$r = k_c \cdot A \cdot f(\Delta G) \tag{4.6}$$

which includes a function of the Gibbs free energy $f(\Delta G)$ for scaling the resulting rate as a function of the saturation state ($f(\Delta G) = 0$ at equilibrium). This saturation state function is not exactly known and can be expressed by different mathematical forms (e.g., Hellmann and Tisserand, 2006; Xu et al., 2012). In this study, the simplest form was used (e.g., Luquot and Gouze, 2009; Rötting et al., 2015)

$$f(\Delta G) = 1 - 10^{SI} \tag{4.7}$$

If not determined experimentally, the kinetic rate constant k_c for calcite dissolution can be calculated according to Chou et al. (1989) using the given rate constants (k_1, k_2, k_3, k_{-3}) and the activities of the carbonate species in the fluid

$$k_c = k_1 \cdot a_{H^+} + k_2 \cdot a_{H_2CO_3{}^*} + k_3 \cdot a_{H_2O} - k_{-3} \cdot a_{Ca^{2+}} a_{CO_3{}^{2-}} \tag{4.8}$$

The geochemical code PHREEQC (Parkhurst, 1995) with the thermodynamic database phreeqc.dat was used to determine the speciation of the carbonate system and to calculate calcite saturation indices.

4.2.3.3 X-ray micro-computed tomography

The core plugs were scanned before the flow-through experiments using a Nikon XT H 225 ST X-Ray system with a voxel resolution of 10–13.7 µm in dependence of the sample size. A total of 3600 projections were acquired during the measurement of each core sample. After reconstruction, the images where denoised by applying a non-local means filter (Buades et al., 2005) implemented in the commercial software package GeoDict 2020 (Math2Market GmbH). The advantage over conventional methods is a better signal-to-noise ratio, while sharp phase boundaries are retained. The beam hardening effect was corrected by a hypersurface fitting beam hardening correction filter which normalises the grey value intensity drop in the middle of the sample. Segmentation into different phases based on X-ray absorption was done by conventional grey scale thresholding with the software AVIZO (version 2019.1).

The GeoDict module PoroDict was used for all subsequent analyses based on the segmented µXCT images of the core plugs. The total geometric surface area of the calcite cement ($GSA_{Cc,total}$) was determined using an implemented algorithm by Ohser and Mücklich (2000).

As only the open porosity was expected to be accessible for the fluid, $GSA_{Cc,total}$ was further scaled by excluding the closed porosity in the sample from the surface area calculation. For normalizing the core scale calcite dissolution rates that were determined indirectly by the measured calcium concentrations in the outlet fluid (Chapter 4.2.3.2), the geometric surface area of the calcite in contact to the open pore space ($GSA_{Cc,open}$) was utilized. In order to compute the open porosity, only pores with an open path to the inlet and outlet in the tangential flow direction were considered. In addition, the size distribution of the calcite cement clusters within the core plugs was analyzed by using an implemented pore size distribution (PSD) algorithm, which was instead applied to the phase that represented the calcite cement. To determine the cluster size distribution geometrically, the entire volume of the segmented phase under consideration is virtually filled with spheres of different sizes.

4.3 Results and discussion

4.3.1 Calcite dissolution rates on surface scale

As described in Chapter 4.2.2, a polished sandstone core sample slice (E7) was reacted step-wise in the flow cell and the surface retreat was subsequently quantified by VSI for twelve areas of interest in six different calcite patches. Backscattered electron images of the unreacted and reacted calcite cement can be found in Figure B3 in Appendix B. The dissolution of the calcite cement patches was not uniform (Figure 4.3). The highest rates were observed for the cement patches m1 and m2 (Figure 4.3b,c), which were located closer to the inlet of the cell (Figure 4.3a). Overall, dissolution was more pronounced at the left interfaces between the calcite cement patch and the surrounding grains. The VSI height maps for all calcite patches and reaction time intervals are provided in Appendix B.

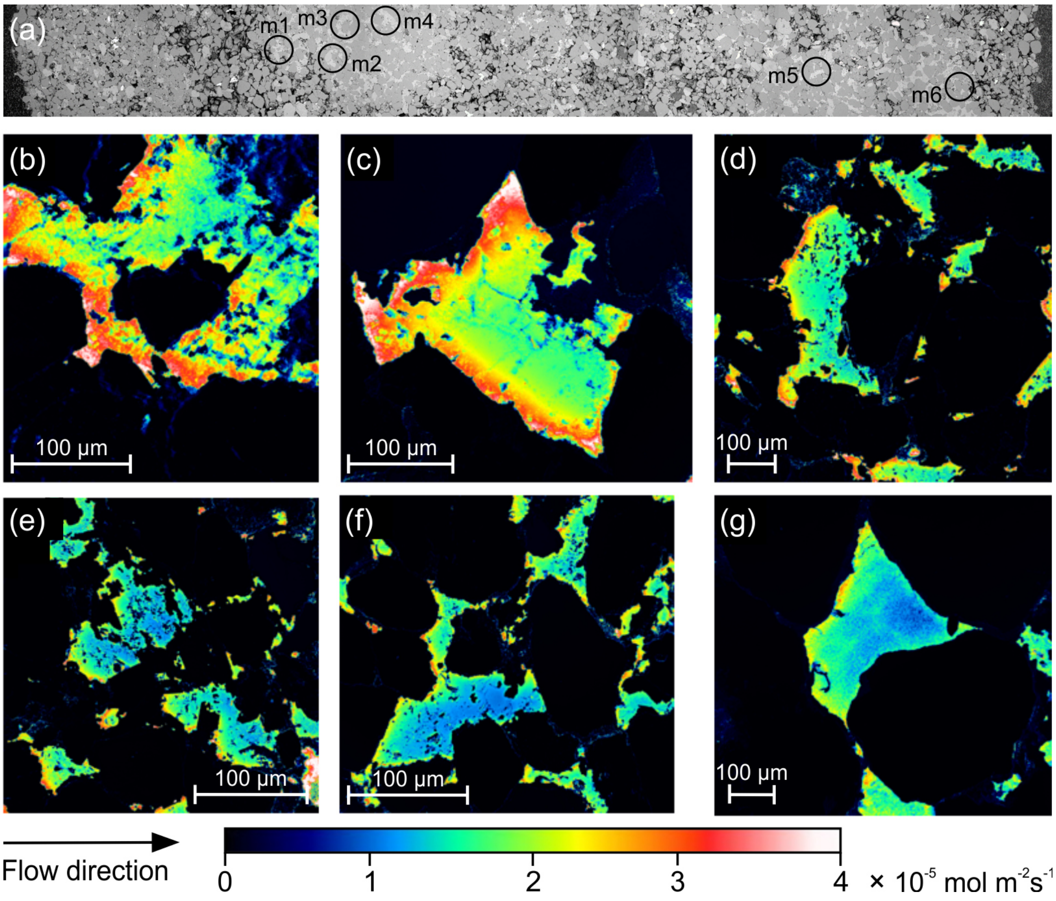

Figure 4.3: Dissolution rate maps m1–m6 of the investigated calcite patches (b–g) and (a) their position in the field of view of the fluid cell. To determine the rates, two distinct areas of interest (as large as possible) were evaluated in each map to exclude unreacted areas (black) from the analysis.

The calcite dissolution rate at the surface scale did not change significantly in time (Figure 4.4a). The calculated average dissolution rate r_{Cc} including all investigated cement patches and reaction times was 1.6 ± 0.8 × 10^{-5} mol m^{-2} s^{-1} and corresponds to an average surface height retreat of 3.5 ± 1.7 µm. The most reactive parts of the calcite cement patches retreated by up to 11.2 µm, which corresponds to a dissolution rate of 1.5 × 10^{-4} mol m^{-2} s^{-1}. A decreasing tendency of dissolution rates with increasing distance of the investigated calcite patch from the inlet of the fluid cell is suggested by Figure 4.4b. Due to the low HRT, it is unlikely that this effect could be governed by chemical gradients, but more experiments would be needed that focus on this behavior. However, the results also show that the variability of rates within the individual areas of interest is much higher (Figure 4.4b, standard deviation bars are very variable) than the variability of rates between individual calcite patches (Figure 4.4a). These results have similarities with the results obtained by Pedrosa et al. (2021, 2019) for the same rock, where also a surface reactivity variability was identified for the calcite cement, but the reaction rates where significantly lower (~ 1.7 × 10^{-6} mol m^{-2} s^{-1}) due to the use of carbonated fluids (pH ~ 8.7). Contrary to the findings in Pedrosa et al. (2021), we did not identify any sharp reactivity interfaces associated to internal differences in the chemical composition, although this could also be a coincidence related to the heterogeneity of the sandstone (Heidsiek et al., 2020).

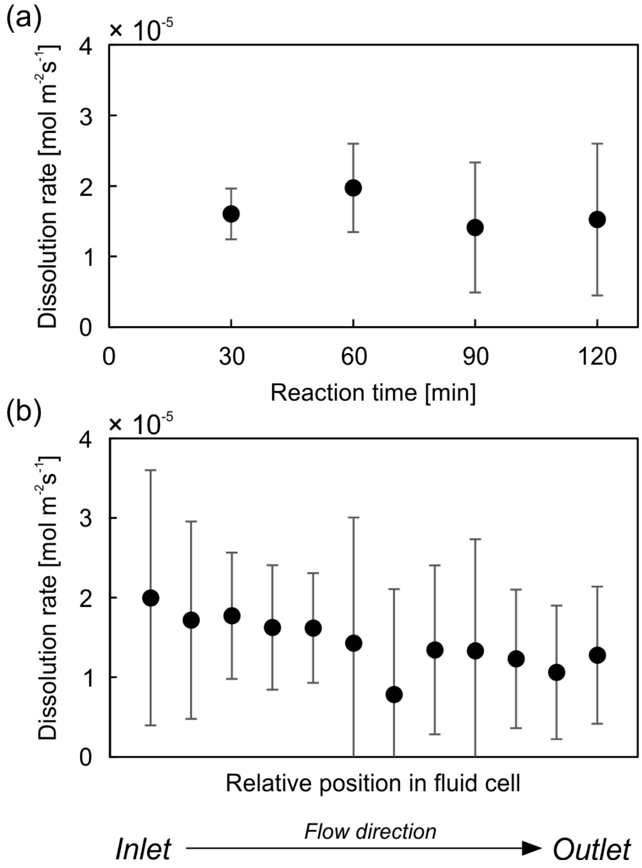

Figure 4.4: Results of the surface dissolution experiments. (a) Changes in mean dissolution rate with reaction time (all data). The standard deviation indicates the differences between the individual areas of interest; (b) average dissolution rate (full reaction time) of the twelve areas of interest within the six calcite patches m1–m6 ordered by their relative position within the field of view of the micro-cell. The standard deviation corresponds to the deviation to the average rate inside each calcite patch.

4.3.2 Calcite dissolution rates on core scale

4.3.2.1 Results of the flow-through experiments

On the core scale, a total of four core samples were reacted for varying time periods (Table 4.1). A continuous dissolution of the calcite cement was observed throughout each flow-through experiment. With regard to the mineralogical composition of the sandstone (Chapter 4.2.1) it was assumed that all calcium present in the solution sampled at the outlet was originating from calcite dissolution. In principle, it is possible that part of the calcium originates from clay minerals in the sandstone, but this contribution would be negligible compared to the amount of calcium originating from calcite dissolution.

Three low-pressure experiments with the triaxial permeability cells (Chapter 4.2.2.2, core plugs F11, C14 and G12, Figure 4.1a) and one high-pressure experiment with the flow-through autoclave (Chapter 4.2.2.3, sample E6, Figure 4.1a) were conducted. The volumetric flow rates in the high-pressure experiment were about three orders of magnitude higher than the flow rates in the low-pressure experiments (Figure 4.5a). Accordingly, the hydraulic residence time (HRT) of the reactive fluid varied over three orders of magnitude (Figure 4.5b). The calcium concentration in the outflowing solution was higher in the low-pressure experiments than in the high-pressure experiment (Figure 4.5c). For all core plugs, the outlet pH was significantly elevated compared to the pH 4.0 infiltration solution, with the highest values occurring in the initial phase (Figure 4.5d).

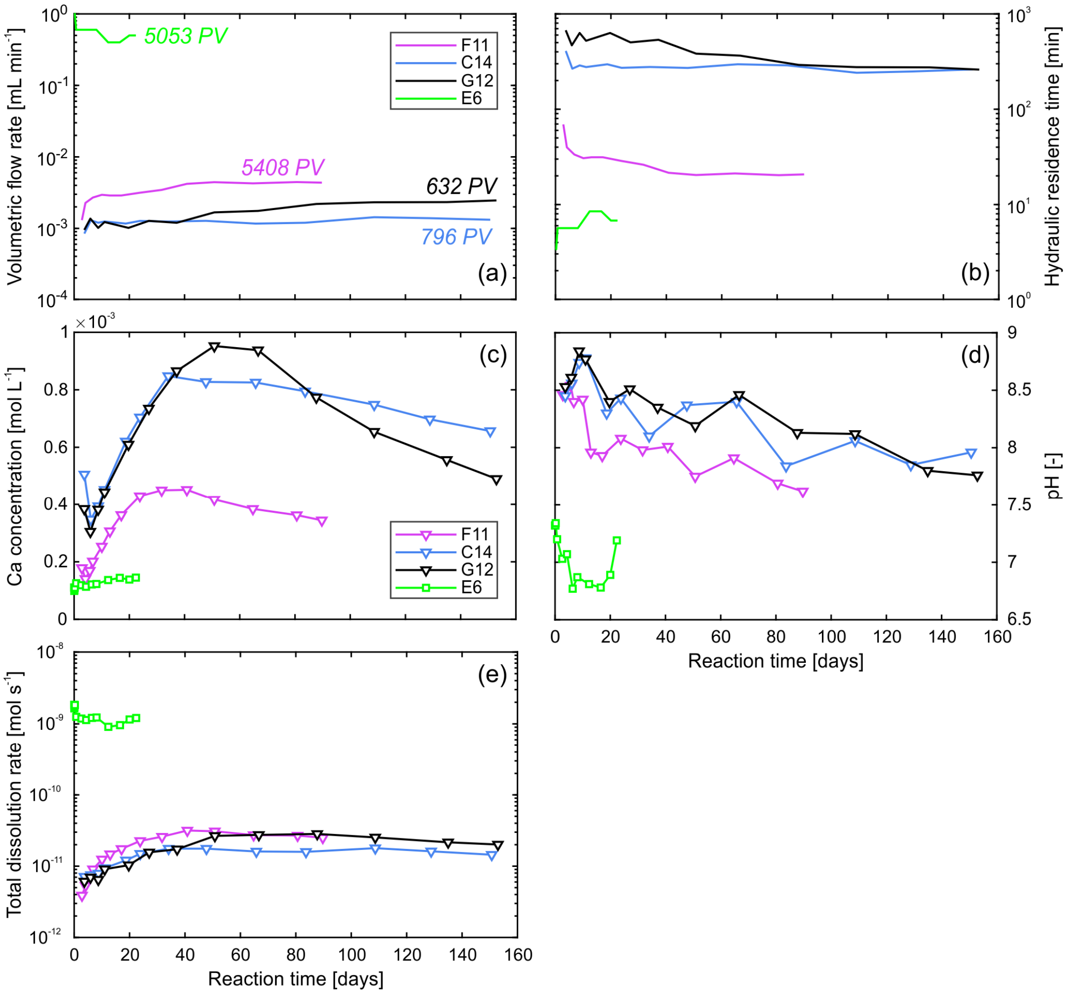

Figure 4.5: Experimental results for the flow-through experiments with triaxial permeameter cells (F11, C14 and G12, triangles) and the flow through-autoclave ICARE4 (sample E6, squares): (a) Volumetric flow-rate and total exchanged pore volumes (PV), (b) hydraulic residence time within the core plug, (c) Ca^{2+} concentration and (d) pH of the fluid samples at the outlet, and (e) total dissolution rate.

The pH of the outlet fluid correlated with the measured Ca^{2+} concentration (correlation coefficient r = 0.52). The Ca^{2+} concentration was directly related to the HRT (r = 0.64) and the volumetric flow rate (r = -0.63). At the inlet of the core plug, the fluid is highly undersaturated with respect to calcite, but while travelling through the sample the saturation state shifts towards equilibrium, accompanied by an increase in calcium concentration and pH and a decrease in dissolution rate. As soon as the outlet pH returns to the level of the infiltration solution, it can be assumed that most of the exposed calcite cement in the core plug was dissolved. According to the common estimation procedure based on the calcium concentration curve (e.g., Luquot et al., 2012; Luquot and Gouze, 2009), only small portions of the initial calcite volume of 0.6 vol.-% (C14) to 2.7 vol.-% (E6) were dissolved in the flow-through experiments.

Compared to the three low-pressure experiments, the total dissolution rate for E6 was approximately two orders of magnitude higher (Figure 4.5e) as expected due to the applied experimental boundary conditions (highest flow rate, cf. Table 4.1). The total rates obtained for samples F11, C14 and F11 showed a similar range of values and a similar behavior over time. After an initial phase, a stabilization of the rates and therefore an almost steady-state behavior was observed with progressing reaction time. A strong correlation of the measured rates with the µXCT derived geometric calcite cement surface in contact with the open pore space $GSA_{Cc,open}$ was evident (r = 0.98). This surface area parameter, which is discussed in more detail in Chapter 4.3.2.2, was therefore used for rate normalization (Chapter 4.3.3).

4.3.2.2 Accessibility and geometry of the calcite cement

The µXCT characterization of the core plugs was mainly applied to parametrize the surface area and the fluid accessibility of the calcite cement in the sandstone (Chapter 4.2.3.3), where it only represents a component of the whole mineral assemblage. Contrastingly, full surface accessibility of the calcite cement is guaranteed in the micro-cell, where the polished core sample slice is overflown by the acidic solution. All parameters and sample properties derived from the segmented µXCT data sets of the unreacted core plugs are summarized in Table 4.2. Four phases could be identified: “pores”, “grains” (quartz, feldspar, clay-rich lithoclasts), weakly absorbing cements (“cements low”) and highly absorbing cements (“cements high”). The calcite cement in the sandstone was represented by the phase “cements low” and was present in proportions of 6–16 vol.-%, whereas the phase “cements high” mainly comprised barite. Despite their spatial proximity within the sandstone block, significant differences in the composition of the core plugs were observed (cf. Appendix B, Figure B13).

As described in Chapter 4.2.3.3, for calculating the µXCT calcite surface area for the normalization of the core rates only the interface between the phase “cements low” and the voxels of the open pore network was considered ($GSA_{Cc,open}$, Table 4.2). Due to the heavy calcite cementation, the Bebertal sandstone is characterized by a very strong heterogeneity already at the mm-scale (Heidsiek et al., 2020). Thus, it was assumed that the parameter $GSA_{Cc,open}$ represents the most appropriate measure to determine the proportion of the calcite surface area that is exposed to the flow field within the different core plugs (hereinafter also referred to as the fluid-accessible surface area). For comparison, the calcite surface area in contact to the total pore space ($GSA_{Cc,total}$) was also calculated.

Table 4.2: Properties of the sandstone samples used for the core scale percolation experiments derived from segmented µXCT images (GSA_{Cc} denotes the geometric surface area of the calcite cement).

		E6	F11	C14	G12	Remark
Sample	Length [cm]	5.0	1.6	1.5	1.5	
	Volume [cm³]	25.2	8.1	7.6	7.9	
X-ray µCT imaging	Voxel resolution [µm]	13.7	10.0	10.0	10.0	
	Pore volume [mL]	3.4	0.1	0.4	0.6	
	Calcite content [vol.-%]	12.0	5.9	16.4	9.7	
	$GSA_{Cc,total}$ [m²] [a]	2.5×10^{-2}	1.3×10^{-5}	2.6×10^{-5}	4.9×10^{-4}	Surface area calcite – *total* porosity
	$GSA_{Cc,open}$ [m²] [a]	6.7×10^{-4}	3.8×10^{-6}	4.0×10^{-6}	1.0×10^{-4}	Surface area calcite – *open* porosity
	$GSA_{Cc,open}$ / $GSA_{Cc,total}$	3 %	28 %	16 %	21 %	

[a] Computed with GeoDict algorithm "Estimation of real surface area" (Ohser and Mücklich, 2000).

The ratio of the two surface area parameters $GSA_{Cc,open}$ and $GSA_{Cc,total}$ (Table 4.2) also provides a measure for estimating the general fluid accessibility of the calcite cement within a sandstone sample. The $GSA_{Cc,open}$ / $GSA_{Cc,total}$ ratio ranges between 3 % (E6) and 28 % (F11). The three-dimensional µXCT images also indicate an increased fluid accessibility of the calcite cement in the core plug F11 (Figure 4.6a). A strongly cemented wedge-shaped structure could be identified in the upper part. However, it does not extend over the entire cross-sectional area, thus allowing the fluid to flow past this structure. In the remaining sample volume, the calcite cement forms small individual clusters. The corresponding calcite cluster size distribution in the core also confirms that sample F11 contains the highest proportion of small clusters, which is advantageous for the fluid accessibility (Figure 4.6b). Although core plug E6 also has relatively small clusters, the calcite cement was mainly accumulated in inclined layered structures that cut completely through the plug, forcing the fluid to penetrate these cemented layers. In the core plugs C14 and G12, much of the intergranular volume was completely filled with calcite cement. Both samples were characterized by a substantially higher median cluster diameter, and especially G12 showed a high proportion (47 vol.-%) of calcite clusters with diameters of at least 100 µm. However, the cement distribution appears more homogeneous for these samples which has an advantageous effect with regard to the fluid accessibility of individual clusters, and is expressed by a medium $GSA_{Cc,open}$ / $GSA_{Cc,total}$ ratio.

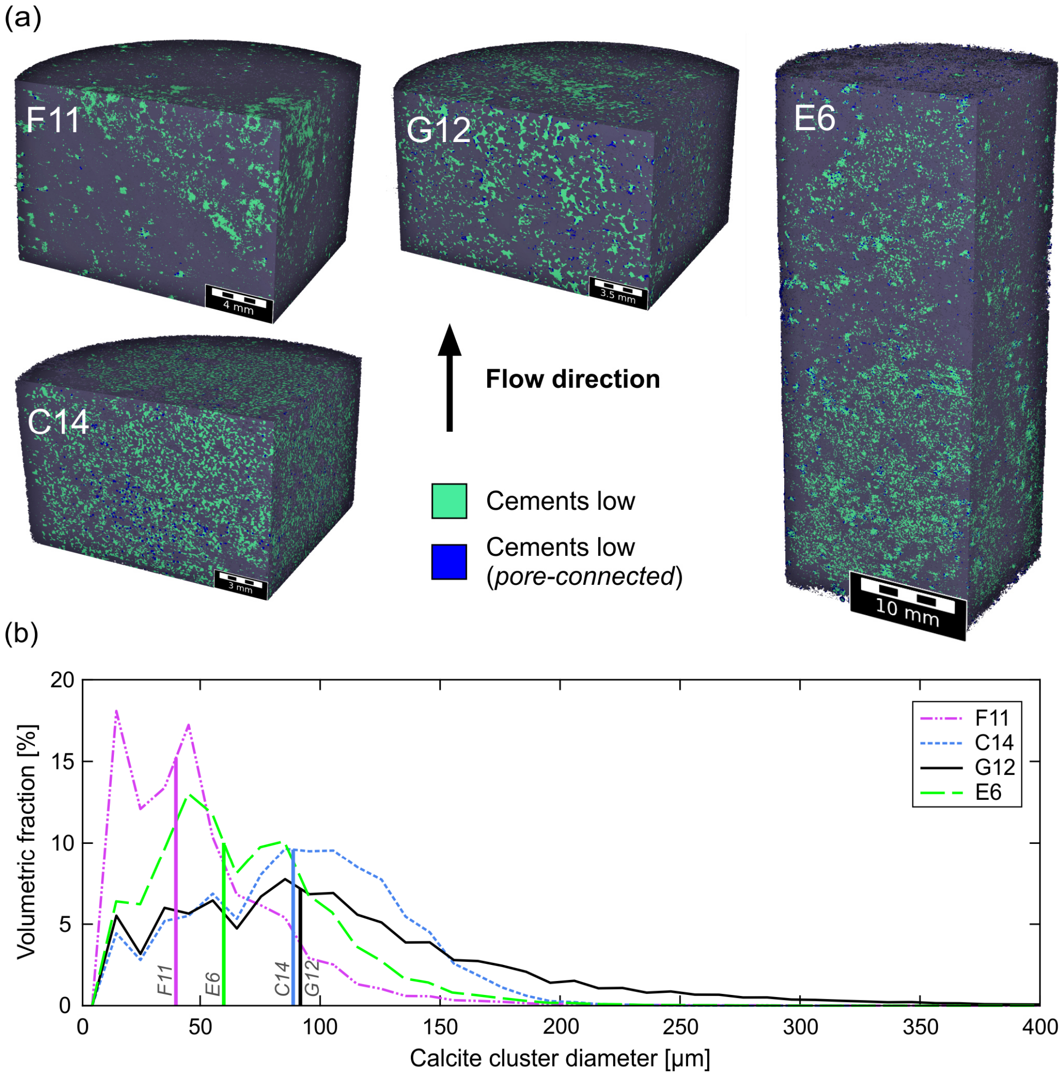

Figure 4.6: Spatial distribution of the phase “cements low” (calcite) within the four core plugs (a) and size distribution of the calcite cement clusters (b). Vertical lines in (b) indicate the median values. The graphs refer to the initial state of the samples before the experiment.

To the authors´ knowledge, estimates of the surface area specifically for calcite or carbonate cements in sandstones are not available in the literature. Published values for the specific surface area of pure carbonate materials are in the range of 0.01 $m^2\ g^{-1}$ for Iceland spar fragments (Molins et al., 2014) and 0.09–2.5 $m^2\ g^{-1}$ for different carbonate rocks (Lai et al., 2015). In contrast, the µXCT surface area of the calcite cement of the Bebertal sandstone varied between $2.0 \times 10^{-7}\ m^2\ g^{-1}$ and $1.1 \times 10^{-5}\ m^2\ g^{-1}$ related to the sample mass, and between $1.2 \times 10^{-6}\ m^2\ g^{-1}$ and $8.1 \times 10^{-5}\ m^2\ g^{-1}$ related to the calcite mass in the core plug. A direct comparison with the literature values is therefore not possible, because the calcite only makes up a portion of the mineral inventory of the sandstone, and as a cement phase it is characterized by a completely different geometry.

4.3.3 Comparison of normalized dissolution rates on surface and core scale

To enable a direct comparison of the experimental rate data between the core and surface scale, normalized rates (in units mol m^{-2} s^{-1}) have to be used to account for the differing system sizes. While VSI allows for a direct determination of surface normalized rates (cf. Eq. (4.2)), the normalized rates for the core scale had to be calculated indirectly using the fluid-accessible surface area determined by μXCT analysis (cf. Eq. (4.4)).

The average dissolution rates for the different core plugs varied between 1.6×10^{-7} and 4.9×10^{-6} mol m^{-2} s^{-1}, and the full range of core dissolution rates was 5.8×10^{-8} – 8.4×10^{-6} mol m^{-2} s^{-1}. Compared to the average surface rate with identical inlet fluid chemistry (1.6×10^{-5} mol m^{-2} s^{-1}, Chapter 4.3.1), the core rates were 0.5–2 orders of magnitude lower (Figure 4.7). From previous studies, calcite dissolution rates are known to vary by 1–2 orders of magnitude under controlled laboratory conditions, and up to several orders of magnitude for different scales or rate determination methods (e.g., Arvidson et al., 2003; Fischer et al., 2014, 2012a; Pereira Nunes et al., 2016). The literature data shown in Figure 4.7 also indicate a rate variability of about one order of magnitude for pH 4. However, since the literature data mainly comprises far-from-equilibrium rates, and this study compares far-from-equilibrium rates with near-equilibrium rates, an even higher deviation was expected between the core scale and the surface scale.

The existing deviation of the core dissolution rates from the surface rates reflects the strongly differing reactive transport conditions. These can be mapped using several parameters summarized in Table 4.3, including the HRT, the saturation index, and the Peclet and Damköhler number (details in Appendix B, Table B1).

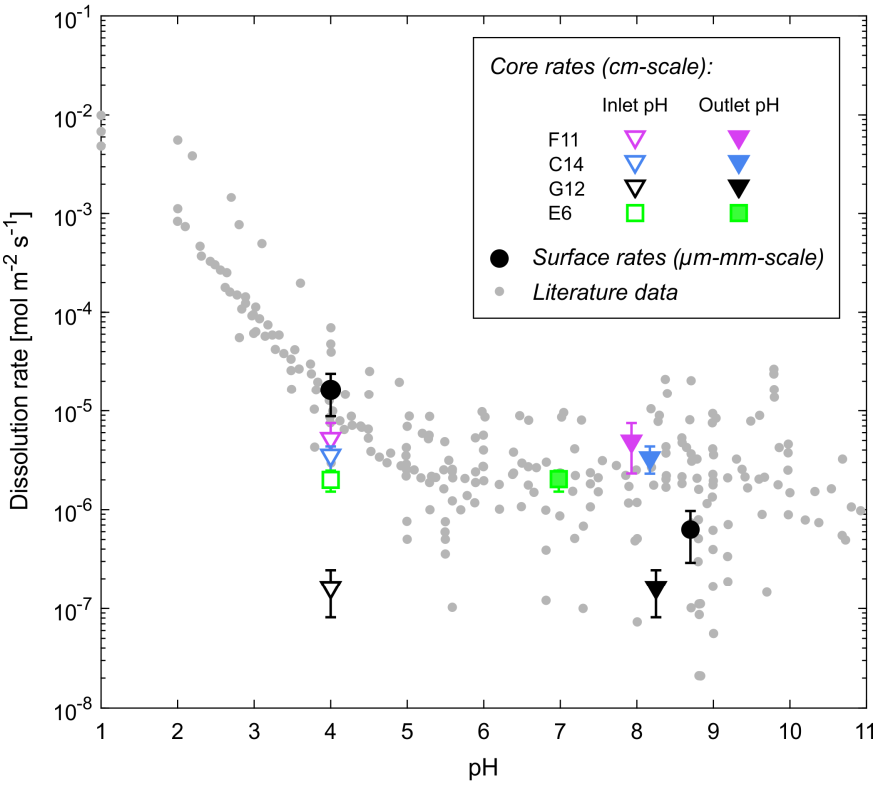

Figure 4.7: Surface dissolution rates (this study and the same sandstone at pH 8.7 from Pedrosa et al. (2019)), core dissolution rates (this study, square = high-pressure experiment, triangles = low-pressure experiments), and literature calcite dissolution rates (data compilations by Arvidson et al. (2003) and Bollermann and Fischer (2020)). The derived core rates are plotted against both the inlet pH (open symbols) and the mean outlet pH (closed symbols).

The flow through the pore space of the core plugs was slow with a HRT in the order of minutes, leading to a buffering of the solution´s acidity and a successive increase of the calcite saturation index (*SI*). This resulted in the formation of strong chemical gradients as indicated by the significant pH difference between the inlet and outlet of each core plug (Figure 4.5d). The Damköhler numbers indicate that the characteristic time for fluid transport through the core plug was in the same order of magnitude as the characteristic time for dissolution or, in case of the low-pressure experiments, even higher. The Peclet numbers confirm a diffusion dominated transport for all core experiments due to the low permeability environment of the Bebertal sandstone with initial rock permeabilities of only 1.1–3.1 mD. In contrast, the micro-cell experiment ensured minimum HRTs and minimum characteristic transport times of the reactive fluid. Far-from-equilibrium conditions were maintained at all times and the flow regime was purely advective with a free flow over the rock surface.

Table 4.3: Transport conditions of the experiments on surface scale (micro-cell) and on core scale (triaxial permeability cell, flow-through autoclave ICARE4).

Reactor	**HRT**	***SI* (outlet)**	**Peclet number**	**Damköhler number**	**Sample**
Micro-cell	3.8 s	<< 0	8.9	<< 1	E7
Triaxial permeability cell	31 – 447 min	- 0.12 – -0.95	0.001 – 0.014	2.11 – 3.95	F11, C14, G12
Flow-through autoclave ICARE4	6.4 min	- 2.78	0.18	0.83	E6

Naturally cemented calcite in sandstones contains variable crystal orientations, different surface morphologies, impurities and grain boundaries, and diverse grain sizes with a variable density of highly reactive crystal corners and edges (Noiriel et al., 2020, 2019; Pedrosa et al., 2021, 2019). The surface rates obtained at pH 4.0 in this study are within the variability of the literature rate data (Figure 4.7). At pH 8.7, the same sandstone also showed a variability of rates found in other calcite sample types. This shows a consistency on the intrinsic dissolution rate variability of natural calcite samples, independent of its bulk form (single cleaved crystals, calcite powders, cement crystals), which is of great importance for the transferability of calcite dissolution rates from prepared sample material to the naturally occurring mineral phase. The higher the pH, the reaction is probably more surface-controlled rather than diffusion-controlled (Arvidson and Morse, 2014). The pH of 4.0 in the experiments is a transition pH, where the rate variability is expected to be associated with both transport and surface effects; i.e., a region where complex kinetics occur (Morse et al., 2007).

With exception of core plug G12, the normalized core dissolution rates were ranging between the surface rates that were analyzed for pH values of 4.0 and 8.7 (Pedrosa et al., 2019). Possible reasons for the strong deviation of the rate for G12 are discussed in Chapter 4.3.4. This strongly suggests that the reported rate discrepancy of several orders of magnitude could be mainly due to an overestimation of the reactive mineral surface area (e.g., usage of single-mineral BET values for components of a multimineral rock), rather than solely due to the rate-reducing effect of transport control. If the specific structure and fluid accessibility of the mineral phase of interest is not explicitly considered for surface area quantification (cf. Chapter 4.3.2.2), or if the surface area is derived from chemically comparable sample material with a completely different geometry (e.g., poikilitic carbonate cement versus micritic limestone), the resulting dissolution rate will most likely be misestimated. The fact that the core rates fit better to the surface dissolution rates at pH 8.7 is plausible, because this value corresponds approximately to the outlet pH measured in the core experiments. Here, the pH of 4.0 only prevails directly at the sample inlet, since the comparatively long transport time through the pore space of the sandstone leads to a significant increase in pH to 6.8–8.8 (Figure 4.5d). Thus, even without performing flow-through experiments, a possible range of values for core-scale rates could be determined based on existing surface rates, provided that the expected buffering of the pH value can be estimated.

To identify possible influencing factors on the relative order of the core rates in Figure 4.7, a correlation analysis (cf. Appendix B, Figure B14) was performed. The normalized core rates correlated most strongly with the initial permeability of the core plug (r = 0.81). With decreasing permeability (i.e., pore connectivity), preferential flow becomes more important. Especially for core plug E6, the formation of preferential flow paths was presumable intensified because this sample was exposed to high differential pressures of up to 19 bar (Chapter 4.2.2.3). This can lead to a reduction of the actual contact surface of the fluid during the experiment which in turn causes lower surface normalized dissolution rates. In addition, due to the larger sample dimensions, the µXCT data set of E6 consists of three stitched scans. Artificial generation of (open) porosity in the overlap regions could also have led to an overestimation of the surface area and thus to an underestimation of the normalized rate. A strong negative correlation with the normalized core rates (r = -0.69) was also found for the median calcite cluster diameter (Figure 4.6b). This fits with the fact that the reactivity of minerals generally increases with smaller grain sizes due to the increased contribution of highly reactive features such as corners and edges (e.g., Noiriel et al., 2020; Pedrosa et al., 2019; Saldi et al., 2017).

4.3.4 Comparison of µXCT geometric surface areas with estimated reactive surface areas

To assess the validity of the µXCT derived surface parameter $GSA_{Cc,open}$ for the normalization of the experimental dissolution rates it was compared to estimated reactive surface areas (cf. Eq. (4.5), Chapter 4.2.3.2). Two different rate constants were used for deriving estimates for the reactive surface area (RSA) of the calcite cement in the core plugs:

(i) Rate constant from the surface dissolution experiments (far from equilibrium), reflecting conditions at the inlet of the core plug ($k_{c,\,surface}$ = 1.63 × 10^{-5} mol m^{-2} s^{-1}, Chapter 4.3.1)

(ii) Conservative rate constant (near equilibrium) calculated by Eq. (4.8) based on the outlet fluid chemistry in the core experiments, reflecting conditions at the outlet of the core plug, ($k_{c,\,fluid}$ = 5.06 × 10^{-8} – 8.17 × 10^{-7} mol m^{-2} s^{-1}).

By applying Eq. (4.5) to $k_{c,\,surface}$ and $k_{c,\,fluid}$, two end members can be obtained that define the expected range of values for the reactive surface area of the calcite cement in the core sample. A comparison of $GSA_{Cc,open}$ with the calculated RSA values shows that three of the four samples are within this range (Figure 4.8). Using $GSA_{Cc,total}$, only one value would be within the specified range. Although the two RSA end members still span over a range of more than an order of magnitude, thus still allowing for misestimation, it can be assumed that the parameter $GSA_{Cc,open}$ provides the most reasonable (measurable) estimates for the studied rock material.

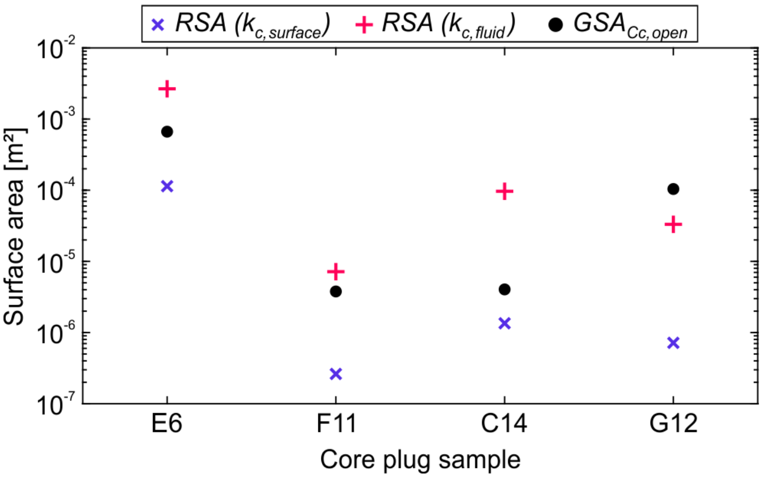

Figure 4.8: Estimated reactive surface areas (RSA) for the core plugs using $k_{c,surface}$ from the surface experiments (blue) and $k_{c,fluid}$ estimated from core experiments (red), and µXCT based geometric surface areas of the calcite cement in contact to the open pore space ($GSA_{Cc,open}$). The values shown refer to the initial state at the beginning of the experiment.

For core plug G12, $GSA_{Cc,open}$ was above the specified range and probably overestimates the calcite cement surface area that is available for reaction. As a result, the normalized dissolution rate for G12 was also extremely low (cf. Figure 4.7). A possible source of error for this deviation could in principle be an over-segmentation of pore space, although the segmentation process was throughout consistent for all core plugs. Alternatively, an overestimation of the open porosity is possible, which was determined based on a geometric identification of pore networks that are connected to the material surface (Chapter 4.2.3.3). Due to the fact that G12 was characterized by the largest calcite cluster sizes (Figure 4.6b), it is likely that small volumes of the void space that were classified as open porosity by the PoroDict algorithm were actually sealed off during percolation by calcite cement "barriers", depending on the flow direction. For future studies, the fluid-effective portion of the porosity network for specific flow directions could be identified more precisely by including fluid flow simulations on the segmented structures (e.g., Jacob et al., 2021).

Noiriel et al. (2020) also used geometric surface areas from µXCT imaging as a parameter for the normalization of calcite dissolution rates. They found a high level of agreement with VSI rates that were obtained for the same sample. Since only a single crystal with a size of 1.8 × 0.6 mm was examined, images with a resolution of 0.325 µm could be achieved (Noiriel et al., 2020). Due to the focus on a single reactive mineral phase in a rock and sample sizes of several centimeters, the surface area calculation in this study is of course limited to the voxel size (10–14 µm). Thus, surface roughness below resolution could not be computed (Table 4.2).

The transferability to other minerals or lithologies has to be demonstrated on a case-by-case basis. Most important, the particular mineral phase has to be optically detectable and thus segmentable in the computed tomography images. In addition, Noiriel et al. (2009) showed that surface area quantification by µXCT is not suitable for materials with high inter-particle microporosity (e.g., sparite and micrite crystals). The applicability of the approach to the studied sandstone can be justified primarily by the fact that the often pore-filling calcite cement mostly forms large contiguous clusters (relative to the voxel size).

4.3.5 Upscaling calcite dissolution rates from surface to core scale

Attempting to link the two scales investigated in this study, the statistical rate information from the surface experiments (Chapter 4.3.1) was used to retrieve upscaled rates for the core scale and to compare them to the measured values. The upscaling was based on a general rate law for calcite dissolution (Eq. (4.6), Lasaga 1998), where the resulting rate is described as the product of an intrinsic rate (or rate constant) k_c, a surface area A (here: $GSA_{Cc,open}$), and a saturation state function $f(\Delta G)$. Here, the results of the surface experiments represent the intrinsic rate k_c of the calcite cement under the chosen fluid chemical conditions of the study. Many authors argue against the use of a single-valued rate constant for predicting dissolution rates and recommend the usage of a multi-rate parametrization to consider the heterogeneity of mineral surface reactivity (e.g., Fischer et al., 2012a; Karimzadeh and Fischer, 2021). Thus, the observed variability of the surface rate in space and time was explicitly included for the parametrization of k_c for the upscaling approach. For the statistical surface rate analysis (Chapter 4.3.1), twelve areas of interest (individual sizes of 651–9730 μm²) within different calcite cement patches were used to define a representative range of rates.

In addition to the variability of the surface dissolution rate, there is also a variability of the fluid´s saturation state with respect to calcite (expressed by $f(\Delta G)$). The temporal variability of this saturation state function can be determined based on the time-dependent fluid sampling in the experiment. Analogous to k_c, also a spatial variability of the fluid´s composition and saturation state exists within the core plug due to the heterogeneity of the pore space that results in a widespread range of fluid velocities (e.g., Al-Khulaifi et al., 2017; Jacob et al., 2021; Miller et al., 2017). However, as this spatial distribution within the sample is not determinable on an experimental basis, $f(\Delta G)$ was parametrized based on the SI of the sampled outlet fluid using Eq. (4.7). The surface area of the reacting mineral also generally evolves with ongoing reaction time (e.g., Luquot and Gouze, 2009; Luttge, 2006; Noiriel et al., 2009). A temporal variability of the surface area was not considered for upscaling because the fluid-accessible geometric surface area from μXCT analysis (Chapter 4.3.2.2) was only available for the initial state.

A clear relationship between the total dissolution rate of the calcite cement (in mol s^{-1}) and $A \cdot f(\Delta G)$ across the studied scales was found (Figure 4.9a). The surface and core rates are scaled in dependence of the geometric surface area, but the distance to equilibrium must necessarily be considered. Since no fluid chemical data was available for the surface experiments, $f(\Delta G) = 1$ was assumed, taking into account the hydraulic residence time of less than four seconds (Table 4.3). The rate data across the two scales can be best described by a power-law function (Figure 4.9a). In addition, the linear relationship between the rate and $A \cdot f(\Delta G)$ is shown, as it would result from Eq. (4.6) based on the transition state theory. The linear function predicts a stronger increase in dissolution rate with increasing $A \cdot f(\Delta G)$ than the fitted power-law function, thus, the deviation from the measured rate data broadens with increasing values for $A \cdot f(\Delta G)$.

Figure 4.9b shows the upscaled rates calculated by Eq. (4.6) using the (variable) intrinsic surface rate and the sample-specific fluid-accessible surface area and $f(\Delta G)$. The rates of the core plugs reacted in the permeability cell (C14, G12 and F11), calculated based on VSI rate data as described above, were misestimated by factors of 0.7–2.9 (deviation of the mean values). Consistent with the above, the largest overestimation by a factor of 7.9 was found for core plug E6 with the largest value for $A \cdot f(\Delta G)$. Bouissonnié et al. (2018) performed simulations of column experiments on the cm-scale (calcite single crystals embedded in inert material) by using VSI derived rates of the calcite (104) face. While the measured calcite dissolution rates of the column experiment could be reproduced by two-dimensional simulations, they were also overestimated by factors of 3 to 20 in the one-dimensional simulations.

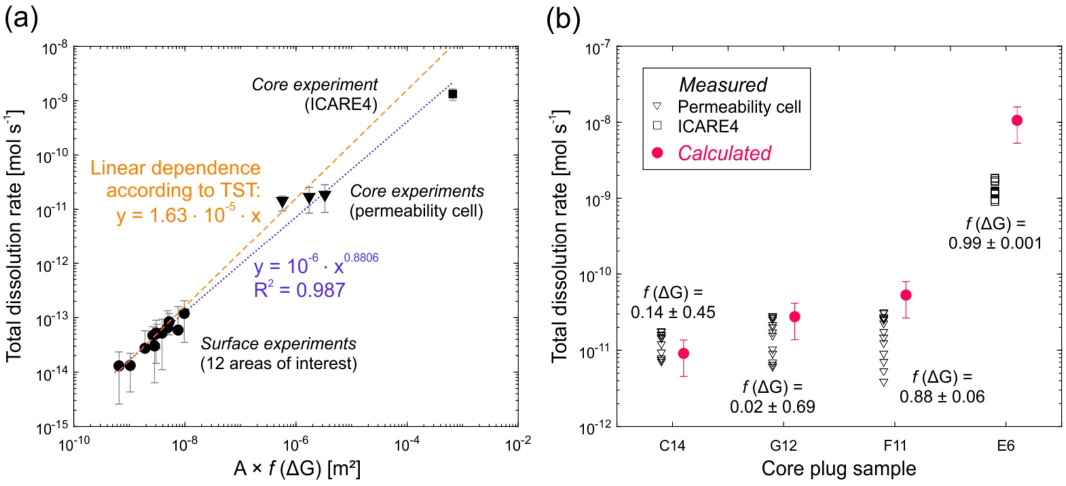

Figure 4.9: (a) Dependence of the measured surface and core total dissolution rates on the product $A \cdot f(\Delta G)$ with linear dependence (dashed line) according to the transition state theory (TST) and fitted power-law relation (dotted line); (b) upscaled dissolution rates calculated from the intrinsic rate range (surface experiments) and the sample specific fluid-accessible surface area and saturation state function.

Other studies have also shown that models or computations based on volume-averaged parameters tend to overestimate rather than underestimate chemical rates for heterogeneous sample material (Kim et al., 2011; Li et al., 2006), which is also supported by the present results. The high deviation for core plug E6 in particular may also be due to the experimental conditions (i.e., high flow rates and fluid velocities). According to Kim and Lindquist (2013), a larger total change of the surface area as well as a higher spatial variability of local surface area changes can be expected when the dissolution reaction occurs far-from-equilibrium under high flow rates. Since the core plug sample E6 was percolated with the highest flow rate, more pronounced changes in surface area are to be expected compared to the other experiments. This is also supported by the highest dissolved calcite volume during the experiment (cf. Chapter 4.3.2.1). Hence, ignoring the variability of the surface area for estimating upscaled rates is a critical factor, especially for higher undersaturation.

Despite the use of sample-averaged parameters for the surface area and the saturation state function, the deviation of the upscaled rates from the measured rates is less than one order of magnitude for all core experiments, which again emphasizes the quality and applicability of the presented methodology to determine the fluid-accessible surface area of the calcite cement. Further improvement of the rate estimations could be achieved by more complex models to account for the temporal and spatial variability of all involved parameters. Still, conceptually, the results show that the statistical surface rate information and the rates obtained from the percolation experiments on the core scale can be linked via μXCT parameters such as geometric calcite surface area and connected pore space.

4.4 Conclusions

This study compares and links dissolution rates of a natural calcite cement in a reservoir sandstone on length scales from micro- to centimeters. Several experiments with different flow reactors were conducted to investigate the dissolution kinetics of calcite at the mineral surface and on the core scale when exposed to an acidic sodium chloride solution (pH 4).

On the surface scale, the statistical analysis of the calcite surface height retreat measured by vertical scanning interferometry (VSI) under far-from-equilibrium conditions indicated an average rate of 1.6×10^{-5} mol m^{-2} s^{-1} with local maximum rates of 1.5×10^{-4} mol m^{-2} s^{-1}. While the surface dissolution rates on the μm- to mm-scale were in agreement with literature data for other calcite sample types, the normalized core dissolution rates on the cm-scale deviated by 0.5–2 orders of magnitude from the surface rates, covering a range of $5.8 \times 10^{-8} - 8.4 \times 10^{-6}$ mol m^{-2} s^{-1}. For such rock materials, these core rates provide a more realistic guide for estimating effective dissolution rates on even larger scales, since the core experiments were performed under reactive transport conditions that would also be expected to occur naturally in such systems. None of the rates are effectively incorrect, they represent the kinetic response to variable external conditions (i.e., free fluid flow over the rock surface versus fluid percolation in a complex porous medium).

Surface area normalization remains the most critical step in quantifying mineral dissolution rates at the core scale. Based on X-ray micro-computed tomography (μXCT) images of the sandstone core plugs, the geometric surface area of the calcite cement was successfully estimated. The μXCT derived surface parameter does not simply relate to the surface area of cubic voxels, but approximates the rounded surface of the segmented phase. The additional approach of further scaling the total geometric surface area by considering only the open pore network tangentially along the flow direction allows to evaluate the fluid accessibility of the cement phase in the core plugs. For the samples examined, the proportion of the fluid-accessible calcite surface area to total calcite surface area ranges between 3 and 28 %. Despite the limited resolution of the μXCT images, the strong variability of the calcite surface area in the sandstone samples over two orders of magnitude shows how much the surface availability can ultimately vary due to heterogeneity. The methodology used can improve the accuracy of the dissolution rates in multi-mineral samples where a direct surface measurement (e.g., BET) is not possible.

Using the statistical VSI rate information from the surface scale, the fluid-accessible µXCT geometric surface area and a saturation state function, the total dissolution rate (calcium output in moles per second) for the individual samples on the core scale was estimated and compared to the measured values. The results indicate that for the low-pressure experiments with slow flow rates and conditions close to equilibrium (i.e., low calcite dissolution volumes), total core dissolution rates can be determined with deviations between - 32 % and + 185 %. Due to the higher deviations of the upscaled calcite dissolution rates for the experiment conducted under high differential pressure, the importance of additionally considering the temporal and spatial variability of the available mineral surface as well as the saturation state of the fluid in the pore space became apparent and should be rigorously addressed in future studies.

Acknowledgments

This work was financially supported by the German Federal Ministry of Education and Research (BMBF) Geological Research for Sustainability (GEO:N) program (grant no. 03G0871) within the framework of Research for Sustainable Development (FONA3). We thank Linda Luquot, Hagen Steger, Olaf Ukelis, Kevin Altinger and Marcos Toro for assistance related to the design and implementation of the flow-through experiments. We also thank Cornelius Fischer and Andreas Lüttge for helpful discussions and valuable suggestions.

RELATED CO-AUTHORED STUDIES

5

In the following, brief summaries of three published studies with significant contributions by the author of this thesis are presented. Chapters 5.1 and 5.2 are thematically related to Study 1 in Chapter 2, and Chapter 5.3 is thematically related to Study 3 in Chapter 4.

5.1 Measuring hydraulic fracture apertures: a comparison of methods

Publication: Cheng, C., Hale, S., Milsch, H., Blum, P., 2020. Measuring hydraulic fracture apertures: a comparison of methods. Solid Earth 11, 2411–2423. https://doi.org/10.5194/se-11-2411-2020

The hydraulic aperture (a_h) is a central parameter for fracture flow as outlined in Chapter 1.2.1. Flow-through tests are generally considered the most reliable method for determining a_h and are normally carried out in the laboratory using fractured core samples under well-controlled conditions. However, a comprehensive and precise analysis of hydraulic fracture apertures on the outcrop scale remains challenging. The aim of the study of Cheng et al. (2020) was therefore to compare three possible measurement methods with regard to accuracy and reliability.

Different artificial fractures in sandstone core samples with varying degrees of roughness and matedness were tested. The study compared a flow-through apparatus (FTA) with the portable air permeameter TinyPerm 3 (TP) and the microscope camera (MC), both described in Chapter 2.2. The FTA was operated at a constant flow rate so that the measured differential pressure between the sample inlet and outlet could be used to determine the fracture permeability and hydraulic aperture a_h by using the cubic law (cf. Chapter 1.2.1). In the FTA, a_h was quantified for several discrete pressure steps during a loading-unloading cycle. By extrapolating the unloading curve, it was possible to quantify a_h for zero effective pressure, which was required for comparison with the other two methods.

A very high agreement of a_h was found between TP and FTA ($R^2 = 0.998$) for all investigated fracture types with a maximum deviation of 2.5 μm. To obtain the best possible result for the TP, it was necessary to measure along the entire fracture profile, especially for more open fractures. Although the values for a_h derived from the microscope camera images were qualitatively correct, they showed significantly higher deviations from the FTA in all cases. For hydraulic fracture apertures between 8 and 66 μm, the air permeameter could therefore be successfully validated under ambient pressure and temperature conditions.

Contribution to this study: As co-author, Sina Hale (SH) undertook the air permeameter measurements and microscopic camera imaging on the fractured core plug samples, including subsequent evaluation of the hydraulic and mechanical fracture aperture. SH contributed to the analysis and interpretation of the results. SH also participated in the conceptualization of the manuscript, final validation of the results and final review and editing.

5.2 Quantification of fracture roughness by change probabilities and Hurst exponents

Publication: Gutjahr, T., Hale, S., Keller, K., Blum, P., Winter, S., 2021. Quantification of fracture roughness by change probabilities and Hurst exponents. Mathematical Geosciences. https://doi.org/ 10.1007/s11004-021-09985-3

The analysis of the surface morphology of natural fractures by means of mathematical methods is a current issue in geosciences. The roughness of the fracture surface governs the occurrence of void spaces and contact areas, which in turn controls the response of the fracture to mechanical or hydraulic impacts (cf. Chapter 1.2.1). Often complex approaches such as Fourier analysis are used to characterize fracture roughness. However, they require certain preconditions that are not necessarily met by natural structures. The study of Gutjahr et al. (2021) introduces the alternative concept of "change probabilities" for fracture roughness analysis. It is based on analyzing the relative order of height values along fracture surface profiles, sequentially and automatically extracted from a three-dimensional fracture surface in different spatial directions.

The presented methodology was based on the identification of specific change patterns (i.e., alignments of height values) in the profile, which were assumed to be characteristic for rough surfaces. The probability of occurrence of these patterns (change probability) directly correlated with the fracture roughness. Furthermore, by continuously increasing the step size for sampling the height values along the roughness profile, the so-called delay τ, a scale-dependent description of the roughness could be obtained.

It was shown that for self-affine fracture surfaces the Hurst exponent can be derived from the change probability. In the absence of self-affinity, a scale-dependent Hurst exponent can be derived from the change probability instead, which takes mutable values depending on τ. A MATLAB code was developed for application to real fracture data. Applying this algorithm to three-dimensional data sets of a natural tensile fracture (bedding joint in the Flechtinger Sandstone, cf. Chapter 2) and a fault-slip surface showed that roughness anisotropy could be detected and visualized, allowing conclusions to be drawn about the fracture formation mechanism. High computational efficiency and a low sensitivity to noise were confirmed to be further advantages of the change probability concept.

Contribution to this study: As co-author, Sina Hale (SH) assisted in literature research, was responsible for data acquisition and data preparation (i.e., 3D fracture surface images for data analysis). SH contributed to the discussion and interpretation of the results and to writing of the Sections “Introduction” and “Application to Natural Fracture Surfaces” of the publication. SH also participated in the conceptualization of the manuscript, final validation of the results and final review and editing.

5.3 Simulating permeability reduction by clay mineral nanopores in a tight sandstone by combining computer X-ray microtomography and focussed ion beam scanning electron microscopy imaging

Publication: Jacob, A., Peltz, M., Hale, S., Enzmann, F., Moravcova, O., Warr, L.N., Grathoff, G., Blum, P., Kersten, M., 2021. Simulating permeability reduction by clay mineral nanopores in a tight sandstone by combining computer X-ray microtomography and focussed ion beam scanning electron microscopy imaging. Solid Earth 12, 1–14. https://doi.org/10.5194/se-12-1-2021

Modern imaging techniques such as X-ray micro-computed tomography (μXCT) or focussed ion beam scanning electron microscopy (FIB-SEM) provide high-resolution 3D images of rocks. When fluid flow simulations are performed on μXCT data sets, a significant overestimation of permeability is a known problem. In particular, this applies to rocks that have small pore sizes and a high clay mineral content, where the achieved scanning resolution is often insufficient to capture these structures. The objective of the study of Jacob et al. (2021) was to improve the accuracy of permeability prediction by Digital Rock Physics (DRP) simulations for the illite-bearing Flechtinger Sandstone (cf. Chapter 4).

First, FIB-SEM was used to capture sub-resolution illite aggregates in the sandstone in order to compute their permeability, which was found to be 2.5×10^{-3} mD. Energy dispersive X-ray spectroscopy (EDX) analyses showed that the illites were mainly concentrated near altered feldspars and occurred as grain coatings or pore fillings. In the next step, microporous voxels were added to the μXCT data set, taking into account the spatial distribution of the illite meshworks determined by EDX, and were parametrized with regard to their permeability. Corresponding to the observed average thickness of the illite grain coatings (~ 5 μm), all pore voxels in the μXCT scan with diameters below this value were assigned microporous properties.

A total of twelve mini-plug samples were considered in the study, and for each sample the permeability was computed based on the original and modified μXCT data set. The fluid-flow simulations were based on Navier-Stokes-Brinkman equations to account for the added microporous domains. As a comparative measure to assess the accuracy of the simulated permeabilities, the rock permeability was determined experimentally using helium permeametry. For the original μXCT data sets, simulated permeabilities were up to 814 % higher than the measured values. By applying the presented analytical methods to take into account sub-voxel structures (illite), the mismatch between the measured and the calculated permeability could be reduced to - 35 %.

Contribution to this study: As co-author, Sina Hale (SH) conducted the measurements needed for the validation of the permeability simulations. This included the determination of the intrinsic rock permeability by helium permeametry and the analysis of pore size distributions using mercury intrusion porosimetry (MIP). SH contributed to writing of the Sections "Analytical procedures" and "Results and Discussion" of the publication. SH also participated in the conceptualization of the manuscript, final validation of the results and final review and editing.

SYNTHESIS

6

6.1 Summary and conclusions

This thesis provides an important contribution to deepen our understanding of coupled hydraulic, mechanical and chemical processes in porous and fractured rocks. The reliable quantification of key parameters forms the necessary basis for the interpretation of occurring phenomena in the respective scale of investigation, but especially for the transferability of coupled HM and HC processes to higher scales (i.e., upscaling) and longer time periods (i.e., prognosis). The thesis therefore identifies, evaluates, refines and develops suitable methodologies and approaches for determining such key parameters. Furthermore, by addressing specific problems and settings, crucial influencing factors are analyzed that determine the system behavior in the HM-coupled host rock and the HC-coupled reservoir rock.

6.1.1 Coupled hydraulic-mechanical processes in fractured rocks

All investigations on HM couplings in fractured rocks are ultimately based on single fracture scenarios. Using a natural bedding joint (~ 45 × 12 cm) in the well-known Flechtinger Sandstone, an important outcrop analog for the gas-bearing Permian sediments of the North German Basin, three modern portable instruments for the determination of mechanical (a_m) and hydraulic apertures (a_h) and fracture roughness are applied and systematically compared in Study 1 (Chapter 2). As these quantities represent key parameters for the description of coupled HM processes in fractured media, an accurate and efficient determination is essential.

The air permeameter represents one of few methods for directly determining a_h. It is based on the evaluation of the time-dependent pressure compensation in response to an initial vacuum pulse imposed onto a fracture. This direct method is contrasted with optical measurements using a digital microscope camera and a 3D laser scanner, yielding a_m as the normal distance between the opposite fracture surfaces of the imaged fracture profile segments. The conversion to a_h is performed using different model assumptions to account for fracture roughness, represented in the study by seven common roughness parameters, including the relative roughness and the joint roughness coefficient (JRC).

The study clearly shows that the air permeameter, despite its simple operating principle, offers substantial advantages over the two optical methods in terms of mobility, time expenditure and data processing, and is highly recommended for attaining accurate and efficient measurements of a_h. The 3D laser scanner only achieves a mean investigation depth of 1.04 mm, and thus mostly captures the rounded transition zone between the rock surface and the deeper void area. This leads to a significant overestimation of a_h (+ 70–260 %) in contrast to the direct air permeameter measurements with investigation depths of > 17 mm. Despite a limited lateral field of view, the microscope camera also yields sufficient investigation depths and realistic estimates for a_m and a_h, only deviating by less than 27 % from the results of the air permeameter.

Since the true hydraulic aperture of the bedding joint was unknown in Study 1, the air permeameter is validated for different artificial fracture types showing an aperture spectrum of 8–66 µm by hydraulic laboratory tests in a separate co-authored study (Cheng et al., 2020; Chapter 5.1). In order to account for realistic differences in surface morphology and fracture matedness, saw-cut and tensile fractures in sandstone core samples are tested with different relative offsets. This validation study only finds negligible deviations for a_h between 0.2 and 2.5 µm. Even for extremely closed fissures below the specified measurement limit of 10 µm, the applicability of the air permeameter is not impaired, which represents important knowledge for the further use of the instrument.

While, according to Study 1, the usability of the 3D laser scanner is limited for aperture determination, it is well suited for a digital acquisition of rough fracture surfaces with high point densities. Thus, based on the collected scan data of the bedding joint surfaces in Study 1, a novel algorithm for three-dimensional roughness analyses is developed in a further co-authored study (Gutjahr et al., 2021; Chapter 5.2). The so-called change probability, describing the probability of occurrence of change patterns in fracture surface profiles, functions as an independent roughness parameter and can also be used for quantifying a scale-dependent Hurst exponent. In contrast to the classical and widely used single-valued Hurst exponent, the scale-dependent formulation is also able to provide information about characteristic sizes of certain structural components. Based on a mathematical proof it is shown that self-affinity is not a necessary condition for the application of the algorithm, which immensely facilitates its applicability for natural fractures. A roughness anisotropy evaluation is schematically performed for the bedding joint in the Flechtinger Sandstone (Chapter 2) and a fault surface. This results in various possible applications for the analysis and description of fractured systems, starting from the identification of fracture formation mechanisms to the upscaling of rough fracture surfaces from the experimental to the field scale.

Building on the comparative studies on single fractures at the cm- and dm-scale (Chapters 2 and 5.1), the performance evaluation of the fracture characterization methods is extended to a discrete fracture network at the m-scale. In Study 2 (Chapter 3), a holistic hydraulic-mechanical characterization of an uncovered excavation damaged zone (EDZ) in the Mont Terri rock laboratory is performed. Such alteration zones around underground cavities are of particular importance for deep geological waste disposal, as they represent mechanical and hydraulic zones of weakness in the otherwise highly impermeable host rock, which is also true for the investigated Opalinus Clay, the target host rock formation in Switzerland. Study 2 affirms the suitability of the presented methodology regardless of lithology and scale. In order to include the claystone matrix, fracture characterization is extended by a mechanical component. Here, needle penetrometer tests (NPTs) allow the estimation of geomechanical and geophysical rock properties based on the resistance of the material to needle indentation.

An enhanced evaluation procedure for the microscopic imaging method using an automated algorithm results in time savings of ~ 60 % per image compared to Study 1, while maintaining the high quality of the distance measurements.

This field measurement campaign clearly demonstrates that the long-term exposure of the tunnel walls over a time span of about 15 years led to a significant decrease in water content by 2.9 wt.-% compared to the initial condition and, as a result, to a strong increase in rock strength and stiffness (e.g., an increase in uniaxial compressive strength (UCS) normal to bedding by 164 %). A comparison with extensive laboratory data sets confirms a reasonably accurate estimation of UCS, Young's Modulus (E) and the P-wave velocity (v_P) by the NPT normal to bedding, while micro cracks cause a significant parameter underestimation in the bedding-parallel direction. Due to suppression of self-sealing processes by desaturation, open flow paths with hydraulic apertures of 21–112 µm still exist. By including fracture geometric aspects, induced tensile fractures (Mode I) and reactivated tectonic discontinuities (faults and splays, Mode II or III) in the EDZ can be distinguished. In addition to the insight into the sensitivity of uncovered EDZs, a practical approach is provided for extending the observation period with respect to continuous HM processes in host rocks due to the possibility of performing repeated measurement campaigns without system disturbance.

6.1.2 Coupled hydraulic-chemical processes in porous rocks

Study 3 (Chapter 4) addresses the dissolution behavior of the calcite cement in the Flechtinger Sandstone within core samples (cm-scale) and at the mineral surface (µm-mm-scale), aiming to provide a link between the acquired experimental rate data as a contribution to improve reaction rate upscaling approaches. The measurement of the calcite surface height retreat by vertical scanning interferometry (VSI) on the µm-mm-scale is a reliable and direct method to obtain local and temporally resolved dissolution rates. Complementary to this, the core-scale percolation experiments are an important tool to study the impact of fluid dynamics and initial sample characteristics on the total (i.e., bulk) reaction rate. By using two different types of percolation experiments (high-pressure and low-pressure setups), the study accounts for different conditions with respect to the hydraulic residence time of the reactive fluid.

One major problem in dissolution rate determination and upscaling is that the reactive surface area is generally unknown, especially imposing difficulties for multimineral rocks where only part of the total surface area is involved in the reaction. Thus, a practical approach is established to quantitatively estimate the reaction-available calcite surface area in the sandstone based on X-ray micro-computed tomography (µXCT) images of the core samples. Based on an algorithm for estimating the true geometric surface area (GSA) of the segmented calcite cement phase, this parameter is additionally scaled by considering only the percentage of surface area with a direct connection to the open pore space. A comparison with calculated estimates for the reactive surface area (RSA) of the calcite cement shows that the introduced fluid-accessible geometric calcite surface area ($GSA_{Cc,open}$) is within the expected range of values for three out of four core samples, and thus can provide a robust estimation capability for accessible mineral surfaces in complex low-permeable rocks.

By normalizing the total core dissolution rates to $GSA_{Cc,open}$ it is shown that the effective differences between both experimental scales (µm-mm versus cm) range between 0.5 and 2 orders of magnitude, reflecting the limited transport efficiency within the core samples. Using the µXCT surface parameter $GSA_{Cc,open}$, the statistical rate information from the surface experiments is scaled up to the core samples. Especially for the long-term experiments, a good agreement with the measured dissolution rates with deviations between - 32 % and + 185 % is achieved. Based on the introduced key parameter $GSA_{Cc,open}$, the heterogeneity in mineral distribution and the accessibility of the reactive mineral phase is mapped. Thus, the predictability of mineral dissolution rates under natural (i.e., near-equilibrium) flow conditions can be significantly improved by the approach presented in Study 3.

While the 3D geometry of the calcite cement was well visible in the µXCT data sets in Study 3, the Flechtinger Sandstone also contains a comparatively high proportion of clay minerals, which are even below the resolution of synchrotron CT images. This fact is particularly relevant for flow simulations by Digital Rock Physics (DRP) concepts. Hence, in the related co-authored study in Chapter 5.3 (Jacob et al., 2021), the permeability influence by illite nanostructures is addressed. Classical Navier-Stokes simulations on CT data sets highly overestimate the rock permeability in comparison to helium gas-driven measurements. In order to consider the sub-resolution clay mineral structures within the digital rock models, these nanostructures are analyzed by means of focussed ion beam scanning electron microscopy (FIB-SEM) and characterized with regard to their permeability. In the next step, microporous voxels are incorporated into the existing CT data sets, according to the spatial distribution of illites occurring as quartz and feldspar grain coatings in the sandstone samples. By applying Navier-Stokes-Brinkman simulations on these modified CT data sets, the permeability misestimation of + 814 % is reduced to - 35 %.

6.2 Perspectives and outlook

6.2.1 Coupled hydraulic-mechanical processes in fractured rocks

Studies 1 and 2 (Chapters 2 and 3) of this thesis clearly confirm the validity of different methods and measuring devices and their suitability for a broad application in the geoscientific community. Nevertheless, there is still potential for optimization and further development.

(i) Method optimization

The presented methodical approach for the on-site characterization of the EDZ in the Mont Terri rock laboratory can easily be transferred to other rocks or fields of application. For example, the usability of the portable devices for extended face mapping in tunneling could be explored. To ensure a reliable determination of fracture and matrix parameters for different geological settings, the following optimization approaches are suggested.

Within the scope of this thesis, the air permeameter was only used for low-permeable rocks (~ 10^{-15} – 10^{-20} m²) (e.g., Blöcher et al., 2009; Heidsiek et al., 2020; Jaeggi and Bossart, 2014). To determine a_h for fractures embedded in high-permeable rocks, the influence of enhanced matrix permeability on the response function of the air permeameter should be systematically examined. It should be checked whether an additional correction factor has to be implemented for such rocks in order to avoid an overestimation of a_h. For optimizing the automatic evaluation approach of the digital microscope camera images using the developed MATLAB code, the threshold value that is required as an input parameter for segmenting the void area could be calibrated for different camera brightness settings and rock colors, e.g., by using different parallel-plate and rough-walled test fractures. Furthermore, the influence of fracture plane inclination (relative to the rock surface) on the quantification of a_m and the relative roughness could be addressed. For the NPT, empirical equations for parameter estimation are already available (cf. Chapter 3.2.4), but represent a variety of different materials (e.g., Aydan, 2012; Aydan et al., 2014; Ulusay and Erguler, 2012). Hence, a rock-specific calibration with measured laboratory values would improve the accuracy of the estimation of physico-mechanical rock parameters by the NPT. Furthermore, the results of the measurement campaign in Mont Terri also suggest that a linear relationship between the needle penetration index and the water content may also be established.

(ii) Building geodatabases

In order to compile field data acquired by air permeameter, microscope camera and needle penetrometer, but also to enable a widespread distribution of such data for reservoir and host rock formations, it is recommended to establish publicly accessible geodatabases. Here, on-site determinable fracture and matrix parameters should ideally be complemented with laboratory data on hydraulic and mechanical rock parameters (e.g., porosity-permeability relations) or chemical parameters (e.g., experimental reaction rates). It would be desirable to provide a comprehensive database for a large number of lithologies and study sites, which could be used by the scientific community, for example, for setting up 3D geological models.

(iii) Design and protocol development for a comprehensive hydraulic-mechanical drill core analysis

The measurement and evaluation methods presented in Studies 1 and 2 could be combined to develop a protocol for a holistic and practical analysis of fractured drill core samples. As a first step in such a proposed workflow, the surface morphology of the disjoint fracture surfaces could be captured by the 3D laser scanner. In this context, markers or reference points could optionally be placed on both sample halves (e.g., Guo et al., 2020; Tatone and Grasselli, 2013). By optically or tactilely recording these reference coordinates in the open and closed state, the relative position of the two fracture surfaces in the closed state could be reconstructed by applying a coordinate transformation operation (e.g., Davis et al., 1997). This enables to generate a digital image of the fracture void structure (e.g., for flow simulations, see point (iv)). For evaluating the 3D fracture roughness, the raw data (3D point cloud) could be transformed into a pgm image for the MATLAB algorithm presented in Chapter 5.2 to automatically quantify the change probability and the scale-dependent Hurst exponent.

Subsequently, the sample could be installed in a custom-made sample holder that fixes the drill core segments and additionally offers the possibility to apply a defined axial pressure. One major limitation of Study 1 was that the pressure applied onto the sample block could only be estimated (cf. Chapter 2.2.1). Microscope camera and air permeameter measurements along accessible fracture profiles would allow to quantify the mechanical and hydraulic fracture aperture distribution within the sample, and needle penetration tests could additionally be used for the estimation of mechanical and geophysical rock parameters. These measurements could be repeated for evaluating the pressure-dependent aperture change by gradually increasing the axial pressure. Furthermore, to analyze the fracture closure behavior for high lithostatic pressures, the acquired 3D fracture data could be used as input for mechanical contact models, such as the elastic-plastic deformation model used by Kling et al. (2018), which is applicable for an initial pre-loading of ≥ 0.25 MPa, or for fully-coupled hydraulic-mechanical models (e.g., Vogler et al., 2018; von Planta et al., 2019). Thus, as a last step in this proposed workflow, the normal fracture closure and reduction of a_m and a_h with increasing overburden could be simulated, either for the original sampling depth or for specific pressure conditions.

(iv) Parametrization and validation of fracture models

Single fracture models for analyzing stress-dependent fluid flow often operate on mechanical aperture fields (e.g., He et al., 2021; Kling et al., 2018; Nemoto et al., 2009). Although laser scanning techniques are frequently utilized to generate realistic model geometries, there is still a need for optimization when matching the two digital fracture surfaces, as the percentage of contact area is difficult to quantify. In many studies, a geometric best fit alignment with a fixed number of contact points is used (e.g., Kling et al., 2018; Vogler et al., 2018). However, measurement uncertainties and errors can result in negative apertures due to local intersections of the two fracture surfaces, which necessarily have to be re-defined as contact area. In this context, the microscope camera could be used as a calibration tool for performance evaluation or even for the development of new matching algorithms for digitized fracture surfaces. Analogously, the air permeameter could be used for the validation of subsequent fluid flow simulations (e.g., Javanmard et al., 2021; Vogler et al., 2016).

For simulating coupled processes in fracture networks by stochastic discrete fracture network (DFN) models, in most cases simple statistical parameters such as arithmetic mean or standard deviation are employed for aperture parametrization (e.g., Lei et al., 2017; Ren et al., 2017; Zhou et al., 2021). However, the use of statistical probability distributions for a_m or a_h would more realistically reflect the properties of a fracture network. Due to their highly efficient measurement principle, the portable devices shown are particularly suited for obtaining a reliable statistical description of fracture apertures. In this context, another link would be to study the variability in aperture distributions of natural fractures, as normal distributions are often observed or applied to DFN models (e.g., Pyrak-Nolte et al., 1997; Stoll et al., 2019; Zhou et al., 2021). In contrast, the investigated bedding joint in the Flechtinger Sandstone can be better described by a log-normal aperture distribution. By collecting large amounts of data using the portable instruments, it would be feasible to test the dependence of the aperture distribution on the lithology or the formation process.

6.2.2 Coupled hydraulic-chemical processes in porous rocks

Study 3 (Chapter 4) focuses on the articulated dissolution of the calcite cement in a low-permeable reservoir analog. This example system serves as a meaningful starting point to address some aspects in more detail.

(i) Analysis of further rate-influencing factors on the µm-mm- and cm-scale

The surface dissolution experiments on the µm-mm-scale (Study 3) reveal an apparent decrease of the averaged rates along the flow direction (cf. Chapter 4.3.1). Due to the minimal hydraulic residence time (HRT) of the reactive fluid, a pure pH effect is unlikely. This phenomenon could be investigated by further micro-cell experiments, for example by applying a successive increase in HRT and analyzing the effect on the surface dissolution rates. With regard to the core experiments (cm-scale), the possible influence of certain sample properties such as initial permeability and calcite cluster size distribution on the rate variability is discussed (cf. Chapter 4.3.3). This could be addressed by a sensitivity study based on a reactive transport model, with feasibility primarily constrained by the available computational power. In principle, this could be realized using the numerical approach discussed under point (v).

(ii) Consideration of further sample sizes and types

To further understand the linkage between calcite dissolution on the µm- and the cm-scale, the inclusion of intermediate sample sizes between the two scales under investigation would be a useful next step, i.e., dissolution experiments on mini- or micro-plugs (e.g., Ivanov et al., 2021; Qajar and Arns, 2016). Such downscaled flow-through experiments with the same reactive fluid under variable conditions with respect to the calcite equilibrium state (i.e., $f(\Delta G)$) represent a logical extension of the data set presented in Study 3. Due to a reduced sample size and, thus, a reduced HRT of the fluid within the sample, the intensity of pH buffering would be more controllable, also allowing to obtain dissolution rates in the intermediate $f(\Delta G)$ value range. Furthermore, long-term percolation experiments with larger core diameters in the dm-scale (e.g., 10 cm) would also extent the existing data set. By modifying the permeability cells presented in Chapter 4.2.2.2, this could be technically implemented with little effort. For example, the influence of stratification and heterogeneity in calcite cement distribution (e.g., Heidsiek et al., 2020) on the effective core rates could be studied in more detail.

Due to the heterogeneity and complex mineralogy of the Flechtinger Sandstone, many influencing factors exist, whose interaction is partly unclear. Combining reactive flow-through experiments on core plugs with tracer tests would be a possibility to determine further transport properties (e.g., diffusion, dispersivity). To create simpler and more controllable initial conditions, flow-through experiments on synthetic sandstones (e.g., Costa et al., 2017; Liu et al., 2017), composed of quartz, calcite and possibly illite, are also recommended.

(iii) Extended studies on the concept of fluid-accessible surface area

In Study 3, the fluid-accessible geometric calcite surface area is quantified by using a purely geometrical approach to identify the connected pore network and the adjacent calcite surfaces (cf. Chapter 4.2.3.3). In this context, fluid flow simulations on the segmented CT data sets of the core plugs (e.g., Jacob et al., 2021, 2019) would provide the opportunity to estimate the flow-effective portion of the segmented pore space even more precisely.

Since only small calcite volumes were dissolved in the core experiments under near-equilibrium conditions, a comparatively small change in surface area with time was assumed in Study 3. However, an even better fit between the upscaled and measured dissolution rates could eventually be achieved by considering the temporal evolution of the calcite surface area in the sandstone cores. Other studies approve the possibility to track the mineral surface retreat with tomographic techniques, either in situ or ex situ (e.g., Al-Khulaifi et al., 2017; Menke et al., 2015; Pereira Nunes et al., 2016), but this approach is merely suitable for mineral surface retreats that are significantly larger than the voxel size. Alternatively, previously published empirical surface evolution models such as the geometrical sugar lump model (Noiriel et al., 2009) could be tested for their applicability to the poikilitic calcite cement, using $GSA_{Cc,open}$ as a starting value.

(iv) Relationship between calcite cement dissolution and porosity-permeability patterns

In light of a long-term reservoir usability, future research should also focus on the temporal evolution of porosity-permeability patterns in the Flechtinger Sandstone and particularly on the differences compared to pure carbonate rocks (e.g., marble, limestone), where various studies already exist (e.g., Al-Khulaifi et al., 2017; Gouze and Luquot, 2011; Luhmann et al., 2014; Pereira Nunes et al., 2016). However, since calcite only represents a reactive phase in the present case, a significant deviation of the porosity-permeability relationship is to be expected. Moreover, the high clay mineral content of the Flechtinger Sandstone also strongly contributes to permeability changes as a superimposed factor through mobilization and clogging effects (e.g., Gkay and Rex, 1966; Wilson et al., 2014) and must not be neglected.

(v) Simulation of core dissolution experiments using reactive transport models

Study 3 provides a comprehensive experimental data set that can be used for the validation of sophisticated, three-dimensional reactive transport models. For this purpose, the statistical rate information on the µm-mm-scale (Chapter 4.3.1) forms a basis to parameterize a representative rate spectrum for the calcite cement (e.g., Karimzadeh and Fischer, 2021) in a forward modelling approach. In further development of the presented approach with volume-averaged values for $GSA_{Cc,open}$ and the saturation index (cf. Chapter 4.3.5), the existing spatial variability of fluid velocities and saturation indices within the pore space of the core plugs should also be addressed in a numerical implementation. The same would be conceivable for the spatial distribution of fluid-accessible calcite surfaces, and possibly their orientation in relation to the direction of flow (e.g., Bouissonnié et al., 2018).

Since segmented µXCT data sets are available for all core plugs, numerical approaches based on such 3D structures would be the preferred option. For example, the application of particle tracking approaches (e.g., Hakoun et al., 2019; Puyguiraud et al., 2019) to the existing digital rock models of the core plugs would be a next logical step. Capturing the dynamics or statistics of particle velocities and the resulting hydrodynamic dispersion at the pore scale is considered a key point for the numerical upscaling of flow and transport processes to the Darcy scale (Puyguiraud et al., 2019).

(vi) Transferability to other mineral phases

Due to the segmentability of barite in the μXCT scans of the Flechtinger Sandstone samples (cf. Chapter 4.3.2.2) and the availability of measured barium concentrations from the flow-through experiments on core scale, the methodical approach of Study 3 can also be applied to this second mineral phase. By performing correlative surface dissolution experiments for barite (cf. Chapter 4.2.2.1), the concept of the fluid-accessible geometric surface area could also be tested for the upscaling of barite dissolution rates, before other lithologies with different pore space geometries would be considered in a next step.

6.2.3 Transfer to coupled hydraulic-chemical processes in fractured rocks

By combining the high-pressure percolation setup described in Chapter 4.2.2.3 with the concept of change probability presented in Chapter 5.2, coupled hydraulic-chemical processes in fractured core samples of the Flechtinger Sandstone could also be addressed. Based on a parallel (time-dependent) change probability analysis, the effect of selective mineral dissolution at the fracture surface on its 3D surface morphology and roughness could be investigated.

Using the same methodological approach, reactive transport experiments with fractured carbonate samples would also be possible, for example in the context of karst conduit formation and evolution (e.g., Dreybrodt, 2012; Ford and Williams, 2013; Goldscheider et al., 2020). Such coupled HC experiments could primarily focus on the temporal change of the fluid transport behavior within the discontinuity due to an increase in aperture and surface roughness alteration, as well as the feedback of these influencing factors on further dissolution processes in the fracture (e.g., Detwiler et al., 2003; Durham et al., 2001; Hanna and Rajaram, 1998; Wang et al., 2021).

APPENDICES

Appendix A

This Appendix refers to Study 2 (Chapter 3). The following content was published in the journal Solid Earth.

The literature data included in Figure 3.6 (Chapter 3.3.2) were mainly taken from Jaeggi and Bossart (2014). This expert report offers a compilation of safety related rock parameters determined for the Opalinus Clay in the Mont Terri URL. All source documents for experimentally derived data on geomechanical and geophysical properties that were utilized in this study are listed in Table A1. Technical Notes (TN) and Technical Reports (TR) of the Mont Terri Project are accessible via https://www.mont-terri.ch/en/documentation/technical-reports.html.

Table A1: Source documents for experimental data on uniaxial compressive strength (UCS), Brazilian tensile strength (BTS), Young´s modulus (E) and elastic P-wave (v_P) and S-wave velocity (v_S) of the Opalinus Clay (shaly facies) in Mont Terri.

Source document	UCS	BTS	E	v_P	v_S
Amann et al. (2011)	●		●	●	
Amann et al. (2012)				●	
Gräsle and Plischke (2010), TR	●	●	●		●
Gräsle and Plischke (2011), TN				●	
Jahns (2010), TN	●	●			
Rummel and Weber (2004), TN	●			●	
Rummel and Weber (2007), TN	●			●	
Schnier and Stührenberg (2007), TR	●				●
Soe et al. (2009)					●
Wild (2010) [a]		●			
Wild et al. (2015)	●	●	●	●	
Wileveau (2005), TR				●	●
Wymann (2013) [a]	●		●	●	
Zimmer (2012) [a]		●		●	

[a] Unpublished final theses, ETH Zurich, Switzerland

Code and data availability: All field data related to this study and the MATLAB code for the evaluation of microscopic fracture trace images are available at https://doi.org/10.6084/m9.figshare.12581144.v2 (Hale et al., 2020b).

Appendix B

This Appendix refers to Study 3 (Chapter 4). The following content was submitted as Supplementary Information (SI) to the journal Environmental Earth Sciences.

Supplementary information related to the µm- to mm-scale

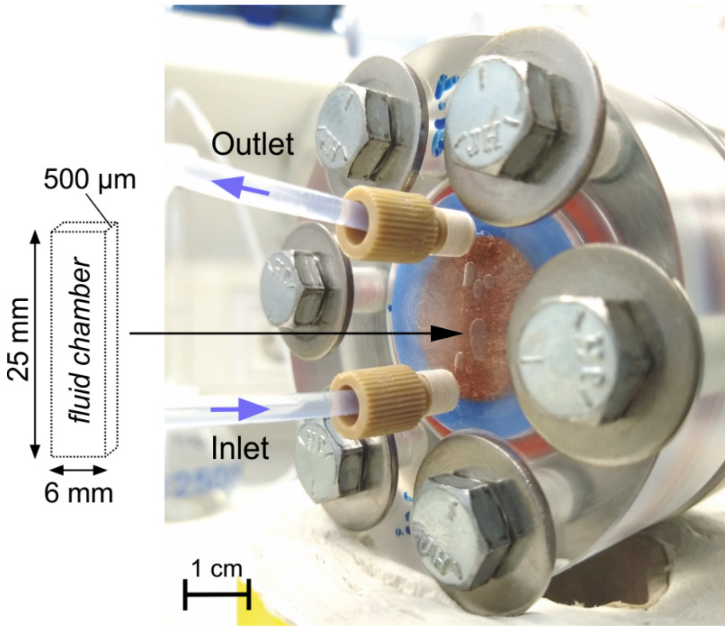

Figure B1: Photo of the closed micro-cell while running. The mounted sandstone sample slice (diameter 2.54 cm) was embedded in semi-transparent resin and polished. The fluid is circulating on top of the core sample slice through the fluid chamber (size indicated).

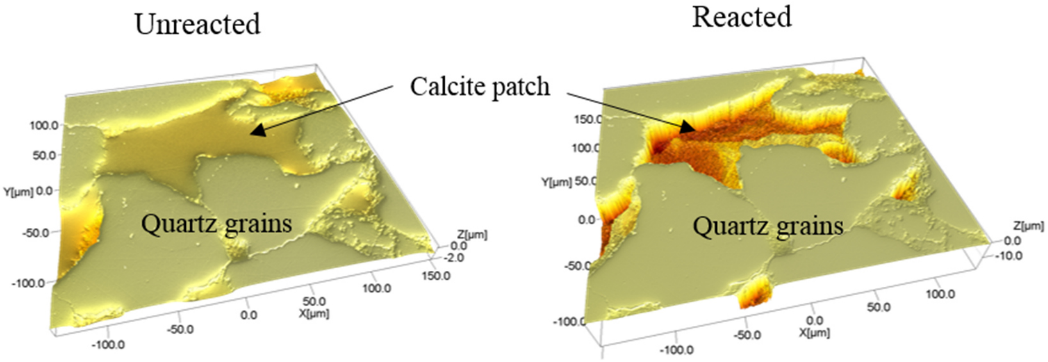

Figure B2: Example of the topography maps measured by vertical scanning interferometry (VSI), showing the retreat of a calcite patch located in between several quartz grains before and after a dissolution experiment.

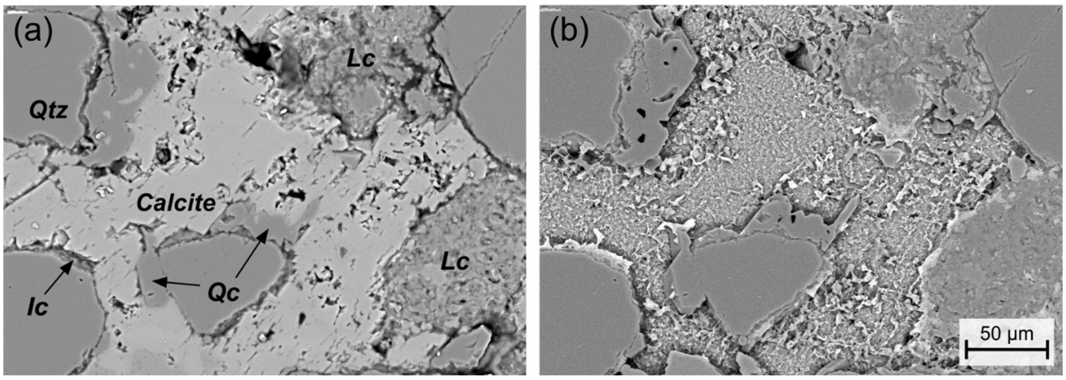

Figure B3: Backscattered electron images of (a) the unreacted sandstone sample surface showing the calcite cement surrounded by grains of quartz (Qtz), quartz cement (Qc), clay-rich lithoclasts (Lc) and illite coatings; (b) the same surface after 120 min reacted with the NaCl/HCl solution (pH 4.0).

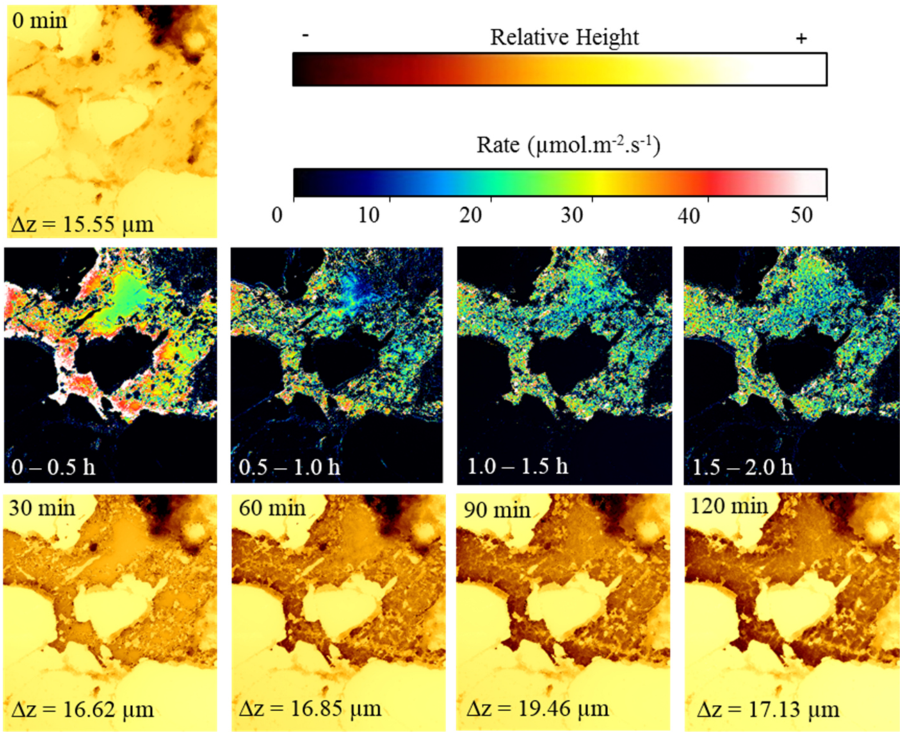

Figure B4: Surface topography and rate maps of calcite cement patch m1. Map size is 267 × 296 µm².

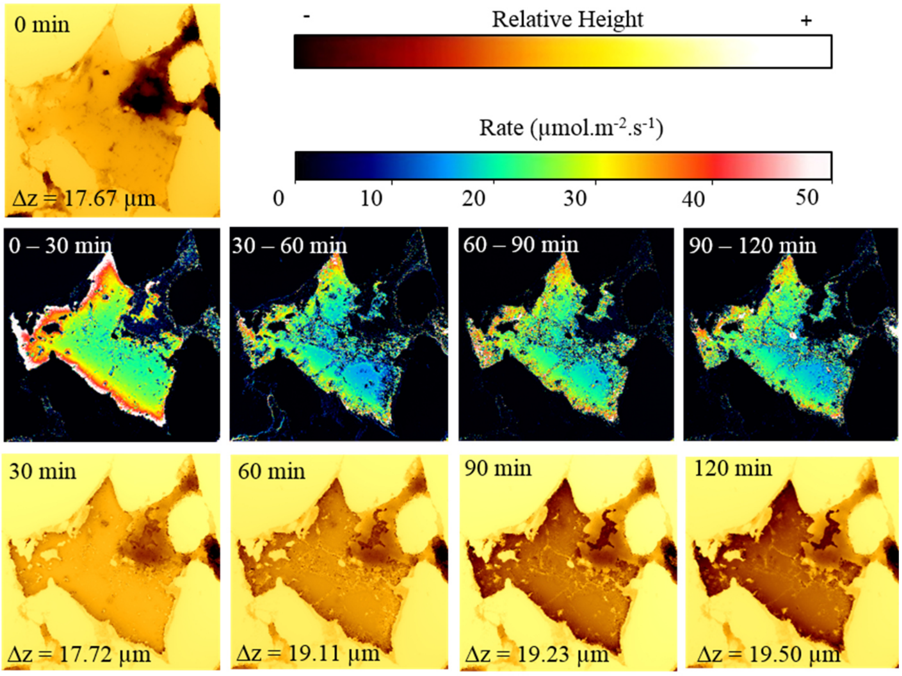

Figure B5: Surface topography and rate maps of calcite cement patch m2. Map size is 283 × 281 µm².

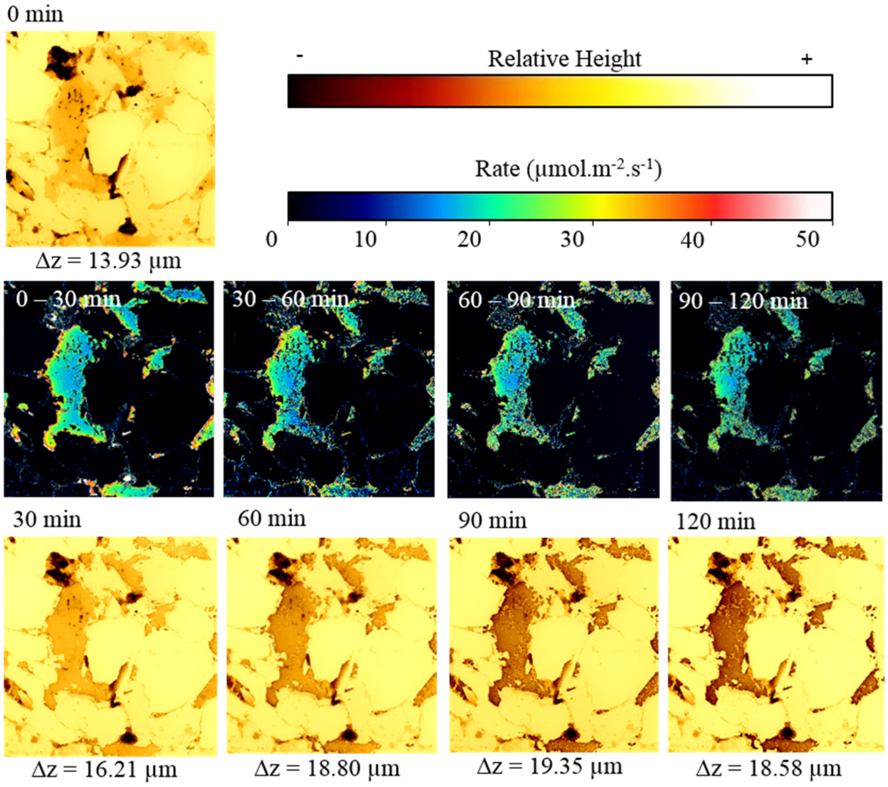

Figure B6: Surface topography and rate maps of calcite cement patch m3. Map size is 720 × 740 µm².

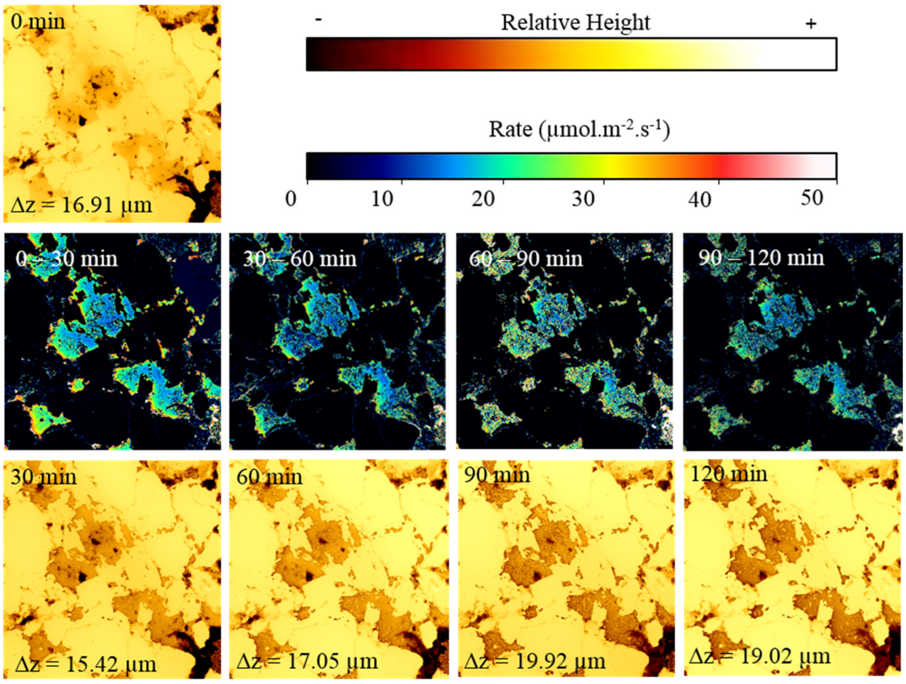

Figure B7: Surface topography and rate maps of calcite cement patch m4. Map size is 282 × 268 µm².

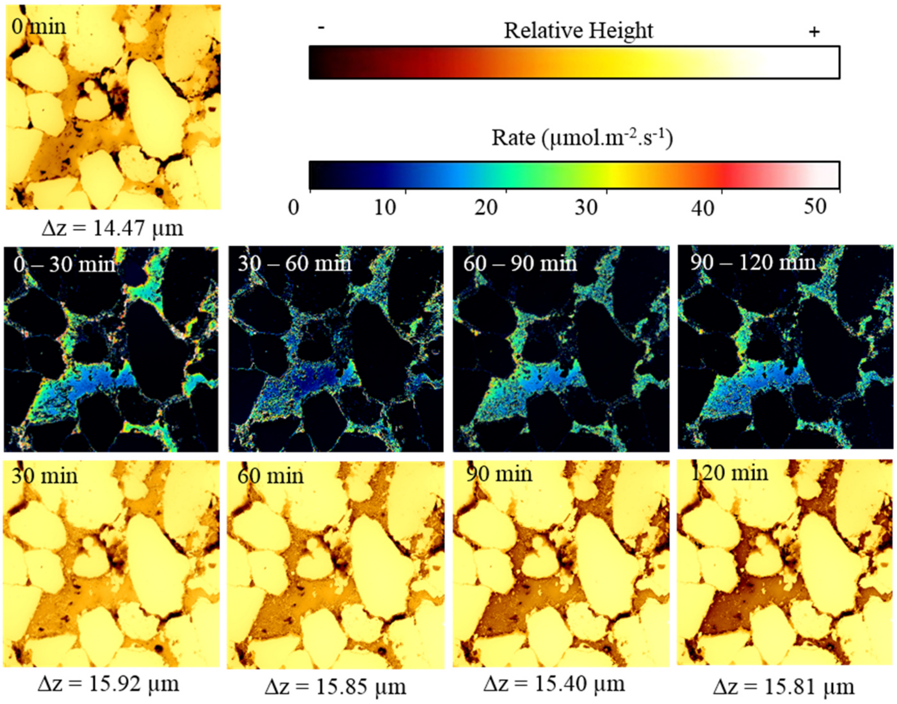

Figure B8: Surface topography and rate maps of calcite cement patch m5. Map size is 282 × 268 µm².

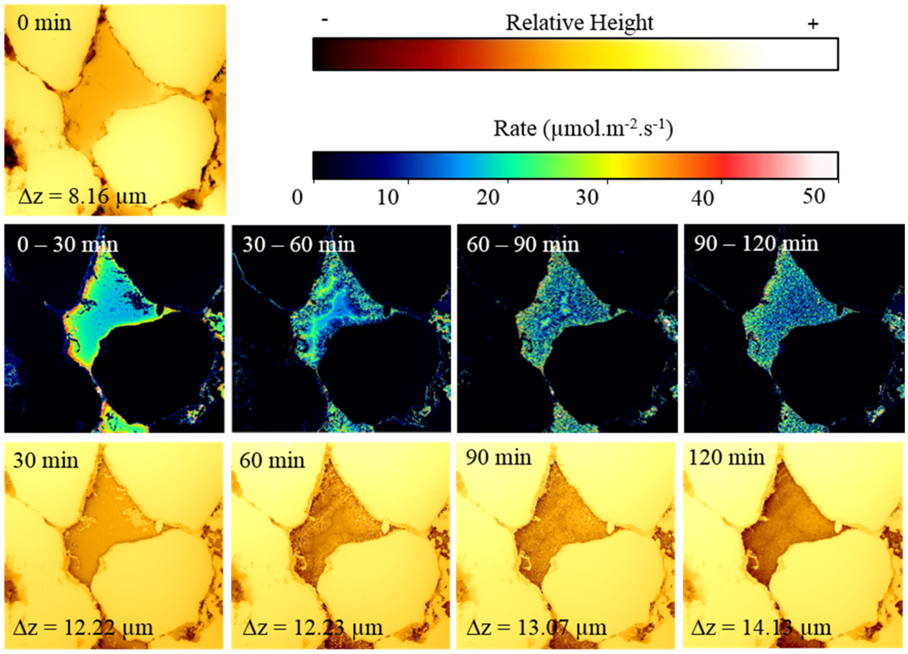

Figure B9: Surface topography and rate maps of calcite cement patch m6. Map size is 754 × 718 µm².

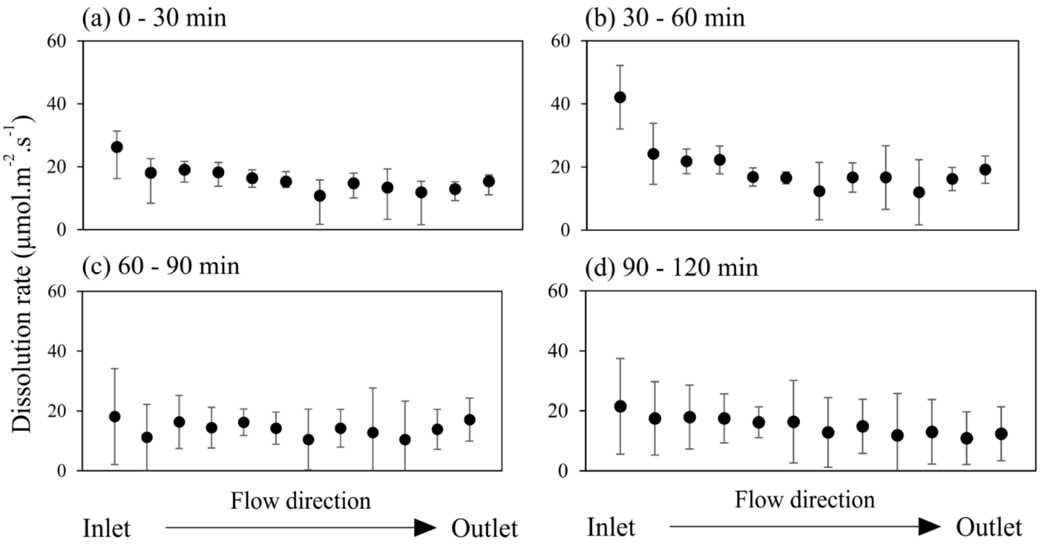

Figure B10: Average dissolution rate and standard deviation for all areas of interest within the investigated calcite cement patches, ordered by their relative position inside the fluid cell (cf. Figure 4.3a).

Supplementary information related to the cm-scale

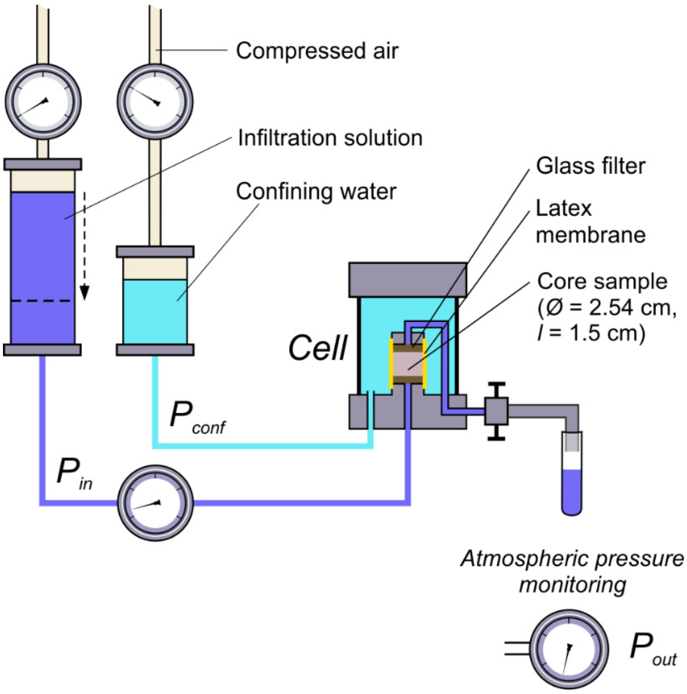

Figure B11: Setup of the flow-through experiment with the triaxial permeability cell under low differential pressure (< 0.5 bar) and ambient conditions.

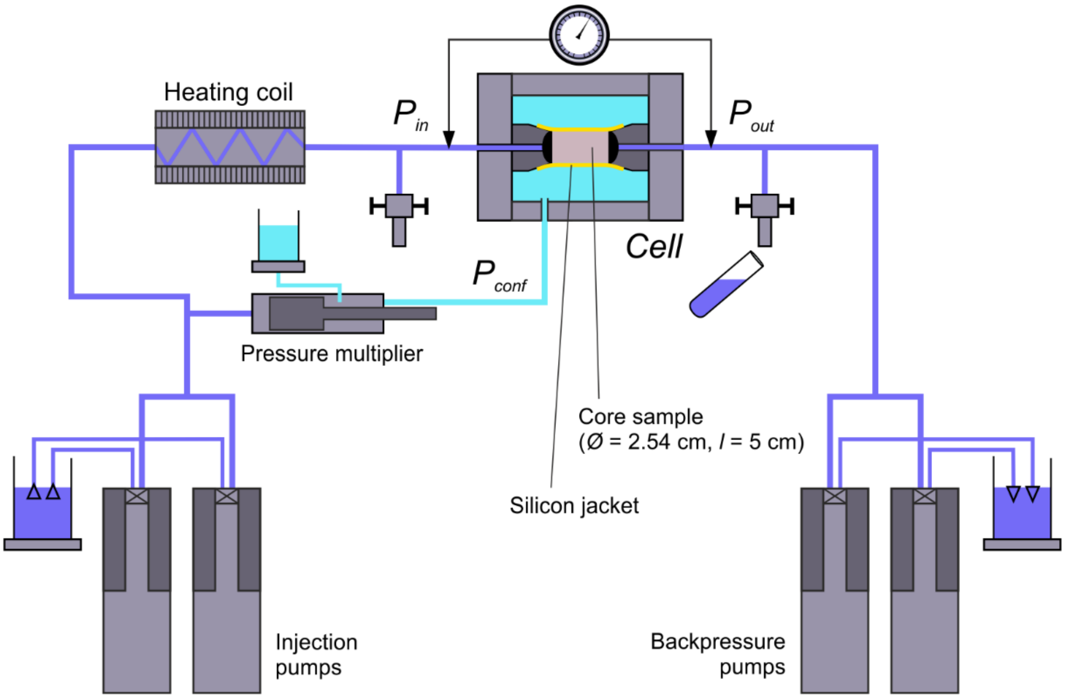

Figure B12: Flow-through autoclave ICARE4 for percolation experiments under elevated differential pressure (1 – 20 bar) and back pressure (> 50 bar).

In order to assess the relative significance of reaction and transport in the core experiments, a core-scale Damköhler number was determined analogously to Salehikhoo et al. (2013) using the relation

$$Da = \frac{\tau_{adv}}{\tau_{react}} = \frac{HRT \cdot r_{Cc,total}}{V_P \cdot C_{Ca,eq}},$$

with $r_{Cc,total}$ the total calcite dissolution rate (in mol s^{-1}), HRT the hydraulic residence time of the fluid, V_P the pore volume of the sample and $C_{Ca,eq}$ the calcium equilibrium concentration calculated with PHREEQC (1.8×10^{-4} mol L^{-1}). Essentially, the hydraulic residence time of the fluid is compared to the time required for the entire core to approach equilibrium. A low Damköhler number indicates that the reaction is slow in comparison to the fluid transport through the sample, whereas a high Damköhler number indicates a local equilibrium regime.

The Peclet number is also a dimensionless parameter and indicates the relative significance of advective and diffusive transport by

$$Pe = \frac{Q \cdot L}{\phi_{open} \cdot S \cdot D_m}.$$

Here, Q denotes the volumetric flow rate, ϕ_{open} the open porosity, S the sample cross-section area and D_m the molecular diffusion coefficient of calcium (7.50×10^{-10} m^2 s^{-1}) (Luquot and Gouze, 2009). For the characteristic length L, the typical pore diameter of the sandstone (10^{-6} m) was used (cf. Jacob et al., 2021).

Table B1: Calculated Peclet and Damköhler numbers and required experimental parameters.

Sample	HRT **[s]**	V_P **[L]**	$r_{Cc,total}$ **[mol s^{-1}]**	Q **[m^3 s^{-1}]**	ϕ_{open} **[-]**	S **[m^2]**	Pe **[-]**	Da **[-]**
E6	382	3.4×10^{-3}	1.3×10^{-9}	8.9×10^{-9}	0.135	5.0×10^{-4}	0.1754	0.83
F11	1848	9.1×10^{-5}	1.9×10^{-11}	6.0×10^{-11}	0.011	5.2×10^{-4}	0.0139	2.11
C14	17050	3.5×10^{-4}	1.3×10^{-11}	2.1×10^{-11}	0.046	5.2×10^{-4}	0.0012	3.66
G12	26845	6.4×10^{-4}	1.7×10^{-11}	3.0×10^{-11}	0.081	5.2×10^{-4}	0.0010	3.95
Micro-cell	3.8			2.0×10^{-8}	1.00	3.0×10^{-6}	8.8889	

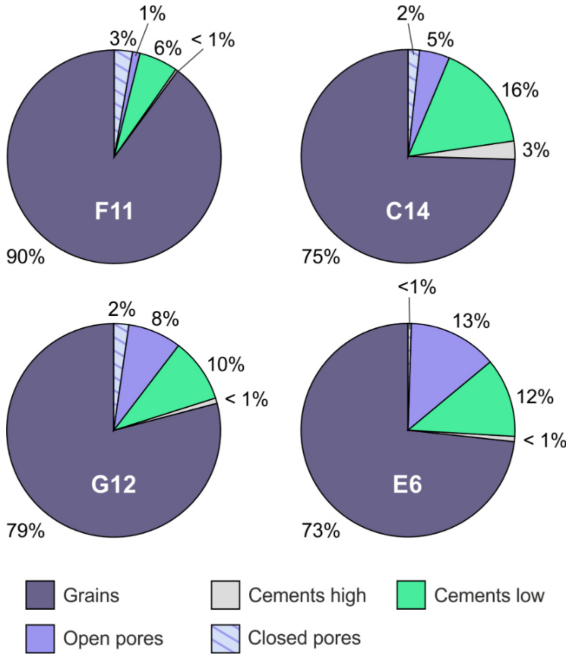

Figure B13: Volumetric fractions of the phases identified by X-ray micro-computed tomography (µXCT) imaging of the different core plugs. The calcite cement of the sandstone is represented by the phase “Cements low”. The phase “Pores” is subdivided into open and closed pore space. The highly absorbing cement phase (“Cements high”) contains various mineral phases, e.g., barite, hematite and amorphous oxides.

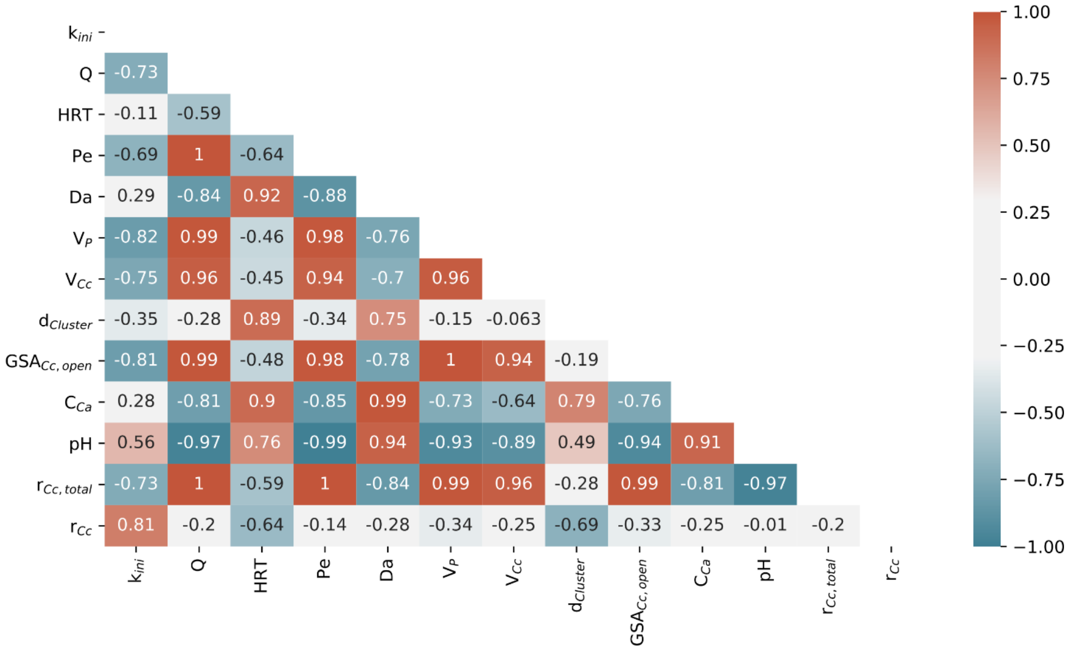

	k_{ini}	Q	HRT	Pe	Da	V_P	V_{Cc}	$d_{Cluster}$	$GSA_{Cc,open}$	C_{Ca}	pH	$r_{Cc,total}$	r_{Cc}
k_{ini}													
Q	-0.73												
HRT	-0.11	-0.59											
Pe	-0.69	1	-0.64										
Da	0.29	-0.84	0.92	-0.88									
V_P	-0.82	0.99	-0.46	0.98	-0.76								
V_{Cc}	-0.75	0.96	-0.45	0.94	-0.7	0.96							
$d_{Cluster}$	-0.35	-0.28	0.89	-0.34	0.75	-0.15	-0.063						
$GSA_{Cc,open}$	-0.81	0.99	-0.48	0.98	-0.78	1	0.94	-0.19					
C_{Ca}	0.28	-0.81	0.9	-0.85	0.99	-0.73	-0.64	0.79	-0.76				
pH	0.56	-0.97	0.76	-0.99	0.94	-0.93	-0.89	0.49	-0.94	0.91			
$r_{Cc,total}$	-0.73	1	-0.59	1	-0.84	0.99	0.96	-0.28	0.99	-0.81	-0.97		
r_{Cc}	0.81	-0.2	-0.64	-0.14	-0.28	-0.34	-0.25	-0.69	-0.33	-0.25	-0.01	-0.2	

Figure B14: Correlation matrix including thirteen different parameters related to the fluid transport conditions, the calcite cement accessibility and geometry, and the calcite dissolution kinetics in the flow-through experiments on the core-scale. The numbers specify the Pearson correlation coefficient between two variables (k_{ini} = initial sample permeability, Q = volumetric flow rate, HRT = hydraulic residence time, Pe = Peclet number, Da = Damköhler number, V_P= pore volume, V_{Cc} = calcite volume, $d_{Cluster}$ = median calcite cluster diameter, $GSA_{Cc,open}$ = geometric calcite surface area in contact to the open pore space, C_{Ca} = calcium concentration, pH = outlet pH, $r_{Cc,total}$ = total dissolution rate, r_{Cc} = surface-normalized dissolution rate).

BACK MATTER

References

Alcolea, A., Kuhlmann, U., Marschall, P., Lisjak, A., Grasselli, G., Mahabadi, O., de La Vaissière, R., Leung, H., Shao, H., 2017. A pragmatic approach to abstract the excavation damaged zone around tunnels of a geological radioactive waste repository: application to the HG-A experiment in Mont Terri. Geological Society, London, Special Publications 443, 127–147. https://doi.org/10.1144/SP443.8

Alcoverro, J., Olivella, S., Alonso, E.E., 2014. Modelling fluid flow in Opalinus Clay excavation damage zone. A semi-analytical approach. Geological Society, London, Special Publications 415, 143–166. https://doi.org/10.1144/SP415.7

Al-Khulaifi, Y., Lin, Q., Blunt, M.J., Bijeljic, B., 2017. Reaction Rates in Chemically Heterogeneous Rock: Coupled Impact of Structure and Flow Properties Studied by X-ray Microtomography. Environmental Science & Technology 51, 4108–4116. https://doi.org/10.1021/acs.est.6b06224

Altenbockum, M., Berens, K., Enzmann, F., Kersten, M., Rüde, T.R., Wieber, G.H.E., 2018. Fallbeispiel Kluftgrundwasserleiter – Charakterisierung eines Grundwasserleiters im Rotliegendsandstein des Saar-Nahe-Beckens. Grundwasser 23, 177–187. https://doi.org/10.1007/s00767-017-0380-1

Amadei, B., Illangasekare, T., 1994. A Mathematical Model for Flow and Solute Transport in Non-homogeneous Rock Fractures. International Journal of Rock Mechanics and Mining Sciences & Geomechanics Abstracts 31, 719–731. https://doi.org/10.1016/0148-9062(94)90011-6

Amann, F., Button, E.A., Evans, K.F., Gischig, V.S., Blümel, M., 2011. Experimental Study of the Brittle Behavior of Clay shale in Rapid Unconfined Compression. Rock Mechanics and Rock Engineering 44, 415–430. https://doi.org/10.1007/s00603-011-0156-3

Amann, F., Kaiser, P., Button, E.A., 2012. Experimental Study of Brittle Behavior of Clay Shale in Rapid Triaxial Compression. Rock Mechanics and Rock Engineering 45, 21–33. https://doi.org/10.1007/s00603-011-0195-9

Amann, F., Wild, K.M., Loew, S., Yong, S., Thoeny, R., Frank, E., 2017. Geomechanical behaviour of Opalinus Clay at multiple scales: results from Mont Terri rock laboratory (Switzerland). Swiss Journal of Geosciences 110, 151–171. https://doi.org/10.1007/s00015-016-0245-0

Amos, R.T., Mayer, K.U., Blowes, D.W., Ptacek, C.J., 2004. Reactive Transport Modeling of Column Experiments for the Remediation of Acid Mine Drainage. Environmental Science & Technology 38, 3131–3138. https://doi.org/10.1021/es0349608

Andra, 2005. Dossier 2005 Argile - Phenomenological Evolution of a Geological Repository. Agence Nationale pour la Gestion des Déchets Radioactifs, Paris, France.

Aoyagi, K., Ishii, E., 2019. A Method for Estimating the Highest Potential Hydraulic Conductivity in the Excavation Damaged Zone in Mudstone. Rock Mechanics and Rock Engineering 52, 385–401. https://doi.org/10.1007/s00603-018-1577-z

Apted, M.J., Ahn, J., 2010. Multiple-barrier geological repository design and operation strategies for safe disposal of radioactive materials, in: Ahn, J., Apted, M.J. (Eds.), Geological Repository Systems for Safe Disposal of Spent Nuclear Fuels and Radioactive Waste, Woodhead Publishing Series in Energy. Woodhead Publishing, pp. 3–28. https://doi.org/10.1533/9781845699789.1.3

Armand, G., Leveau, F., Nussbaum, C., de La Vaissiere, R., Noiret, A., Jaeggi, D., Landrein, P., Righini, C., 2014. Geometry and Properties of the Excavation-Induced Fractures at the Meuse/Haute-Marne URL Drifts. Rock Mechanics and Rock Engineering 47, 21–41. https://doi.org/10.1007/s00603-012-0339-6

Arvidson, R.S., Ertan, I.E., Amonette, J.E., Luttge, A., 2003. Variation in calcite dissolution rates: A fundamental problem? Geochimica et Cosmochimica Acta 67, 1623–1634. https://doi.org/10.1016/S0016-7037(02)01177-8

Arvidson, R.S., Morse, J.W., 2014. Formation and Diagenesis of Carbonate Sediments, in: Mackenzie, F.T. (Ed.), Sediments, Diagenesis and Sedimentary Rocks: Treatise on Geochemistry. Elsevier, Oxford, pp. 61–101. https://doi.org/10.1016/B978-0-08-095975-7.00703-8

Asadi, M.S., Rasouli, V., Barla, G., 2013. A Laboratory Shear Cell Used for Simulation of Shear Strength and Asperity Degradation of Rough Rock Fractures. Rock Mechanics and Rock Engineering 46, 683–699. https://doi.org/10.1007/s00603-012-0322-2

Aydan, Ö., 2012. The inference of physico-mechanical properties of soft rocks and the evaluation of the effect of water content and weathering on their mechanical properties from needle penetration tests. Presented at the 46th US Rock Mechanics/Geomechanics Symposium, American Rock Mechanics Association, Chicago, Illinois.

Aydan, Ö., Sato, A., Yagi, M., 2014. The Inference of Geo-Mechanical Properties of Soft Rocks and their Degradation from Needle Penetration Tests. Rock Mechanics and Rock Engineering 47, 1867–1890. https://doi.org/10.1007/s00603-013-0477-5

Aydin, A., 2009. ISRM Suggested method for determination of the Schmidt hammer rebound hardness: Revised version. International Journal of Rock Mechanics & Mining Sciences 46, 627–634. https://doi.org/10.1016/j.ijrmms.2008.01.020

Bachu, S., Adams, J.J., 2003. Sequestration of CO2 in geological media in response to climate change: capacity of deep saline aquifers to sequester CO2 in solution. Energy Conversion and Management 44, 3151–3175. https://doi.org/10.1016/S0196-8904(03)00101-8

Baechler, S., Lavanchy, J.M., Armand, G., Cruchaudet, M., 2011. Characterisation of the hydraulic properties within the EDZ around drifts at level −490m of the Meuse/Haute-Marne URL: A methodology for consistent interpretation of hydraulic tests. Physics and Chemistry of the Earth, Parts A/B/C 36, 1922–1931. https://doi.org/10.1016/j.pce.2011.10.005

Bandis, S.C., Lumsden, A.C., Barton, N.R., 1983. Fundamentals of rock joint deformation. International Journal of Rock Mechanics and Mining Sciences & Geomechanics Abstracts 20, 249–268. https://doi.org/10.1016/0148-9062(83)90595-8

Barton, N., 1982. Modelling rock joint behavior from in situ block tests: implications for nuclear waste repository design. Office of Nuclear Waste Isolation, Battelle Project Management Division, Columbus, Ohio.

Barton, N., 1973. Review of a new shear-strength criterion for rock joints. Engineering Geology 7, 287–332. https://doi.org/10.1016/0013-7952(73)90013-6

Barton, N., 1972. A model study of air transport from underground openings situated below groundwater level. Percolation Through Fissured Rock, Proceedings of an International Symposium on Rock Mechanics, Stuttgart, Paper T3-A.

Barton, N., Bandis, S., Bakhtar, K., 1985. Strength, deformation and conductivity coupling of rock joints. International Journal of Rock Mechanics and Mining Sciences & Geomechanics Abstracts 22, 121–140. https://doi.org/10.1016/0148-9062(85)93227-9

Barton, N., Choubey, V., 1977. The shear strength of rock joints in theory and practice. Rock Mechanics 10, 1–54. https://doi.org/10.1007/BF01261801

Barton, N., de Quadros, E.F., 1997. Joint aperture and roughness in the prediction of flow and groutability of rock masses. International Journal of Rock Mechanics and Mining Sciences 34, Paper No. 252. https://doi.org/10.1016/S1365-1609(97)00081-6

Bastiaens, W., Bernier, F., Li, X.L., 2007. SELFRAC: Experiments and conclusions on fracturing, self-healing and self-sealing processes in clays. Physics and Chemistry of the Earth, Parts A/B/C 32, 600–615. https://doi.org/10.1016/j.pce.2006.04.026

Beckingham, L.E., Mitnick, E.H., Steefel, C.I., Zhang, S., Voltolini, M., Swift, A.M., Yang, L., Cole, D.R., Sheets, J.M., Ajo-Franklin, J.B., DePaolo, D.J., Mito, S., Xue, Z., 2016. Evaluation of mineral reactive surface area estimates for prediction of reactivity of a multi-mineral sediment. Geochimica et Cosmochimica Acta 188, 310–329. https://doi.org/10.1016/j.gca.2016.05.040

Beer, A.J., Stead, D., Coggan, J.S., 2002. Technical note. Estimation of the Joint Roughness Coefficient (JRC) by Visual Comparison. Rock Mechanics and Rock Engineering 35, 65–74. https://doi.org/10.1007/s006030200009

Bernier, F., Li, X.L., Bastiaens, W., Ortiz, L., Van Geet, M., Wouters, L., Frieg, B., Blümling, P., Desrues, J., Viaggiani, G., Coll, C., Chanchole, S., De Greef, V., Hamza, R., Malinsky, L., Vervoort, A., Vanbrabant, Y., Debecker, B., Verstraelen, J., Govaerts, A., Wevers, M., Labiouse, V., Escoffier, S., Mathier, J.-F., Gastaldo, L., Bühler, Ch., 2007. SELFRAC: Fractures and self-healing within the excavation disturbed zone in clays. Final Technical Publishable Report EUR 22585, European Commission.

Bibi, I., Arvidson, R., Fischer, C., Lüttge, A., 2018. Temporal Evolution of Calcite Surface Dissolution Kinetics. Minerals 8, 256. https://doi.org/10.3390/min8060256

Bigi, S., Battaglia, M., Alemanni, A., Lombardi, S., Campana, A., Borisova, E., Loizzo, M., 2013. CO2 flow through a fractured rock volume: Insights from field data, 3D fractures representation and fluid flow modeling. International Journal of Greenhouse Gas Control 18, 183–199. https://doi.org/10.1016/j.ijggc.2013.07.011

Birkholzer, J., Houseworth, J., Tsang, C.-F., 2012. Geologic Disposal of High-Level Radioactive Waste: Status, Key Issues, and Trends. Annual Review of Environment and Resources 37, 79–106. https://doi.org/10.1146/annurev-environ-090611-143314

Birkholzer, J.T., Tsang, C.-F., Bond, A.E., Hudson, J.A., Jing, L., Stephansson, O., 2019. 25 years of DECOVALEX - Scientific advances and lessons learned from an international research collaboration in coupled subsurface processes. International Journal of Rock Mechanics and Mining Sciences 122, 103995. https://doi.org/10.1016/j.ijrmms.2019.03.015

Bjørlykke, K., Ramm, M., Saigal, G.C., 1989. Sandstone diagenesis and porosity modification during basin evolution. Geologische Rundschau 78, 243–268. https://doi.org/10.1007/BF01988363

Blechschmidt, I., Vomvoris, S., 2010. Underground research facilities and rock laboratories for the development of geological disposal concepts and repository systems, in: Ahn, J., Apted, M.J. (Eds.), Geological Repository Systems for Safe Disposal of Spent Nuclear Fuels and Radioactive Waste, Woodhead Publishing Series in Energy. Woodhead Publishing, pp. 82–118. https://doi.org/10.1533/9781845699789.1.82

Blöcher, G., Zimmermann, G., Milsch, H., 2009. Impact of Poroelastic Response of Sandstones on Geothermal Power Production. Pure and Applied Geophysics 166, 1107–1123. https://doi.org/10.1007/s00024-009-0475-4

Blowes, D.W., Ptacek, C.J., Jambor, J.L., Weisener, C.G., Paktunc, D., Gould, W.D., Johnson, D.B., 2014. The Geochemistry of Acid Mine Drainage, in: Holland, H.D., Turekian, K.K. (Eds.), Treatise on Geochemistry. Elsevier, pp. 131–190. https://doi.org/10.1016/B978-0-08-095975-7.00905-0

Blum, P., Mackay, R., Riley, M.S., 2009. Stochastic simulations of regional scale advective transport in fractured rock masses using block upscaled hydro-mechanical rock property data. Journal of Hydrology 369, 318–325. https://doi.org/10.1016/j.jhydrol.2009.02.009

Blum, P., Mackay, R., Riley, M.S., Knight, J.L., 2005. Performance assessment of a nuclear waste repository: Upscaling coupled hydro-mechanical properties for far-field transport analysis. International Journal of Rock Mechanics and Mining Sciences 42, 781–792. https://doi.org/10.1016/j.ijrmms.2005.03.015

Blum, P., Steger, H., Erguler, Z., 2013. Bestimmung geotechnischer Parameter von Tonsteinen mit dem Nadelpenetrometertest (Determination of geotechnical parameters of clay rocks using needle penetration test). Presented at the 19. Tagung für Ingenieurgeologie, Munich, Germany.

Blümling, P., Bernier, F., Lebon, P., Derek Martin, C., 2007. The excavation damaged zone in clay formations time-dependent behaviour and influence on performance assessment. Physics and Chemistry of the Earth, Parts A/B/C 32, 588–599. https://doi.org/10.1016/j.pce.2006.04.034

BMWi, 2021. Die Energie der Zukunft. 8. Monitoring-Bericht zur Energiewende - Berichtsjahre 2018 und 2019. Bundesministerium für Wirtschaft und Energie (BMWi), Berlin, Germany.

Bock, H., 2009. RA Experiment. Updated review of the rock mechanics properties of the Opalinus Clay of the Mont Terri URL based on laboratory and field testing. Unpublished Mont Terri Technical Report, TR 2008-04.

Boehler, W., Vicent, M.B., Marbs, A., 2003. Investigating laser scanner accuracy. The International Archives of Photogrammetry, Remote Sensing and Spatial Information Sciences 34, 696–701.

Bollermann, T., Fischer, C., 2020. Temporal evolution of dissolution kinetics of polycrystalline calcite. American Journal of Science 320, 53–71. https://doi.org/10.2475/01.2020.04

Bons, P.D., Elburg, M.A., Gomez-Rivas, E., 2012. A review of the formation of tectonic veins and their microstructures. Journal of Structural Geology 43, 33–62. https://doi.org/10.1016/j.jsg.2012.07.005

Bossart, P., Bernier, F., Birkholzer, J., Bruggeman, C., Connolly, P., Dewonck, S., Fukaya, M., Herfort, M., Jensen, M., Matray, J.-M., Mayor, J.C., Moeri, A., Oyama, T., Schuster, K., Shigeta, N., Vietor, T., Wieczorek, K., 2017. Mont Terri rock laboratory, 20 years of research: introduction, site characteristics and overview of experiments. Swiss Journal of Geosciences 110, 3–22. https://doi.org/10.1007/s00015-016-0236-1

Bossart, P., Meier, P.M., Moeri, A., Trick, T., Mayor, J.-C., 2002. Geological and hydraulic characterisation of the excavation disturbed zone in the Opalinus Clay of the Mont Terri Rock Laboratory. Engineering Geology 66, 19–38. https://doi.org/10.1016/S0013-7952(01)00140-5

Bossart, P., Thury, M., 2008. Characteristics of the Opalinus Clay at Mont Terri. Mont Terri Rock Laboratory. Project, programme 1996 to 2007 and results. Reports of the Swiss Geological Survey No. 3, Federal Office of Topography (swisstopo), Wabern, Switzerland.

Bossart, P., Trick, T., Meier, P.M., Mayor, J.-C., 2004. Structural and hydrogeological characterisation of the excavation-disturbed zone in the Opalinus Clay (Mont Terri Project, Switzerland). Applied Clay Science 26, 429–448. https://doi.org/10.1016/j.clay.2003.12.018

Bouissonnié, A., Daval, D., Marinoni, M., Ackerer, P., 2018. From mixed flow reactor to column experiments and modeling: Upscaling of calcite dissolution rate. Chemical Geology 487, 63–75. https://doi.org/10.1016/j.chemgeo.2018.04.017

Boutt, D.F., Grasselli, G., Fredrich, J.T., Cook, B.K., Williams, J.R., 2006. Trapping zones: The effect of fracture roughness on the directional anisotropy of fluid flow and colloid transport in a single fracture. Geophysical Research Letters 33, L21402. https://doi.org/10.1029/2006GL027275

Brantley, S.L., Conrad, C.F., 2008. Analysis of Rates of Geochemical Reactions, in: Brantley, S.L., Kubicki, J.D., White, A.F. (Eds.), Kinetics of Water-Rock Interaction. Springer New York, pp. 1–37. https://doi.org/10.1007/978-0-387-73563-4_1

Brown, S., Smith, M., 2013. A transient-flow syringe air permeameter. Geophysics 78, D307–D313. https://doi.org/10.1190/geo2012-0534.1

Brown, S.R., 1987. Fluid flow through rock joints: the effect of surface roughness. Journal of Geophysical Research: Solid Earth 92, 1337–1347. https://doi.org/10.1029/JB092iB02p01337

Buades, A., Coll, B., Morel, J.-M., 2005. A Non-Local Algorithm for Image Denoising, in: IEEE Computer Society Conference on Computer Vision and Pattern Recognition

(CVPR'05). Presented at the IEEE Computer Society Conference on Computer Vision and Pattern Recognition (CVPR'05), San Diego, California, pp. 60–65. https://doi.org/10.1109/CVPR.2005.38

Buckley, S.J., Howell, J.A., Enge, H.D., Kurz, T.H., 2008. Terrestrial laser scanning in geology: data acquisition, processing and accuracy considerations. Journal of the Geological Society 165, 625–638. https://doi.org/10.1144/0016-76492007-100

Buyuksagis, I.S., Goktan, R.M., 2007. The effect of Schmidt hammer type on uniaxial compressive strength prediction of rock. International Journal of Rock Mechanics and Mining Sciences 44, 299–307. https://doi.org/10.1016/j.ijrmms.2006.07.008

Cammarata, G., Fidelibus, C., Cravero, M., Barla, G., 2007. The Hydro-Mechanically Coupled Response of Rock Fractures. Rock Mechanics and Rock Engineering 40, 41–61. https://doi.org/10.1007/s00603-006-0081-z

Candela, T., Renard, F., Klinger, Y., Mair, K., Schmittbuhl, J., Brodsky, E.E., 2012. Roughness of fault surfaces over nine decades of length scales. Journal of Geophysical Research 117, B08409. https://doi.org/10.1029/2011JB009041

Cao, N., Lei, G., Dong, P., Li, H., Wu, Z., Li, Y., 2018. Stress-Dependent Permeability of Fractures in Tight Reservoirs. Energies 12, 117. https://doi.org/10.3390/en12010117

Cardona, A., Finkbeiner, T., Santamarina, J.C., 2021. Natural Rock Fractures: From Aperture to Fluid Flow. Rock Mechanics and Rock Engineering 54, 5827–5844. https://doi.org/10.1007/s00603-021-02565-1

Chagneau, A., Claret, F., Enzmann, F., Kersten, M., Heck, S., Madé, B., Schäfer, T., 2015. Mineral precipitation-induced porosity reduction and its effect on transport parameters in diffusion-controlled porous media. Geochemical Transactions 16, 13. https://doi.org/10.1186/s12932-015-0027-z

Chapman, N., Hooper, A., 2012. The disposal of radioactive wastes underground. Proceedings of the Geologists' Association 123, 46–63. https://doi.org/10.1016/j.pgeola.2011.10.001

Chen, Y., Ma, G., Wang, H., 2018. Heat extraction mechanism in a geothermal reservoir with rough-walled fracture networks. International Journal of Heat and Mass Transfer 126, 1083–1093. https://doi.org/10.1016/j.ijheatmasstransfer.2018.05.103

Cheng, C., Hale, S., Milsch, H., Blum, P., 2020. Measuring hydraulic fracture apertures: a comparison of methods. Solid Earth 11, 2411–2423. https://doi.org/10.5194/se-11-2411-2020

Cheng, C., Milsch, H., 2021. Hydromechanical Investigations on the Self-propping Potential of Fractures in Tight Sandstones. Rock Mechanics and Rock Engineering 54, 5407–5432. https://doi.org/10.1007/s00603-021-02500-4

Chou, L., Garrels, R.M., Wollast, R., 1989. Comparative study of the kinetics and mechanisms of dissolution of carbonate minerals. Chemical Geology 78, 269–282. https://doi.org/10.1016/0009-2541(89)90063-6

Colón, C.F.J., Oelkers, E.H., Schott, J., 2004. Experimental investigation of the effect of dissolution on sandstone permeability, porosity, and reactive surface area. Geochimica et Cosmochimica Acta 68, 805–817. https://doi.org/10.1016/j.gca.2003.06.002

Corradetti, A., McCaffrey, K., De Paola, N., Tavani, S., 2017. Evaluating roughness scaling properties of natural active fault surfaces by means of multi-view photogrammetry. Tectonophysics 717, 599–606. https://doi.org/10.1016/j.tecto.2017.08.023

Corradetti, A., Zambrano, M., Tavani, S., Tondi, E., Seers, T.D., 2020. The impact of weathering upon the roughness characteristics of a splay of the active fault system responsible for the massive 2016 seismic sequence of the Central Apennines, Italy. Geological Society of America Bulletin 130. https://doi.org/10.1130/B35661.1

Costa, S.E.D., Barros Neto, E.L., Oliveira, M.C.A., Santos, J.S.C., 2017. Mechanical and petrophysical analysis of synthetic sandstone for enhanced oil recovery applications. Brazilian Journal of Petroleum and Gas 11, 131–140. https://doi.org/10.5419/bjpg2017-0011

Crawshaw, J.P., Boek, E.S., 2013. Multi-scale Imaging and Simulation of Structure, Flow and Reactive Transport for CO2 Storage and EOR in Carbonate Reservoirs. Reviews in Mineralogy and Geochemistry 77, 431–458. https://doi.org/10.2138/rmg.2013.77.12

Curtis, G.P., Davis, J.A., Naftz, D.L., 2006. Simulation of reactive transport of uranium(VI) in groundwater with variable chemical conditions. Water Resources Research 42, W04404. https://doi.org/10.1029/2005WR003979

Cuss, R.J., Milodowski, A., Harrington, J.F., 2011. Fracture transmissivity as a function of normal and shear stress: First results in Opalinus Clay. Physics and Chemistry of the Earth, Parts A/B/C 36, 1960–1971. https://doi.org/10.1016/j.pce.2011.07.080

Damjanac, B., Cundall, P., 2016. Application of distinct element methods to simulation of hydraulic fracturing in naturally fractured reservoirs. Computers and Geotechnics 71, 283–294. https://doi.org/10.1016/j.compgeo.2015.06.007

Dao, L.-Q., Cui, Y.-J., Tang, A.-M., Pereira, J.-M., Li, X.-L., Sillen, X., 2015. Impact of excavation damage on the thermo-hydro-mechanical properties of natural Boom Clay. Engineering Geology 195, 196–205. https://doi.org/10.1016/j.enggeo.2015.06.011

Daval, D., Hellmann, R., Saldi, G.D., Wirth, R., Knauss, K.G., 2013. Linking nm-scale measurements of the anisotropy of silicate surface reactivity to macroscopic dissolution rate laws: New insights based on diopside. Geochimica et Cosmochimica Acta 107, 121–134. https://doi.org/10.1016/j.gca.2012.12.045

Davis, G.H., Reynolds, S.J., Kluth, C.F., 2011. Structural Geology of Rocks and Regions, 3rd ed. John Wiley & Sons.

Davis, M.H., Khotanzad, A., Flamig, D.P., Harms, S.E., 1997. A physics-based coordinate transformation for 3-D image matching. IEEE Transactions on Medical Imaging 16, 317–328. https://doi.org/10.1109/42.585766

de La Vaissière, R., Armand, G., Talandier, J., 2015. Gas and water flow in an excavation-induced fracture network around an underground drift: A case study for a radioactive waste repository in clay rock. Journal of Hydrology 521, 141–156. https://doi.org/10.1016/j.jhydrol.2014.11.067

Delage, P., 2014. Unsaturated issues in claystones, in: Khalili, N., Russell, A., Khoshghalb, A. (Eds.), Unsaturated Soils: Research & Applications. CRC Press, London, United Kingdom, pp. 99–105. https://doi.org/10.1201/b17034

Delay, J., Bossart, P., Ling, L.X., Blechschmidt, I., Ohlsson, M., Vinsot, A., Nussbaum, C., Maes, N., 2014. Three decades of underground research laboratories: what have we learned? Geological Society, London, Special Publications 400, 7–32. https://doi.org/10.1144/SP400.1

Deng, H., Ellis, B.R., Peters, C.A., Fitts, J.P., Crandall, D., Bromhal, G.S., 2013. Modifications of carbonate fracture hydrodynamic properties by CO2-acidified brine flow. Energy & Fuels 27, 4221–4231. https://doi.org/10.1021/ef302041s

Detwiler, R.L., Glass, R.J., Bourcier, W.L., 2003. Experimental observations of fracture dissolution: The role of Peclet number on evolving aperture variability. Geophysical Research Letters 30, 1648. https://doi.org/10.1029/2003GL017396

Dreybrodt, W., 2012. Processes in Karst Systems: Physics, Chemistry, and Geology, Springer Series in Physical Environment. Springer Science & Business Media, Berlin, Heidelberg.

Durham, W.B., Bourcier, W.L., Burton, E.A., 2001. Direct observation of reactive flow in a single fracture. Water Resources Research 37, 1–12. https://doi.org/10.1029/2000WR900228

Erguler, Z.A., Ulusay, R., 2009. Water-induced variations in mechanical properties of clay-bearing rocks. International Journal of Rock Mechanics and Mining Sciences 46, 355–370. https://doi.org/10.1016/j.ijrmms.2008.07.002

Fairhurst, C., 2004. Nuclear waste disposal and rock mechanics: contributions of the Underground Research Laboratory (URL), Pinawa, Manitoba, Canada. International Journal of Rock Mechanics and Mining Sciences 41, 1221–1227. https://doi.org/10.1016/j.ijrmms.2004.09.001

Feng, Q., Fardin, N., Jing, L., Stephansson, O., 2003. A New Method for In-situ Non-contact Roughness Measurement of Large Rock Fracture Surfaces. Rock Mechanics and Rock Engineering 36, 3–25. https://doi.org/10.1007/s00603-002-0033-1

Filomena, C.M., Hornung, J., Stollhofen, H., 2014. Assessing accuracy of gas-driven permeability measurements: a comparative study of diverse Hassler-cell and probe permeameter devices. Solid Earth 5, 1–11. https://doi.org/10.5194/se-5-1-2014

Fischer, C., Arvidson, R.S., Luttge, A., 2012a. How predictable are dissolution rates of crystalline material? Geochimica et Cosmochimica Acta 98, 177–185. https://doi.org/10.1016/j.gca.2012.09.011

Fischer, C., Dunkl, I., Von Eynatten, H., Wijbrans, J.R., Gaupp, R., 2012b. Products and timing of diagenetic processes in Upper Rotliegend sandstones from Bebertal (North German Basin, Parchim Formation, Flechtingen High, Germany). Geological Magazine 149, 827–840. https://doi.org/10.1017/S0016756811001087

Fischer, C., Gaupp, R., Dimke, M., Sill, O., 2007. A 3D high resolution model of bounding surfaces in aeolian-fluvial deposits: an outcrop analogue study from the Permian Rotliegend, Northern Germany. Journal of Petroleum Geology 30, 257–273. https://doi.org/10.1111/j.1747-5457.2007.00257.x

Fischer, C., Kurganskaya, I., Schäfer, T., Luttge, A., 2014. Variability of crystal surface reactivity: What do we know? Applied Geochemistry 43, 132–157. https://doi.org/10.1016/j.apgeochem.2014.02.002

Flukiger, F., Bernard, D., 2009. A new numerical model for pore scale dissolution of calcite due to CO2 saturated water flow in 3D realistic geometry: Principles and first results. Chemical Geology 265, 171–180. https://doi.org/10.1016/j.chemgeo.2009.05.004

Ford, D., Williams, P.D., 2013. Karst Hydrogeology and Geomorphology. John Wiley & Sons, Ltd., Chichester.

Fredd, C.N., Fogler, H.S., 1999. Optimum Conditions for Wormhole Formation in Carbonate Porous Media: Influence of Transport and Reaction. SPE Journal 4, 196–205. https://doi.org/10.2118/56995-PA

Ganguly, S., Mohan Kumar, M.S., 2012. Geothermal reservoirs — A brief review. Journal of the Geological Society of India 79, 589–602. https://doi.org/10.1007/s12594-012-0098-8

Gaucher, E., Schoenball, M., Heidbach, O., Zang, A., Fokker, P.A., van Wees, J.-D., Kohl, T., 2015. Induced seismicity in geothermal reservoirs: A review of forecasting approaches. Renewable and Sustainable Energy Reviews 52, 1473–1490. https://doi.org/10.1016/j.rser.2015.08.026

Geological Society of London, 2012. The Geological Society of London. https://www.geolsoc.org.uk/. Accessed 12 December 2021.

Ghasemizadeh, R., Hellweger, F., Butscher, C., Padilla, I., Vesper, D., Field, M., Alshawabkeh, A., 2012. Review: Groundwater flow and transport modeling of karst aquifers, with particular reference to the North Coast Limestone aquifer system of Puerto Rico. Hydrogeology Journal 20, 1441–1461. https://doi.org/10.1007/s10040-012-0897-4

Giger, S.B., Marschall, P., Lanyon, B., Martin, C.D., 2015. Hydro-mechanical response of Opalinus Clay during excavation works - a synopsis from the Mont Terri URL. Geomechanics and Tunnelling 8, 421–425. https://doi.org/10.1002/geot.201500021

Gkay, D.H., Rex, R.W., 1966. Formation damage in sandstones caused by clay dispersion and migration, in: Bailey, S.W. (Ed.), Clays and Clay Minerals. Pergamon, pp. 355–366. https://doi.org/10.1016/B978-0-08-011908-3.50033-5

Goggin, D.J., Thrasher, R.L., Lake, L.W., 1988. A theoretical and experimental analysis of minipermeameter response including gas slippage and high velocity flow effects. In Situ 12, 79–116.

Goldscheider, N., Chen, Z., Auler, A.S., Bakalowicz, M., Broda, S., Drew, D., Hartmann, J., Jiang, G., Moosdorf, N., Stevanovic, Z., Veni, G., 2020. Global distribution of carbonate rocks and karst water resources. Hydrogeology Journal 28, 1661–1677. https://doi.org/10.1007/s10040-020-02139-5

Golfier, F., Zarcone, C., Bazin, B., Lenormand, R., Lasseux, D., Quintard, M., 2002. On the ability of a Darcy-scale model to capture wormhole formation during the dissolution of a porous medium. Journal of Fluid Mechanics 457, 213–254. https://doi.org/10.1017/S0022112002007735

Gouze, P., Luquot, L., 2011. X-ray microtomography characterization of porosity, permeability and reactive surface changes during dissolution. Journal of Contaminant Hydrology 120–121, 45–55. https://doi.org/10.1016/j.jconhyd.2010.07.004

Gräsle, W., Plischke, I., 2011. LT-A Experiment: Mechanical Behavior of Opalinus Clay, Data Report from Phase 15. Unpublished Mont Terri Technical Note, TN 2010-86.

Gräsle, W., Plischke, I., 2010. Laboratory Testing (LT) Experiment: Mechanical Behavior of Opalinus Clay, Final report from Phases 6 - 14. Unpublished Mont Terri Technical Report, TR 2009-07.

Grasselli, G., 2011. Shear strength of rock joints based on quantified surface description (PhD thesis). Ecole polytechnique federale de Lausanne.

Grathoff, G.H., Peltz, M., Enzmann, F., Kaufhold, S., 2016. Porosity and permeability determination of organic-rich Posidonia shales based on 3-D analyses by FIB-SEM microscopy. Solid Earth 7, 1145–1156. https://doi.org/10.5194/se-7-1145-2016

Gray, F., Anabaraonye, B., Shah, S., Boek, E., Crawshaw, J., 2018. Chemical mechanisms of dissolution of calcite by HCl in porous media: Simulations and experiment. Advances in Water Resources 121, 369–387. https://doi.org/10.1016/j.advwatres.2018.09.007

Greiner, R., Prill, T., Iliev, O., van Setten, B.A.A.L., Votsmeier, M., 2019. Tomography based simulation of reactive flow at the micro-scale: Particulate filters with wall integrated catalyst. Chemical Engineering Journal 378, 121919. https://doi.org/10.1016/j.cej.2019.121919

Guo, B., Wang, C., Wang, L., Chen, Y., Cheng, T., 2020. A Modified Cubic Law for Rough-Walled Marble Fracture by Embedding Peak Density. Advances in Civil Engineering 2020, 1–10. https://doi.org/10.1155/2020/9198356

Gustafson, G., Fransson, Å., 2006. The use of the Pareto distribution for fracture transmissivity assessment. Hydrogeology Journal 14, 15–20. https://doi.org/10.1007/s10040-005-0440-y

Gutjahr, T., Hale, S., Keller, K., Blum, P., Winter, S., 2021. Quantification of Fracture Roughness by Change Probabilities and Hurst Exponents. Mathematical Geosciences. https://doi.org/10.1007/s11004-021-09985-3

Haffen, S., Geraud, Y., Diraison, M., Dezayes, C., 2013. Determination of fluid-flow zones in a geothermal sandstone reservoir using thermal conductivity and temperature logs. Geothermics 46, 32–41. https://doi.org/10.1016/j.geothermics.2012.11.001

Hakami, E., 1995. Aperture distribution of rock fractures (PhD thesis). Royal Institute of Technology, Stockholm.

Hakami, E., Larsson, E., 1996. Aperture measurements and flow experiments on a single natural fracture. International Journal of Rock Mechanics and Mining Sciences & Geomechanics Abstracts 33, 395–404. https://doi.org/10.1016/0148-9062(95)00070-4

Hakoun, V., Comolli, A., Dentz, M., 2019. Upscaling and Prediction of Lagrangian Velocity Dynamics in Heterogeneous Porous Media. Water Resources Research 55, 3976–3996. https://doi.org/10.1029/2018WR023810

Hale, S., Naab, C., Butscher, C., Blum, P., 2020a. Method Comparison to Determine Hydraulic Apertures of Natural Fractures. Rock Mechanics and Rock Engineering 53, 1467–1476. https://doi.org/10.1007/s00603-019-01966-7

Hale, S., Ries, X., Jaeggi, D., Blum, P., 2020b. Mechanical and hydraulic properties of the excavation damaged zone (EDZ) in the Opalinus Clay of the Mont Terri Rock Laboratory, Switzerland. figshare. https://doi.org/10.6084/m9.figshare.12581144.v2

Hanna, R.B., Rajaram, H., 1998. Influence of aperture variability on dissolutional growth of fissures in karst formations. Water Resources Research 34, 2843–2853. https://doi.org/10.1029/98WR01528

Hassanzadegan, A., Blöcher, G., Milsch, H., Urpi, L., Zimmermann, G., 2014. The Effects of Temperature and Pressure on the Porosity Evolution of Flechtinger Sandstone. Rock Mechanics and Rock Engineering 47, 421–434. https://doi.org/10.1007/s00603-013-0401-z

Hassanzadegan, A., Blöcher, G., Zimmermann, G., Milsch, H., 2012. Thermoporoelastic properties of Flechtinger sandstone. International Journal of Rock Mechanics and Mining Sciences 49, 94–104. https://doi.org/10.1016/j.ijrmms.2011.11.002

He, X., Santoso, R., Zhu, W., Hoteit, H., AlSinan, M.M., Kwak, H.T., 2021. Coupled Flow-Normal-Shear Influence on Fracture Permeability: Analysis and Modeling. Presented at the ARMA/DGS/SEG 2nd International Geomechanics Symposium, Virtual, OnePetro.

Heidsiek, M., Butscher, C., Blum, P., Fischer, C., 2020. Small-scale diagenetic facies heterogeneity controls porosity and permeability pattern in reservoir sandstones. Environmental Earth Sciences 79, 425. https://doi.org/10.1007/s12665-020-09168-z

Hellmann, R., Tisserand, D., 2006. Dissolution kinetics as a function of the Gibbs free energy of reaction: An experimental study based on albite feldspar. Geochimica et Cosmochimica Acta 70, 364–383. https://doi.org/10.1016/j.gca.2005.10.007

Henkel, S., Pudlo, D., Werner, L., Enzmann, F., Reitenbach, V., Albrecht, D., Würdemann, H., Heister, K., Ganzer, L., Gaupp, R., 2014. Mineral Reactions in the Geological Underground Induced by H2 and CO2 Injections. Energy Procedia 63, 8026–8035. https://doi.org/10.1016/j.egypro.2014.11.839

Hillier, S., Wilson, M.J., Merriman, R.J., 2006. Clay mineralogy of the Old Red Sandstone and Devonian sedimentary rocks of Wales, Scotland and England. Clay Minerals 41, 433–471. https://doi.org/10.1180/0009855064110203

Hinz, C., Enzmann, F., Kersten, M., 2019. Pore scale modelling of calcite cement dissolution in a reservoir sandstone matrix. E3S Web of Conferences 98, 05010. https://doi.org/10.1051/e3sconf/20199805010

Hodson, M.E., 2006. Searching for the perfect surface area normalizing term—a comparison of BET surface area-, geometric surface area- and mass-normalized dissolution rates of anorthite and biotite. Journal of Geochemical Exploration 88, 288–291. https://doi.org/10.1016/j.gexplo.2005.08.058

Hopkins, D.L., Cook, N.G.W., Myer, L.R., 1987. Fracture stiffness and aperture as a function of applied stress and contact geometry. Presented at the 28th US Symposium on Rock Mechanics (USRMS), Tucson, Arizona.

Hostettler, B., Reisdorf, A.G., Jaeggi, D., Deplazes, G., Bläsi, H., Morard, A., Feist-Burkhardt, S., Waltschew, A., Dietze, V., Menkveld-Gfeller, U., 2017. Litho- and biostratigraphy of the Opalinus Clay and bounding formations in the Mont Terri rock laboratory (Switzerland). Swiss Journal of Geosciences 110, 23–37. https://doi.org/10.1007/s00015-016-0250-3

Hucka, V., 1965. A rapid method of determining the strength of rocks in situ. International Journal of Rock Mechanics and Mining Sciences & Geomechanics Abstracts 2, 127–134. https://doi.org/10.1016/0148-9062(65)90009-4

Hudson, J.A., Stephansson, O., Andersson, J., 2005. Guidance on numerical modelling of thermo-hydro-mechanical coupled processes for performance assessment of radioactive waste repositories. International Journal of Rock Mechanics and Mining Sciences 42, 850–870. https://doi.org/10.1016/j.ijrmms.2005.03.018

Huq, F., Haderlein, S.B., Cirpka, O.A., Nowak, M., Blum, P., Grathwohl, P., 2015. Flow-through experiments on water–rock interactions in a sandstone caused by CO2 injection at pressures and temperatures mimicking reservoir conditions. Applied Geochemistry 58, 136–146. https://doi.org/10.1016/j.apgeochem.2015.04.006

IAEA, 2006. Safety of radioactive waste disposal, in: Proceedings of an International Conference on the Safety of Radioactive Waste Disposal, Organized by the International Atomic Energy Agency. Tokyo, Japan.

Iliev, O., Lakdawala, Z., Neßler, K.H.L., Prill, T., Vutov, Y., Yang, Y., Yao, J., 2017. On the Pore-Scale Modeling and Simulation of Reactive Transport in 3D Geometries. Mathematical Modelling and Analysis 22, 671–694. https://doi.org/10.3846/13926292.2017.1356759

Ivanov, E., Korobkov, D., Sidorenkov, A., Varfolomeev, I., Stukan, M., 2021. Digital Rock Extension of Laboratory Core Test Results for Acid Treatment Optimization. Presented at the SPE Russian Petroleum Technology Conference, Virtual, OnePetro. https://doi.org/10.2118/206591-MS

Jacob, A., Enzmann, F., Hinz, C., Kersten, M., 2019. Analysis of Variance of Porosity and Heterogeneity of Permeability at the Pore Scale. Transport in Porous Media 130, 867–887. https://doi.org/10.1007/s11242-019-01342-7

Jacob, A., Peltz, M., Hale, S., Enzmann, F., Moravcova, O., Warr, L.N., Grathoff, G., Blum, P., Kersten, M., 2021. Simulating permeability reduction by clay mineral nanopores in a tight sandstone by combining computer X-ray microtomography and focussed ion beam scanning electron microscopy imaging. Solid Earth 12, 1–14. https://doi.org/10.5194/se-12-1-2021

Jaeggi, D., Bossart, P., 2014. Kompilation der lithologischen Variabilität und Eigenschaften des Opalinus-Ton im Felslabor Mont Terri. Expert Report for ENSI, Federal Office of Topography (swisstopo), Wabern, Switzerland.

Jahns, E., 2010. RA Experiment: Opalinus Clay Rock Characterization. Unpublished Mont Terri Technical Note, TN 2008-55rev.

Jakubick, A.T., Franz, T., 1993. Vacuum testing of the permeability of the excavation damaged zone. Rock Mechanics and Rock Engineering 26, 165–182.

Javanmard, H., Ebigbo, A., Walsh, S.D.C., Saar, M.O., Vogler, D., 2021. No-Flow Fraction (NFF) Permeability Model for Rough Fractures Under Normal Stress. Water Resources Research 57. https://doi.org/10.1029/2020WR029080

Jørgensen, P.R., Hoffmann, M., Kistrup, J.P., Bryde, C., Bossi, R., Villholth, K.G., 2002. Preferential flow and pesticide transport in a clay-rich till: Field, laboratory, and modeling analysis. Water Resources Research 38, 1246. https://doi.org/10.1029/2001WR000494

Kabuth, A., Dahmke, A., Beyer, C., Bilke, L., Dethlefsen, F., Dietrich, P., Duttmann, R., Ebert, M., Feeser, V., Görke, U.-J., Köber, R., Rabbel, W., Schanz, T., Schäfer, D., Würdemann, H., Bauer, S., 2017. Energy storage in the geological subsurface: dimensioning, risk analysis and spatial planning: the ANGUS+ project. Environmental Earth Sciences 76, 23. https://doi.org/10.1007/s12665-016-6319-5

Kahl, W.-A., Yuan, T., Bollermann, T., Bach, W., Fischer, C., 2020. Crystal surface reactivity analysis using a combined approach of X-ray micro-computed tomography and vertical scanning interferometry. American Journal of Science 320, 27–52. https://doi.org/10.2475/01.2020.03

Karimzadeh, L., Fischer, C., 2021. Implementing Heterogeneous Crystal Surface Reactivity in Reactive Transport Simulations: The Example of Calcite Dissolution. ACS Earth and Space Chemistry 5, 2408–2418. https://doi.org/10.1021/acsearthspacechem.1c00099

Kaufmann, G., Dreybrodt, W., 2007. Calcite dissolution kinetics in the system CaCO3–H2O–CO2 at high undersaturation. Geochimica et Cosmochimica Acta 71, 1398–1410. https://doi.org/10.1016/j.gca.2006.10.024

Kieffer, B., Jové, C.F., Oelkers, E.H., Schott, J., 1999. An experimental study of the reactive surface area of the Fontainebleau sandstone as a function of porosity, permeability, and fluid flow rate. Geochimica et Cosmochimica Acta 63, 3525–3534. https://doi.org/10.1016/S0016-7037(99)00191-X

Kim, D., Lindquist, W.B., 2013. Effects of network dissolution changes on pore-to-core upscaled reaction rates for kaolinite and anorthite reactions under acidic conditions. Water Resources Research 49, 7575–7586. https://doi.org/10.1002/2013WR013667

Kim, D., Peters, C.A., Lindquist, W.B., 2011. Upscaling geochemical reaction rates accompanying acidic CO2-saturated brine flow in sandstone aquifers. Water Resources Research 47, W01505. https://doi.org/10.1029/2010WR009472

Kirch, W., 2008. Validity Measurement, in: Kirch, W. (Ed.), Encyclopedia of Public Health. Springer Netherlands, Dordrecht, pp. 1440–1440. https://doi.org/10.1007/978-1-4020-5614-7_3671

Kleditzsch, O., Kurze, M., 1993. Ergebnisse petrographischer Untersuchungen an Sandsteinen des tieferen Oberrotliegenden im Raum Altmark/Westmecklenburg. Geologisches Jahrbuch. Reihe A, Allgemeine und regionale Geologie BR Deutschland und Nachbargebiete, Tektonik, Stratigraphie, Paläontologie 131, 141–178.

Kling, T., Huo, D., Schwarz, J.-O., Enzmann, F., Benson, S., Blum, P., 2016. Simulating stress-dependent fluid flow in a fractured core sample using real-time X-ray CT data. Solid Earth 7, 1109–1124. https://doi.org/10.5194/se-7-1109-2016

Kling, T., Schwarz, J.-O., Wendler, F., Enzmann, F., Blum, P., 2017. Fracture flow due to hydrothermally induced quartz growth. Advances in Water Resources 107, 93–107. https://doi.org/10.1016/j.advwatres.2017.06.011

Kling, T., Vogler, D., Pastewka, L., Amann, F., Blum, P., 2018. Numerical simulations and validation of contact mechanics in a granodiorite fracture. Rock Mechanics and Rock Engineering 51, 2805–2824. https://doi.org/10.1007/s00603-018-1498-x

Kolditz, O., Shao, H., Wang, W., Bauer, S. (Eds.), 2015. Thermo-Hydro-Mechanical-Chemical Processes in Fractured Porous Media: Modelling and Benchmarking: Closed-Form Solutions, Terrestrial Environmental Sciences. Springer International Publishing, Cham, Switzerland. https://doi.org/10.1007/978-3-319-11894-9

Kubicki, J.D., 2008. Transition State Theory and Molecular Orbital Calculations Applied to Rates and Reaction Mechanisms in Geochemical Kinetics, in: Brantley, S.L., Kubicki, J.D., White, A.F. (Eds.), Kinetics of Water-Rock Interaction. Springer New York, pp. 39–72. https://doi.org/10.1007/978-0-387-73563-4_2

Kupferschmied, N., Wild, K.M., Amann, F., Nussbaum, C., Jaeggi, D., Badertscher, N., 2015. Time-dependent fracture formation around a borehole in a clay shale. International Journal of Rock Mechanics and Mining Sciences 77, 105–114. https://doi.org/10.1016/j.ijrmms.2015.03.027

Kurganskaya, I., Churakov, S.V., 2018. Carbonate Dissolution Mechanisms in the Presence of Electrolytes Revealed by Grand Canonical and Kinetic Monte Carlo Modeling. The Journal of Physical Chemistry C 122, 29285–29297. https://doi.org/10.1021/acs.jpcc.8b08986

Kurganskaya, I., Luttge, A., 2016. Kinetic Monte Carlo Approach To Study Carbonate Dissolution. The Journal of Physical Chemistry C 120, 6482–6492. https://doi.org/10.1021/acs.jpcc.5b10995

Labiouse, V., Vietor, T., 2014. Laboratory and In Situ Simulation Tests of the Excavation Damaged Zone Around Galleries in Opalinus Clay. Rock Mechanics and Rock Engineering 47, 57–70. https://doi.org/10.1007/s00603-013-0389-4

Lai, P., Moulton, K., Krevor, S., 2015. Pore-scale heterogeneity in the mineral distribution and reactive surface area of porous rocks. Chemical Geology 411, 260–273. https://doi.org/10.1016/j.chemgeo.2015.07.010

Lamur, A., Kendrick, J.E., Eggertsson, G.H., Wall, R.J., Ashworth, J.D., Lavallée, Y., 2017. The permeability of fractured rocks in pressurised volcanic and geothermal systems. Scientific Reports 7, 6173. https://doi.org/10.1038/s41598-017-05460-4

Lamy-Chappuis, B., Angus, D., Fisher, Q., Grattoni, C., Yardley, B.W.D., 2014. Rapid porosity and permeability changes of calcareous sandstone due to CO2-enriched brine injection. Geophysical Research Letters 41, 399–406. https://doi.org/10.1002/2013GL058534

Landrot, G., Ajo-Franklin, J.B., Yang, L., Cabrini, S., Steefel, C.I., 2012. Measurement of accessible reactive surface area in a sandstone, with application to CO2 mineralization.

Chemical Geology 318–319, 113–125. https://doi.org/10.1016/j.chemgeo.2012.05.010

Lasaga, A.C., 1998. Kinetic Theory in the Earth Sciences, Princeton Series in Geochemistry. Princeton University Press.

Lavanchy, J.M., Mettier, R., 2012. HA (Hydrogeological analysis) Experiment: Hydraulic database, Phases 1-16, Version 1.0. Unpublished Mont Terri Technical Note, TN 2010-74.

Lee, J., Babadagli, T., 2021. Effect of roughness on fluid flow and solute transport in a single fracture: A review of recent developments, current trends, and future research. Journal of Natural Gas Science and Engineering 91, 103971. https://doi.org/10.1016/j.jngse.2021.103971

Lee, T., Kim, K., Lee, K., Lee, H., Lee, W., 2018. Development of fluid flow and heat transfer model in naturally fractured geothermal reservoir with discrete fracture network method. Geosciences Journal 22, 477–485. https://doi.org/10.1007/s12303-017-0035-3

Lei, Q., Wang, X., Xiang, J., Latham, J.-P., 2017. Polyaxial stress-dependent permeability of a three-dimensional fractured rock layer. Hydrogeology Journal 25, 2251–2262. https://doi.org/10.1007/s10040-017-1624-y

Li, H., Tang, J., Lu, Y., Zhou, L., Han, S., Dai, R., 2018. Experimental Measurements of Shale Fracture Conductivity Under Cyclic Loading. Arabian Journal for Science and Engineering 43, 6315–6324. https://doi.org/10.1007/s13369-017-3032-y

Li, L., Peters, C.A., Celia, M.A., 2007. Effects of mineral spatial distribution on reaction rates in porous media. Water Resources Research 43, W01419. https://doi.org/10.1029/2005WR004848

Li, L., Peters, C.A., Celia, M.A., 2006. Upscaling geochemical reaction rates using pore-scale network modeling. Advances in Water Resources 29, 1351–1370. https://doi.org/10.1016/j.advwatres.2005.10.011

Li, Q., Xing, H., Liu, J., Liu, X., 2015. A review on hydraulic fracturing of unconventional reservoir. Petroleum 1, 8–15. https://doi.org/10.1016/j.petlm.2015.03.008

Li, S., Feng, X.-T., Li, Z., Zhang, C., Chen, B., 2012. Evolution of fractures in the excavation damaged zone of a deeply buried tunnel during TBM construction. International Journal of Rock Mechanics and Mining Sciences 55, 125–138. https://doi.org/10.1016/j.ijrmms.2012.07.004

Li, X., Wang, Q., Shen, X., Pedrosa, E.T., Luttge, A., 2021. Multiscale investigation of olivine (0 1 0) face dissolution from a surface control perspective. Applied Surface Science 549, 149317. https://doi.org/10.1016/j.apsusc.2021.149317

Li, Y., Zhang, Y., 2015. Quantitative estimation of joint roughness coefficient using statistical parameters. International Journal of Rock Mechanics and Mining Sciences 77, 27–35. https://doi.org/10.1016/j.ijrmms.2015.03.016

Liang, Y., Baer, D.R., 1997. Anisotropic dissolution at the CaCO3(1014)-water interface. Surface Science 373, 275–287. https://doi.org/10.1016/S0039-6028(96)01155-7

Lisjak, A., Garitte, B., Grasselli, G., Müller, H.R., Vietor, T., 2015. The excavation of a circular tunnel in a bedded argillaceous rock (Opalinus Clay): Short-term rock mass response and FDEM numerical analysis. Tunnelling and Underground Space Technology 45, 227–248. https://doi.org/10.1016/j.tust.2014.09.014

Lisjak, A., Tatone, B.S.A., Mahabadi, O.K., Grasselli, G., Marschall, P., Lanyon, G.W., de La Vaissière, R., Shao, H., Leung, H., Nussbaum, C., 2016. Hybrid Finite-Discrete Element Simulation of the EDZ Formation and Mechanical Sealing Process Around a Microtunnel in Opalinus Clay. Rock Mechanics and Rock Engineering 49, 1849–1873. https://doi.org/10.1007/s00603-015-0847-2

Liu, E., 2005. Effects of fracture aperture and roughness on hydraulic and mechanical properties of rocks: implication of seismic characterization of fractured reservoirs. Journal of Geophysics and Engineering 2, 38–47. https://doi.org/10.1088/1742-2132/2/1/006

Liu, M., Shabaninejad, M., Mostaghimi, P., 2018. Predictions of permeability, surface area and average dissolution rate during reactive transport in multi-mineral rocks. Journal of Petroleum Science and Engineering 170, 130–138. https://doi.org/10.1016/j.petrol.2018.06.010

Liu, Y., Teng, Y., Jiang, L., Zhao, J., Zhang, Y., Wang, D., Song, Y., 2017. Displacement front behavior of near miscible CO2 flooding in decane saturated synthetic sandstone cores revealed by magnetic resonance imaging. Magnetic Resonance Imaging 37, 171–178. https://doi.org/10.1016/j.mri.2016.12.003

Liu, Z., 2018. Multiphysics in Porous Materials. Springer International Publishing, Cham, Switzerland. https://doi.org/10.1007/978-3-319-93028-2

Louis, C., 1969. A study of groundwater flow in jointed rock and its influence on the stability of rock masses (PhD thesis). Imperial College, London.

Luhmann, A.J., Kong, X.-Z., Tutolo, B.M., Garapati, N., Bagley, B.C., Saar, M.O., Seyfried, W.E., 2014. Experimental dissolution of dolomite by CO2-charged brine at 100°C and 150bar: Evolution of porosity, permeability, and reactive surface area. Chemical Geology 380, 145–160. https://doi.org/10.1016/j.chemgeo.2014.05.001

Luquot, L., Andreani, M., Gouze, P., Camps, P., 2012. CO2 percolation experiment through chlorite/zeolite-rich sandstone (Pretty Hill Formation – Otway Basin–Australia). Chemical Geology 294–295, 75–88. https://doi.org/10.1016/j.chemgeo.2011.11.018

Luquot, L., Gouze, P., 2009. Experimental determination of porosity and permeability changes induced by injection of CO2 into carbonate rocks. Chemical Geology 265, 148–159. https://doi.org/10.1016/j.chemgeo.2009.03.028

Luquot, L., Rodriguez, O., Gouze, P., 2014. Experimental Characterization of Porosity Structure and Transport Property Changes in Limestone Undergoing Different Dissolution Regimes. Transport in Porous Media 101, 507–532. https://doi.org/10.1007/s11242-013-0257-4

Luttge, A., 2006. Crystal dissolution kinetics and Gibbs free energy. Journal of Electron Spectroscopy and Related Phenomena 150, 248–259. https://doi.org/10.1016/j.elspec.2005.06.007

Lüttge, A., 2005. Etch pit coalescence, surface area, and overall mineral dissolution rates. American Mineralogist 90, 1776–1783. https://doi.org/10.2138/am.2005.1734

Luttge, A., Arvidson, R.S., 2008. The mineral–water interface, in: Brantley, S.L., Kubicki, J.D., White, A.F. (Eds.), Kinetics of Water-Rock Interaction. Springer New York, pp. 73–107.

Maerz, N.H., Franklin, J.A., Bennett, C.P., 1990. Joint roughness measurement using shadow profilometry. International Journal of Rock Mechanics and Mining Sciences & Geomechanics Abstracts 27, 329–343. https://doi.org/10.1016/0148-9062(90)92708-M

Magsipoc, E., Zhao, Q., Grasselli, G., 2020. 2D and 3D Roughness Characterization. Rock Mechanics and Rock Engineering 53, 1495–1519. https://doi.org/10.1007/s00603-019-01977-4

Maher, K., Navarre-Sitchler, A., 2019. Reactive Transport Processes that Drive Chemical Weathering: From Making Space for Water to Dismantling Continents. Reviews in Mineralogy and Geochemistry 85, 349–380. https://doi.org/10.2138/rmg.2018.85.12

Malmström, M.E., Destouni, G., Martinet, P., 2004. Modeling Expected Solute Concentration in Randomly Heterogeneous Flow Systems with Multicomponent Reactions. Environmental Science & Technology 38, 2673–2679. https://doi.org/10.1021/es030029d

Mandelbrot, B.B., 1985. Self-affine fractals and fractal dimension. Physica Scripta 32, 257–260. https://doi.org/10.1088/0031-8949/32/4/001

Mao, X., Prommer, H., Barry, D.A., Langevin, C.D., Panteleit, B., Li, L., 2006. Three-dimensional model for multi-component reactive transport with variable density groundwater flow. Environmental Modelling & Software 21, 615–628. https://doi.org/10.1016/j.envsoft.2004.11.008

Marchand, S., Mersch, O., Selzer, M., Nitschke, F., Schoenball, M., Schmittbuhl, J., Nestler, B., Kohl, T., 2020. A Stochastic Study of Flow Anisotropy and Channelling in Open Rough Fractures. Rock Mechanics and Rock Engineering 53, 233–249. https://doi.org/10.1007/s00603-019-01907-4

Markussen, Ø., Dypvik, H., Hammer, E., Long, H., Hammer, Ø., 2019. 3D characterization of porosity and authigenic cementation in Triassic conglomerates/arenites in the Edvard Grieg field using 3D micro-CT imaging. Marine and Petroleum Geology 99, 265–281. https://doi.org/10.1016/j.marpetgeo.2018.10.015

Marsch, K., Wujanz, D., Fernandez-Steeger, T.M., 2020. On the usability of different optical measuring techniques for joint roughness evaluation. Bulletin of Engineering Geology and the Environment 79, 811–830. https://doi.org/10.1007/s10064-019-01606-y

Marschall, P., Giger, S., de la Vassière, R., Shao, H., Leung, H., Nussbaum, C., Trick, T., Lanyon, B., Senger, R., Lisjak, A., Alcolea, A., 2017. Hydro-mechanical evolution of the EDZ as transport path for radionuclides and gas: insights from the Mont Terri rock laboratory (Switzerland). Swiss Journal of Geosciences 110, 173–194. https://doi.org/10.1007/s00015-016-0246-z

Martin, C., Lanyon, G.W., Bossart, P., Blümling, P., 2004. Excavation Disturbed Zone (EDZ) in Clay Shale: Mont Terri. Unpublished Mont Terri Technical Report, TR 2001-01.

Martin, P., Gaitero, J.J., Dolado, J.S., Manzano, H., 2021. New Kinetic Monte Carlo Model to Study the Dissolution of Quartz. ACS Earth and Space Chemistry 5, 516–524. https://doi.org/10.1021/acsearthspacechem.0c00303

Matsuki, K., Lee, J.-J., Sakaguchi, K., Hayashi, K., 1999. Size effect in flow conductance of a closed small-scale hydraulic fracture in granite. Geothermal Science and Technology 6, 113–138.

Mayr, S.I., Stanchits, S., Langenbruch, C., Dresen, G., Shapiro, S.A., 2011. Acoustic emission induced by pore-pressure changes in sandstone samples. Geophysics 76, MA21–MA32. https://doi.org/10.1190/1.3569579

McDuff, D.R., Shuchart, C.E., Jackson, S.K., Postl, D., Brown, J.S., 2010. Understanding Wormholes in Carbonates: Unprecedented Experimental Scale and 3-D Visualization. Presented at the SPE Annual Technical Conference and Exhibition, OnePetro, Florence, Italy. https://doi.org/10.2118/134379-MS

McLeod, H.O., 1984. Matrix Acidizing. Journal of Petroleum Technology 36, 2055–2069. https://doi.org/10.2118/13752-PA

Meier, P.M., Trick, T., Blümling, P., Vockaert, G., 2000. Self-healing of fractures within the EDZ at the Mont Terri Rock Laboratory: results after one year of experimental work, in: Proceedings of the International Workshop on Geomechanics, Hydromechanical and Thermohydro-Mechanical Behaviour of Deep Argillaceous Rocks: Theory and Experiments. Paris, France, 11-12 Oct 2000, pp. 275–283.

Meile, C., Tuncay, K., 2006. Scale dependence of reaction rates in porous media. Advances in Water Resources 29, 62–71. https://doi.org/10.1016/j.advwatres.2005.05.007

Menaceur, H., Delage, P., Tang, A.M., Conil, N., 2016. On the Thermo-Hydro-Mechanical Behaviour of a Sheared Callovo-Oxfordian Claystone Sample with Respect to the EDZ Behaviour. Rock Mechanics and Rock Engineering 49, 1875–1888. https://doi.org/10.1007/s00603-015-0897-5

Menke, H.P., Andrew, M.G., Blunt, M.J., Bijeljic, B., 2016. Reservoir condition imaging of reactive transport in heterogeneous carbonates using fast synchrotron tomography — Effect of initial pore structure and flow conditions. Chemical Geology 428, 15–26. https://doi.org/10.1016/j.chemgeo.2016.02.030

Menke, H.P., Bijeljic, B., Andrew, M.G., Blunt, M.J., 2015. Dynamic three-dimensional pore-scale imaging of reaction in a carbonate at reservoir conditions. Environmental Science & Technology 49, 4407–4414. https://doi.org/10.1021/es505789f

Menke, H.P., Bijeljic, B., Blunt, M.J., 2017. Dynamic reservoir-condition microtomography of reactive transport in complex carbonates: Effect of initial pore structure and initial brine pH. Geochimica et Cosmochimica Acta 204, 267–285. https://doi.org/10.1016/j.gca.2017.01.053

Menke, H.P., Reynolds, C.A., Andrew, M.G., Pereira Nunes, J.P., Bijeljic, B., Blunt, M.J., 2018. 4D multi-scale imaging of reactive flow in carbonates: Assessing the impact of heterogeneity on dissolution regimes using streamlines at multiple length scales. Chemical Geology 481, 27–37. https://doi.org/10.1016/j.chemgeo.2018.01.016

Merkel, B.J., Planer-Friedrich, B., 2008. Groundwater geochemistry: a practical guide to modeling of natural and contaminated aquatic systems, 2nd ed. Springer, Berlin, Heidelberg.

Miller, K., Vanorio, T., Keehm, Y., 2017. Evolution of permeability and microstructure of tight carbonates due to numerical simulation of calcite dissolution: Permeability Trend Due to Dissolution. Journal of Geophysical Research: Solid Earth 122, 4460–4474. https://doi.org/10.1002/2017JB013972

Min, K.-B., Rutqvist, J., Tsang, C.-F., Jing, L., 2004. Stress-dependent permeability of fractured rock masses: a numerical study. International Journal of Rock Mechanics and Mining Sciences 41, 1191–1210. https://doi.org/10.1016/j.ijrmms.2004.05.005

Mo, P., Li, Y., 2019. Estimating the three-dimensional joint roughness coefficient value of rock fractures. Bulletin of Engineering Geology and the Environment 78, 857–866. https://doi.org/10.1007/s10064-017-1150-0

Moeck, I.S., 2014. Catalog of geothermal play types based on geologic controls. Renewable and Sustainable Energy Reviews 37, 867–882. https://doi.org/10.1016/j.rser.2014.05.032

Mohajan, H.K., 2017. Two criteria for good measurements in research: validity and reliability. Annals of Spiru Haret University-Economic Series 17, 59–82. https://doi.org/10.26458/1746

Mohd Amin, S., Weiss, D.J., Blunt, M.J., 2014. Reactive transport modelling of geologic CO2 sequestration in saline aquifers: The influence of pure CO2 and of mixtures of CO2 with CH4 on the sealing capacity of cap rock at 37°C and 100bar. Chemical Geology 367, 39–50. https://doi.org/10.1016/j.chemgeo.2014.01.002

Molins, S., Trebotich, D., Yang, L., Ajo-Franklin, J.B., Ligocki, T.J., Shen, C., Steefel, C.I., 2014. Pore-Scale Controls on Calcite Dissolution Rates from Flow-through Laboratory and Numerical Experiments. Environmental Science & Technology 48, 7453–7460. https://doi.org/10.1021/es5013438

Monsees, A.C., Biebricher, S.F., Busch, B., Feinendegen, M., Ziegler, M., Hilgers, C., 2021a. Coupling of diagenetic alterations and mechanical properties of Lower Permian siliciclastic sandstones: a pilot study. Environmental Earth Sciences 80, 141. https://doi.org/10.1007/s12665-021-09376-1

Monsees, A.C., Busch, B., Hilgers, C., 2021b. Compaction control on diagenesis and reservoir quality development in red bed sandstones: a case study of Permian Rotliegend sandstones. International Journal of Earth Sciences 110, 1683–1711. https://doi.org/10.1007/s00531-021-02036-6

Morad, S., 1998. Carbonate cementation in sandstones: distribution patterns and geochemical evolution, in: Morad, S. (Ed.), Carbonate Cementation in Sandstones, Special Publication Number 26 of the International Association of Sedimentologists. Blackwell Science, pp. 1–26. https://doi.org/10.1002/9781444304893.ch1

Möri, A., Bossart, P., Matray, J.M., Franck, E., Fatmi, H., Ababou, R., 2010. Mont Terri Project: cyclic deformations in the Opalinus clay, in: Proceedings of the International Meeting of Clay in Natural and Engineered Barriers for Radioactive Waste Confinements. Nantes, France, pp. 103–124.

Morse, J.W., Arvidson, R.S., 2002. The dissolution kinetics of major sedimentary carbonate minerals. Earth-Science Reviews 58, 51–84. https://doi.org/10.1016/S0012-8252(01)00083-6

Morse, J.W., Arvidson, R.S., Luttge, A., 2007. Calcium Carbonate Formation and Dissolution. Chemical Reviews 107, 342–381. https://doi.org/10.1021/cr050358j

Morse, J.W., Mackenzie, F.T., 1990. Geochemistry of Sedimentary Carbonates, Developments in Sedimentology 48. Elsevier, Amsterdam.

Myrttinen, A., Jeandel, E., Ukelis, O., Becker, V., van Geldern, R., Blum, P., Barth, J.A.C., 2012. Stable carbon isotope techniques to quantify CO2 trapping under pre-equilibrium conditions and elevated pressures and temperatures. Chemical Geology 320–321, 46–53. https://doi.org/10.1016/j.chemgeo.2012.05.008

Nagra, 2019. Implementation of the Full-scale Emplacement Experiment at Mont Terri: Design, Construction and Preliminary Results. Nagra Technical Report 15-02, Wettingen, Switzerland.

Nagra, 2002. Project Opalinus Clay: Safety Report: Demonstration of disposal feasibility for spent fuel, vitrified high-level waste and long-lived intermediate-level waste (Entsorgungsnachweis). Nagra Technical Report 02-05, Wettingen, Switzerland.

Navarre-Sitchler, A., Steefel, C.I., Yang, L., Tomutsa, L., Brantley, S.L., 2009. Evolution of porosity and diffusivity associated with chemical weathering of a basalt clast. Journal of Geophysical Research 114, F02016. https://doi.org/10.1029/2008JF001060

Nelson, R.A., 2001. Geologic Analysis of Naturally Fractured Reservoirs, 2nd ed. Elsevier, Houston, Texas.

Nemoto, K., Watanabe, N., Hirano, N., Tsuchiya, N., 2009. Direct measurement of contact area and stress dependence of anisotropic flow through rock fracture with heterogeneous aperture distribution. Earth and Planetary Science Letters 281, 81–87. https://doi.org/10.1016/j.epsl.2009.02.005

New England Research, Inc., 2015. TinyPerm3. https://www.ner.com/site/systems/tinyperm3.html. Accessed 29 July 2019.

Nikon Metrology, NV, 2010a. ModelMaker MMDx-MMC product information.

Nikon Metrology, NV, 2010b. MCA II Articulated Arms product information.

Noiriel, C., Luquot, L., Madé, B., Raimbault, L., Gouze, P., van der Lee, J., 2009. Changes in reactive surface area during limestone dissolution: An experimental and modelling study. Chemical Geology 265, 160–170. https://doi.org/10.1016/j.chemgeo.2009.01.032

Noiriel, C., Oursin, M., Daval, D., 2020. Examination of crystal dissolution in 3D: A way to reconcile dissolution rates in the laboratory? Geochimica et Cosmochimica Acta 273, 1–25. https://doi.org/10.1016/j.gca.2020.01.003

Noiriel, C., Oursin, M., Saldi, G., Haberthür, D., 2019. Direct Determination of Dissolution Rates at Crystal Surfaces Using 3D X-ray Microtomography. ACS Earth and Space Chemistry 3, 100–108. https://doi.org/10.1021/acsearthspacechem.8b00143

Noiriel, C., Soulaine, C., 2021. Pore-Scale Imaging and Modelling of Reactive Flow in Evolving Porous Media: Tracking the Dynamics of the Fluid–Rock Interface. Transport in Porous Media 140, 181–213. https://doi.org/10.1007/s11242-021-01613-2

Novakowski, K.S., Lapcevic, P.A., 1994. Field measurement of radial solute transport in fractured rock. Water Resources Research 30, 37–44. https://doi.org/10.1029/93WR02401

Nussbaum, C., Bossart, P., Amann, F., Aubourg, C., 2011. Analysis of tectonic structures and excavation induced fractures in the Opalinus Clay, Mont Terri underground rock laboratory (Switzerland). Swiss Journal of Geosciences 104, 187–210. https://doi.org/10.1007/s00015-011-0070-4

Nussbaum, C., Bossart, P., von Rütte, J., Meier, O., Badertscher, N., 2005. EZ-B Experiment: Small-scale Mapping of Tectonic and Artificial (EDZ) Fractures of the EZ-B Niche. Unpublished Mont Terri Technical Note, TN 2005-30.

Ohser, J., Mücklich, F., 2000. Statistical Analysis of Microstructures in Materials Science. John Wiley & Sons, Ltd., Chichester, United Kingdom.

Okada, S., Izumiya, Y., Iizuka, Y., Horiuchi, S., 1985. The estimation of soft rock strength around a tunnel by needle penetration test. Japanese Society of Soil Mechanics and Foundation Engineering 33, 35–38.

Olsson, R., Barton, N., 2001. An improved model for hydromechanical coupling during shearing of rock joints. International Journal of Rock Mechanics and Mining Sciences 38, 317–329. https://doi.org/10.1016/S1365-1609(00)00079-4

Pandey, S.N., Vishal, V., Chaudhuri, A., 2018. Geothermal reservoir modeling in a coupled thermo-hydro-mechanical-chemical approach: A review. Earth-Science Reviews 185, 1157–1169. https://doi.org/10.1016/j.earscirev.2018.09.004

Parkhurst, D.L., 1995. User's guide to PHREEQC: A computer program for speciation, reaction-path, advective-transport, and inverse geochemical calculations. USGS Water-Resources Investigation Report 95-4227.

Patir, N., Cheng, H.S., 1978. An Average Flow Model for Determining Effects of Three-Dimensional Roughness on Partial Hydrodynamic Lubrication. Journal of Lubrication Technology 100, 12–17. https://doi.org/10.1115/1.3453103

Pearson, F.J., Arcos, D., Bath, A., Boisson, J.-Y., Fernández, A.M., Gäbler, H.-E., Gaucher, E., Gautschi, A., Griffault, L., Hernán, P., Waber, H.N., 2003. Mont Terri Project: Geochemistry of Water in the Opalinus Clay Formation at the Mont Terry Rock Laboratory. Reports of the Federal Office for Water and Geology (FOWG), Geology Series No. 5, Bern-Ittigen, Switzerland.

Pedrosa, E.T., Fischer, C., Morales, L.F.G., Rohlfs, R.D., Luttge, A., 2021. Influence of chemical zoning on sandstone calcite cement dissolution: The case of manganese and iron. Chemical Geology 559, 119952. https://doi.org/10.1016/j.chemgeo.2020.119952

Pedrosa, E.T., Kurganskaya, I., Fischer, C., Luttge, A., 2019. A Statistical Approach for Analysis of Dissolution Rates Including Surface Morphology. Minerals 9, 458. https://doi.org/10.3390/min9080458

Peng, C., Crawshaw, J.P., Maitland, G.C., Trusler, J.P.M., 2015. Kinetics of calcite dissolution in CO2-saturated water at temperatures between (323 and 373) K and pressures up to 13.8 MPa. Chemical Geology 403, 74–85. https://doi.org/10.1016/j.chemgeo.2015.03.012

Pereira Nunes, J.P., Blunt, M.J., Bijeljic, B., 2016. Pore-scale simulation of carbonate dissolution in micro-CT images. Journal of Geophysical Research: Solid Earth 121, 558–576. https://doi.org/10.1002/2015JB012117

Peters, C.A., 2009. Accessibilities of reactive minerals in consolidated sedimentary rock: An imaging study of three sandstones. Chemical Geology 265, 198–208. https://doi.org/10.1016/j.chemgeo.2008.11.014

Petrie, E.S., Petrie, R.A., Evans, J.P., 2014. Identification of reactivation and increased permeability associated with a fault damage zone using a multidisciplinary approach. Journal of Structural Geology 59, 37–49. https://doi.org/10.1016/j.jsg.2013.11.008

Plein, E., 1993. Bemerkungen zum Ablauf der paläogeographischen Entwicklung im Stefan und Rotliegend des Norddeutschen Beckens. Geologisches Jahrbuch. Reihe A, Allgemeine und regionale Geologie BR Deutschland und Nachbargebiete, Tektonik, Stratigraphie, Paläontologie 131, 99–116.

Plummer, L.N., Wigley, T.M.L., Parkhurst, D.L., 1978. The kinetics of calcite dissolution in CO2-water systems at 5° to 60°C and 0.0 to 1.0 atm CO2. American Journal of Science 278, 179–216. https://doi.org/10.2475/ajs.278.2.179

Pokrovsky, O.S., Golubev, S.V., Schott, J., Castillo, A., 2009. Calcite, dolomite and magnesite dissolution kinetics in aqueous solutions at acid to circumneutral pH, 25 to 150 °C and 1 to 55 atm pCO2: New constraints on CO2 sequestration in sedimentary basins. Chemical Geology 265, 20–32. https://doi.org/10.1016/j.chemgeo.2009.01.013

Popp, T., Salzer, K., Minkley, W., 2008. Influence of bedding planes to EDZ-evolution and the coupled HM properties of Opalinus Clay. Physics and Chemistry of the Earth, Parts A/B/C 33, S374–S387. https://doi.org/10.1016/j.pce.2008.10.018

Possemiers, M., Huysmans, M., Peeters, L., Batelaan, O., Dassargues, A., 2012. Relationship between sedimentary features and permeability at different scales in the Brussels Sands. Geologica Belgica 15, 156–164.

Power, W.L., Durham, W.B., 1997. Topography of natural and artificial fractures in granitic rocks: implications for studies of rock friction and fluid migration. International Journal of Rock Mechanics & Mining Sciences 34, 979–989. https://doi.org/10.1016/S1365-1609(97)80007-X

Prill, T., Fischer, C., Gavrilenko, P., Iliev, O., 2021. Implementing the Variability of Crystal Surface Reactivity in Reactive Transport Modeling. Transport in Porous Media 140, 535–557. https://doi.org/10.1007/s11242-021-01697-w

Pruess, K., 1990. Modeling of geothermal reservoirs: Fundamental processes, computer simulation and field applications. Geothermics 19, 3–15. https://doi.org/10.1016/0375-6505(90)90062-G

Pusch, R., Stanfors, R., 1992. The zone of disturbance around blasted tunnels at depth. International Journal of Rock Mechanics and Mining Sciences & Geomechanics Abstracts 29, 447–456. https://doi.org/10.1016/0148-9062(92)92629-Q

Puyguiraud, A., Gouze, P., Dentz, M., 2019. Stochastic Dynamics of Lagrangian Pore-Scale Velocities in Three-Dimensional Porous Media. Water Resources Research 55, 1196–1217. https://doi.org/10.1029/2018WR023702

Pyrak-Nolte, L.J., Montemagno, C.D., Nolte, D.D., 1997. Volumetric imaging of aperture distributions in connected fracture networks. Geophysical Research Letters 24, 2343–2346. https://doi.org/10.1029/97GL02057

Pyrak-Nolte, L.J., Morris, J.P., 2000. Single fractures under normal stress: The relation between fracture specific stiffness and fluid flow. International Journal of Rock Mechanics and Mining Sciences 37, 245–262. https://doi.org/10.1016/S1365-1609(99)00104-5

Qajar, J., Arns, C.H., 2016. Characterization of reactive flow-induced evolution of carbonate rocks using digital core analysis- part 1: Assessment of pore-scale mineral dissolution and deposition. Journal of Contaminant Hydrology 192, 60–86. https://doi.org/10.1016/j.jconhyd.2016.06.005

Rasouli, V., Hosseinian, A., 2011. Correlations Developed for Estimation of Hydraulic Parameters of Rough Fractures Through the Simulation of JRC Flow Channels. Rock Mechanics and Rock Engineering 44, 447–461. https://doi.org/10.1007/s00603-011-0148-3

Ren, F., Ma, G., Fan, L., Wang, Y., Zhu, H., 2017. Equivalent discrete fracture networks for modelling fluid flow in highly fractured rock mass. Engineering Geology 229, 21–30. https://doi.org/10.1016/j.enggeo.2017.09.013

Renshaw, C.E., 1995. On the relationship between mechanical and hydraulic apertures in rough-walled fractures. Journal of Geophysical Research: Solid Earth 100, 24629–24636. https://doi.org/10.1029/95JB02159

Renshaw, C.E., Dadakis, J.S., Brown, S.R., 2000. Measuring fracture apertures: A comparison of methods. Geophysical Research Letters 27, 289–292. https://doi.org/10.1029/1999GL008384

Reuther, C.-D., 2012. Grundlagen der Tektonik: Kräften und Spannungen der Erde auf der Spur. Springer-Verlag, Berlin, Heidelberg. https://doi.org/10.1007/978-3-8274-2724-3

Rimstidt, J.D., Brantley, S.L., Olsen, A.A., 2012. Systematic review of forsterite dissolution rate data. Geochimica et Cosmochimica Acta 99, 159–178. https://doi.org/10.1016/j.gca.2012.09.019

Rohlfs, R., Fischer, C., Kurganskaya, I., Luttge, A., 2018. Crystal Dissolution Kinetics Studied by a Combination of Monte Carlo and Voronoi Methods. Minerals 8, 133. https://doi.org/10.3390/min8040133

Rötting, T.S., Luquot, L., Carrera, J., Casalinuovo, D.J., 2015. Changes in porosity, permeability, water retention curve and reactive surface area during carbonate rock dissolution. Chemical Geology 403, 86–98. https://doi.org/10.1016/j.chemgeo.2015.03.008

Rubin, Y., 2003. Applied stochastic hydrogeology. Oxford University Press, Oxford, New York.

Rummel, F., Weber, U., 2007. Rock Mechanics Analyses (RA) Experiment: Mont Terri Project, Phase 10: Results of Uniaxial and Triaxial Tests on Opalinus Clay Samples. Unpublished Mont Terri Technical Note, TN 2005-57.

Rummel, F., Weber, U., 2004. RA Experiment (Rock Mechanics Analysis): Rock Mechanical Testing and Characterization on Drillcores of Boreholes BRA-1 and BRA-2. Unpublished Mont Terri Technical Note, TN 2004-38.

Rutqvist, J., Stephansson, O., 2003. The role of hydromechanical coupling in fractured rock engineering. Hydrogeology Journal 11, 7–40. https://doi.org/10.1007/s10040-002-0241-5

Saif, T., Lin, Q., Butcher, A.R., Bijeljic, B., Blunt, M.J., 2017. Multi-scale multi-dimensional microstructure imaging of oil shale pyrolysis using X-ray micro-tomography, automated ultra-high resolution SEM, MAPS Mineralogy and FIB-SEM. Applied Energy 202, 628–647. https://doi.org/10.1016/j.apenergy.2017.05.039

Saldi, G.D., Voltolini, M., Knauss, K.G., 2017. Effects of surface orientation, fluid chemistry and mechanical polishing on the variability of dolomite dissolution rates. Geochimica et Cosmochimica Acta 206, 94–111. https://doi.org/10.1016/j.gca.2017.02.007

Salehikhoo, F., Li, L., Brantley, S.L., 2013. Magnesite dissolution rates at different spatial scales: The role of mineral spatial distribution and flow velocity. Geochimica et Cosmochimica Acta 108, 91–106. https://doi.org/10.1016/j.gca.2013.01.010

Sato, T., Kikuchi, T., Sugihara, K., 2000. In-situ experiments on an excavation disturbed zone induced by mechanical excavation in Neogene sedimentary rock at Tono mine, central Japan. Engineering Geology 56, 97–108. https://doi.org/10.1016/S0013-7952(99)00136-2

Saxena, N., Hows, A., Hofmann, R., Alpak, F.O., Freeman, J., Hunter, S., Appel, M., 2018. Imaging and computational considerations for image computed permeability: Operating envelope of Digital Rock Physics. Advances in Water Resources 116, 127–144. https://doi.org/10.1016/j.advwatres.2018.04.001

Scesi, L., Gattinoni, P., 2007. Roughness control on hydraulic conductivity in fractured rocks. Hydrogeology Journal 15, 201–211. https://doi.org/10.1007/s10040-006-0076-6

Schmittbuhl, J., Gentier, S., Roux, S., 1993. Field measurements of the roughness of fault surfaces. Geophysical Research Letters 20, 639–641. https://doi.org/10.1029/93GL00170

Schnier, H., Stührenberg, D., 2007. LT Experiment: Strength tests on cylindrical specimens, documentation and evaluation (phases 8 & 9). Unpublished Mont Terri Technical Report, TR 2003-04.

Schröder, L., Plein, E., Bachmann, G.-H., Gast, R.E., Gebhardt, U., Graf, R., Helmuth, H.-J., Pasternak, M., Porth, H., Süssmuth, S., 1995. Stratigraphische Neugliederung des Rotliegend im Norddeutschen Becken. Geologisches Jahrbuch Reihe A 148, 3–21.

Schuster, K., Amann, F., Yong, S., Bossart, P., Connolly, P., 2017. High-resolution mini-seismic methods applied in the Mont Terri rock laboratory (Switzerland). Swiss Journal of Geosciences 110, 213–231. https://doi.org/10.1007/s00015-016-0241-4

Schutjens, P.M.T.M., Hanssen, T.H., Hettema, M.H.H., Merour, J., de Bree, P., Coremans, J.W.A., Helliesen, G., 2004. Compaction-Induced Porosity/Permeability Reduction in Sandstone Reservoirs: Data and Model for Elasticity-Dominated Deformation. SPE Reservoir Evaluation & Engineering 7, 202–216. https://doi.org/10.2118/88441-PA

Scislewski, A., Zuddas, P., 2010. Estimation of reactive mineral surface area during water–rock interaction using fluid chemical data. Geochimica et Cosmochimica Acta 74, 6996–7007. https://doi.org/10.1016/j.gca.2010.09.015

Shafiq, M.U., Chong, Y.J., Mahmud, H.K.B., Hossain, M.M., Rezaee, R., Testamanti, N., 2019. Application of emulsified acids on sandstone formation at elevated temperature conditions: an experimental study. Journal of Petroleum Exploration and Production Technology 9, 1323–1329. https://doi.org/10.1007/s13202-018-0567-8

Shahraini, A., Ali, A., Jakobsen, M., 2011. Characterization of fractured reservoirs using a consistent stiffness-permeability model: focus on the effects of fracture aperture.

Geophysical Prospecting 59, 492–505. https://doi.org/10.1111/j.1365-2478.2010.00934.x

Shaik, A.R., Rahman, S.S., Tran, N.H., Tran, T., 2011. Numerical simulation of Fluid-Rock coupling heat transfer in naturally fractured geothermal system. Applied Thermal Engineering 31, 1600–1606. https://doi.org/10.1016/j.applthermaleng.2011.01.038

Shao, H., Schuster, K., Sönnke, J., Bräuer, V., 2008. EDZ development in indurated clay formations – In situ borehole measurements and coupled HM modelling. Physics and Chemistry of the Earth, Parts A/B/C 33, S388–S395. https://doi.org/10.1016/j.pce.2008.10.031

Shen, B., Barton, N., 1997. The disturbed zone around tunnels in jointed rock masses. International Journal of Rock Mechanics and Mining Sciences 34, 117–125.

Sheng, Q., Yue, Z.Q., Lee, C.F., Tham, L.G., Zhou, H., 2002. Estimating the excavation disturbed zone in the permanent shiplock slopes of the Three Gorges Project, China. International Journal of Rock Mechanics and Mining Sciences 39, 165–184. https://doi.org/10.1016/S1365-1609(02)00015-1

Shiraki, R., Dunn, T.L., 2000. Experimental study on water-rock interactions during CO2 flooding in the Tensleep Formation, Wyoming, USA. Applied Geochemistry 15, 265–279. https://doi.org/10.1016/S0883-2927(99)00048-7

Shu, B., Zhu, R., Tan, J., Zhang, S., Liang, M., 2019. Evolution of permeability in a single granite fracture at high temperature. Fuel 242, 12–22. https://doi.org/10.1016/j.fuel.2019.01.031

Sidle, R.C., Nilsson, B., Hansen, M., Fredericia, J., 1998. Spatially varying hydraulic and solute transport characteristics of a fractured till determined by field tracer tests, Funen, Denmark. Water Resources Research 34, 2515–2527. https://doi.org/10.1029/98WR01735

Sjöberg, E.L., Rickard, D.T., 1984. Calcite dissolution kinetics: Surface speciation and the origin of the variable pH dependence. Chemical Geology 42, 119–136. https://doi.org/10.1016/0009-2541(84)90009-3

Smart, B.G.D., Somerville, J.M., Edlman, K., Jones, C., 2001. Stress sensitivity of fractured reservoirs. Journal of Petroleum Science and Engineering 29, 29–37. https://doi.org/10.1016/S0920-4105(00)00088-7

Smith, L., Mase, C.W., Schwartz, F.W., 1987. Estimation of fracture aperture using hydraulic and tracer tests. Presented at the 28th US Symposium on Rock Mechanics (USRMS), American Rock Mechanics Association, Tucson, Arizona.

Snow, D.T., 1965. A parallel plate model of fractured permeable media (PhD thesis). University of California, Berkeley.

Soe, A.K.K., Osada, M., Takahashi, M., Sasaki, T., 2009. Characterization of drying-induced deformation behaviour of Opalinus Clay and tuff in no-stress regime. Environmental Geology 58, 1215–1225. https://doi.org/10.1007/s00254-008-1616-2

Soler, J.M., 2001. The effect of coupled transport phenomena in the Opalinus Clay and implications for radionuclide transport. Journal of Contaminant Hydrology 53, 63–84. https://doi.org/10.1016/S0169-7722(01)00140-1

Steefel, C., Depaolo, D., Lichtner, P., 2005. Reactive transport modeling: An essential tool and a new research approach for the Earth sciences. Earth and Planetary Science Letters 240, 539–558. https://doi.org/10.1016/j.epsl.2005.09.017

Steefel, C.I., Maher, K., 2009. Fluid-rock interaction: A reactive transport approach. Reviews in Mineralogy and Geochemistry 70, 485–532. https://doi.org/10.2138/rmg.2009.70.11

Stephansson, O., Hudson, J., Jing, L., 2004. Coupled Thermo-Hydro-Mechanical-Chemical Processes in Geo-systems. Elsevier.

Stigsson, M., Mas Ivars, D., 2019. A Novel Conceptual Approach to Objectively Determine JRC Using Fractal Dimension and Asperity Distribution of Mapped Fracture Traces. Rock Mechanics and Rock Engineering 52, 1041–1054. https://doi.org/10.1007/s00603-018-1651-6

Stoll, M., Huber, F.M., Trumm, M., Enzmann, F., Meinel, D., Wenka, A., Schill, E., Schäfer, T., 2019. Experimental and numerical investigations on the effect of fracture geometry and fracture aperture distribution on flow and solute transport in natural fractures. Journal of Contaminant Hydrology 221, 82–97. https://doi.org/10.1016/j.jconhyd.2018.11.008

Strauhal, T., Loew, S., Holzmann, M., Zangerl, C., 2016. Detailed hydrogeological analysis of a deep-seated rockslide at the Gepatsch reservoir (Klasgarten, Austria). Hydrogeology Journal 24, 349–371. https://doi.org/10.1007/s10040-015-1341-3

Sturzenegger, M., Stead, D., 2009. Close-range terrestrial digital photogrammetry and terrestrial laser scanning for discontinuity characterization on rock cuts. Engineering Geology 106, 163–182. https://doi.org/10.1016/j.enggeo.2009.03.004

Su, Y., Yang, F., Wang, B., Jia, Z., Duan, Z., 2018. Reinjection of cooled water into sandstone geothermal reservoirs in China: a review. Geosciences Journal 22, 199–207. https://doi.org/10.1007/s12303-017-0019-3

Svensson, U., Trinchero, P., Ferry, M., Voutilainen, M., Gylling, B., Selroos, J.-O., 2019. Grains, grids and mineral surfaces: approaches to grain-scale matrix modeling based on X-ray micro-computed tomography data. SN Applied Sciences 1, 1277. https://doi.org/10.1007/s42452-019-1254-1

Swoboda-Colberg, N.G., Drever, J.I., 1993. Mineral dissolution rates in plot-scale field and laboratory experiments. Chemical Geology 105, 51–69. https://doi.org/10.1016/0009-2541(93)90118-3

Tan, Q., You, L., Kang, Y., Zhang, X., Meng, S., 2020. Changes in pore structures and porosity-permeability evolution of saline-lacustrine carbonate reservoir triggered by fresh water-rock reaction. Journal of Hydrology 580, 124375. https://doi.org/10.1016/j.jhydrol.2019.124375

Tatone, B.S.A., Grasselli, G., 2013. An Investigation of Discontinuity Roughness Scale Dependency Using High-Resolution Surface Measurements. Rock Mechanics and Rock Engineering 46, 657–681. https://doi.org/10.1007/s00603-012-0294-2

Thoeny, R., 2014. Geomechanical analysis of excavation-induced rock mass behavior of faulted Opalinus Clay at the Mont Terri Underground Rock Laboratory (Switzerland) (PhD thesis). ETH Zurich, Switzerland.

Thörn, J., Fransson, Å., 2015. A new apparatus and methodology for hydromechanical testing and geometry scanning of a rock fracture under low normal stress. International Journal of Rock Mechanics and Mining Sciences 79, 216–226. https://doi.org/10.1016/j.ijrmms.2015.08.015

Trajković, G., 2008. Measurement: Accuracy and Precision, Reliability and Validity, in: Kirch, W. (Ed.), Encyclopedia of Public Health. Springer Netherlands, Dordrecht, pp. 888–892. https://doi.org/10.1007/978-1-4020-5614-7_2081

Tsang, C.F., Barnichon, J.D., Birkholzer, J., Li, X.L., Liu, H.H., Sillen, X., 2012. Coupled thermo-hydro-mechanical processes in the near field of a high-level radioactive waste repository in clay formations. International Journal of Rock Mechanics and Mining Sciences 49, 31–44. https://doi.org/10.1016/j.ijrmms.2011.09.015

Tsang, C.-F., Bernier, F., Davies, C., 2005. Geohydromechanical processes in the Excavation Damaged Zone in crystalline rock, rock salt, and indurated and plastic clays—in the context of radioactive waste disposal. International Journal of Rock Mechanics and Mining Sciences 42, 109–125. https://doi.org/10.1016/j.ijrmms.2004.08.003

Tsang, C.-F., Neretnieks, I., Tsang, Y., 2015. Hydrologic issues associated with nuclear waste repositories. Water Resources Research 51, 6923–6972. https://doi.org/10.1002/2015WR017641

Tsang, Y.W., Witherspoon, P.A., 1983. The dependence of fracture mechanical and fluid flow properties on fracture roughness and sample size. Journal of Geophysical Research 88, 2359. https://doi.org/10.1029/JB088iB03p02359

Tsang, Y.W., Witherspoon, P.A., 1981. Hydromechanical behavior of a deformable rock fracture subject to normal stress. Journal of Geophysical Research: Solid Earth 86, 9287–9298. https://doi.org/10.1029/JB086iB10p09287

Uchida, N., Etoh, Y., Ono, H., Miura, N., 2004. Strength evaluation of deep mixing soil–cement by needle penetration test. Japanese Society of Soil Mechanics and Foundation Engineering 52, 23-25 (in Japanese).

Ulusay, R., Aydan, Ö., Erguler, Z.A., Ngan-Tillard, D.J.M., Seiki, T., Verwaal, W., Sasaki, Y., Sato, A., 2014. ISRM Suggested Method for the Needle Penetration Test. Rock Mechanics and Rock Engineering 47, 1073–1085. https://doi.org/10.1007/s00603-013-0534-0

Ulusay, R., Erguler, Z.A., 2012. Needle penetration test: Evaluation of its performance and possible uses in predicting strength of weak and soft rocks. Engineering Geology 149–150, 47–56. https://doi.org/10.1016/j.enggeo.2012.08.007

Ungemach, P., 2003. Reinjection of cooled geothermal brines into sandstone reservoirs. Geothermics 32, 743–761. https://doi.org/10.1016/S0375-6505(03)00074-9

United Nations, 2015. Transforming our world: the 2030 Agenda for Sustainable Development (No. A/RES/70/1). Resolution adopted by the General Assembly on 25 September, 2015.

Valès, F., Nguyen-Minh, D., Gharbi, H., Rejeb, A., 2004. Experimental study of the influence of the degree of saturation on physical and mechanical properties in Tournemire shale (France). Applied Clay Science 26, 197–207. https://doi.org/10.1016/j.clay.2003.12.032

Van Loon, L.R., Soler, J.M., Jakob, A., Bradbury, M.H., 2003. Effect of confining pressure on the diffusion of HTO, 36Cl− and 125I− in a layered argillaceous rock (Opalinus Clay): diffusion perpendicular to the fabric. Applied Geochemistry 18, 1653–1662. https://doi.org/10.1016/S0883-2927(03)00047-7

Vinson, M.D., Luttge, A., 2005. Multiple length-scale kinetics: an integrated study of calcite dissolution rates and strontium inhibition. American Journal of Science 305, 119–146. https://doi.org/10.2475/ajs.305.2.119

Vogler, D., 2016. Hydro-mechanically coupled processes in heterogeneous fractures: experiments and numerical simulations (PhD thesis). ETH Zurich, Switzerland.

Vogler, D., Settgast, R., Annavarapu, C., Bayer, P., Amann, F., 2016. Hydro-Mechanically Coupled Flow through Heterogeneous Fractures. Presented at the 41st Workshop on Geothermal Reservoir Engineering, Stanford University, Stanford, California.

Vogler, D., Settgast, R.R., Annavarapu, C., Madonna, C., Bayer, P., Amann, F., 2018. Experiments and simulations of fully hydro-mechanically coupled response of rough fractures exposed to high-pressure fluid injection. Journal of Geophysical Research: Solid Earth 123, 1186–1200. https://doi.org/10.1002/2017JB015057

Vogler, D., Walsh, S.D.C., Bayer, P., Amann, F., 2017. Comparison of Surface Properties in Natural and Artificially Generated Fractures in a Crystalline Rock. Rock Mechanics and Rock Engineering 50, 2891–2909. https://doi.org/10.1007/s00603-017-1281-4

von Planta, C., Vogler, D., Chen, X., Nestola, M.G.C., Saar, M.O., Krause, R., 2019. Simulation of hydro-mechanically coupled processes in rough rock fractures using an immersed boundary method and variational transfer operators. Computational Geosciences 23, 1125–1140. https://doi.org/10.1007/s10596-019-09873-0

Waldmann, S., Busch, A., van Ojik, K., Gaupp, R., 2014. Importance of mineral surface areas in Rotliegend sandstones for modeling CO2–water–rock interactions. Chemical Geology 378–379, 89–109. https://doi.org/10.1016/j.chemgeo.2014.03.014

Walsh, R., Nasir, O., Leung, H., Avis, J., 2015. Numerical Characterization of the Excavation Damaged Zone in the HG-A Experiment. Presented at the International High-Level Radioactive Waste Management, Charleston, South Carolina.

Wang, M., Chen, Y.-F., Ma, G.-W., Zhou, J.-Q., Zhou, C.-B., 2016. Influence of surface roughness on nonlinear flow behaviors in 3D self-affine rough fractures: Lattice

Boltzmann simulations. Advances in Water Resources 96, 373–388. https://doi.org/10.1016/j.advwatres.2016.08.006

Wang, X., Aliouache, M., Wang, Y., Lei, Q., Jourde, H., 2021. The role of aperture heterogeneity in incipient karst evolution in natural fracture networks: Insights from numerical simulations. Advances in Water Resources 156, 104036. https://doi.org/10.1016/j.advwatres.2021.104036

Wang, Z., Xu, C., Dowd, P., 2018. A Modified Cubic Law for single-phase saturated laminar flow in rough rock fractures. International Journal of Rock Mechanics and Mining Sciences 103, 107–115. https://doi.org/10.1016/j.ijrmms.2017.12.002

Weede, M., Hötzl, H., 2005. Strömung und Transport in einer natürlichen Einzelkluft in poröser Matrix—Experimente und Modellierung. Grundwasser 10, 137–145. https://doi.org/10.1007/s00767-005-0090-y

Wernecke, C., Marsch, K., 2015. Mapping rock surface roughness with photogrammetry. Presented at the ISRM Regional Symposium EUROCK 2015 - Future Development of Rock Mechanics, Österr. Ges. für Geomechanik, Salzburg, Austria.

White, A.F., Brantley, S.L., 2003. The effect of time on the weathering of silicate minerals: why do weathering rates differ in the laboratory and field? Chemical Geology 202, 479–506. https://doi.org/10.1016/j.chemgeo.2003.03.001

Wigger, C., Van Loon, L.R., 2018. Effect of the pore water composition on the diffusive anion transport in argillaceous, low permeability sedimentary rocks. Journal of Contaminant Hydrology 213, 40–48. https://doi.org/10.1016/j.jconhyd.2018.05.001

Wild, K.M., Wymann, L.P., Zimmer, S., Thoeny, R., Amann, F., 2015. Water Retention Characteristics and State-Dependent Mechanical and Petro-Physical Properties of a Clay Shale. Rock Mechanics and Rock Engineering 48, 427–439. https://doi.org/10.1007/s00603-014-0565-1

Wileveau, Y., 2005. THM behaviour of host rock (HE-D experiment): Progress Report September 2003 – October 2004, Part 1. Unpublished Mont Terri Technical Report, TR 2005-03.

Wilson, K.J., Berryman, K.R., 2010. Assessing the long-term stability of geological environments for safe disposal of radioactive waste, in: Ahn, J., Apted, M.J. (Eds.), Geological Repository Systems for Safe Disposal of Spent Nuclear Fuels and Radioactive Waste, Woodhead Publishing Series in Energy. Woodhead Publishing, pp. 188–221. https://doi.org/10.1533/9781845699789.2.188

Wilson, M.J., Wilson, L., Patey, I., 2014. The influence of individual clay minerals on formation damage of reservoir sandstones: a critical review with some new insights. Clay Minerals 49, 147–164. https://doi.org/10.1180/claymin.2014.049.2.02

Witherspoon, P.A., Wang, J.S.Y., Iwai, K., Gale, J.E., 1980. Validity of Cubic Law for fluid flow in a deformable rock fracture. Water Resources Research 16, 1016–1024. https://doi.org/10.1029/WR016i006p01016

Wu, F., Liu, J., Liu, T., Zhuang, H., Yan, C., 2009. A method for assessment of excavation damaged zone (EDZ) of a rock mass and its application to a dam foundation case. Engineering Geology 104, 254–262. https://doi.org/10.1016/j.enggeo.2008.11.005

Xiao, F., Zhao, Z., 2018. Evaluation of equivalent hydraulic aperture (EHA) for rough rock fractures. Canadian Geotechnical Journal. https://doi.org/10.1139/cgj-2018-0274

Xiong, X., Li, B., Jiang, Y., Koyama, T., Zhang, C., 2011. Experimental and numerical study of the geometrical and hydraulic characteristics of a single rock fracture during shear. International Journal of Rock Mechanics and Mining Sciences 48, 1292–1302. https://doi.org/10.1016/j.ijrmms.2011.09.009

Xu, J., Fan, C., Teng, H.H., 2012. Calcite dissolution kinetics in view of Gibbs free energy, dislocation density, and pCO2. Chemical Geology 322–323, 11–18. https://doi.org/10.1016/j.chemgeo.2012.04.019

Xue, Y., Dang, F., Shi, F., Li, R., Cao, Z., 2018. Evaluation of Gas Migration and Rock Damage Characteristics for Underground Nuclear Waste Storage Based on a Coupled Model.

Science and Technology of Nuclear Installations 2018, 1–10. https://doi.org/10.1155/2018/2973279

Yang, Y., Li, Y., Yao, J., Iglauer, S., Luquot, L., Zhang, K., Sun, H., Zhang, L., Song, W., Wang, Z., 2020. Dynamic Pore-Scale Dissolution by CO2-Saturated Brine in Carbonates: Impact of Homogeneous Versus Fractured Versus Vuggy Pore Structure. Water Resources Research 56. https://doi.org/10.1029/2019WR026112

Yang, Z.Y., Lo, S.C., Di, C.C., 2001. Reassessing the joint roughness coefficient (JRC) estimation using Z2. Rock Mechanics and Rock Engineering 34, 243–251. https://doi.org/10.1007/s006030170012

Ye, Z., Wang, J.G., 2020. A Thermal-Hydraulic-Mechanical Coupling Study of Heat Extraction from the Geothermal Reservoir with a Discrete Fracture Network. Geofluids 2020, 1–18. https://doi.org/10.1155/2020/8875918

Yong, S., 2007. A three-dimensional analysis of excavation-induced perturbations in the Opalinus Clay at the Mont Terri Rock Laboratory (PhD thesis). ETH Zurich, Switzerland.

Yong, S., Kaiser, P.K., Loew, S., 2010. Influence of tectonic shears on tunnel-induced fracturing. International Journal of Rock Mechanics and Mining Sciences 47, 894–907. https://doi.org/10.1016/j.ijrmms.2010.05.009

Yong, S., Loew, S., Schuster, K., Nussbaum, C., Fidelibus, C., 2017. Characterisation of Excavation-Induced Damage Around a Short Test Tunnel in the Opalinus Clay. Rock Mechanics and Rock Engineering 50, 1959–1985. https://doi.org/10.1007/s00603-017-1212-4

Younesian-Farid, H., Sadeghnejad, S., 2020. Modeling geochemical reactions of citric acid with ankerite cement during sandstone matrix acidizing. Journal of Petroleum Science and Engineering 185, 106650. https://doi.org/10.1016/j.petrol.2019.106650

Yu, X., Regenauer-Lieb, K., Tian, F.-B., 2020. Effects of surface roughness and derivation of scaling laws on gas transport in coal using a fractal-based lattice Boltzmann method. Fuel 259, 116229. https://doi.org/10.1016/j.fuel.2019.116229

Yu, X., Vayssade, B., 1991. Joint profiles and their roughness parameters. International Journal of Rock Mechanics and Mining Sciences & Geomechanics Abstracts 28, 333–336. https://doi.org/10.1016/0148-9062(91)90598-G

Yurikov, A., Lebedev, M., Pervukhina, M., Gurevich, B., 2019. Water retention effects on elastic properties of Opalinus shale. Geophysical Prospecting 67, 984–996. https://doi.org/10.1111/1365-2478.12673

Zambrano, M., Pitts, A.D., Salama, A., Volatili, T., Giorgioni, M., Tondi, E., 2019. Analysis of fracture roughness control on permeability using SfM and fluid flow simulations: Implications for carbonate reservoir characterization. Geofluids 2019, 4132386. https://doi.org/10.1155/2019/4132386

Zeeb, C., Göckus, D., Bons, P., Al Ajmi, H., Rausch, R., Blum, P., 2010. Fracture flow modelling based on satellite images of the Wajid Sandstone, Saudi Arabia. Hydrogeology Journal 18, 1699–1712. https://doi.org/10.1007/s10040-010-0609-x

Zhang, C.-L., 2018. Thermo-hydro-mechanical behavior of clay rock for deep geological disposal of high-level radioactive waste. Journal of Rock Mechanics and Geotechnical Engineering 10, 992–1008. https://doi.org/10.1016/j.jrmge.2018.03.006

Zhang, C.-L., 2016. The stress–strain–permeability behaviour of clay rock during damage and recompaction. Journal of Rock Mechanics and Geotechnical Engineering 8, 16–26. https://doi.org/10.1016/j.jrmge.2015.10.001

Zhang, C.-L., Rothfuchs, T., Su, K., Hoteit, N., 2007. Experimental study of the thermo-hydro-mechanical behaviour of indurated clays. Physics and Chemistry of the Earth, Parts A/B/C 32, 957–965. https://doi.org/10.1016/j.pce.2006.04.038

Zhang, X., Ma, F., Yin, S., Wallace, C.D., Soltanian, M.R., Dai, Z., Ritzi, R.W., Ma, Z., Zhan, C., Lü, X., 2021. Application of upscaling methods for fluid flow and mass transport in multi-scale heterogeneous media: A critical review. Applied Energy 303, 117603. https://doi.org/10.1016/j.apenergy.2021.117603

Zhao, J., 1997. Joint surface matching and shear strength part A: joint matching coefficient (JMC). International Journal of Rock Mechanics and Mining Sciences 34, 173–178. https://doi.org/10.1016/S0148-9062(96)00062-9

Zhao, Z., 2017. Application of discrete element approach in fractured rock masses, in: Shojaei, A.K., Shao, J. (Eds.), Porous Rock Fracture Mechanics. Elsevier, pp. 145–176. https://doi.org/10.1016/B978-0-08-100781-5.00007-5

Zhao, Z., Jing, L., Neretnieks, I., Moreno, L., 2011. Numerical modeling of stress effects on solute transport in fractured rocks. Computers and Geotechnics 38, 113–126. https://doi.org/10.1016/j.compgeo.2010.10.001

Zheng, S., Kumar, A., Gala, D.P., Shrivastava, K., Sharma, M.M., 2019. Simulating Production from Complex Fracture Networks: Impact of Geomechanics and Closure of Propped/Unpropped Fractures, in: Proceedings of the 7th Unconventional Resources Technology Conference. Presented at the Unconventional Resources Technology Conference, Denver, Colorado. https://doi.org/10.15530/urtec-2019-21

Zhou, D., Tatomir, A., Niemi, A., Tsang, C.-F., Sauter, M., 2021. Study of Fracture Aperture Variation in a Fracture Network on Heat Production from an Enhanced Geothermal System (EGS). SSRN Electronic Journal. https://doi.org/10.2139/ssrn.3918922

Zhu, C., 2005. In situ feldspar dissolution rates in an aquifer. Geochimica et Cosmochimica Acta 69, 1435–1453. https://doi.org/10.1016/j.gca.2004.09.005

Ziefle, G., Matray, J.-M., Maßmann, J., Möri, A., 2017. Coupled hydraulic-mechanical simulation of seasonally induced processes in the Mont Terri rock laboratory (Switzerland). Swiss Journal of Geosciences 110, 195–212. https://doi.org/10.1007/s00015-016-0252-1

Zimmerman, R.W., Bodvarsson, G.S., 1996. Hydraulic conductivity of rock fractures. Transport in Porous Media 23, 1–30. https://doi.org/10.1007/BF00145263

Zou, C., Zhai, G., Zhang, Guangya, Wang, H., Zhang, Guosheng, Li, J., Wang, Z., Wen, Z., Ma, F., Liang, Y., Yang, Z., Li, X., Liang, K., 2015. Formation, distribution, potential and prediction of global conventional and unconventional hydrocarbon resources. Petroleum Exploration and Development 42, 14–28. https://doi.org/10.1016/S1876-3804(15)60002-7

Zou, L., Dong, L., Ning, M., Huang, K., Peng, Y., Qin, S., Yuan, H., Shen, B., 2019. Quantifying the carbon source of pedogenic calcite veins in weathered limestone: implications for the terrestrial carbon cycle. Acta Geochimica 38, 481–496. https://doi.org/10.1007/s11631-019-00348-8

Acknowledgments

At this point, I would like to thank all the people who have continuously given me their support and have accompanied me on this journey.

I am grateful to …

… my supervisor Prof. Dr. Philipp Blum for the opportunity and encouragement to do a PhD. I want to thank you for your effort in motivating me to be more “pragmatic”, and of course for many conversations, discussions and brainstorming-sessions that always helped me to improve my work and skills. Thank you for always believing in me.

… Prof. Dr. Christoph Hilgers for his spontaneous willingness to be my co-examiner,

… PD Dr. Cornelius Fischer und Prof. Dr. Christoph Butscher for sharing their scientific experience, supporting my PhD, and for being in my board of examiners,

… the Federal Ministry of Education and Research (BMBF) for funding my PhD within the projects ResKin, ResKin_Move and SUBI,

… my co-authors Dr.-Ing. Christoph Naab, Xavier Ries, Dr. David Jaeggi, Dr. Elisabete Trindade Pedrosa, Marcel Reinhardt, Dr. Arne Jacob, Apl.-Prof. Dr. Frieder Enzmann and Prof. Dr. Michael Kersten for the great collaboration in paper-writing,

… Dr. Harald Milsch, Dr. Chaojie Cheng, Prof. Dr. Karsten Keller, Tim Gutjahr and PD Dr. Steffen Winter for the nice cross-institute, inter-university and interdisciplinary collaboration,

… the ResKin people Prof. Dr. Andreas Lüttge, Dr. Inna Kurganskaya, Ricarda Rohlfs, Prof. Dr. Laurence Warr, Dr. Georg Grathoff, Markus Peltz, Prof. Dr. Oleg Iliev, Dr. Torben Prill and Dr. Sebastian Osterroth for the continuous exchange during many project meetings and lots of fruitful discussions,

… Dr. Hagen Steger, Olaf Ukelis, Dr. Petra Huttenloch, Thomas Mutschler, Dr. Maria Carme Chaparro, Larissa Blesch, Claudia Riester, Dr. Linda Luquot and Kevin Altinger for the great support with my experiments and setups in the lab and beyond,

… Dr. Arne Jacob for his optimism and the evening bouldering sessions during our project meetings,

… Nicole Suteu, Ines Knoch, Janina Pech, Petra Linder and Elis Engelmann for their support in administrative matters,

… Kristie Ussher for proof-reading my papers,

… all colleagues from the Engineering and Hydrogeology group for the nice working atmosphere and the summer and Christmas parties,

… my colleagues and friends Dr. Carolin Tissen, Linda Schindler, Luisa Bienstein, Dr. Simon Schüppler, Dr. Paul Fleuchaus, Dr. Markus Merk, Dr. Simon Frank and Dr. Simon Breuer, for the great time in the office, unforgettable nights and – not to forget – for countless coffee breaks,

… my parents Mark and Karin Hale, my sister Julia Hale, Nikolai Fahrmeier and Kevin Altinger for your unwavering faith in me. You are and have been my biggest source of motivation and inspiration. I simply couldn´t have done this without you!

Declaration of authorship

Study 1 (Chapter 2)

Hale, S., Naab, C., Butscher, C., Blum, P., 2020. Method comparison to determine hydraulic apertures of natural fractures. Rock Mechanics and Rock Engineering 53, 1467–1476. https://doi.org/10.1007/s00603-019-01966-7

Sina Hale (SH) did all the measurements and analyzed the data with support from Christoph Naab (CN). Christoph Butscher (CB) and Philipp Blum (PB) provided scientific supervision. SH wrote the initial draft and all authors (SH, CN, CB and PB) discussed the results and substantially contributed to editing and reviewing the manuscript.

Study 2 (Chapter 3)

Hale, S., Ries, X., Jaeggi, D., Blum, P., 2021. Mechanical and hydraulic properties of the excavation damaged zone (EDZ) in the Opalinus Clay of the Mont Terri rock laboratory, Switzerland. Solid Earth 12, 1581–1600. https://doi.org/10.5194/se-12-1581-2021

Sina Hale (SH), Xavier Ries (XR) and Philipp Blum (PB) carried out the field measurements in the Mont Terri underground rock laboratory, David Jaeggi (DJ) handled the organization and implementation of the field work. Formal analysis was done by SH and XR. PB supervised SH and XR and was responsible for funding acquisition. SH wrote the initial draft and all authors (SH, XR, DJ and PB) discussed and interpreted the results and substantially contributed to editing and reviewing the manuscript.

Study 3 (Chapter 4)

Hale, S., Pedrosa, E.T., Jacob, A., Reinhardt, M., Enzmann, F., Kersten, M., Butscher, C., Blum, P. Upscaling calcite dissolution rates in a tight reservoir sandstone. Environmental Earth Sciences (under review)

Conceptualization of the experiments and the manuscript was developed by Sina Hale (SH), Elisabete Trindade Pedrosa (ETP), Arne Jacob (AJ), Marcel Reinhardt (MR), Frieder Enzmann (FE), Michael Kersten (MK), Christoph Butscher (CB) and Philipp Blum (PB). SH and ETP prepared the samples and carried out the experiments. AJ, MR and FE were responsible for the computer tomography measurements. SH, ETP, AJ and MR analyzed the data, performed necessary computations and visualized the results. FE, MK, CB and PB provided critical feedback and contributed to the interpretation of the results. FE, MK, CB and PB were responsible for funding acquisition, project administration and supervision. SH wrote the original draft of the manuscript with support from ETP and AJ. All authors substantially contributed to editing and reviewing the paper.

Statements on the contribution of Sina Hale (SH) to the studies of Cheng et al. (2020), Gutjahr et al. (2021) and Jacob et al. (2021) can be found directly in Chapters 5.1, 5.2 and 5.3.

Eidesstattliche Versicherung

Eidesstattliche Versicherung gemäß § 6 Abs. 1 Ziff. 4 der Promotionsordnung des Karlsruher Instituts für Technologie (KIT) für die KIT-Fakultät für Bauingenieur-, Geo- und Umweltwissenschaften

1. Bei der eingereichten Dissertation zu dem Thema *„Coupled hydraulic-mechanical-chemical processes in porous and fractured rocks“* handelt es sich um meine eigenständig erbrachte Leistung.
2. Ich habe nur die angegebenen Quellen und Hilfsmittel benutzt und mich keiner unzulässigen Hilfe Dritter bedient. Insbesondere habe ich wörtlich oder sinngemäß aus anderen Werken übernommene Inhalte als solche kenntlich gemacht.
3. Die Arbeit oder Teile davon habe ich bislang nicht an einer Hochschule des In- oder Auslands als Bestandteil einer Prüfungs- oder Qualifikationsleistung vorgelegt.
4. Die Richtigkeit der vorstehenden Erklärungen bestätige ich.
5. Die Bedeutung der eidesstattlichen Versicherung und die strafrechtlichen Folgen einer unrichtigen oder unvollständigen eidesstattlichen Versicherung sind mir bekannt.

Ich versichere an Eides statt, dass ich nach bestem Wissen die reine Wahrheit erklärt und nichts verschwiegen habe.

Karlsruhe, 10.01.2022 M.Sc. Sina Katrin Hale